
Aerosol microphysical properties during anticyclonic flow conditions over Europe

Thomas Hamburger



München 2010

Aerosol microphysical properties during anticyclonic flow conditions over Europe

Thomas Hamburger

Dissertation
an der Fakultät für Physik
der Ludwig-Maximilians-Universität
München

vorgelegt von
Thomas Hamburger
aus München

München, den 22. Dezember 2010

Erstgutachter: PD Dr. Andreas Petzold

Zweitgutachter: Prof. Dr. Bernhard Mayer

Tag der mündlichen Prüfung: 23. Februar 2011

Contents

Contents	i
1 Introduction	1
2 Basics of aerosol microphysical properties	7
2.1 Aerosol sources, transformations and sinks	7
2.2 Aerosol size distribution	11
2.3 Aerosol optical properties	14
2.3.1 Scattering and absorption of light by aerosol particles	14
2.3.2 Changes of optical properties due to changes in aerosol composition	19
2.3.3 Changes of optical properties due to changes in relative humidity	21
3 Methods and implementation of aerosol airborne measurements	25
3.1 Methods of aerosol airborne measurements and data analysis	25
3.1.1 Aerosol number concentrations	25
3.1.2 Aerosol size distributions	26
3.1.3 Aerosol mixing state	28
3.1.4 Scattering and absorption of light by aerosol particles	30
3.1.5 Processing the data of aerosol airborne measurements	32
3.2 Development of a new method to analyse air mass trajectories	36
3.2.1 Air mass trajectories	36
3.2.2 The trajectory calculation and analysis tool FLYTUL	37
3.2.3 The EDGAR 3.2 Fast Track 2000 dataset	39
3.2.4 Boundary layer indices	41
3.2.5 Classification of air mass trajectories using time weighted averaging	42
3.3 The EUCAARI-LONGREX campaign	46
3.3.1 Objectives and strategy of the EUCAARI-LONGREX campaign	47
3.3.2 The aircraft and instrumental setup	48
3.3.3 Implementation of the EUCAARI-LONGREX campaign	50

4	Results and discussion of aerosol measurements obtained during the EUCAARI-LONGREX campaign in May 2008	55
4.1	The meteorological situation in May 2008	55
4.1.1	The evolution of the meteorological situation over Europe	55
4.1.2	The anticyclonic blocking event	58
4.1.3	The synoptic situation within a climatological context	59
4.1.4	The transport pathways of anthropogenic pollution within the anticyclonic wind field	61
4.2	The impact of anthropogenic pollution on aerosol microphysical properties in remote regions: A case study southwest of Ireland	64
4.2.1	Aerosol optical depth retrieved from satellite imagery and LIDAR profiles	64
4.2.2	Vertical profiles of in-situ measured aerosol microphysical properties	67
4.2.3	Aerosol size distributions and deduced optical properties within the observed pollution layers	70
4.2.4	Transport analysis of polluted air masses	76
4.2.5	Comparison of airborne measurements with previous studies at Mace Head, Ireland	77
4.3	Temporal evolution of the pollution situation over Europe in May 2008: Analysis of ground based measurements	80
4.3.1	Ground based measurements: Time series data	80
4.3.2	Ground based measurements: Discussion	87
4.3.3	Anthropogenic origin of increased accumulation mode number concentrations measured at the ground stations	89
4.3.4	Ground based measurements compared with airborne measurements	90
4.4	The vertical aerosol distribution over Europe in May 2008	93
4.4.1	The temporal evolution of the vertical number concentration over South Germany	93
4.4.2	Regional vertical profiles during anticyclonic conditions	97
4.5	The horizontal aerosol distribution over Europe in May 2008	104
4.5.1	Vertical classification of the troposphere	104
4.5.2	Horizontal distribution of aerosol microphysical properties during anticyclonic conditions	105
4.5.3	Size distributions measured over Europe	109
4.5.4	Chemical composition of aerosol particles measured aboard the BAe-146	113

5	Application of a new trajectory analysis method	115
5.1	Comparison of model data with in-situ measurements	116
5.2	Source strength and cloud cover	119
5.3	Air mass classification using temporal weighted averages	126
5.3.1	Classification of air masses into defined age classes	126
5.3.2	Air mass classification for ground based measurements	127
5.3.3	Air mass classification using different sigma factors sf	130
5.3.4	Air mass classification for airborne measurements	132
5.4	The applicability of FLYTUL	134
6	Summary & conclusion	137
	Bibliography	141
A	Tables	159
B	Figures	167
	List of symbols	175
	List of abbreviations	179
	Acknowledgements	181
	Curriculum Vitae	183

Abstract

Aerosols play an important role in atmospheric physics. The airborne particles in diameters of a few nanometres to some micrometres affect the climate system by altering the energy balance of the atmosphere. However, the quantification of the climate effect is an open question until today. Large uncertainties exist in the knowledge of the global aerosol distribution and their properties.

The present work assesses the spatial and temporal distribution and variability of aerosol particles and their properties above Europe during stable synoptic conditions. A data set of airborne measurements unique in its spatial dimensions over Europe was obtained within this work in May 2008. It covers microphysical aerosol properties throughout the whole tropospheric column above Central and Western Europe. The airborne aerosol measurements were performed aboard the DLR Falcon 20 within the EUCAARI-LONGREX field campaign. The aircraft operated from Oberpfaffenhofen, Germany.

The influence of source contributions on the aerosol particles and ageing processes over a densely populated region were measured and analysed using a new developed trajectory analysis tool (FLYTUL). The trajectory analysis tool uses the EDGAR 3.2 Fast Track 2000 dataset to quantify the source contributions along each trajectory of a trajectory bundle for a qualitative classification of the air mass. Meteorological information along the air mass transport pathway is retrieved from the ECMWF.

The prevailing anticyclonic conditions led to an increase of particulate matter in the continental boundary layer. Total aerosol number concentrations reached 22000 cm^{-3} , number concentrations of accumulation mode particles 1600 cm^{-3} . The volume fraction of secondary aerosol matter increased to 95 % for submicron particles due to coagulation processes and condensation of the abundant aerosol precursor gases within the dry and stable meteorological conditions.

A positive gradient of particulate matter was observed along the anticyclonic transport pathway from the Baltic Sea towards the Benelux States and Southern England. The vertical aerosol distribution featured clean conditions with respect to particles in the lower free troposphere and suggested a trapping of aerosol particles inside the boundary layer.

Undisturbed transport of continental anthropogenic pollutants to remote regions was observed and a direct effect on the radiative properties of the aerosol population was found. 90 % of the aerosol optical depth above the Atlantic southwest of Ireland was caused by the pollution layers, which originated from continental Europe.

The analysis of air mass transport and ageing processes indicated that the main coagulation process of aerosol particles happens within the first 12–24 h. The saturation of the coagulation process occurred after two days.

Kurzfassung

Aerosole spielen eine wichtige Rolle im Bereich der Atmosphärenphysik. Partikel mit Durchmessern von wenigen Nanometern bis einigen Mikrometern beeinflussen das Klima indem sie die Energiebilanz der Atmosphäre ändern. Die Quantifizierung dieses Effektes ist jedoch bis heute ein ungelöstes Problem. Das Wissen um die globale Aerosolverteilung und deren Eigenschaften ist mit großen Unsicherheiten behaftet.

Die vorliegende Arbeit bestimmt die räumliche und zeitliche Verteilung und Variabilität von Aerosolpartikeln und deren Eigenschaften während stabilen synoptischen Bedingungen über Europa. Während dieser Arbeit wurde ein in seiner räumlichen Ausdehnung über Europa einmaliger Datensatz von flugzeuggetragenen Messungen gewonnen. Mikrophysikalische Aerosoleigenschaften wurden über den gesamten Höhenbereich der Troposphäre über Mittel- und Westeuropa gemessen. Die Messungen wurden auf dem Forschungsflugzeug DLR Falcon 20 während der EUCAARI-LONGREX Messkampagne im Mai 2008 durchgeführt. Die Flüge starteten von Oberpfaffenhofen, Deutschland aus.

Der Einfluss verschiedener Quellbeiträge über dicht bevölkerten Gebieten und von Alterungsprozessen auf Aerosolpartikel wurde gemessen und mit Hilfe eines neu entwickelten Trajektorienanalyseprogramms ausgewertet (FLYTUL). Das Trajektorienanalyseprogramm verwendet die EDGAR 3.2 Fast Track 2000 Datenbank um Quellbeiträge entlang jeder einzelnen Trajektorie eines Trajektorienbündels zu bestimmen. Somit kann eine Klassifizierung der gemessenen Luftmassen durchgeführt werden. Meteorologische Parameter entlang des Transportweges werden vom ECMWF geliefert.

Die vorherrschenden Hochdruckbedingungen führten zu einer Anhäufung von Partikeln in der kontinentalen Grenzschicht. Die Gesamtanzahlkonzentration der Partikel erreichte Werte um 22000 cm^{-3} , die Anzahlkonzentration der Akkumulationsmode 1600 cm^{-3} . Durch Koagulation von Partikeln und Kondensation von Aerosolvorläufergasen erhöhte sich der Volumenanteil des sekundären Aerosols auf 95 % für Partikel im Sub-Mikrometerbereich.

Eine Zunahme der Partikelmasse konnte während des Luftmassentransports von der Ostsee über die Beneluxstaaten nach Südengland beobachtet werden. Der ungehinderte Transport von kontinentalen anthropogenen Verschmutzungen in abgelegene Gebiete wurde beobachtet und ein direkter Effekt auf die optischen Eigenschaften des lokalen Aerosols gefunden. 90 % der optischen Dicke über dem Atlantik südwestlich von Irland wurde von Verschmutzungsschichten erzeugt, welche von Kontinentaleuropa stammten.

Die Analyse des Luftmassentransports und der Alterungsprozesse wiesen darauf hin, dass innerhalb der ersten 12–24 h der Großteil des Koagulationsprozesses abläuft. Die Koagulation erfährt ihre Sättigung nach zwei Tagen.

Parts of this work are published in:

Hamburger, T., McMeeking, G., Minikin, A., Birmili, W., Dall'Osto, M., O'Dowd, C., Flentje, H., Henzing, B., Junninen, H., Kristensson, A., de Leeuw, G., Stohl, A., Burkhart, J. F., Coe, H., Krejci, R., and Petzold, A.: Overview of the synoptic and pollution situation over Europe during the EUCAARI-LONGREX field campaign, *Atmospheric Chemistry and Physics*, 11, 1065–1082, 2011.

McMeeking, G. R., Hamburger, T., Liu, D., Flynn, M., Morgan, W. T., Northway, M., Highwood, E. J., Krejci, R., Allan, J. D., Minikin, A., and Coe, H.: Black carbon measurements in the boundary layer over western and northern Europe, *Atmospheric Chemistry and Physics*, 10, 9393–9414, 2010.

Hamburger, T., Minikin, A., Dörnbrack, A., Petzold, A., Rüba, H., Schlager, H., Scheibe, M., Ibrahim, A., Coe, H., McMeeking, G., Morgan, W. T., and Stohl, A.: Aerosol microphysics during anticyclonic conditions over Europe during EUCAARI-LONGREX, *European Aerosol Conference 2009, Karlsruhe*, Abstract T170A21

Hamburger, T., Minikin, A., Petzold, A., McMeeking, G. R., Coe, H., Junninen, H., Kristensson, A., Henzing, B., Dall'Osto, M., Birmili, W., Flentje, H., and Krejci, R.: Aerosol microphysical properties during anticyclonic conditions over Europe during EUCAARI-LONGREX, *International Aerosol Conference 2010, Helsinki*, Abstract 6C4

Chapter 1

Introduction

Aerosol is a mixture of liquid or solid particles in a carrier gas. The aerosol particles are small airborne particles, which occur all over our atmosphere. Although every kind of airborne particle can be considered as an aerosol particle independent of its size, only particles in diameters less than a few micrometers are usually the scope of aerosol science. Larger particles in the atmosphere most commonly exist of hydrometeors, i.e. cloud droplets or ice crystals, and are covered by cloud physics. Nevertheless, aerosol and cloud physics are strongly related to each other. Aerosol particles appear to be small and normally cannot be detected by human eyes. However, their effects on our life and environment are significant and can take considerable scales.

Why do we care about aerosol particles?

The effects of aerosols reach from human health problems to the influence of particles on the global radiation budget and climate effects (Oberdörster et al., 2005; Kulmala, 1999). Most problems in aerosol science have in common that the detailed processes and interactions of particles with their environment are not well understood. For instance, several studies using statistical approaches demonstrated that aerosols could have health effects on people exposed to fine particles. Fine particles generated by combustion engines may cause sensitization to allergic reactions (Pöschl, 2005) or malfunctions of heart and lung (Kennedy, 2007). In addition, not only exposures to aerosol particles close to the sources might cause health effects. Increased mortality due to lung cancer and cardiopulmonary deceases could be connected to intercontinental transport of polluted air masses (Liu et al., 2009). Nevertheless, the authors point out that the details in the interaction between aerosol particles and the cardiopulmonary system is yet not well understood.

Next to the effects of aerosols on human health, the effect of airborne particles on the climate system of our earth is the major field in aerosol science. The alteration of visible light due to airborne particles is for example an effect we can directly observe almost every day (Horvath, 1981). The extinction of light by particles causes blue haze due to natural particles over forest areas (Went, 1960) or reduces the visibility due to increasing concentrations of anthropogenic particles in urban areas (White and Roberts, 1977; Patterson and Wagman, 1977). Also meteorological conditions and air mass history have an impact on the visibility as they alter the physicochemical properties of the prevailing particles (Fenn et al., 1981). Most studies, which focus on the impact of aerosol particles on atmospheric visibility, have been performed in the last decades. However, John Tyndall made first experiments on the effect of particles and gaseous molecules on solar radiation as long ago as the nineteenth century (Gentry, 1997). He discovered that fine particles can be detected by light which is scattered by the occurring particles. This effect is now known as the Tyndall effect. Tyndall used this effect e.g. to detect pollution constituents in the air or in water. He also suggested that fine particles and gaseous species have influence on the energy balance to the earth, i.e. alter the radiative heat transfer in the atmosphere.

The effect of aerosol particles on atmospheric radiative transfer and thus on climate is still an open question to the present. Aerosols can have a cooling effect on the atmosphere by increasing the albedo, i.e. more solar radiation is scattered back into space (e.g. Haywood and Boucher, 2000). On the other hand they can heat the atmosphere due to particles containing light absorbing substances (Charlson and Pilat, 1969). The quantification of the effect of aerosols on climate was one of the major tasks in aerosol science in the last years and the complexity of the problem limits the accuracy of the statements until today. The effects are classified into the direct aerosol effect, i.e. the direct interaction of particles with radiation, and the indirect aerosol effect, i.e. the influence of particles on clouds and the subsequent radiative effects (e.g. Penner et al., 2004). The complexity of the problem gets apparent by having a short look to the indirect aerosol effect. Increasing concentrations of particles, which act as condensation nuclei for cloud droplets, increase the concentration of cloud droplets. As a result of the increased concentration of cloud droplets the optical depth of the cloud and the cloud albedo increase (Twomey effect; Twomey (1977c)). In addition, the increased concentration of particles leads to smaller cloud droplets at constant water content and therefore may prevent or delay precipitation. This results in an extension of the lifetime of clouds. Models indicate that both effects cool the atmosphere. On the other hand particles containing absorbing matter may cause evaporation of cloud particles and reduce cloud cover and cloud optical depth. This semi-direct effect might cause a

warming of the earth-atmosphere system (Lohmann and Feichter, 2005). According to current knowledge (Forster et al., 2007), the overall aerosol effect cools the atmosphere and thus counteracts the warming by greenhouse gases. However, the cooling effect of aerosol particles is far from being quantified and the uncertainties are large. Major uncertainties appear to result from insufficient quantification of the global aerosol load leading to uncertainties in emission factors used for modelling the atmospheric burden of greenhouse and particle precursor gases and aerosol species. In addition, large uncertainties arise in the quantification of the indirect aerosol effect. Measurements of trace gases and aerosol particles help to improve models and emission databases and are therefore an essential tool to decrease the uncertainties (Laj et al., 2009).

What has been done so far in aerosol measurements?

A major part of in-situ observations is realised by ground-based measurements. Ground-based measurements are frequently performed at permanent measurement sites build for atmospheric research. Several measurement sites are associated in European and worldwide networks built for air quality monitoring, e.g. EUSAAR (European Super-sites for Atmospheric Aerosol Research), EMEP (European Monitoring and Evaluation Programme), and Global Atmosphere Watch (GAW). The networks provide long-term in-situ data of near-ground air pollutants (van Dingenen et al., 2004; Putaud et al., 2004, 2010). The measurement sites over Europe cover urban sites located close or within cities as well as remote sites in rural areas. Depending on their location, the measurements serve to gain knowledge of different aerosol species and processes. The constituents and evolution of marine aerosol can be observed at sites located close to the ocean like Ireland (Kleefeld et al., 2002; Jennings et al., 2003; Junker et al., 2006; Yoon et al., 2007; O'Connor et al., 2008) and new particle formation in clean air masses can be studied preferably at remote regions e.g. in Scandinavia (Kulmala et al., 2004; Lyubovtseva et al., 2005; dal Maso et al., 2007; Sogacheva et al., 2008). Anthropogenic influence on particles can be best observed in the densely populated regions of Central Europe. The observations range from measurements for air quality purposes in cities and urban areas (Mayer, 1999; Kukkonen et al., 2005) to studies of changing (decreasing) concentrations of pollutants in formerly highly polluted regions in Eastern Germany (Müller, 1999; Hamed et al., 2010) and measurements of rural and free tropospheric aerosol at elevated stations located on hills and mountains (Hock et al., 2008; Venzac et al., 2009). Particular attention is paid to the transport of aerosol particles and their impact on the aerosol budget at remote regions. The effect of air mass transport and subsequently the effect of meteorological conditions and source regions along the transport pathway was studied in combination with the

ground-based measurements at remote sites in Western and Northern Europe (Huang et al., 2001; Tunved et al., 2003, 2005; Niemi et al., 2009) and rural regions in Central Europe (Spindler et al., 2010).

However, as the name already indicates, ground-based in-situ measurements are limited to the ground. Even if some ground stations are located on hills and mountains, a lack of vertical information on aerosol species is apparent. Ground based remote sensing measurement networks like AERONET (Aerosol Robotic Network) provide vertical information retrieved from sun photometer and radiometer measurements. However, the remote sensing data have to be validated with in-situ measurements. Airborne aerosol in-situ measurements provide the ideal platform to retrieve essential information of the vertical particle distribution. A lot of effort was made in the last decade to retrieve aerosol data throughout the tropospheric column. Among other studies above the European continent aerosol radiative properties were analysed over Eastern Germany (Ansmann et al., 2002; Petzold et al., 2002), long-range transport of North American anthropogenic emissions and forest fire plumes were measured over Western Europe (Methven et al., 2006; Petzold et al., 2007), and ship emissions were probed in the marine boundary layer above the English Channel (Petzold et al., 2008). In-situ measurements in the upper troposphere comprised studies of the outflow of thunderstorms (Huntrieser et al., 2002), aerosol and cirrus cloud properties (Minikin et al., 2003) and aircraft emissions and contrails (Voigt et al., 2010). Like all other airborne in-situ measurements, these campaigns delivered valuable data about atmospheric aerosol. Nevertheless, the measurements focussed either on certain locations or on specific altitude ranges over Europe depending on the scope of the respective campaign. All measurements together provide a dataset, which covers almost the complete European continent. However, the flights were performed during different years and different seasons. Therefore, measurements covering the whole troposphere over a wide horizontal range performed during similar conditions would be useful to derive an entire overview of the aerosol distribution over Europe.

What will be done in this work?

Chin et al. (2009) points out the importance of aerosol measurements to reduce the uncertainties in assessing the anthropogenic impacts on climate. To evaluate the effects of aerosol particles on climate one has to take the high spatial and temporal variability of aerosol concentration and properties into account. Formation and evolution of aerosol particles have to be measured. Chin et al. (2009) set these tasks to high priority in the report on atmospheric aerosol properties and climate impacts by the U.S. Climate

Change Science Program (CCSP).

Stable synoptic conditions during high pressure situations lead to favourable conditions to observe the spatial and temporal distribution and evolution of aerosol particles on a continental scale during several consecutive days. The present work comprises airborne measurements and the analysis of atmospheric aerosol properties as well as air mass transport analysis to contribute to answering the following questions on microphysical aerosol properties during stable synoptic conditions over Europe:

- What is the spatial and temporal distribution and variability of aerosol particles?
- How do stable synoptic conditions affect the aerosol particles in the boundary layer and free troposphere?
- How do fresh or aged emissions affect the aerosol properties?
- What is the turnover time from fresh to aged aerosol particles and when comes the ageing process to its saturation?

A data set of airborne measurements unique in its spatial dimensions over Europe was collected within this work to achieve the listed objectives. The flights reached a horizontal extension from Austria to the Baltic Sea and from Western Poland to the Atlantic west of Ireland. They covered the whole tropospheric column. The measurements open the possibility to quantify the probed aerosol properties over a wide horizontal and vertical range at comparable conditions. The retrieved dataset also enables the investigation of formation and transformation of atmospheric aerosol over a variety of different source regions. Meteorological analysis and an air mass transport analysis tool developed within this work (FLYTUL) are used to interpret the retrieved data with a focus on the prevailing meteorological conditions and air mass history.

The tasks of the present work covered:

- Preparation of the aerosol in-situ measurements aboard the DLR Falcon 20 aircraft.
- Meteorological forecast for flight planning.
- Airborne aerosol in-situ measurements.
- Development of a trajectory analysis tool specified for airborne aerosol measurements.
- Meteorological analysis.

- Analysis of aerosol measurements with a focus on the prevailing meteorological conditions and air mass history.

The present section is followed by a short introduction to the basics of aerosol microphysical properties (Section 2), which are required to understand the methods of aerosol in-situ measurements (Section 3.1) and the subsequent analysis. The new trajectory analysis tool is presented in Section 3.2. After a short overview of the measurement campaign (Section 3.3) and the analysis of the meteorological conditions during the campaign (Section 4.1) a case study above the Atlantic southwest of Ireland shows the effect of European anthropogenic pollution on aerosol properties in remote regions (Section 4.2). The vertical and horizontal distribution of aerosol properties over Europe is analysed in Sections 4.3 and 4.5. The trajectory analysis tool will finally be employed to the measurements in Section 5.

Chapter 2

Basics of aerosol microphysical properties

2.1 Aerosol sources, transformations and sinks

Aerosol particles evolve from an abundance of sources on the earth's surface and the atmosphere. The aerosol comprises natural particles consisting of biological material, wind-borne dust or sea spray, and anthropogenic particles mainly resulting from combustion processes or agricultural land use. The properties of aerosol particles are strongly correlated to the particle sources and the subsequent transformation processes. Considering the different sources particles can be classified into two major groups, *primary particles* directly emitted into the atmosphere and *secondary particles* formed by chemical interactions of so-called aerosol precursor gases in the atmosphere. The two different source types result in particles of two distinct size classes. Secondary aerosol usually contains fine particles in diameters smaller than 1 μm , primary aerosol contains coarse particles in diameters larger than 1 μm . A variety of exceptions occur of course in the field, e.g. soot particles from combustion sources which are considered as primary particles appear in the low sub-micron size range. A schematic evolution following the transformations due to condensation of precursor gases, coagulation of particles, chemical interactions, and activation as condensation nuclei and subsequent formation of cloud droplets is outlined in Figure 2.1 (Raes et al., 2000).

Nucleation is the formation process of secondary particles. Two processes describe the formation of particles through nucleation. The *homogeneous nucleation*, which describes the self-nucleation of precursor gases forming particles, and the *heterogeneous nucleation*, which describes the condensation of the precursor gases on pre-existing condensation nuclei. Major compounds of aerosol precursor gases are sulphur from combustion of fossil fuel or organic matter and biological decay, nitrogen from fuel

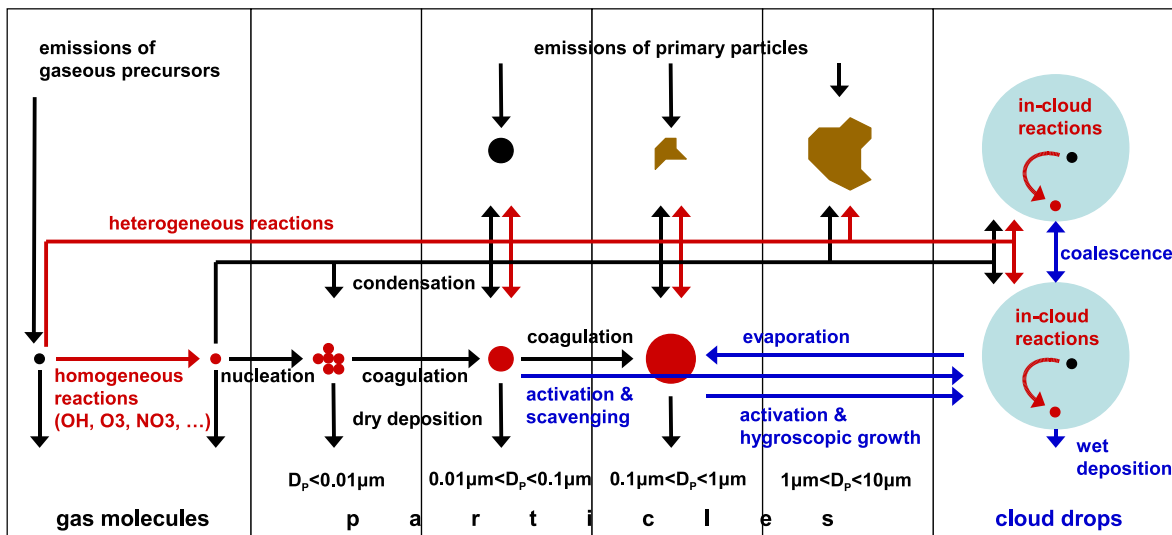


Figure 2.1: Evolution of the tropospheric aerosol after Raes et al. (2000).

burning especially at high temperatures and use of fertilizer, and hydrocarbons like α -pinene and β -pinene emitted by e.g. pines or spruces. The vapour species are oxidized in the atmosphere and undergo photochemical processes. Major products of the oxidation process, which serve as condensable vapours are e.g. sulphuric acid (H_2SO_4), nitric acid (HNO_3), or pinic acid (Seinfeld, 1986).

To determine the conditions for particle nucleation we consider a cluster of molecules from aerosol precursor gases as a continuous particle embryo. Thus, we can describe the energetic state of the molecule cluster neglecting the structure and orientation of the single molecules. For the following, we only need to know if the molecule is inside, outside or on the surface of the particle embryo, or in the gaseous phase. The energy dissipated or released during the phase transition of the molecules can be written as the Gibbs free energy ΔG of a spherical particle embryo (Twomey, 1977a):

$$\Delta G = \frac{4\pi}{3} r^3 \Delta G_V + 4\pi r^2 \sigma. \quad (2.1)$$

The first term describes the change of Gibbs free energy due to the change of the volume of the condensed phase without changing the surface (ΔG_V). The second term depicts the change of energy due to the change of the surface of the particle embryo with radius r . The free surface energy σ is equivalent to the surface tension. As σ is always positive ΔG will always increase for positive ΔG_V . Thus, more energy would be required to increase the radius of the particle and evaporation would be energetically more favourable. For negative ΔG_V we can find a maximum of ΔG at a particle radius

$$r^* = -\frac{2\sigma}{\Delta G_V}. \quad (2.2)$$

If the particle radius r exceeds the critical radius r^* , the Gibbs free energy ΔG decreases and the system gets into an energetically more favourable state for larger particles, i.e. condensation and particle growth occur. Using the first law of thermodynamics and the ideal gas law we can derive the Kelvin or Thomson-Gibbs equation from Equation 2.2 (Hinds, 1999)

$$S_R = \exp\left(\frac{2\sigma M}{\rho RT r^*}\right). \quad (2.3)$$

S_R is the saturation ratio at temperature T for a particle embryo of density ρ , M the molecular mass, and R the gas constant. S_R defines the ratio of the vapour pressure of the precursor gas above the particle surface to its saturated vapour pressure and is always greater than 1. This means that equilibrium between evaporation and condensation only occurs for supersaturation. S_R decreases for increasing particle radius and precursor gases can condensate at lower vapour pressures. The effect of decreased S_R above larger particles with less curvature of the surface is called Kelvin effect. The saturation vapour pressure also decreases if the particle consists of different chemical components. The effect is known as Raoult's law. However, the contribution of the Kelvin effect is three times as large as the effect given by Raoult's law at the point of critical saturation (Seinfeld, 1986).

Existing particles covered with a thin film of condensed precursor gases act like larger particles of the vapour species. The saturation vapour pressure over the surface is reduced and heterogeneous nucleation and condensation takes place at the cost of homogeneous nucleation. Thus, conditions in the absence of pre-existing particles are favourable for homogeneous nucleation. If particles already exist, they will grow due to the condensation of the precursor gases on the particles on the cost of newly formed secondary aerosol. Another growth process is coagulation of particles, i.e. the particles collide and adhere. Particles collide due to Brownian motion, inter-particle forces like van der Waals and Coulomb forces, turbulent motion, or gravitational settling (Seinfeld, 1986). Further particles grow due to chemical processing in non-precipitating clouds (O'Dowd et al., 2000).

Sinks of aerosol particles are dry and wet deposition. The removing processes of the aerosol particles can vary for different particle sizes. Dry deposition of fine particles happens by diffusion of the particles to the earth's surface while coarse particles settle gravitationally. Dry removal of fine particles in the diameter range between 0.1-1.0 μm

is a very slow process and wet removal is the dominating sink. The particles are activated in clouds and removed by subsequent precipitation (Raes et al., 2000).

2.2 Aerosol size distribution

Regarding the different sources, evolution processes and sinks one can understand that aerosol particles in the atmosphere cover a large size range. Aerosol particles cover particles in diameters of a few nanometres resulting from nucleation, accumulated particles in the sub-micron size range formed by condensation and coagulation, and reach the size of coarse particles consisting of sea salt or dust in diameters of a few micrometres. In Section 2.1 we have introduced the separation into fine and coarse particles based on the different sources, evolution processes and sinks. A further size resolved classification leads to the traditional definition of four aerosol size modes. The *nucleation mode* (Nuc: $D_p < 0.01 \mu\text{m}$), the *Aitken mode* (Ait: $0.01 \mu\text{m} < D_p < 0.1 \mu\text{m}$), the *accumulation mode* (Acc: $0.1 \mu\text{m} < D_p < 1 \mu\text{m}$), and the *coarse mode* (Coa: $D_p > 1 \mu\text{m}$). The total aerosol comprises the sum of the different single aerosol modes. The aerosol modes do not only cover a large size range, the number concentrations of particles in several modes can vary by the order of magnitudes from 10 to 10000 cm^{-3} . To cover the features of each aerosol mode, concentrations per particle size (*size distributions*) are presented on logarithmic scales for concentrations and particle sizes (Raes et al., 2000).

It was found that log-normal distributions fit single aerosol modes. Although these distributions are only empirical fits to the atmospheric aerosol distribution and a physical basis is still missing they are widely used to describe the particle size distribution (Whitby, 1978). The number size distribution defines the concentration of particles per diameter interval (Seinfeld, 1986)

$$dN = n(D_p)dD_p, \quad (2.4)$$

$$\text{with } n(D_p) = \frac{N}{\sqrt{2\pi}D_p \ln GSD} \exp\left(-\frac{(\ln D_p - \ln CMD)^2}{2(\ln GSD)^2}\right). \quad (2.5)$$

The log-normal distribution is defined by the number concentration N , the count median diameter CMD , and the geometric standard deviation GSD . The CMD is the median diameter of the particle population associated with the log-normal distribution. The GSD governs the width of the aerosol mode and gives an indication on the heterogeneity of the particles that form the mode with respect to their sizes. A GSD of unity indicates *monodisperse aerosol*, a GSD greater than 1 *polydisperse aerosol* due to the logarithmic nature of the distribution. Finally, we can calculate the number size distribution per interval of the decadic logarithm of the diameters:

$$\frac{dN}{d \log D_p} = n(D_p) \frac{dD_p}{d \log D_p}. \quad (2.6)$$

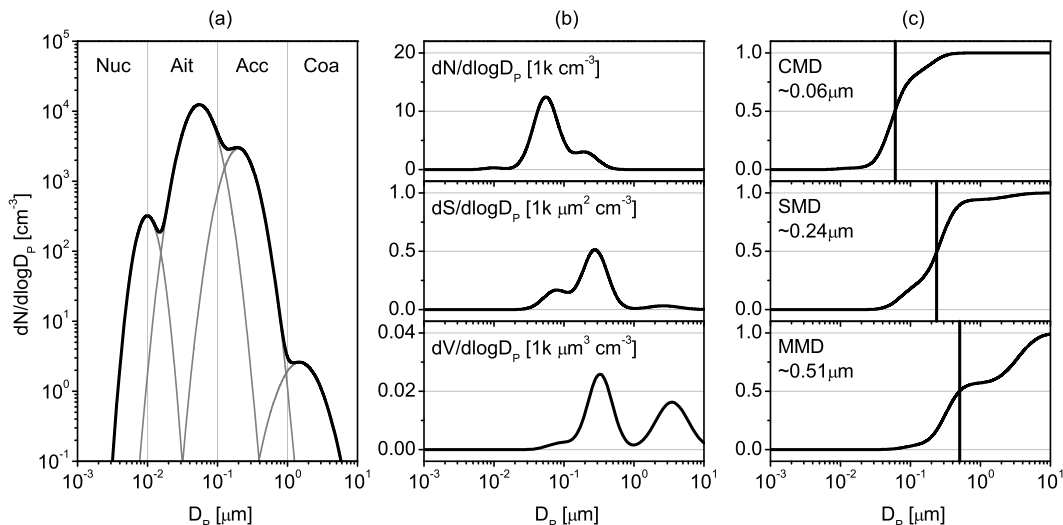


Figure 2.2: Example of a typical multimodal size distribution of urban air masses. The left panel shows the single modes of the size distribution (Nuc: nucleation mode, Ait: Aitken mode, Acc: Accumulation mode, Coa: coarse mode). The panel in the centre shows the number, surface, and volume size distribution from top to bottom, respectively. The cumulative distribution of number, surface and volume is shown in the right panel and the respective count median diameter CMD , surface median diameter SMD , and mass median diameter MMD are indicated by vertical lines.

Based on the number size distribution we can also derive the surface and volume size distributions for spherical particles to analyse the aerosol surface area and volume with respect to particle size:

$$\frac{dS}{d \log D_p} = \pi D_p^2 n(D_p) \frac{dD_p}{d \log D_p}, \quad (2.7)$$

$$\frac{dV}{d \log D_p} = \frac{1}{6} \pi D_p^3 n(D_p) \frac{dD_p}{d \log D_p}. \quad (2.8)$$

A typical aerosol size distribution containing the number size distributions of the single modes (Nuc, Ait, Acc, and Coa) is shown in Figure 2.2 a. The area under the curve reflects the number concentrations of particles within a certain diameter range. This gets more evident in Figure 2.2 b. The graphs show the number, surface, and volume size distributions from the top to the bottom. Concentrations are plotted on a linear scale. Now we see clearly which aerosol mode dominates the respective dis-

tributions. The Aitken mode dominates the number of the total aerosol distribution whereas the accumulation mode provides the surface. Both, the accumulation and the coarse mode, affect the total aerosol volume. A similar result arises using the respective median diameters. The median diameter defines the diameter for which 50% of the total cumulated distribution of a parameter is reached by summing up all concentrations for diameters smaller than the median diameter. Figure 2.2 c shows that the median diameter increases from number, via surface to volume.

Size resolved concentrations of the atmospheric aerosol give important additional information to describe properties of the aerosol bulk. Aerosol particles of different sizes have different effects on e.g. forming cloud droplets (Twomey, 1977b) or altering the transport of radiation through the atmosphere and decreasing visibility (Horvath, 1981). The basics of aerosol optical properties are discussed in the following section. Detailed optical theory of aerosol particles can be found in Bohren and Huffman (1983).

2.3 Aerosol optical properties

It is known since decades that aerosol particles have direct effects on the atmospheric radiative transfer (e.g., Ångström, 1962; Charlson and Pilat, 1969). However, the quantification of these effects is difficult due to the uncertainties in the quantification of the global aerosol distribution and aerosol properties. Hence, these effects are still within the scope of research and occupy a large part of recent aerosol science (Forster et al., 2007, and references therein). To examine the effects of known aerosol particles on the radiative transfer within the atmosphere we have to consider the optical properties of these particles and of the single aerosol particles in particular. The optical effects of an aerosol particle result from scattering and absorption of radiation on the particle (Bohren and Huffman, 1983). Basically scattering can be considered as the excitation of the electric charges of a particle by an electromagnetic wave and its reradiation into space. The transformation of the incident electromagnetic wave into other forms of energy like thermal energy describes the absorption of radiation by the particle. Both, scattering and absorption are considered together as extinction. The optical properties of aerosol particles and their effects strongly depend on the size, shape, and composition of the particles. Their theoretical basics will be discussed briefly in the following.

2.3.1 Scattering and absorption of light by aerosol particles

The discussion of extinction of light by aerosol particles and single particles in particular follows in general the work of Bohren and Huffman (1983).

General considerations

The ability of a particle to scatter or absorb electromagnetic radiation can be quantified with its scattering cross section C_{sca} and its absorption cross section C_{abs} . The quantities have the dimension of an area and the sum gives the extinction cross section C_{ext} :

$$C_{ext} = C_{sca} + C_{abs}. \quad (2.9)$$

The cross sections can be considered as the ratio of energy scattered (W_{sca}) or absorbed (W_{abs}) across the surface area A of a sphere to the incoming irradiance I_0

$$C_{ext} = \frac{W_{ext}}{I_0}, \quad C_{sca} = \frac{W_{sca}}{I_0}, \quad C_{abs} = \frac{W_{abs}}{I_0}, \quad (2.10)$$

where $W_{ext} = W_{sca} + W_{abs}$. To obtain the net rate at which electromagnetic energy crosses the surface A of the sphere we have to make use of the so called Poynting-Vector (Poynting, 1884)

$$\mathbf{S} = \mathbf{E} \times \mathbf{H}. \quad (2.11)$$

\mathbf{S} specifies the magnitude and direction of the rate of transfer of electromagnetic energy in the electromagnetic field (\mathbf{E}, \mathbf{H}) . The time averaged Poynting-Vector of a plane wave is

$$\bar{\mathbf{S}} = \frac{1}{2} Re\{\mathbf{E} \times \mathbf{H}^*\}. \quad (2.12)$$

Its magnitude is called irradiance I (W m^{-2}). $\bar{\mathbf{S}}$ propagates into the direction of the electromagnetic wave. $\bar{\mathbf{S}}$ can be written as the sum of $\bar{\mathbf{S}}_i$, the pointing vector of the incident field, $\bar{\mathbf{S}}_{sca}$, the pointing vector of the scattered field, and $\bar{\mathbf{S}}_{ext}$, describing the interaction of the incident with the scattered waves:

$$\bar{\mathbf{S}} = \bar{\mathbf{S}}_i + \bar{\mathbf{S}}_{sca} + \bar{\mathbf{S}}_{ext}. \quad (2.13)$$

The net rate of electromagnetic energy crossing the surface A of a sphere can be written as the integral

$$W = - \int_A \bar{\mathbf{S}} \cdot \hat{\mathbf{e}}_r dA. \quad (2.14)$$

Using Equation 2.13 we can derive

$$W = W_i - W_{sca} + W_{ext}, \quad (2.15)$$

where W_i , W_{sca} , and W_{ext} are

$$W_i = - \int_A \bar{\mathbf{S}}_i \cdot \hat{\mathbf{e}}_r dA, \quad W_{sca} = \int_A \bar{\mathbf{S}}_{sca} \cdot \hat{\mathbf{e}}_r dA, \quad W_{ext} = - \int_A \bar{\mathbf{S}}_{ext} \cdot \hat{\mathbf{e}}_r dA. \quad (2.16)$$

For a non absorbing medium W_i vanishes and Equation 2.15 becomes

$$W_{ext} = W_{sca} + W. \quad (2.17)$$

To derive the electromagnetic field that we need to obtain $\bar{\mathbf{S}}$ in the particle and at all points of the medium surrounding the particle we have to find the solutions of (\mathbf{E}, \mathbf{H}) which satisfy the Maxwell equations. Thus, the components of the electromagnetic field have to be continuous although a discontinuity of electromagnetic properties exists at the boundary between the particle and the medium.

The scattering problem has to be solved for two orthogonal polarization states of the electromagnetic waves. The incident electric field will be divided into components parallel ($E_{\parallel i}$) and perpendicular ($E_{\perp i}$) to the scattering plane to find the solutions of the electromagnetic field. The relation between the incident (\mathbf{E}_i) and scattered (\mathbf{E}_s) electric fields is expressed by the amplitude scattering matrix $\tilde{\mathbf{S}}(\theta, \phi)$:

$$\begin{pmatrix} E_{\parallel s} \\ E_{\perp s} \end{pmatrix} = \frac{e^{ik(r-z)}}{-ikr} \tilde{\mathbf{S}} \begin{pmatrix} E_{\parallel i} \\ E_{\perp i} \end{pmatrix}, \quad (2.18)$$

$$\text{with } \tilde{\mathbf{S}} = \begin{pmatrix} S_2 & S_3 \\ S_4 & S_1 \end{pmatrix}. \quad (2.19)$$

$\tilde{\mathbf{S}}(\theta, \phi)$ depends on the scattering angle θ and the azimuthal angle ϕ . Using the vector scattering amplitude \mathbf{X} , which is related to $\tilde{\mathbf{S}}(\theta, \phi)$ as follows

$$\mathbf{X} = (S_2 \cos \phi + S_3 \sin \phi) \hat{\mathbf{e}}_{\parallel s} + (S_4 \cos \phi + S_1 \sin \phi) \hat{\mathbf{e}}_{\perp s} \quad (2.20)$$

we have now the basic equations to derive C_{ext} and C_{sca} to quantify the scattering and absorption of light by a particle:

$$C_{ext} = \frac{4\pi}{k^2} \text{Re}\{(\mathbf{X} \cdot \hat{\mathbf{e}}_x)_{\theta=0}\}, \quad (2.21)$$

$$C_{sca} = \int_0^{2\pi} \int_0^\pi \frac{|\mathbf{X}|^2}{k^2} \sin \theta \, d\theta \, d\phi = \int_{4\pi} \frac{|\mathbf{X}|^2}{k^2} \, d\Omega. \quad (2.22)$$

Scattering of light by a single spherical particle

The problem of scattering of light by a particle can be simplified by assuming a spherical shape of the particle. An analytical solution of the problem was developed by Mie (1908). The Mie theory allows quantifying scattering and absorption of light on particles. However the theory developed by Gustav Mie has to be implemented in a numerical algorithm for the quantification of the scattering effects. A widely used numerical code is presented in Bohren and Huffman (1983) (BHMIE). The computation of aerosol optical properties in this work is based on the BHMIE-code.

According to the Mie theory we derive extinction cross sections C_{ext} and scattering cross section C_{sca} that are now independent of the azimuthal angle ϕ due to the symmetry of rotation of the simplified problem. The cross sections can now be written as:

$$C_{ext} = \frac{2\pi}{k^2} \sum_{n=1}^{\infty} (2n+1) \operatorname{Re}\{a_n + b_n\}, \quad (2.23)$$

$$C_{sca} = \frac{2\pi}{k^2} \sum_{n=1}^{\infty} (2n+1) (|a_n|^2 + |b_n|^2), \quad (2.24)$$

where a_n and b_n are the scattering coefficients

$$a_n = \frac{m\psi_n(mx)\psi'_n(x) - \psi_n(x)\psi'_n(mx)}{m\psi_n(mx)\xi'_n(x) - \xi_n(x)\psi'_n(mx)}, \quad (2.25)$$

$$b_n = \frac{\psi_n(mx)\psi'_n(x) - m\psi_n(x)\psi'_n(mx)}{\psi_n(mx)\xi'_n(x) - m\xi_n(x)\psi'_n(mx)}. \quad (2.26)$$

The scattering coefficients are simplified with the Riccati-Bessel functions $\psi_n(\rho)$ and $\xi_n(\rho)$ and have to be calculated by numerical means. a_n and b_n , and thus C_{ext} and C_{sca} , depend on the size parameter x and the relative refractive index m . The size parameter describes the ratio of particle size (i.e. particle diameter D_p) to the wavelength λ of the incident radiation

$$x = \frac{\pi N_m D_p}{\lambda}. \quad (2.27)$$

N_m is the refractive index of the medium containing the particle. We can assume $N_m \simeq 1$ if the medium consists of common air (Edlén, 1966; Ciddor, 1996). The relative refractive index is defined as the ratio of the refractive index of the particle N_p to the refractive index of the medium N_m with its real part n and imaginary part k :

$$m = n + ik = \frac{N_p}{N_m}. \quad (2.28)$$

If the particle solely contains non-absorbing matter the imaginary part $k = 0$.

Three examples of angle-dependent scattering were calculated for spherical ammonium sulphate particles in different particle diameters. The incident light has a visible wavelength of 530 nm. The polar plots of the scattered irradiance are shown in Figure 2.3. Please note that the magnitude of the scattered irradiance is plotted on a logarithmic scale. The scattering function is symmetrical in forward and backward scattering direction for particles in diameter $D_p \ll 1 \mu\text{m}$. For particles in diameter $D_p \geq 1 \mu\text{m}$ the scattering function becomes asymmetrical towards the forward direction ($\theta = 0^\circ$). For larger particles in diameter $D_p = 3 \mu\text{m}$ the irradiance scattered in forward direction is larger by two orders of magnitude. The dominant forward scattered irradiance can already be observed in the sub-micron size range but intensifies for particles in the

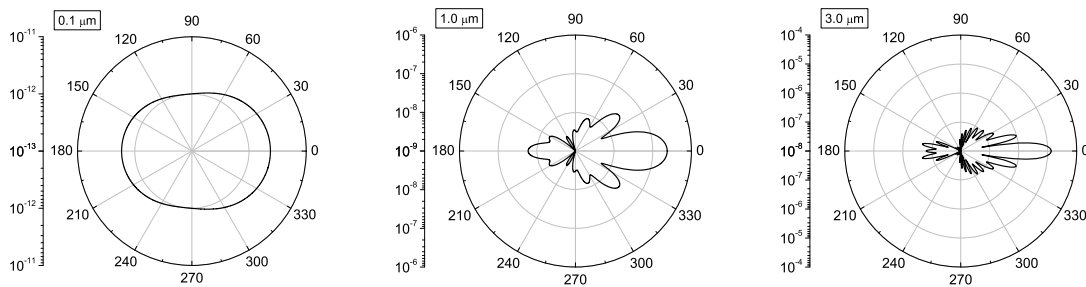


Figure 2.3: Angle-dependent scattering for spherical ammonium sulphate particles in different particle diameters (0.1 μm , 1 μm , 3 μm). The scattered irradiance was calculated from Mie theory for a wavelength of 530 nm.

super-micron size range.

Further simplifications of the Mie theory can be done if particles are small compared to the wavelength of the incident irradiance. This implies that the size parameter $x \ll 1$. The modified scattering theory is referred to as Rayleigh scattering and the respective particle size range as Rayleigh regime. For visible light the Rayleigh scattering is valid for particles $D_p \lesssim 0.1 \mu\text{m}$. The Rayleigh theory describes that for sufficient small particles the scattered irradiance I_s is indirect proportional to fourth power of the wavelength of the incident light:

$$I_s \propto \frac{D_p^6}{\lambda^4}. \quad (2.29)$$

The angular distribution of I_s is symmetrical in the forward and backward direction and differs significantly from the angle dependent scattering of particles in the micron size range in the Mie regime (cf. left panel of Figure 2.3).

Optical aerosol parameters

To quantify the ability of an aerosol particle to interact with electromagnetic radiation we defined the scattering cross section C_{sca} and absorption cross section C_{abs} . Based on the cross sections we can directly define the dimensionless parameters of the efficiencies for extinction, scattering and absorption of spherical particles:

$$Q_{ext} = \frac{4}{\pi D_p^2} C_{ext}, \quad Q_{sca} = \frac{4}{\pi D_p^2} C_{sca}, \quad Q_{abs} = \frac{4}{\pi D_p^2} C_{abs}. \quad (2.30)$$

The efficiencies describe the ratio of scattered and/or absorbed irradiance by the particle to the incoming radiation. If we go back to the Rayleigh regime we derive the following relationships for sufficient small particles:

$$Q_{sca} \propto \frac{1}{\lambda^4}, \quad Q_{abs} \propto \frac{1}{\lambda}. \quad (2.31)$$

Electromagnetic radiation of short wavelength is more affected by the aerosol particles than radiation of long wavelength in both, scattering and absorption.

So far we focussed on single particles. To describe the effect of a bulk of aerosol particles on radiation we can define the extinction coefficient (m^{-1}) for a monodisperse aerosol and a number concentration of N spherical particles per unit of volume (Hinds, 1982):

$$\sigma_{ext} = \frac{\pi D_p^2 N}{4} Q_{ext} = N C_{ext}. \quad (2.32)$$

The scattering coefficient σ_{sca} and absorption coefficient σ_{abs} of a bulk of aerosol particles are defined likewise. The extinction coefficient can again be expressed as the sum of σ_{sca} and σ_{abs} :

$$\sigma_{ext} = \sigma_{sca} + \sigma_{abs}. \quad (2.33)$$

To derive the extinction coefficient of polydisperse aerosol we have to calculate the integral of σ_{ext} for the size distribution of the present aerosol population:

$$\sigma_{ext} = \int_{D_p} \frac{\pi D_p^2}{4} Q_{ext} \frac{dN}{d \log D_p} d \log D_p. \quad (2.34)$$

Knowing the extinction coefficient of aerosol within an atmospheric column of depth Δz we can calculate the attenuation of light within this column following the Lambert-Beer Law:

$$I = I_0 e^{-\sigma_{ext} \Delta z}, \quad (2.35)$$

where I_0 is the incident irradiance and I the irradiance traversing the aerosol.

2.3.2 Changes of optical properties due to changes in aerosol composition

The ability of particles to scatter or absorb electromagnetic radiation and consequently to attenuate light depends strongly on the chemical composition of the particle which

is expressed by its relative refractive index m . As described before the relative refractive index defines the ratio of the refractive index of the particle N_p to the refractive index of the medium N_m . We can set $m \simeq N_p$ as the refractive index of air $N_m \simeq 1$ (Edlén, 1966; Ciddor, 1996). The refractive indices of a lot of substances are well known and Figure 2.4 a shows the wavelength dependency of soot, a major product of combustion processes, and ammonium sulphate $(\text{NH}_4)_2\text{SO}_4$, one of the most frequently observed volatile component of atmospheric aerosol (Junge, 1954; Eggleton, 1969; Heard and Wiffen, 1969). The plot illustrates the dependency of the refractive index on the wavelength (Twitty and Weinman, 1971; Volz, 1972; Toon et al., 1976). However, the refractive indices of the two chosen components remain almost constant for the wavelength spectrum of visible light.

In the atmosphere, homogeneous particles can rarely be found and the total aerosol comprises particles consisting of different chemical components. Thus, we have to consider an effective refractive index that takes the different components with known refractive indices into account. Only the two components ammonium sulphate and soot are used in the present work to consider one non-absorbing and one absorbing component to simplify the problem and to give a first approximation of the effective refractive index m_e for an internally mixed aerosol. Several solutions can be found to compute m_e (Chýlek et al., 1988). A simple approach is the volume average of the refractive index:

$$m_e = v_1 m_1 + v_2 m_2, \quad (2.36)$$

where m_1 and m_2 are the refractive indices of the components and v_1 and v_2 the respective volume fractions with $v_1 + v_2 = 1$. A second approach is the Maxwell-Garnett mixing rule that defines the effective refractive index of an internally mixed particle with absorbing inclusions (m_2) in the non-absorbing matrix (m_1):

$$m_e^2 = m_1^2 \frac{m_2^2 + 2m_1^2 + 2v_2(m_2^2 - m_1^2)}{m_2^2 + 2m_1^2 - v_2(m_2^2 - m_1^2)}. \quad (2.37)$$

Chýlek et al. (1988) and Srivastava et al. (1989) recommend the Maxwell-Garnett mixing rule for internally mixed particles with absorbing inclusions. Equation 2.37 will be used for internally mixed aerosol of non-absorbing and absorbing components in the present work to comply with the recommendations. Figure 2.4 b shows the trend of the effective refractive index for different volume fractions. While m_e follows a linear function for the volume average, the function of the Maxwell-Garnett mixing rule shows a convex curvature. However, the differences between the two mixing rules remain small with a maximum deviation of 1 %.

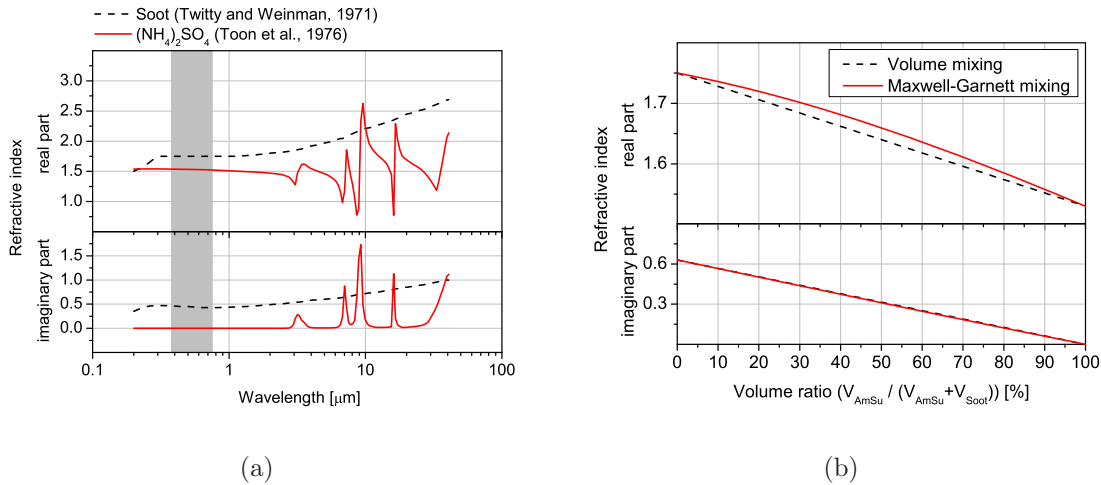


Figure 2.4: Figure a: Wavelength dependency of complex refractive indices for soot (Twitty and Weinman, 1971) and ammonium sulfate (Toon et al., 1976). The grey shade indicates the wavelength spectrum of visible light. Figure b: Change of the complex refractive index due to internal mixing of soot ($m = 1.75 \pm 0.63i$) and ammonium sulfate ($m = 1.53 \pm 0.00i$) particles.

2.3.3 Changes of optical properties due to changes in relative humidity

Condensation of water vapour on aerosol particles due to increased relative humidity leads to an increase in size and altering of the refractive index of the particles. This makes it necessary to consider the effects on particles as their optical properties change with the variation of the humidity. Hygroscopic particles are affected if the relative humidity rises above 70 % (Waggoner et al., 1981). The work of Hänel (1976) provides a comprehensive discussion of the effects of relative humidity on mass, size, mean density, and refractive index of aerosol particles. It will be used for the following corrections of size and refractive index as functions of relative humidity.

The change in particle size is related to the uptake of mass by condensation and to the relative humidity f . If the water activity of the particle equals the relative humidity the following equation can be used to describe the growth of a dry particle with initial radius r_0 :

$$r = r_0 \left(1 + \frac{\rho_0 m_w}{\rho_w m_0} \right)^{\frac{1}{3}} \simeq r_0 \left(1 + \frac{\rho_0 \mu_m f}{\rho_w (1-f)} \right)^{\frac{1}{3}}, \quad (2.38)$$

r is the radius of the wet spherical particle. ρ_0 and ρ_w are the density and m_0 and m_w the mass of the dry particle and the condensed water, respectively. μ_m depicts the linear mass increase coefficient of the particle and is a function of f . The equation is only valid for particles in radii greater than $1\ \mu\text{m}$. The curvature correction using the Kelvin equation (Equation 2.3) has to be taken into account for smaller particles. The following formula is valid for relative humidity between 0.70–0.99 and dry radii larger than $0.04\ \mu\text{m}$:

$$r \simeq r_0 \left(\left(1 + \frac{\rho_0}{\rho_w} \mu_m \frac{f}{1-f} \right)^{\frac{1}{3}} - \frac{2\sigma v_w}{R_w T r_0} \frac{f}{1-f} \left(1 + \frac{\rho_0}{\rho_w} \mu_m \frac{f}{1-f} \right)^{-\frac{1}{3}} \right). \quad (2.39)$$

σ is the surface tension of the wet particle surface, v_w the specific volume and R_w the specific gas constant for water.

The equations for the refractive index $m = n + ik$ are derived using the average volume mixing rule for the particle and the condensed water (see Equation 2.36). The equations for the real part n and imaginary part k of the refractive index can be expressed as functions of relative humidity:

$$n = n_w + (n_0 - n_w) \left(1 + \frac{\rho_0}{\rho_w} \mu_m \frac{f}{1-f} \right)^{-1}, \quad (2.40)$$

$$k = k_w + (k_0 - k_w) \left(1 + \frac{\rho_0}{\rho_w} \mu_m \frac{f}{1-f} \right)^{-1}. \quad (2.41)$$

Equations 2.40 and 2.41, assuming a homogeneous internally mixed particle, can also be used for inhomogeneous internally mixed particles to consider the humidity effect. Deviations may occur for particles in the accumulation mode for decreasing wavelength (Tuomi, 1980). Figure 2.5 a shows the effect of increasing humidity on the particle size using Equations 2.39, 2.40 and 2.41. For relative humidity lower than 90% aerosol particles in dry diameter of $1\ \mu\text{m}$ grow by a factor between 1 and 1.5. The particle size starts to increase strongly for relative humidity larger than 95% by factors larger than 2. The relative increase in size is larger for initially larger particles in diameter $1\ \mu\text{m}$ than in diameter $0.1\ \mu\text{m}$. In addition, the absolute increase of the resulting scattering cross section C_{sca} is larger for larger particles, whereas the relative increase of C_{sca} with relative humidity is larger for smaller particles (Figure 2.5 b). This is caused by the strong relative increase of C_{sca} with increasing particle size for small particles compared to large particles. E.g. C_{sca} extends between five orders of magnitude for particles in diameter $0.1\text{--}1.0\ \mu\text{m}$ compared to three orders of magnitude for particles in diameter $1\text{--}10\ \mu\text{m}$ for ammonium sulphate particles at visible light.

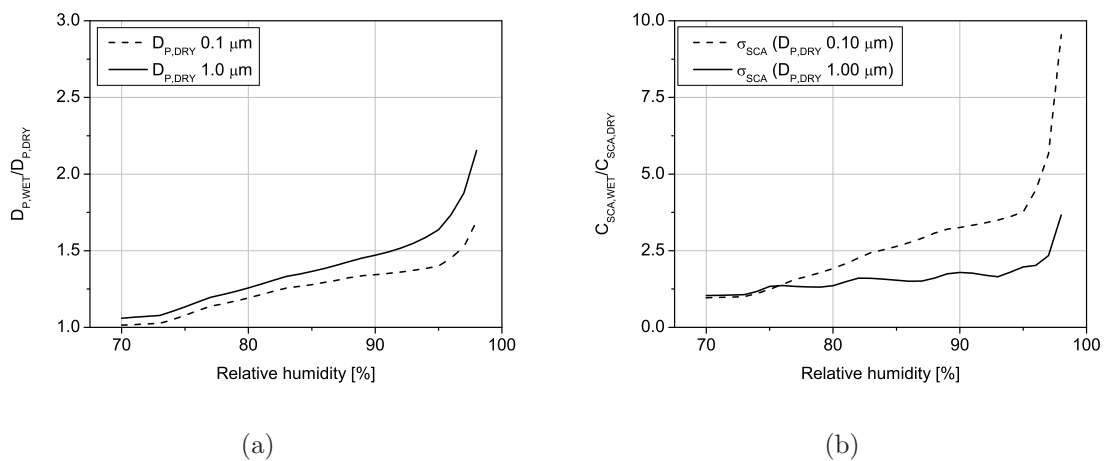


Figure 2.5: Relative increase of particle diameters (Figure a) and scattering cross sections (Figure b) for increasing relative humidity. The scattering cross sections C_{sca} were calculated for ammonium sulphate particles at a wavelength of 530 nm.

Chapter 3

Methods and implementation of aerosol airborne measurements

3.1 Methods of aerosol airborne measurements and data analysis

Microphysical properties of atmospheric aerosol particles are measured by systems using the properties based on aerosol theory. The measurement systems make use of known ambient conditions like temperature, pressure, electric field, or wavelength of the light scattered or absorbed by airborne particles to investigate related aerosol properties. The following section gives an overview of the measurement techniques used for the analysis of the aerosol microphysical properties in the present work.

3.1.1 Aerosol number concentrations

So-called Condensation Nucleus Counters (CNCs) or Condensation Particle Counters (CPCs, this term is used within this work) make use of a popular technique to measure total number concentrations with a high temporal resolution (Hinds, 1999). They solve the problem of counting particles, which are too small to be detected by optical means, using the growth of particles due to condensation of supersaturated vapours on particles (see Section 2.1). In principal CPCs consist of three parts: a saturation chamber, a condenser tube, and the optical detection unit (Agarwal and Sem, 1980; Hinds, 1999). The sampled aerosol particles enter the heated saturation chamber through an inlet. The saturation chamber is enriched with evaporated liquids, which usually consist of alcohols (e.g. Butanol) or water. The aerosol vapour mixture subsequently enters the condenser tube where thermal cooling leads to a supersaturation and condensation of the vapour on the particles. The level of supersaturation depends on the temperature

difference between the saturation chamber and the end of the condenser tube and the length of the condensation section. Supersaturation up to 400 % (Hinds, 1999) enable particles in diameter down to 3 nm to grow to a detectable size. The optical detection unit finally counts the grown aerosol particles. The lower measurement range between 0.003–0.02 μm depends on the design of the respective CPCs and is characterized by the counting efficiency curve and the 50 % detection efficiency diameter of each CPC (Wiedensohler et al., 1997; Banse et al., 2001). The lower detection limit can be increased by the use of diffusion screens, which are set in front of a CPC. Fine particles collide with the mesh of the diffusion screen due to Brownian motion and are deposited on the mesh and removed from the aerosol population. Larger particles of the sub-micron range follow the streamlines around the mesh. The penetration efficiency of particles at given diameter can be set by the number of diffusion screens and the total surface of the contained wire (Feldpausch et al., 2006). The possibility of different lower detection limits due to the variation of the condenser characteristics and the use of diffusion screens allow the size resolved measurement of fine particles in the sub-micron range. CPCs with different lower detection limits can be combined to a battery of particle counters to derive the number concentrations of particle populations with different lower cut off diameters (Stein et al., 2001).

3.1.2 Aerosol size distributions

A more common method used to retrieve size resolved information of the aerosol population and to measure particle size distributions is the measurement of scattered light by optical particle counters (OPCs). The OPCs measure the intensity of light scattered by a particle by photoelectric means (Gucker and Rose, 1954). The scattered light is focussed upon a photomultiplier and the resulting electrical pulses are classified by their heights. The measured intensity of the scattered light depends on the wavelength of the light and the detected scattering angle, which are given by the instrument. Further it depends on the refractive index and thus on the chemical composition, which has to be assumed or measured by chemical analysis, and on the shape of the particle and its sphericity, which can be assumed to be spherical in the ideal case. However, the size of the particle has the largest impact on the intensity of the scattered light within a specified angle (see Section 2.3) and this effect is finally used by the OPCs to measure the size of a single particle.

OPCs measure the size distribution for particles in diameter larger than 0.1 μm . To detect the upper and lower limits of the channels, which count the classified pulse heights, i.e. the channel borders, the OPCs used for this work were calibrated using monodisperse aerosol particles of various non-absorbing substances with known

refractive index. Particles used for the calibration consisted of Di-Ethyl-Hexyl-Sebacat (DEHS), polystyrene latex (PSL), ammonium sulphate and sodium chloride. A differential mobility analyzer (DMA) (Knutson and Whitby, 1975; Liu and Pui, 1975) was used to select monodisperse particles from the polydisperse aerosol population. Although monodisperse aerosol is used for the calibration, particles are counted in several channels around the channel of the respective particle size. To determine the mean channel number of the monodisperse aerosol population the following formula was used (Liu et al., 1992):

$$\overline{CH} = \frac{\sum N_i CH_i}{\sum N_i}. \quad (3.1)$$

N_i is the number of particles counted in channel CH_i . The size of the aerosol particles should be selected close to the border between two channels. Thus, particles are detected equally in two subsequent channels.

After the determination of the bin limits at given refractive indices probe response curves were calculated from Mie theory for each instrument. The probe response describes the measured intensity of scattered light integrated over a certain scattering angle θ . The minimum and maximum scattering angles are defined by the specifications of the instruments. The OPCs used in this work operate with the following light detection angles: Grimm Sky-OPC 30°–150° (Grimm, 2007), Passive Cavity Aerosol Spectrometer Probe (PCASP-100X) 35°–120° (DMT, 2009), and Forward Scattering Spectrometer Probe (FSSP-300) 6°–15° (Fiebig, 2001). The probe response of the instrument is independent of the refractive index. Once the probe response is known bin limits can be calculated for different substances from Mie theory using the probe response curves of the respective refractive indices. Figure 3.1 shows the probe response curves of the instruments for ammonium sulphate. The probe response curves, especially for the FSSP-300, indicate that particles of different sizes can produce a signal, which accounts for more than one bin limit. Thus, channels have to be grouped according to the response curve to avoid regions of multivalued response due to Mie-ambiguities (Pinnick and Auvermann, 1979; Pinnick and Rosen, 1979).

Channel borders of the OPCs listed above and used for the calculation of size distributions in this work are listed in Tables A.2 and A.3. They were retrieved from calibration and theoretical calculations.

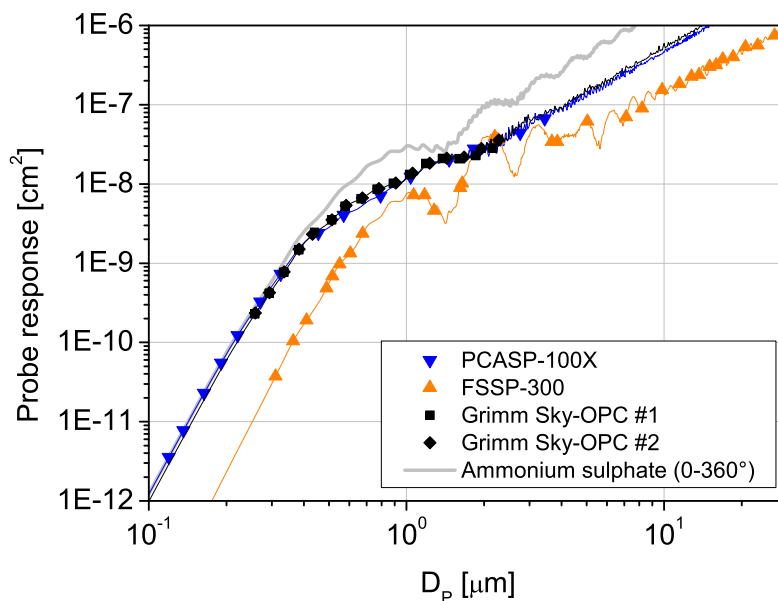


Figure 3.1: Probe response curves for Grimm Sky-OPCs, PCASP-100X and FSSP-300 for ammonium sulphate.

3.1.3 Aerosol mixing state

An intensive aerosol property and independent from the extensive properties measured with the methods mentioned above is the mixing state. The mixing state of aerosol particles can be classified into two major states: *external mixing* and *internal mixing*. The external mixed aerosol describes an aerosol population where particles of different compounds e.g. soot from combustion processes and ammonium sulphate from natural sources can be found side by side in the carrier gas. In contrary internal mixed aerosol consists of particles where the different compounds are mixed internally within each particle. Coagulation processes of different particles or condensation of aerosol precursor gases on existing particles can result in the internal mixing state. The internal mixing state can be divided into homogenous and heterogeneous mixing depending on the solubility of the compounds within the particle (see Figure 3.2). E.g., a particle consisting of a non-soluble core coated by condensed matter can be classified as heterogeneous internally mixed. The fraction of internally mixed aerosol increases with the age of the aerosol population (Riemer et al., 2004) as it undergoes condensation and coagulation processes with preceding time. Thus, the analysis of the mixing state gives an indication whether fresh or aged aerosol was measured.

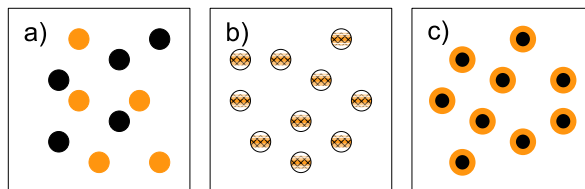


Figure 3.2: Mixing state of volatile (orange) and non-volatile (black) particles after Bond and Bergstrom (2006): a) external, b) internal homogenous, and c) internal heterogeneous.

A so-called thermodenuder was used in this study to separate different compounds of the aerosol particles by heat. The thermodenuder heats the probed aerosol to 250°C and evaporates volatile and semi volatile compounds like ammonium sulphate (Slanina et al., 1981). In the following the nomenclature of *volatile particles* will be used for substances that evaporated or decomposed at 250°C. The residual particles will be named *non-volatile particles*. Total number concentrations and size distributions in the diameter range 0.25–2.5 μm of volatile and non-volatile particles were measured by the use of CPCs and two Grimm Sky-OPCs without and in combination with the thermodenuder, respectively. This instrument setup allowed the measurement of number and volume ratios of non-volatile particles on the total aerosol.

The mixing state of the aerosol has a large impact on the optical properties of the particles (see Section 2.3.2) and subsequently on their measurements by optical means (see Section 3.1.2). Average number and volume ratios of non-volatile particles were used to retrieve the average refractive index of the aerosol probed during each horizontal flight leg and to calculate the respective size distributions measured by PCASP-100X and FSSP-300. The chemical compounds governing the average refractive index could only be assumed due to the vast diversity of different sources above Central Europe. In a first approximation it was assumed that volatile matter consists of ammonium sulphate with $m = 1.53 \pm 0.00i$ (Toon et al., 1976) and non-volatile matter of soot resulting from combustion processes with $m = 1.75 \pm 0.63i$ (Pluchino et al., 1980; Bond and Bergstrom, 2006). Combustion processes are a major source of primary i.e. non-volatile particles over a densely populated region like Central Europe. The refractive index of the mixed aerosol was calculated using Equation 2.36 for external mixing state and Equation 2.37 for internal mixing state. The Grimm Sky-OPC measurements of the size distribution of volatile and non-volatile aerosol give the required volume ratios. If the number ratio of non-volatile particles exceeded 80% an internal mixing

state was assumed, otherwise external mixing. The mixing of the absorbing with the non-absorbing component was calculated for particles smaller $1\ \mu\text{m}$ as soot from anthropogenic combustion processes dominantly appears in the submicron particle size range (Rose et al., 2006). Particles larger $1\ \mu\text{m}$ were assumed to consist of ammonium sulphate. Corrections of the measured size distributions due to high relative humidity were calculated after the methods described in Section 2.3.3.

3.1.4 Scattering and absorption of light by aerosol particles

To analyse the optical properties of the atmospheric aerosol we have to derive the scattering coefficient σ_{sca} and the absorption coefficient σ_{abs} (see Section 2.3.1) from in-situ measurements. The direct in-situ measurement of light scattering by aerosol particles is known since several decades (Crosby and Koerber, 1963; Charlson et al., 1967). If no direct in-situ measurements of σ_{sca} are performed the scattering of light by aerosol can be estimated by theoretical considerations. The scattering cross section C_{sca} can be calculated for each measured particle size at a known refractive index. σ_{sca} can be calculated from the measured size distribution retrieved by the OPCs using Equation 2.34 for polydisperse aerosol in the measurement size range of the OPCs.

One of the most popular methods to measure the absorption coefficient of aerosols is based on filter sampling of aerosol particles. The absorption is derived from the change in light transmission through the filter on which the particles are collected (Bond et al., 1999). In the present study a 3λ -PSAP (Particle Soot Absorption Photometer) (Virkkula et al., 2005) was used to determine the absorption coefficient. The 3λ -PSAP measures the attenuation of light at 467 nm, 530 nm, and 660 nm.

To derive the absorption coefficient σ_{abs} we have to correct the outgoing signal of the instrument σ_{PSAP} . First corrections have to be implemented for the flow and the spot size due to deviations between different instruments (Bond et al., 1999). The PSAP signal σ_{PSAP} has to be multiplied with the following correction factors:

$$F_{flow} = \frac{Q_{PSAP}}{Q_{meas}} \text{ and} \quad (3.2)$$

$$F_{spot} = \frac{A_{PSAP}}{A_{meas}} \quad (3.3)$$

where Q_{PSAP} and Q_{meas} are the flow given by the PSAP and the flow measured downstream the instrument by an external flowmeter, respectively. The spot sizes given by the manufacturer and measured for the operating instrument are $A_{PSAP} = 17.81\ \text{mm}$

and $A_{meas} = 16.62$ mm. The flow correction could not be accomplished for the present work as no external flowmeter was used during the measurements.

The following corrections are of empirical nature. The PSAP signal has to be corrected for the change of transmission as the filter gets darker with preceding measurement time which is expressed in the transmission correction function $f(Tr)$. In addition, purely scattering particles on the filter alter the transmission and have to be taken into account for the calculation of the absorption coefficient with the scattering correction factor s . As the transmission correction function after Bond et al. (1999) is already implemented in the firmware the absorption coefficient can be written as:

$$\sigma_{abs} = f(Tr)\sigma_0 - s \cdot \sigma_{sca} = \sigma_{PSAP} - s \cdot \sigma_{sca}. \quad (3.4)$$

σ_0 depicts the uncorrected response in the instrument. The correction procedure used in the present work follows the corrections given by Virkkula et al. (2005) and Virkkula (2010). To use the transmission correction function of Virkkula et al. (2005) and Virkkula (2010) we have to calculate σ_0 from σ_{PSAP} using the transmission correction function of Bond et al. (1999):

$$f_{bond}(Tr) = \frac{1}{1.0796 \cdot Tr + 0.71} \quad (3.5)$$

where Tr is the transmission measured by the PSAP. The correction functions given by Virkkula et al. (2005) and Virkkula (2010) consider the influence of grey aerosol by using the single scattering albedo

$$\omega_0 = \frac{\sigma_{sca}}{\sigma_{sca} + \sigma_{abs}}. \quad (3.6)$$

To retrieve a first approximation of ω_0 we have to calculate σ_{abs} using

$$\sigma_{abs} = k_0 + k_1 \ln Tr \sigma_0 - s \sigma_{sca}. \quad (3.7)$$

σ_{abs} will now be determined iteratively using the following equation until σ_{abs} does not change significantly:

$$\sigma_{abs} = (k_0 + k_1(h_0 + h_1\omega_0) \ln Tr) \sigma_0 - s \sigma_{sca}. \quad (3.8)$$

The constants k_0 , k_1 , h_0 , h_1 , and s are given for each wavelength in Virkkula (2010) and listed in Table 3.1. The scattering coefficient σ_{sca} used for the scattering correction was retrieved from the measured size distributions of the Grimm Sky-OPC as the OPC and the PSAP probed the same aerosol inside the cabin.

Table 3.1: Constants for Equations 3.7 and 3.8 after Virkkula (2010).

	467 nm	530 nm	660 nm
k0	0.377	0.358	0.352
k1	-0.640	-0.640	-0.674
h0	1.16	1.17	1.14
h1	-0.63	-0.71	-0.72
s	0.015	0.017	0.022

3.1.5 Processing the data of aerosol airborne measurements

The measurements realised by the DLR were conducted aboard the research aircraft DLR Falcon 20. The aircraft was modified for atmospheric in-situ measurements and remote sensing and can accommodate a payload of up to 1100 kg of scientific instrumentation. The scientific payload can be mounted inside the cabin and underneath it, as well as under the wings. The DLR Falcon 20 has a maximum range of approximately 3700 km which allows an approximate flight and measurement duration of 5 h. The maximum flight altitude of 12.8 km makes in-situ measurements throughout the whole tropospheric column possible.

Several aspects of airborne aerosol in-situ measurements have to be taken into account. The aircraft flies with horizontal velocities up to 250 m s^{-1} . This means that the aerosol particles have to be sampled from a moving aerosol stream. An isokinetic inlet constructed for the specifications of the DLR Falcon 20 is used to ensure that the sampled aerosol represents the atmospheric state (Hinds, 1982; Fiebig, 2001). In isokinetic conditions, the flow of the gas carrying the particles is not altered by any acceleration caused by the inlet and the particles follow the streamlines into the sampler (Addlesee, 1980). Anisokinetic sampling would lead to a distortion of the sampled aerosol number concentration and size distribution at the nozzle of the sampling inlet (Belyaev and Levin, 1974; Liu et al., 1989). To achieve isokinetic conditions the flow velocities inside and outside the inlet should be similar. The flow velocity surrounding the inlet usually exceeds the flow velocity inside the inlet for airborne measurements. A diffuser cone mounted around the inlet reduces the flow velocity by increasing the flow cross-sectional area. The inlet samples the carrier gas from a streamline in the centre of the diffuser cone to avoid turbulent flow, which may occur at the walls of the diffuser. Expansion angles smaller than 7° reduce the possibility that the flow separates from the walls and causes turbulent flow (Baumgardner and Huebert, 1993). Although many efforts were made in airborne aerosol measurements to achieve a sampling method, which represents the atmospheric state after sampling, losses in number concentrations

in different particle size ranges cannot be avoided yet. Porter et al. (1992) and Sheridan and Norton (1998) reported losses of more than 50% in the super-micron size range and 10–20% for sub-micron particles.

To account for losses due to inlet effects the sampling efficiencies of the inlet have to be considered to characterise the inlet properties. The sampling efficiency $E(D_p)$ is a function of the particle diameter and defines the ratio of the sampled number of particles $n_s(D_p)$ to the number of particles in the atmosphere $n_a(D_p)$:

$$E(D_p) = \frac{n_s(D_p)}{n_a(D_p)}. \quad (3.9)$$

The median upper cut off particle diameter $D_{p,50}$ ($E(D_{p,50}) = 0.5$) can be calculated once the sampling efficiency per particle diameter is determined. However, $D_{p,50}$ strongly depends on the ambient conditions and the properties of the carrier gas in addition to the specifications of the sampling inlet. To derive an inlet specific value that characterises its sampling efficiency the Stokes number St can be calculated for $D_{p,50}$ (Liu et al., 1989):

$$St = \frac{\rho_p D_p^2 C_c v}{18 \mu_a d_i}. \quad (3.10)$$

ρ_p is the particle density, v the free stream velocity, and d_i the inner diameter of the sampling tube. The slip correction (Cunningham) factor C_c is a function of the mean free path l and viscosity μ_a in air (Jennings, 1988; Seinfeld and Pandis, 1998).

The sampling efficiency and median upper cut off particle diameter were determined for this work using the size distributions measured by optical particle counters inside the cabin (Grimm Sky-OPC) and outside mounted on a wing port (PCASP-100X). The number concentrations per particle diameter to calculate $E(D_p)$ were derived from linear interpolation of the measured number concentrations to the logarithm of the respective particle diameters:

$$n_s(D_p) = N_{s,CH0} + \frac{N_{s,CH1} - N_{s,CH0}}{\log D_{p,s,CH1} - \log D_{p,s,CH0}} (\log D_p - \log D_{p,s,CH0}), \quad (3.11)$$

$$n_a(D_p) = N_{a,CH0} + \frac{N_{a,CH1} - N_{a,CH0}}{\log D_{p,a,CH1} - \log D_{p,a,CH0}} (\log D_p - \log D_{p,a,CH0}). \quad (3.12)$$

The particle diameter D_p is larger than $D_{p,CH0}$ and smaller than $D_{p,CH1}$. N_{CH0} and N_{CH1} are the number concentrations measured in the respective channels $CH0$ and $CH1$. The index s indicates measurements inside, the index a measurements outside cabin. Measurements used for the determination of the sampling efficiency were

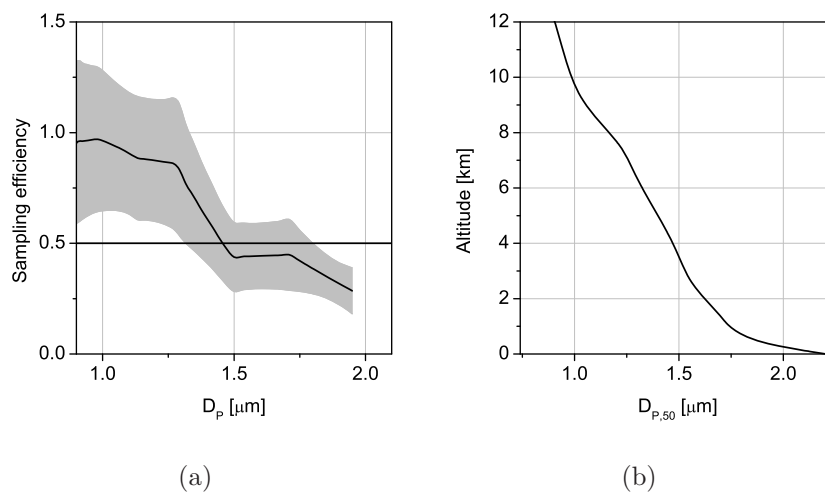


Figure 3.3: Inlet efficiency (Figure a) and vertical distribution of the median upper cut off diameter $D_{p,50}$ (Figure b) for ammonium sulphate particles.

taken from flight sequences performed inside the boundary layer and decoupled pollution layers to ensure high number concentrations and consequently low relative errors due to detection limits. Average parameters of each single flight sequence that were used to characterise the aerosol inlet are listed in Table A.1. Ammonium sulphate particles were used for the calculation of St . The characterisation led to an average median upper cut off diameter $D_{p,50} = 1.54 \mu\text{m} \pm 0.24 \mu\text{m}$ (Figure 3.3 a) and an average Stokes number $St = 0.471 \pm 0.126$. This is in agreement with the Stokes number $St = 0.486 \pm 0.137$ reported by Fiebig (2001) who characterised the aerosol inlet of the DLR Falcon 20 using the wing mounted PCASP-100X and a Nephelometer inside the cabin. Figure 3.3 b shows the variation of $D_{p,50}$ with altitude. Average values of temperature, pressure, and flight velocity as measured during the EUCAARI-LONGREX field campaign were used for the calculation. $D_{p,50}$ decreases with altitude from approximately 2.2 μm at the ground to less than 1.0 μm above 10 km.

In addition to the inlet considerations for airborne aerosol measurements one has to consider the wide range of humidities, temperatures and pressures that occur throughout the tropospheric column (Sheridan and Norton, 1998). The variety of ambient conditions complicates the comparison of the different aerosol measurements. Thus, it can be useful from case to case to correct the aerosol properties to standard conditions, e.g. to low relative humidity (see Section 2.3.3) or to standard pressure and temperature. Ambient concentrations (N_{amb}) can easily be transformed to concentrations at standard conditions (N_{stp}) using the following equation:

$$N_{stp} = \frac{1013.25 \text{ hPa}}{p_{amb}} \frac{T_{amb}}{273.15 \text{ K}} N_{amb}. \quad (3.13)$$

p_{amb} and T_{amb} are pressure and temperature at ambient conditions. Further one has to consider that the conditions on the measurement platform vary during the measurements, i.e. the aircraft changes its pitch and roll angle depending on flight velocity and direction. Thus, the inflow direction to the sampling inlets can vary by time and the inlet characteristics will change. Some measurement instruments may also be insensitive to fast changes in ambient pressure and take some time to adapt to the new conditions after ascend or descend. Hence, it is important to consider the flight conditions for the analysis of the measurements. Best measuring conditions can be found during horizontal flight legs when the aircraft is heading towards one direction. The flight velocity of maximum 250 m s^{-1} also requires a high temporal resolution of the measured data. The aircraft covers a distance of 15 km in one minute of flight and an instrument with a low time resolution would average over a variety of possibly different air masses. Thus, a temporal resolution of a few seconds suits the requirements of airborne aerosol measurements.

3.2 Development of a new method to analyse air mass trajectories

Air mass transport analysis is an essential tool to support the interpretation of aerosol measurements with additional information of the history of the probed air masses. The transport analysis can provide information of aerosol source regions, the age of the aerosol or the evolution of the meteorological conditions along the transport pathway. This section describes the methods developed for transport analysis in the present work.

3.2.1 Air mass trajectories

Trajectory models are a widely used method to examine air mass transport within the atmosphere. In the last decades several different types of trajectory models have been developed. Out of the different approaches to calculate trajectories several studies showed that three-dimensional models using the horizontal and vertical wind components derived from meteorological fields are the most accurate trajectory type (Stohl et al., 1995). Nevertheless, trajectories have to be treated with attention. Several errors have to be considered to estimate the accuracy of trajectories. Stohl et al. (1995) diagnosed that the temporal resolution of the input field leads to the largest uncertainties. Especially the temporal interpolation of the vertical wind component has to be considered a significant source of error for trajectories. Further errors due to inhomogeneities of the wind field, turbulent and convective motions and precipitation processes lead to uncertainties in the appointment of air parcel pathways. Although the quality of the input meteorological fields increased in the last years, one still has to consider a position error of 20 % of the travel distance using an input wind field on a $0.5^\circ \times 0.5^\circ$ and a temporal resolution of 3 h (Stohl, 1998).

A trajectory represents the pathway of an infinitesimal air parcel. Because of the error that has to be taken into account a single trajectory is not sufficient for a description of the path. Thus, ensembles of trajectories were utilized for many foregoing studies (e.g., Merrill et al., 1985; Kahl, 1993). Although the ensemble method does not produce more accurate trajectories, it gives a reliable estimation of the sensitivity of the trajectories to initial errors and other errors (Stohl, 1998).

3.2.2 The trajectory calculation and analysis tool FLYTUL

The trajectory analysis program FLYTUL (FLight analysis Tool Using LAGRANTO) was developed and implemented to provide a trajectory calculation and analysis program easy to use for the analysis of aircraft field campaigns. It comprises the calculation of air mass trajectories, the combination of the trajectories with meteorological fields and emission data bases (Sections 3.2.3 and 3.2.4), and the classification of each trajectory using requested parameters (Section 3.2.5). FLYTUL is written in Python 2.5. It contains the core Fortran routine `newcaltra.f` of the Lagrangian Analysis Tool (LAGRANTO) developed by Wernli (Wernli and Davies, 1997; Wernli, 1997). LAGRANTO is a three-dimensional trajectory model using the wind field data u , v , and w . Comparisons of the LAGRANTO model with two other trajectory models (TRAJKS and FLEXTRA) showed that the accuracy of the trajectories depends more on the quality of the input data than on the choice of the trajectory model (Stohl et al., 2001). The study also recommended the use of a temporal resolution of three hours rather than six hours of the input wind field. Thus, the trajectory calculations improve significantly and produce stronger vertical motion.

The input data for the trajectory calculation was retrieved from the ECMWF operational archive (Persson and Grazzini, 2007). The horizontal resolution of the input data was $0.5^\circ \times 0.5^\circ$. The maximum horizontal resolution of the ECMWF data is $0.225^\circ \times 0.225^\circ$. The lower resolution used for the trajectory calculation was chosen because of storage limitations on the local computer. The vertical resolution is split into 91 vertical levels. Analysis data was available for a six hourly resolution at 00, 06, 12, 18 UT. To provide a temporal resolution of three hours prognostic data (+3h) were retrieved for 03, 09, 15, and 21 UT.

The trajectory calculation module of FLYTUL sets the start points of the trajectories and converts the output of LAGRANTO into files based on the widely used NASA Ames Format. A box of a specified size is set up around each given start point. Within the box, an ensemble of trajectories is started to estimate the sensitivity of the trajectories. The start points of the ensemble are randomly distributed inside the box. The dimensions of the box for the present analysis was set to a maximum horizontal distance of 500 m and a maximum vertical distance of 100 m to the given start point and a total number 100 ensemble trajectories. The start points can be selected individually or a list of start points can be read in automatically, e.g. a flight track. For the trajectory analysis of the DLR Falcon 20 flights one ensemble of trajectories was started every minute along the flight track and calculated backwards for 240 h. Ensembles of back trajectories starting from ground stations were started in 6 hourly intervals

and calculated backwards for 168 h. The calculation time step was set to 30 min. The start time of the trajectories can only be set to a multiple of the calculation time step. Hence the temporal resolution of the trajectory start times had to be set to 30 min. If trajectories go below the ground, i.e. where the pressure becomes larger than the surface pressure, they are lifted by 10 hPa to continue the calculation.

The resulting trajectories can be used to calculate meteorological parameters along each single trajectory pathway in combination with ECMWF fields, which contain the required additional meteorological parameters. The ECMWF fields can contain two dimensional surface data like mean sea level pressure or boundary layer height, or three dimensional data like temperature, humidity or cloud cover. Based on the position data and time information of the single trajectories the parameters are interpolated in space and time along the transport pathways. The spatial interpolation method used in the FLYTUL program is IDW (inverse distance weighting, e.g. Goovaerts (2000), Lloyd (2005), and Lu and Wong (2008)). As the name indicates the method uses a weight factor which decreases with increasing distance to the desired interpolation point and is multiplied with the respective values of the surrounding points. The interpolation method can be written as:

$$u(x) = \frac{\sum_{k=0}^N w_k(x)u_k}{\sum_{k=0}^N w_k(x)}, \quad w_k(x) = \frac{1}{d(x, x_k)^p} \quad (3.14)$$

where $u(x)$ is the value at point x , u_k the values at the surrounding points, N the number of surrounding points and $d(x, x_k)$ the distance between the given point x and the surrounding points. $w_k(x)$ is the IDW weighting factor and can be controlled with the power parameter p . FLYTUL uses a typical power parameter of 2, i.e. the inverse square distance for the weighted interpolation method. If parameters of a three dimensional field are interpolated the 8 grid points surrounding the trajectory position and their respective distances in metres are used. After the spatial interpolation the two values of the model time steps before and after the trajectory position time are interpolated linearly.

FLYTUL also provides several tools to display the results of the trajectory calculation graphically. An example of the median vertical cross section of the troposphere derived from a bunch of trajectories is shown in Figure 3.4.

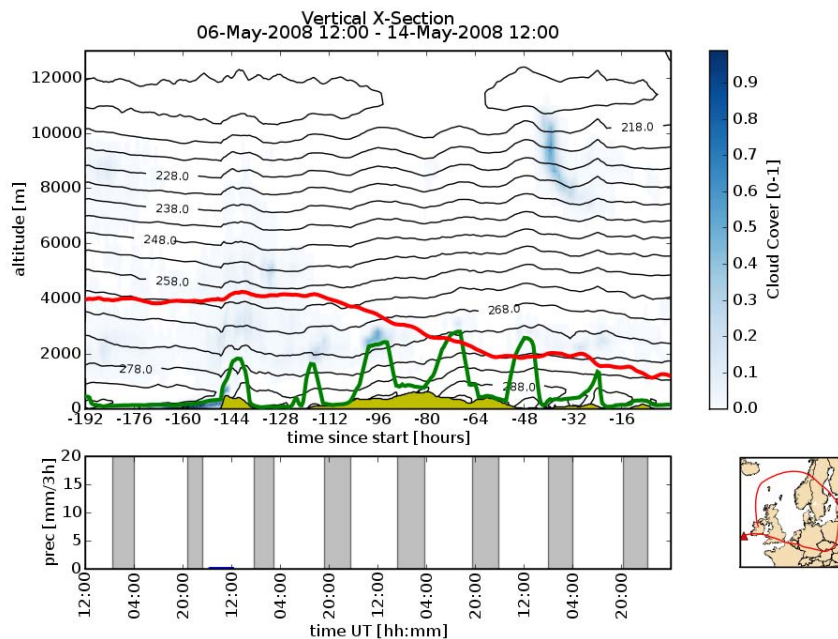


Figure 3.4: Vertical cross section of the troposphere showing median values of a bunch of back trajectories starting south west of Ireland. The upper panel shows the trajectory (red line), boundary layer height (green line), cloud cover (blue shade), temperature (black lines), and orography (yellow shade). The lower panel precipitation (blue columns) and night times (grey shade).

3.2.3 The EDGAR 3.2 Fast Track 2000 dataset

The EDGAR database (Emissions Database for Global Atmospheric Research) EDGAR 3.2 Fast Track 2000 dataset (32FT2000) was used to define the regional variation of the source strength from anthropogenic emissions. To facilitate the naming of the dataset the EDGAR 32FT2000 dataset is always discussed in the following if only EDGAR database is mentioned. Detailed information of the EDGAR database can be found in van Aardenne et al. (2005) and Olivier (2002) or on the project webpage <http://www.mnp.nl/edgar/>. The database provides information of global anthropogenic emissions for the year 2000 of Kyoto Protocol greenhouse gases CO_2 , CH_4 , N_2O , and F-gases (HFCs, PFCs and SF_6) and of the air pollutants CO, NMVOC, NO_x and SO_2 which also serve as aerosol precursor gases. The main advantage of the EDGAR database are the classification of emissions into source categories and its availability on a $1^\circ \times 1^\circ$ grid. The gridded data provides an easy use of the EDGAR archive for atmospheric models and, essential for this work, for trajectory analysis. The EDGAR database is available via the project webpage. The information provided

by the EDGAR database was mostly taken from international statistical data sources and international publications.

The classification of emissions for the gridded dataset comprises the following source types: fuel combustion (including fuel production/transmission)*, biofuel combustion*, industrial processes (non-combustion) and solvent use*, agriculture and biomass burning*, waste handling*, natural sources, and air traffic. The source types marked with an asterisk (*) were selected to determine the total ground based anthropogenic emissions for the present work and summed to a total emission value per grid cell (E_{SUM}). Further studies not discussed within the present work were performed with different groupings of sources (e.g. agricultural and industrial sources) but did not provide significant additional outcomes for the analysis of the measured aerosol properties over Central Europe.

The EDGAR database is used within the present trajectory analysis to provide qualitative information of emissions for different regions. A normalized emission factor E_{NORM} is calculated for each grid cell to derive a qualitative value for the source strength of a region relative to the global emissions. E_{NORM} is calculated by normalizing the sum of the source types of each grid cell to the 95th percentile of the global sums E_{GLOBAL} not taking 0 values into account:

$$E_{GLOBAL} = \{x \mid x \in \{E_{SUM,0}, \dots, E_{SUM,n}\} \wedge x > 0\}, \quad (3.15)$$

$$E_{P95} = P95(E_{GLOBAL}), \quad (3.16)$$

$$E_{NORM} = \frac{E_{SUM}}{E_{P95}}. \quad (3.17)$$

The global 95th percentile of ground based anthropogenic emissions E_{P95} reaches ~ 7.5 Mt/a. All values E_{NORM} greater than 1 are set to 1. The resulting normalized emission factors E_{NORM} are shown in Figure 3.5 a and b for Europe and Asia, respectively. The mapping of E_{NORM} shows that the major source regions of anthropogenic emissions in Europe are England, the Benelux States, Germany, and Northern Italy. A more recent version of the EDGAR database was released within 2009 and covers emission data bases till the year 2005. Information of the EDGAR v4.0 database can be found on the project webpage <http://edgar.jrc.ec.europa.eu/>.

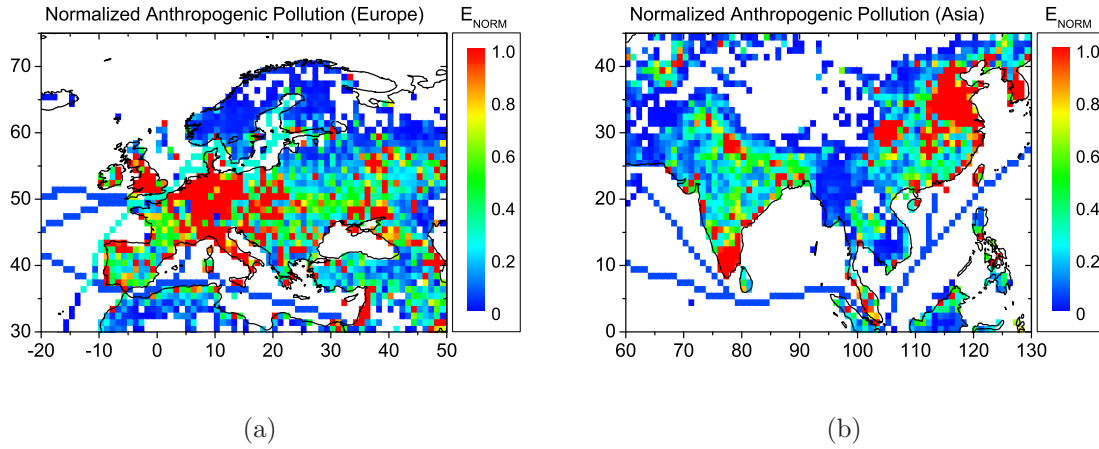


Figure 3.5: Normalized emission factors E_{NORM} for ground based anthropogenic sources calculated from the EDGAR 3.2 Fast Track 2000 dataset for Europe (a) and Asia (b).

3.2.4 Boundary layer indices

The combination of the boundary layer height interpolated along the trajectories, their position over the oceans or continental land masses and the source strength of respective regions can be used to define simple indices along each trajectory pathway. On the basis of three initial indices further indices can be calculated for individual requirements. The initial indices are:

$$\begin{aligned}
 MI &\in \{0; 1\} \text{ (maritime index),} \\
 CI &\in \{0; 1\} \text{ (continental index),} \\
 BI &\in \{0; 1\} \text{ (boundary layer index).}
 \end{aligned}$$

The BI can be calculated using the boundary layer height retrieved from the ECMWF data or a fixed boundary layer height. If the trajectory height a.s.l. is lower than the boundary layer height a.s.l. BI is 1, else 0. Based on these three indices further useful indices can be defined:

$$\begin{aligned}
 MBI &= BI \cdot MI, \quad MBI \in \{0; 1\} \text{ (maritime boundary layer index),} \\
 CBI &= BI \cdot CI, \quad CBI \in \{0; 1\} \text{ (continental boundary layer index).}
 \end{aligned}$$

To assess the amount or the strength of emissions affecting the air masses along their transport pathway at each time step the mission factor E_{NORM} defined in Section 3.2.3

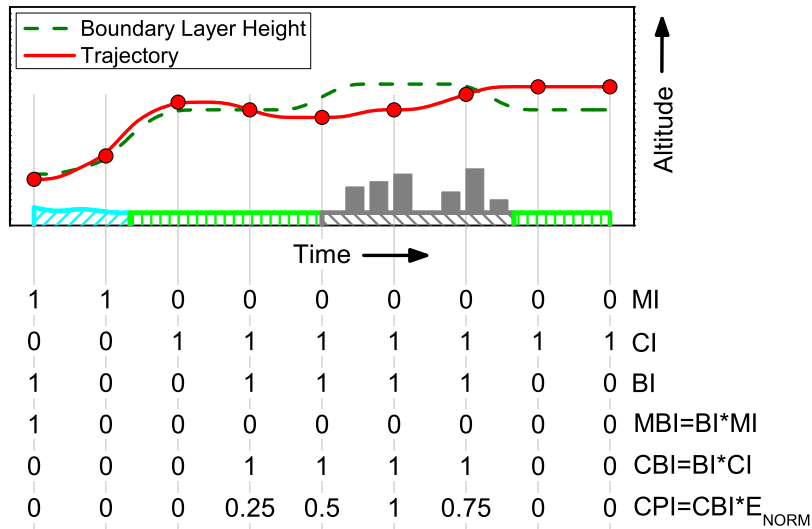


Figure 3.6: Schematic description of the construction of several indices along an air mass trajectory. For the respective index definitions we refer to the text.

can be combined with the previous indices. Thus, it can be assured that anthropogenic sources solely will be considered if the trajectory is located within the boundary layer above the respective source region. The continental pollution index is defined as followed:

$$CPI = CBI \cdot E_{NORM}, \quad CPI \in [0, 1] \text{ (continental pollution index).}$$

Figure 3.6 shows a schematic description of the construction of the several indices.

3.2.5 Classification of air mass trajectories using time weighted averaging

The analysis along each trajectory pathway regarding the meteorological conditions and different source regions provide already useful information for the interpretation of the probed air masses. However, it is still an ambitious task to compare the trajectories and the several different historical backgrounds of the air masses with each other in an objective way. To characterize the probed air masses on the basis of their transport history they have to be classified by single factors. These factors can comprise the

meteorological history like cloud cover or the history of emission contributions like the previously introduced continental pollution index *CPI*. To derive one factor per parameter for each trajectory a time weighted averaging method was introduced for the use with flytul. The function and function parameters have to take into account the lifetime of aerosols and the dominating effect of recently occurring events, e.g. fresh aerosol source contributions. The typical lifetime of aerosols was found to be $t_a \approx 48$ h in the boundary layer and up to $t_a \approx 720$ h (30 days) in the free troposphere (Williams et al., 2002; Riemer et al., 2004; Cubison et al., 2006). The aerosol lifetime is used to estimate a maximum time after that a distinct signal of aerosols originating from a certain source region cannot be detected anymore. The distinct signal vanishes due to processes occurring during the air mass transport like condensation, coagulation, or sedimentation.

The Gaussian distribution function was chosen to estimate the probability to measure an aerosol signal originating from a certain source region. It is used to calculate a decreasing weighting factor along a trajectory with increasing temporal distance from the trajectory starting point, e.g. the measurement site. The weighting factor is applied to several parameters along the trajectory like pollution indices or meteorological properties.

The mean of the distribution function μ is set to 0. The variance σ^2 is the free parameter of the distribution function and can be varied depending on the weight that has to be given to fresh or aged contributions. The distribution function is calculated for three σ^2 values to investigate the different impacts on the time weighted parameters. σ^2 is set to one third, half, and the whole aerosol lifetime. Thus, respectively 99.73 %, 95.45 %, and 68.27 % of the total weight (w_{GAUSS}) lies within the aerosol life time. The Gaussian weight can be derived from:

$$g(t) = \frac{1}{\sqrt{2\pi\sigma^2}} \exp\left(-\frac{1}{2} \frac{(t-\mu)^2}{\sigma^2}\right), \quad \mu = 0, \quad (3.18)$$

$$\sigma^2 = sf \cdot t_a, \quad sf = \left\{\frac{1}{3}; \frac{1}{2}; 1\right\}, \quad (3.19)$$

$$w_{GAUSS}(t) = \frac{g(t)}{\max(g)}. \quad (3.20)$$

The Gaussian weight is normalized between 0 and 1. If one or more transitions happen between the boundary layer and the free troposphere the new weighting function will start at its weighting factor $w_{GAUSS}(t = t_{transition})$. Figure 3.7 shows the weighting functions for the free troposphere, the boundary layer and for a mixed case scenario.

Using the weighting function the time averaged factor \overline{u}_t of the required parameter can finally be written as:

$$\overline{u}_t = \frac{\sum_{t=0}^{t_{max}} w_{GAUSS}(t) u(t)}{\sum_{t=0}^{t_{max}} w_{GAUSS}(t)}. \quad (3.21)$$

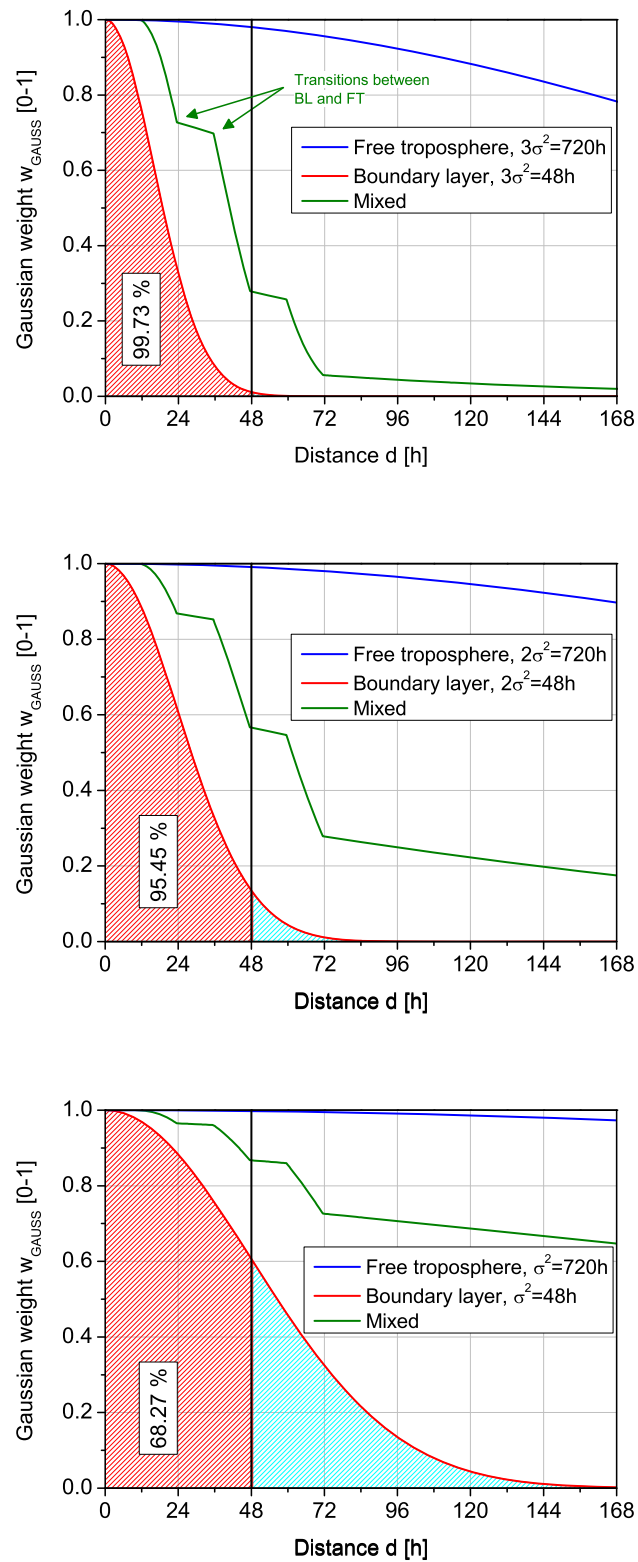


Figure 3.7: Weighting functions for time weighted averaging using a Gaussian distribution function. Displayed are the functions for the free troposphere (blue line), the boundary layer (red line) and a mixed case scenario (green line).

3.3 The EUCAARI-LONGREX campaign

The European Aerosol Cloud Climate and Air Quality Interactions project EUCAARI is a multidisciplinary integrated project which focuses on understanding the interactions of climate and air pollution. The two overall objectives of the EUCAARI project are (Kulmala et al., 2009):

1. Reduction of the current uncertainty of the impact of aerosol particles on climate by 50% and quantification of the relationship between anthropogenic aerosol particles and regional air quality.
2. Quantification of the side effects of European air quality directives on global and regional climate, and provide tools for future quantifications for different stakeholders.

The project focusses on problems like the quantification of emissions of primary aerosol and secondary aerosol precursors from anthropogenic sources, the transformation and ageing of these emissions during the transport from, into and within Europe and the impact of these emissions on regional air quality. 48 partners from 25 countries worked on the modelling of aerosol and climate interactions from nano to global scale, the development of instrumentation, laboratory experiments, satellite measurements, long-time measurements and measurement campaigns to examine the objectives and problems (see Figure 3.8).

The measurement campaigns can be divided into two specific approaches. Long-time measurements and intensive observing periods (IOP) at selected European atmospheric

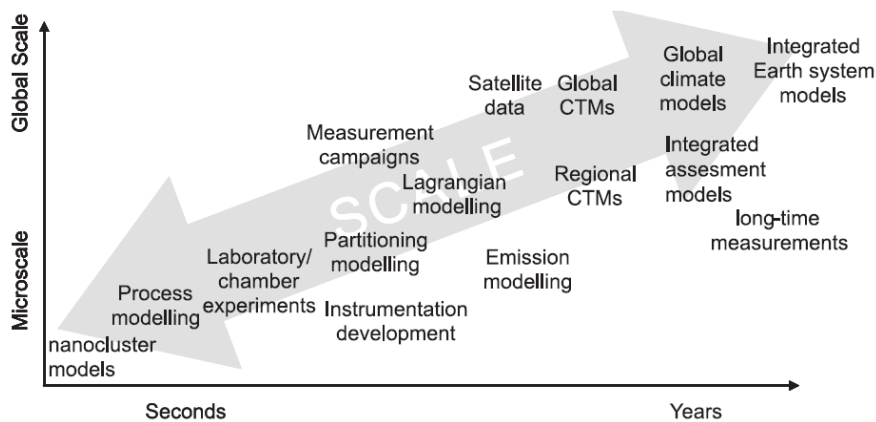


Figure 3.8: Model and data integration philosophy over spatio-temporal scales. CTM is Chemical Transport Model (Kulmala et al., 2009).

supersites and aircraft field campaigns. Ground based measurements were conducted at the following supersites: Kosetice (Czech Republic), Hyytiälä and Pallas (Finland), Puy de Dome (France), Melpitz and Hohenpeißenberg (Germany), Finokalia (Greece), K-Puzta (Hungary), Mace Head (Ireland), San Pietro Capofiume (Italy), Vavihill (Sweden), Jungfrauoch (Switzerland), and Cabauw (The Netherlands). The IOP took place in 2008 between 15 May–15 June. In May 2008 two aircraft field campaigns were conducted. The Intensive Observation Period at Cabauw Tower (IMPACT) was a joint campaign of ground based measurements at the CESAR tower at Cabauw and airborne measurements with the French ATR–42 operated by the Service des Avions Français Instrumentés pour la Recherche en Environnement (SAFIRE) and with a helicopter operated by the Leibniz-Institut für Troposphärenforschung (IfT). The main objective of the IMPACT campaign focussed on the observation of the boundary layer and aerosol-cloud interactions. The second aircraft field campaign was the Long-Range Experiment (LONGREX). Its objectives and its implementation will be described in the following Sections 3.3.1, 3.3.2 and 3.3.3.

3.3.1 Objectives and strategy of the EUCAARI-LONGREX campaign

The LONGREX aircraft campaign was part of the EUCAARI work package (WP) 4.3 Airborne infrastructure (Kulmala et al., 2007). Aircraft campaigns provide the link between regional ground based measurements and large scale information of atmospheric properties retrieved by satellite measurements. The LONGREX campaign focussed on the horizontal and vertical distribution of aerosol and trace gases on a continental scale throughout the tropospheric column. The aim was to examine the evolution of aerosol properties along west-east and north-south transects including semi-lagrangian flights. Thus, gradients in aerosol properties from marine or biogenic air masses to polluted air masses or from rural and agricultural dominated regions to industrial dominated regions could be observed. The semi-lagrangian flights were designed to observe the transformation processes during air mass transport within the boundary layer or long-range transport in the free troposphere. However, the completion of semi-lagrangian flights was strongly limited by the meteorological situations and air traffic restrictions within the highly frequented European air space.

The British aircraft FAAM BAe-146 (Facility for Airborne Atmospheric Measurements) operated by Directflight and the German Falcon-20 operated by the Deutsches Zentrum für Luft- und Raumfahrt (DLR) operated from Oberpfaffenhofen in May 2008. To get simultaneous measurements of air masses inside the boundary layer and the free tro-

posphere during continental transects the flights were mainly planned as coordinated flights of both aircraft. The BAe-146 focussed on chemical, optical and microphysical aerosol properties and trace gas measurements inside the boundary layer whereas the DLR Falcon 20 measured aerosol microphysical and optical properties and trace gases basically in the free troposphere. In addition a light detection and ranging (LIDAR) system was installed aboard the DLR Falcon 20. Thus the DLR Falcon 20 could serve as a pathfinder for the BAe-146 by detecting specific pollution layers inside the boundary layer. The aircraft were limited to real air routes due to restrictions of the national air traffic controls (ATC). Because of different air routes inside the boundary layer and the free troposphere both aircraft could not take exactly the same horizontal path. Nevertheless, the maximum deviation of both air routes could be limited to acceptable 50 km.

The DLR Falcon 20 flew stacked horizontal legs with an approximate duration of 5 min each at different altitudes to obtain in-situ measurements throughout the tropospheric column above certain regions. These so called vertical profiles have a horizontal extension of approximately 50–100 km and reach a vertical extension of 10–12 km. Vertical profiles and overflights of ground stations performed by the DLR Falcon 20 were conducted in the larger regions of the EUSAAR sites Melpitz, Hohenpeißenberg, Mace Head, Vavihill, and Cabauw. The regions for the vertical profiles were limited by ATC like the air routes. Thus vertical profiles had to be performed during take off and landing and in Temporary Reserved Areas (TRA).

3.3.2 The aircraft and instrumentational setup

The present work focuses on the in-situ measurements aboard the DLR Falcon 20. Thus, the description of the aircraft and instrumentation setup will be limited mainly to the DLR Falcon 20.

The DLR Falcon 20 is a twin jet aircraft with a maximum range of 2000–5000 km depending on the flight altitude. The maximum flight time is 4–5 h. The aircraft reaches a maximum flight altitude of 42000 ft (12800 m) and flies with an average true air speed of 410 KTAS (210 m s^{-1}). Its unique modifications allow the employment of additional scientific instrumentation inside the cabin and outside on special wing ports. During the EUCAARI-LONGREX campaign a set of trace gas and aerosol in-situ instruments as well as a High Spectral Resolution Lidar (HRSL) (Esselborn et al., 2008) for remote measurements were used aboard the aircraft. Table 3.2 lists the instruments and the measured properties. Figure 3.9 shows the setup of the aerosol in-situ instrumentation employed inside the cabin. The aerosol instrumentation allows the measurement of the

Table 3.2: Scientific payload aboard the DLR Falcon 20 during the EUCAARI-LAONGREX campaign.

Instrument	Measured parameter
Aerosol in-situ	
CPC1 (TSI 3760) + TD250	non-volatile number concentration $D_p > 14 \text{ nm}$
CPC2 (TSI 3760) + DS7 + TD250	non-volatile number concentration $D_p > \sim 100 \text{ nm}$
CPSA1 + DS3 (+ TD250)	(non-volatile) number concentration $D_p > \sim 50 \text{ nm}$
CPSA2	number concentration $D_p > 10 \text{ nm}$
CPSA3	number concentration $D_p > 4 \text{ nm}$
Grimm Sky-OPC (1.129)	dry size distribution $0.25 < D_p < \sim 2.5 \mu\text{m}$
Grimm Sky-OPC (1.129) + TD250	non-volatile size distribution $0.25 < D_p < \sim 2.5 \mu\text{m}$
PCASP-100X	dry size distribution $0.15 < D_p < 3 \mu\text{m}$
FSSP-300	in-situ size distribution $0.3 < D_p < 20 \mu\text{m}$
NAIS	Neutral Cluster - Air Ion Spectrometer by University of Tartu (Estonia) dry size distribution $0.8 < D_p < 42 \text{ nm}$
3 λ -PSAP	absorption coefficient
Trace gas in-situ	
CO and O ₃	
Remote sensing	
HSRL	High Spectral Resolution Lidar extinction profile at 532 nm backscatter at 532, 925 and 1064 nm water vapor at 532 nm

Abbreviations:

TD250: Thermodenuder (250°C), DSx: Number of diffusion screens

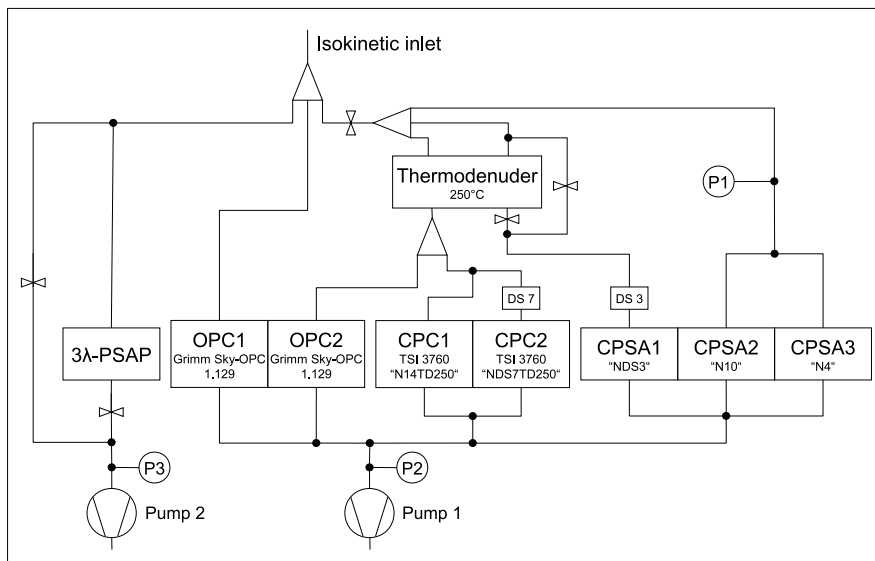


Figure 3.9: Instrument setup for aerosol measurements aboard the DLR Falcon 20.

total number concentration for particles larger 4 nm and the aerosol size distribution in the size range 0.15–30 μm . In addition, number concentrations and size distributions of non-volatile particles and the absorption by aerosol particles were measured. The DLR Falcon 20 also provides the measurement of meteorological properties like temperature, pressure, or humidity.

3.3.3 Implementation of the EUCAARI-LONGREX campaign

16 measurement flights of the BAe-146 aircraft and 15 measurement flights (plus one test flight) of the DLR Falcon 20 were realized during the LONGREX campaign. This section gives an overview of the objectives of the several flights. A summary of the flights is given in Table 3.3, the flight tracks are plotted in Figure 3.10.

The first coordinated double flights with a stopover at Rotterdam were performed on 6 May (BAe-146: b362, b363; DLR Falcon 20: 080506a, 080506b). The objective was to fly first transects over Germany and the Benelux States within high pressure conditions (Section 4.1) and to measure strong pollution over the British Channel on the west coast of England. Vertical profiles during the flight were conducted in a military area close to Melpitz and on the west coast of England.

On the following day, only one flight was performed by the BAe-146 (b364) to compare

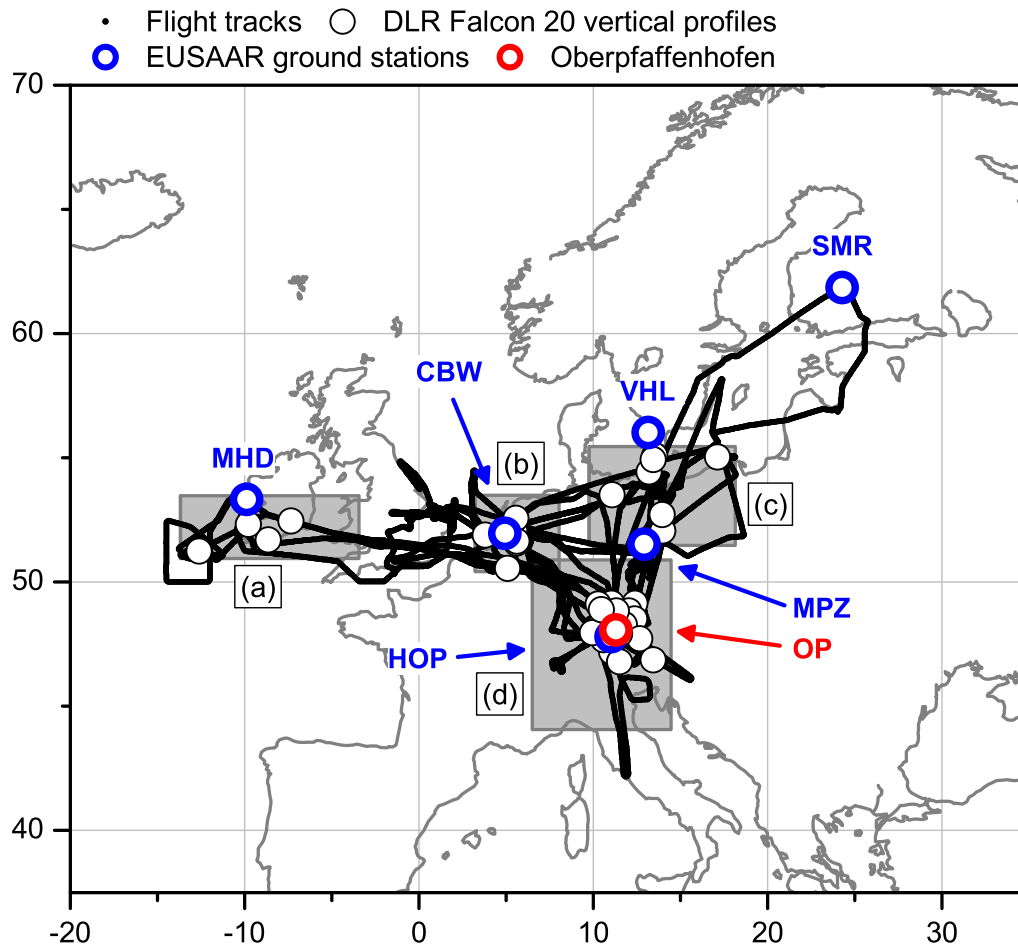


Figure 3.10: Flight tracks of DLR Falcon 20 and FAAM BAe-146 during the EUCAARI-LONGREX campaign. Black circles denote the position of vertical in-situ profiles measured aboard the DLR Falcon 20. The following EUSAAR sites are shown in blue circles: Cabauw (CBW), Mace Head (MHD), Melpitz (MPZ), Hyytiälä (SMR), Vavihill (VHL), Hohenpeißenberg (HPB). The gray shades depict regions used for the classification of vertical profiles (see Section 4.4): Atlantic and southwest of Ireland (a), Benelux States (b), Baltic Sea and North-east Germany (c), and South Germany (d).

both PCASP-100X mounted on the wing pylon of the aircraft. Still favourable conditions for airborne aerosol measurements allowed for further coordinated double flights

on 8 May (BAe-146: b365, b366; DLR Falcon 20: 080508a, 080508b). The objective of the mission flights was the characterization of aerosol sources in Eastern Germany, Western Poland and over the Baltic Sea under conditions of relatively clean inflow of Scandinavian air masses. After a stop at Rostock, ageing and mixing processes between fresh emissions and aged background aerosol were observed over Western Germany and the Netherlands. Vertical profiles were performed close to Leipzig, over the Baltic Sea and in a TRA close to the CESAR tower in Cabauw.

On 9 May an intercomparison flight with the three aircraft BAe-146, SAFIRE ATR-42 and DLR Falcon 20 was conducted in the TRA Allgäu west of Oberpfaffenhofen.

The BAe-146 performed two more double flights on 10 May and 12 May. During the first double flight, the BAe-146 (b368, b369) headed towards Riga to measure recirculated pollution from Northern Germany and local pollution over the Baltic Sea up to Southern Finland. This way an extensive north-south transect with an extension between 48°N – 62°N could be performed. The second double flight (b370, b371) focussed again on the aerosol distribution over Germany, the Benelux States, the North Sea and the Baltic Sea during stable high pressure conditions. Stopover was in Rostock.

On 13 May an extensive east-west transect from Oberpfaffenhofen to Shannon (Ireland) was performed with both aircraft. During the first flight of the day the DLR Falcon 20 made a return flight from and to Oberpfaffenhofen heading to the Baltic Sea (080513a). The flight included a vertical profile between Cottbus and Berlin to measure aged pollution on site. The second flight followed polluted continental European air masses that were advected via the British Isles towards Ireland and the North East Atlantic (080513b). The BAe-146 followed the westward air mass transport at low level via the Benelux States and along the south coast of England and Ireland to Shannon (b372, b373).

The aged European pollution southwest of Ireland was measured in the morning of 14 May (BAe-146: b374, DLR Falcon 20: 080514a). Both aircraft operated from Shannon with the BAe-146 flying at low levels and the DLR Falcon 20 in the upper troposphere to detect the pollution layers with LIDAR measurements. Subsequent to the LIDAR measurements the DLR Falcon 20 performed a horizontal profile over the Atlantic south west of Ireland into the pollution layer. Both flights in the afternoon were direct transfer flights from Shannon to Oberpfaffenhofen (BAe-146: b375, DLR Falcon 20: 080514b).

A further north-south transect to the Baltic Sea including a vertical profile on the

southern tip of Sweden was performed with the DLR Falcon 20 on 20 May (080520a). The DLR Falcon 20 flew back to Oberpfaffenhofen at low levels to measure in-situ latitudinal gradients of aerosol concentrations right above or inside the boundary layer.

The next coordinated flight was conducted on 21 May (BAe-146: b379, DLR Falcon 20: 080521a, 080521b). The flight route directed the aircraft to the Baltic Sea to measure clean air masses arriving from Scandinavia and to the Netherlands into air masses affected by anthropogenic pollution. The DLR Falcon 20 made a stop in Rotterdam. Vertical profiles were performed over the Baltic Sea and inside the TRA close to Cabauw.

The last measurement flight of the BAe-147 within the LONGREX campaign took place on 22 May (b380). Another south-north transect followed by an east-west transect guided the aircraft to North East Germany and via the Benelux states back to England. The DLR Falcon 20 operated as a pathfinder only at high altitudes (080522a, 080522b). A stopover had to be made at Charleroi (Belgium).

The last flight of the DLR Falcon 20 was performed on 24 May (080524a) within the framework of the EUFAR TA project AMAPUV of the University of Graz and other Austrian research institutions to measure the vertical aerosol distribution over two observatories in Austria (Sonnblick, Kanzelhöhe/Gerlitz).

Table 3.3: Flight summary of DLR Falcon 20 and BAe-146 during the EUCAARI-LONGREX campaign containing time of the flights and the median mean sea level pressure (MSLP) along each flight track. The MSLP was retrieved from the ECMWF operational archive.

Date	Flight ID	DLR Falcon 20			BAe-146			
		Take Off	Landing	MSLP	Flight ID	Take Off	Landing	MSLP
2 May 2008	080502a	09:01	11:57	1021.81				
6 May 2008	080506a	09:36	12:25	1026.21	b362	09:09	13:51	1025.63
7 May 2008	080506b	15:26	18:00	1025.00	b363	15:13	18:25	1024.83
8 May 2008	080508a	08:08	11:47	1020.65	b364	13:27	15:51	1019.73
9 May 2008	080508b	13:45	17:31	1016.61	b365	08:24	12:30	1020.10
10 May 2008	080509a	11:39	15:03	1014.69	b366	13:54	17:09	1016.99
12 May 2008					b367	12:22	16:50	1014.51
13 May 2008	080513a	10:41	13:55	1017.08	b368	08:04	13:00	1021.55
14 May 2008	080513b	14:56	17:43	1016.41	b369	14:30	18:12	1022.68
20 May 2008	080514a	09:16	12:58	1015.34	b370	06:15	12:36	1019.39
21 May 2008	080514b	14:21	16:38	1011.90	b371	13:51	18:04	1018.89
22 May 2008	080520a	10:25	14:02	1016.82	b372	08:56	13:28	1017.59
24 May 2008	080521a	07:59	11:11	1020.17	b373	14:46	18:27	1015.92
	080521b	12:31	15:10	1016.55	b374	09:41	14:39	1014.90
	080522a	08:55	11:55	1015.47	b375	15:54	18:18	1011.95
	080522b	12:44	13:44	1015.02	b379	08:03	13:27	1017.66
	080524a	06:26	10:22	1012.79	b380	08:57	13:20	1015.70

Chapter 4

Results and discussion of aerosol measurements obtained during the EUCAARI-LONGREX campaign in May 2008

4.1 The meteorological situation in May 2008

The analysis of the meteorological situation was a key part of this work and is published in Hamburger et al. (2011). The following sections describe the synoptic situation in May 2008 with its spatial and temporal focus on the measurement flights, which were mostly performed over Central Europe. The data used for the analysis was retrieved from the operational archive of the ECMWF. The model has a spectral resolution of T799/L91. Hess and Brezowsky Grosswetterlagen (GWL) (Hess and Brezowsky, 1952; Gerstengarbe and Werner, 2005), describing large-scale circulation patterns over Europe and the North-East Atlantic (James, 2007), are used to describe the general circulation over Europe. The German Weather Service DWD provides the GWL data (<http://www.dwd.de/GWL>).

4.1.1 The evolution of the meteorological situation over Europe

The synoptic situation in May 2008 can be divided into two major periods with an approximate duration of two weeks each. The first half of May (1 May–15 May; hereafter period a) was dominated by an anticyclone blocking event, whereas the second half (16 May–31 May; hereafter period b) was dominated by westerly flow and passage of frontal systems over Central Europe. The following description of the synoptic situation focuses on the days during the EUCAARI-LONGREX campaign when measurement flights were performed with the FAAM BAe-146 and the DLR Falcon 20. Figure 4.1

shows the mean geopotential height at 850 hPa and the integrated precipitation per flight day, calculated for a time span between 0–24 UTC of the respective day. The plots are overlaid by the flight tracks of the FAAM BAe-146 and the DLR Falcon 20 aircraft. The GWL occurring in May 2008 are listed in Table 4.1.

Between the measurement flights on 6 May until 11 May dry and stable conditions could be observed over Central Europe caused by a high over Central Europe (Hoch Mitteleuropa: HM). The centre of the anticyclone remained approximately stationary over the North Sea and Denmark. Its maximum surface pressure values averaged at 1032 hPa on 6 May. Horizontal wind speeds at 850 hPa level in the core region of the anticyclone were quite low with $0\text{--}7\text{ m s}^{-1}$ compared to its western, northern and eastern borders. Wind speeds increased up to $10\text{--}20\text{ m s}^{-1}$ due to the higher pressure gradient along these borders, caused by surrounding cyclones. These surrounding cyclones also led to an intensification and maintenance of the “ Ω ” shaped anticyclone which can be described as a blocking event.

Subsiding air masses in the core region of the anticyclone caused almost clear sky conditions with only few clouds (mainly cu and strcu) occurring rarely on the top of the continental and marine boundary layer. Thick cloud cover and precipitation occurred over Southwest Europe and west of the British Isles associated with the frontal systems of the surrounding cyclones. In addition precipitation occurred on the west side of the Scandinavian Mountains induced by the eastward transport of moist marine air masses from the Norwegian Sea.

The anticyclone left its stationary position on 11 May and moved until 14 May westwards into the Atlantic north east of the British Isles and turned from an Ω -blocking into a so-called split-flow block (Barriopedro et al., 2006). The general circulation pattern was identified as an Icelandic high with a ridge over Central Europe (Hoch Nordmeer-Inland, antizyklonal: HNa). The ridge inducing the high pressure reached from the British Isles towards Northern Germany and maintained stable synoptic conditions in this region. Cyclones moving from the Atlantic towards continental Europe via the Bay of Biscay south of the anticyclone led to a westward transport of air masses from Central Europe to the Atlantic. The anticyclone started to decay on 14 May.

A trough over Central Europe (Trog Mitteleuropa: TM) evolved on 16 May and lasted until 18 May. Frontal systems associated with the trough led to the first precipitation over the Benelux states and Germany since the first measurement flights had been performed. They changed the flow regime from westward to eastward air mass transport. Arctic air masses were now advected via the North Sea towards Northern Germany.

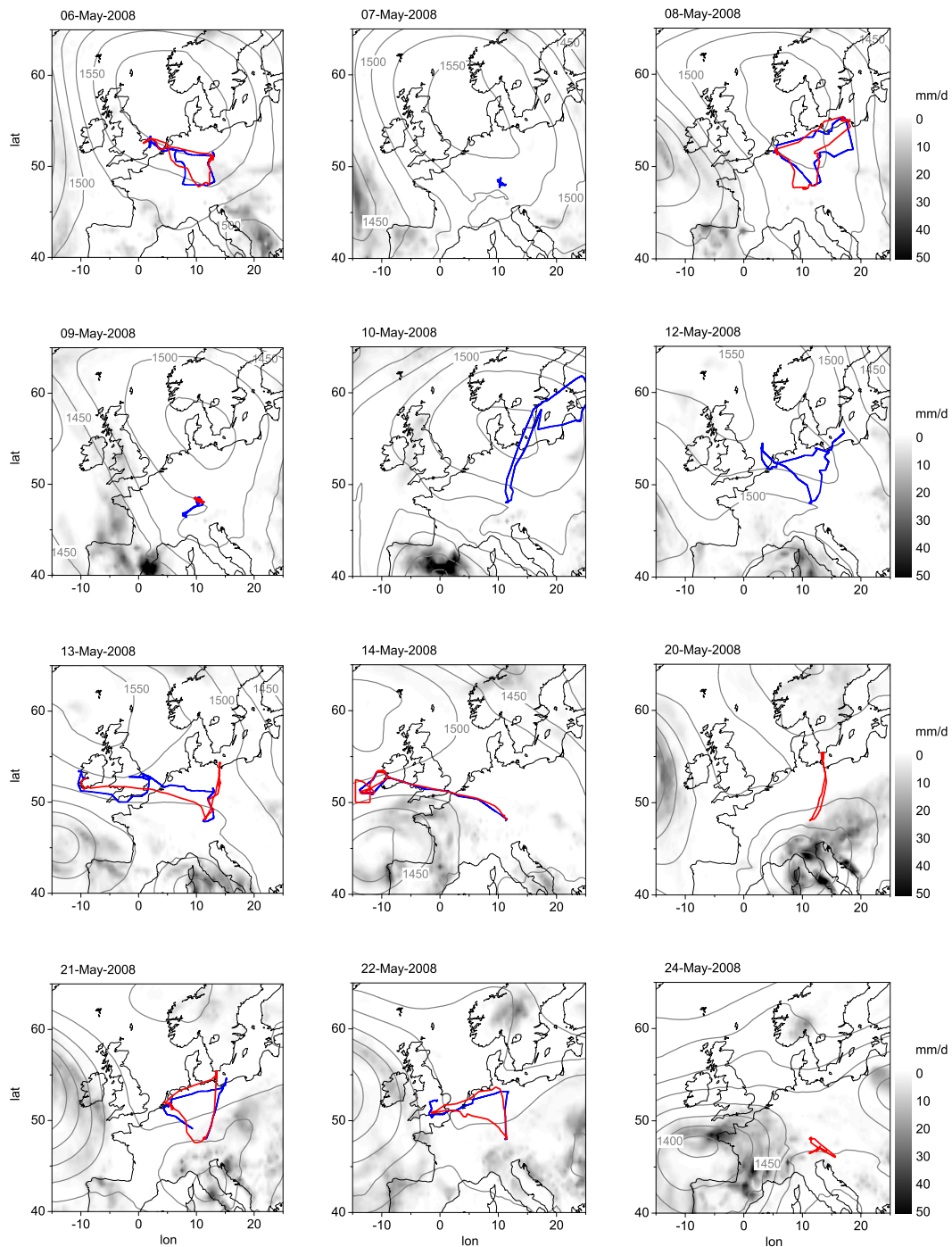


Figure 4.1: FAAM BAe-146 (blue line) and DLR Falcon 20 (red line) flight tracks. Meteorological situation on the flight days showing mean geopotential height [m] at 850 hPa (solid gray line) and sum of daily precipitation [mm d^{-1}] (white to black shading). Mean and sum values are calculated for 00–24 UTC on the respective day.

The flow regime changed again its wind direction over Central Europe beginning with 18 May with the onset of an anticyclonic North-Easterly pattern (Nordostlage, antizyklonal, NEa). Two cyclones formed consecutively over Northern Italy with a minimum sea level pressure of 997 hPa on 20 May. These cyclones induced an easterly flow with horizontal wind speeds between $5\text{--}15\text{ m s}^{-1}$ at 850 hPa level over Central Europe on the northern border of these cyclones. The easterly flow merged with the northerly flow associated with a further cyclone located over Scandinavia. The cyclones located over Northern Italy advected warm and moist air masses from the Mediterranean via the Balkan Peninsula towards Central and Eastern Europe. In contrast, the cyclone located over Scandinavia advected cold air masses along the Norwegian Sea and the North Sea towards Central Europe. The front line of these two air masses extended from the Alps, the Czech Republic, Southern Poland and Belarus to Russia, and caused thick cloud cover and precipitation. This front of air masses remained from 18 May until 22 May. Only few cumulus and stratocumulus clouds occurred in the cold air masses over land north of this front.

A ridge located over Italy and Germany caused quite fair weather over the Eastern part of the Alps in the morning of 24 May. Light convection formed some cumulus clouds during the day.

4.1.2 The anticyclonic blocking event

The major synoptic event occurring during the airborne measurements of EUCAARI-LONGREX was the blocking over Central and Northern Europe during the first weeks of the campaign (3–14 May). Thus, we will take a closer look on its evolution.

The evolution of the geopotential height at 500 hPa level in the centre of the anticyclone is used to identify the lifecycle of the blocking event in May 2008 (e.g., Lupo, 1997; Lupo and Smith, 1998). Downstream a trough a large-scale ridge started to form over Western Europe on 2 May. From 3 and 4 May a cyclone associated with the trough over the Atlantic started to increase. It remained almost stationary for the next days. At the same time the ridge reached an extension over Central Europe and the North Sea and the anticyclone blocking started to develop what can be seen in the increasing geopotential height in Figure 4.2 a. With the occurrence of another cyclone over Northern Scandinavia on 5 May the blocking intensified and formed into a “ Ω ” shaped blocking. The centre of the blocking was located over the centre of the North Sea and remained almost stationary until 11 May (Figure 4.2 b). From 6 May, the

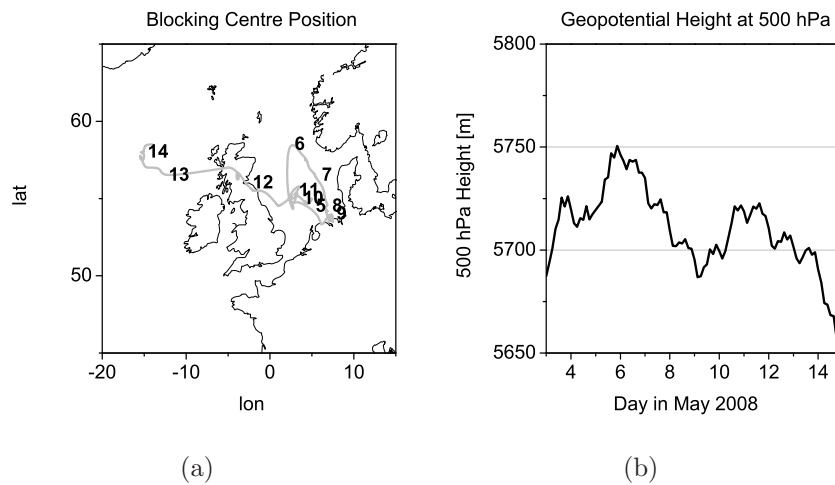


Figure 4.2: Figure a: Centre position of the blocking anticyclone obtained by its centre position at 500 hPa. Numbers denote the date in May 2008. Figure b: Maximum geopotential height [m] at 500 hPa level of the blocking anticyclone versus the date in May 2008.

cyclones over the Atlantic and Northern Scandinavia started to fill in and the blocking began to attenuate until 9 May. This mid-life decay ended on 9 May when a cut-off low north of the Iberian Peninsula upstream the anticyclone started to form and another cyclone downstream intensified. The geopotential height at 500 hPa started to increase again. Due to the cut-off low, which was advected westwards over the Mediterranean south of the anticyclone, the Ω -block turned into a split-flow block. The centre of the blocking began to leave its former almost stationary position over the North Sea on 11 May and moved via Northern Great Britain into the Atlantic between the British Isles and Iceland. The blocking decayed on 14 May.

4.1.3 The synoptic situation within a climatological context

Synoptic weather types over Central Europe have been classified into GWL since 1881 (Hess and Brezowsky, 1952), giving the possibility to place the synoptic situation encountered during EUCAARI-LONGREX into a climatological context. The overall number of large-scale circulation patterns (29 GWLs) is too large to reasonably study the statistics of frequency and duration per month or season of each single pattern, even though the data have been collected since more than one century (Gerstengarbe and Werner, 2005). Thus the patterns will be grouped into two categories for the present study and the statistics will be calculated for the months April, May and June

between 1977–2007. The first group comprises the patterns representing high pressure over Europe and the second group all patterns leading to an anticyclonic flow pattern over Europe.

The first group contains amongst others the patterns HFa, HM and NEa which occurred during EUCAARI-LONGREX (see Table 4.1). The patterns HFa and HM were part of the blocking event and led to 9 consecutive days of high pressure over Europe. NEa formed during period (b) and lasted for 5 days. The median duration of consecutive patterns representing high pressure for the months April, May and June between 1977–2007 is 5.5 days, the 75th percentile 9 days. The sum of the duration of the two patterns HFa and HM in May 2008 equals 9 days. In average similar consecutive patterns with an overall duration of 9 days or more occur approximately once between April and June per year.

The second group contains the patterns mentioned above including HNa, the third pattern which was part of the life cycle of the blocking event. It lasted for 3 days. Hence the blocking event covered 12 consecutive days of anticyclonic flow pattern over Europe. This is twice as long as the median duration of 6 days for the period between April and June between 1977–2007 but less than the 75th percentile of 13 days. Consecutive patterns inducing an anticyclonic flow over Europe and lasting 12 days or longer occur approximately twice between April and June per year.

The anticyclonic blocking event and its stationary position was a special though not exceptional synoptic situation. Several climatologies of blocking events have shown that the European Atlantic region, at the end of the Atlantic storm track, is the region with the highest frequency of blocking events followed by the eastern Pacific region (e.g., Barriopedro et al., 2006; Tyrlis and Hoskins, 2008). The annual cycle shows maximum frequencies in the cold season. A primary blocking episode genesis area for the eastern Atlantic region was found at 0° longitude (Barriopedro et al., 2006), compared to approximately 5° E for the blocking in May 2008. The described blocking was located between 50° N– 60° N, the latitude where most blocking events occur. The mean duration of blocking events over Europe was found to be between 7.6–8 days (Tyrlis and Hoskins, 2008). Thus, the blocking event in May 2008 which lasted 12 days, was exceptionally persistent.

Table 4.1: Grosswetterlagen (GWL) in May 2008 given by the DWD.

GWL	Original definition (German)	Date in 2008
	Translated definition (English)	
TB	Tief Britische Inseln Low over the British Isles	28 Apr–02 May
HFa	Hoch Fennoskandien, antizyklonal Scandinavian High, Ridge C. Europe	03 May–06 May
HM	Hoch Mitteleuropa High over Central Europe	07 May–11 May
HNa	Hoch Nordmeer-Inland, antizyklonal Icelandic High, Ridge C. Europe	12 May–14 May
TrW	Trog Mitteleuropa Trough over Central Europe	16 May–18 May
NEa	Nordostlage, antizyklonal Anticyclonic North-Easterly	19 May–24 May
NEz	Nordostlage, zyklonal Cyclonic North-Easterly	25 May–27 May
SEz	Südostlage, zyklonal Cyclonic South-Easterly	28 May–31 May

4.1.4 The transport pathways of anthropogenic pollution within the anticyclonic wind field

The meteorological situation and the prevailing wind field govern the distribution of anthropogenic emissions above a certain region. The distribution of airborne particulate pollutants over Europe primarily originating from anthropogenic sources is one of the key points of the present work. Transport model analysis help to gain a first insight into the main transport path ways governed by the meteorological situation over Europe in May 2008.

Figure 4.3 shows the horizontal distribution of column-integrated BC mass concentrations from European anthropogenic emissions obtained from a simulation with the Lagrangian particle dispersion model FLEXPART (Stohl et al., 2005). The panels show 48 hours intervals beginning with the high pressure over Central Europe on 6 May until the displacement of the anticyclone into the North-East Atlantic which occurred between 11 and 14 May. On 10 May the anthropogenic emissions were concentrated inside the boundaries of the anticyclone with its core situated over Denmark. Within this core region Central European pollution re-circulated via the North Sea and Southern Scandinavia back to Northern Germany. The polluted region reached a northward

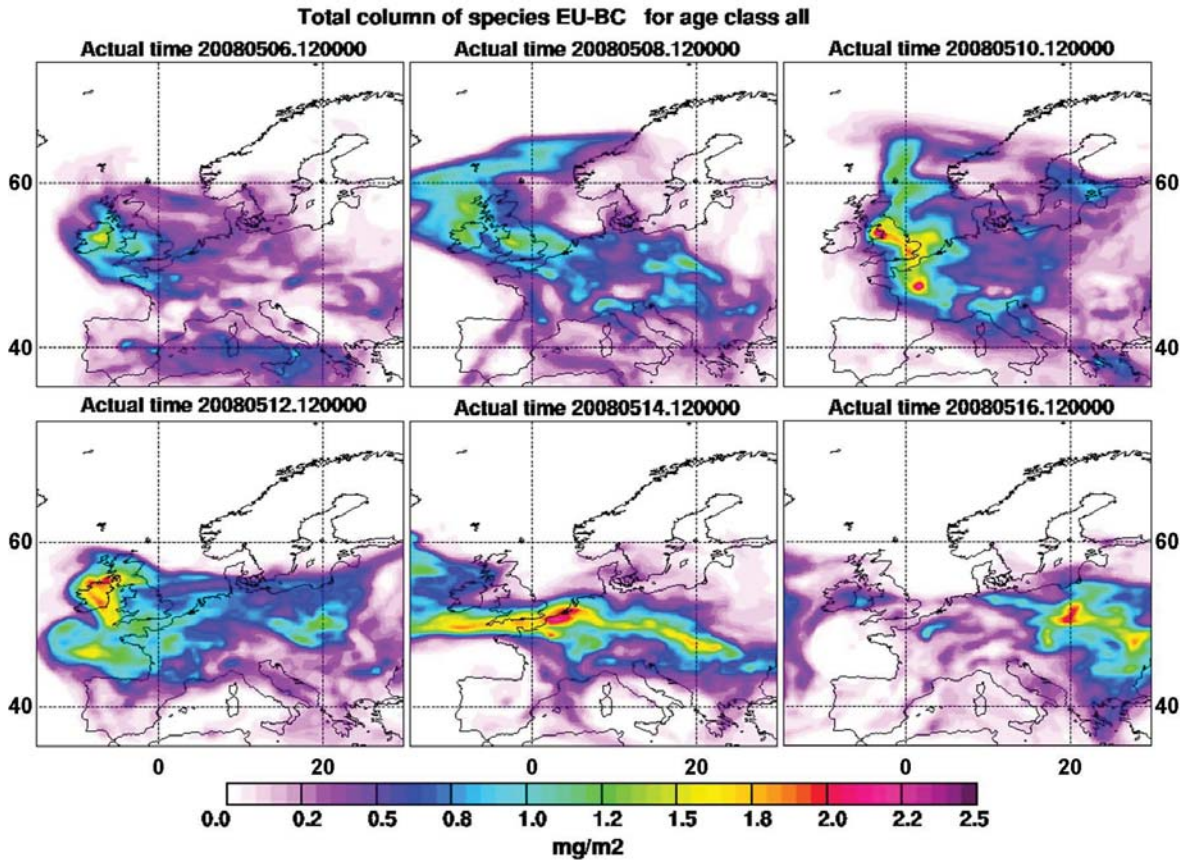


Figure 4.3: BC column mass concentrations retrieved from FLEXPART analysis between 6 May 2008 and 16 May 2008.

extension to approximately 65° N and shows a clear zonal gradient between 15° W– 20° E with increasing concentrations from East to West due to the westward transport of continental air masses. With the displacement of the anticyclone the re-circulation of pollutants ceased and the polluted continental air masses were advected towards the British Isles and into the North-East Atlantic. After the anticyclone decayed, a trough over Western Europe formed on 16 May. Maximum concentrations of European anthropogenic BC occurred over Eastern Europe at this time indicating an eastward transport of pollutants. The northern border between clean Nordic and polluted Central European air masses appeared at approximately 55° N on this day.

The special meteorological situation enabled measurements during a period of stable synoptic conditions. The aerosol distribution and evolution over Europe in May 2008 will be analysed and discussed in the following sections. The discussion focuses on the

impact of the stable anticyclonic conditions on airborne aerosol at different locations all over Central and Western Europe within the tropospheric column. The next section points out the effect of the special meteorological situation on the aerosol microphysical properties in remote regions. This will be examined on a case study of aerosol measurements above the Atlantic southwest of Ireland.

4.2 The impact of anthropogenic pollution on aerosol microphysical properties in remote regions: A case study southwest of Ireland

With the beginning of 10 May continental European air masses were advected towards the British Isles, Ireland and into the north eastern Atlantic. The westward transport benefited from the displacement of the anticyclone from Central Europe into the Atlantic between the British Isles and Iceland. The re-circulation of pollutants over North Germany and the North Sea ceased and the air masses followed the zonal transport pathway. The time series of accumulation mode number concentrations and BC-mass concentrations at Mace Head which was discussed in Section 4.3.1 and FLEXPART analysis (Figure 4.3) show that the pollution plume reached Ireland on 12 May.

Three flights performed with the DLR Falcon 20 (080513b, 080514a, 080514b) and three flights performed with the FAAM BAe-146 (b373, b374, b375) were planned on the basis of FLEXPART forecasts to measure the transported and aged pollution plumes originating from continental Europe and South England on the south west coast of Ireland and over the Atlantic south west of Ireland. Measurements were conducted during all flights. The analysis of this case study focuses on the main measurement flight of the DLR Falcon 20 (080514a) which was conducted in the morning of 14 May.

4.2.1 Aerosol optical depth retrieved from satellite imagery and LIDAR profiles

Satellite imagery help to gain overview of the horizontal distribution of the transported pollution south west of Ireland on 14 May. A cloud free region above the north east Atlantic close to Ireland can be seen in the MODIS (Moderate Resolution Imaging Spectroradiometer) Terra picture (Figure 4.4) at 12:10 UT. Between approximately 49°N and 52°N at the northern border of a cloud band a haze layer developed above the ocean and lightens the dark colour of the water. This lightening indicates increased scattering of radiation above the ocean within the haze layer and an increased aerosol optical depth (AOD) within the vertical column of the troposphere.

PARASOL AOD measurements aboard the Myriade microsatellite at radiation wavelength of $\lambda=670\text{ nm}$ prove the assumption of the increased AOD between 49°N – 52°N . Figure 4.5 shows the AOD measured by PARASOL and the AOD retrieved from HSRL measurements aboard the DLR Falcon 20. The original PARASOL AOD at $\lambda=670\text{ nm}$



Figure 4.4: MODIS Terra satellite image on 14 May 2008 at 12:10 UT. Brightness and contrast are increased over the ocean.

was converted to $\lambda=532$ nm using the equation of extinction of light by aerosol given by Ångström (1964):

$$\tau_0 = \beta \lambda_0^{-\alpha}, \quad (4.1)$$

$$\tau(\lambda) = \tau_0 \left(\frac{\lambda}{\lambda_0} \right)^{-\alpha}. \quad (4.2)$$

The Ångström exponent α is also retrieved from PARASOL measurements. Converting the PARASOL AOD makes the satellite measurements comparable to HSRL measurements which were performed with a downward looking LIDAR at high altitudes of approximately 9 km to cover a maximum vertical range of the tropospheric column. However, temporal deviations and different spatial resolution have to be considered while comparing the two measurements. A box was selected to average the PARASOL data within a region widely covering the HSRL measurements (see Figure 4.5). The lower left corner of the box is located at 14.0°E , 50.5°N and the upper right corner at 11.0°E , 52.0°N . The average AOD $\tau_{\text{PARASOL}}=0.31\pm 0.03$ appears to be similar to the overall average AOD of the HSRL measurements $\tau_{\text{HSRL}}=0.36\pm 0.05$ inside the given box. The maximum AOD measured by the HSRL along the high altitude flight legs above the ocean was 0.51. In contrast, PARASOL AOD on the west coast of Ireland

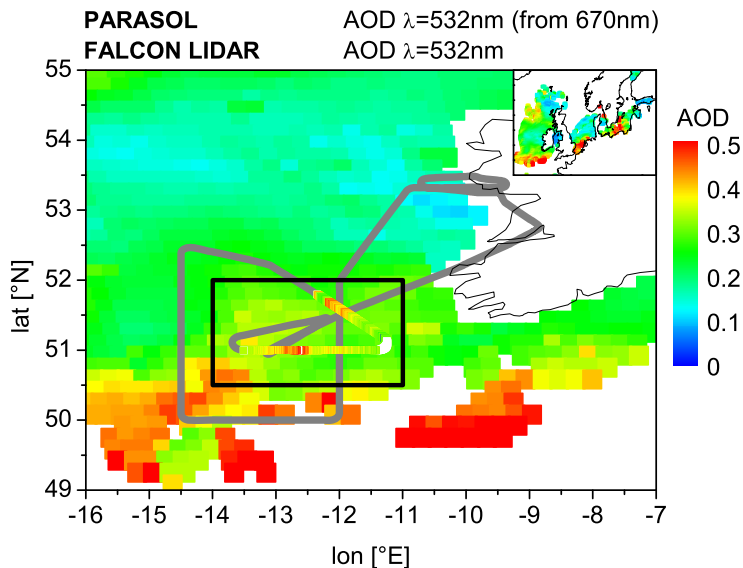


Figure 4.5: Aerosol optical thickness (AOD) at $\lambda=532$ nm retrieved from satellite (PARASOL) measurements and LIDAR measurements aboard the DLR Falcon 20 on 14 May. The flight track (grey) is overlaid by the colourscale for AOD where LIDAR measurements are available.

north of 52.0°N was between approximately 0.1–0.3.

AOD values between 0.1–0.3 for the wavelength spectrum of green light are typical and were observed during previous studies at coastlines and on open sea (Hoyningen-Huene and Wendisch, 1994; Sakerin and Kabanov, 1997; Zielinski and Zielinski, 2002). Knobelspiesse et al. (2004) reported global average AOD values over oceans of 0.10 for maritime aerosol, 0.21 for non-dust continental aerosol and 0.41 for dust aerosol. The overall average AOD over the north east Atlantic and the North Sea retrieved from PARASOL measurements in May 2008 was $\bar{\tau}_{\text{PARASOL}}=0.20\pm 0.11$ at $\lambda=532$ nm and lies right in between the values reported in literature. The average AOD within the box described above and measured with the HSRL south west of Ireland on 14 May reaches the upper limit of the typical values. The maximum AOD exceeds the overall average in May 2008 by a factor 2.5. Hence a region of increased AOD could be observed above the Atlantic containing air masses which originated from continental Europe and Great Britain. The vertical structure of the troposphere above this region is discussed in the following section.

4.2.2 Vertical profiles of in-situ measured aerosol microphysical properties

The European pollution layers advected over the Atlantic were characterised using the LIDAR measurements aboard the DLR Falcon 20 and by flying into the pollution layers starting from the top of the troposphere and descending into the marine boundary layer to perform in-situ measurements. The vertical profile 080514aV2 (see Table A.4 and Figure B.3) covers detailed in-situ measurements of aerosol microphysical proper-

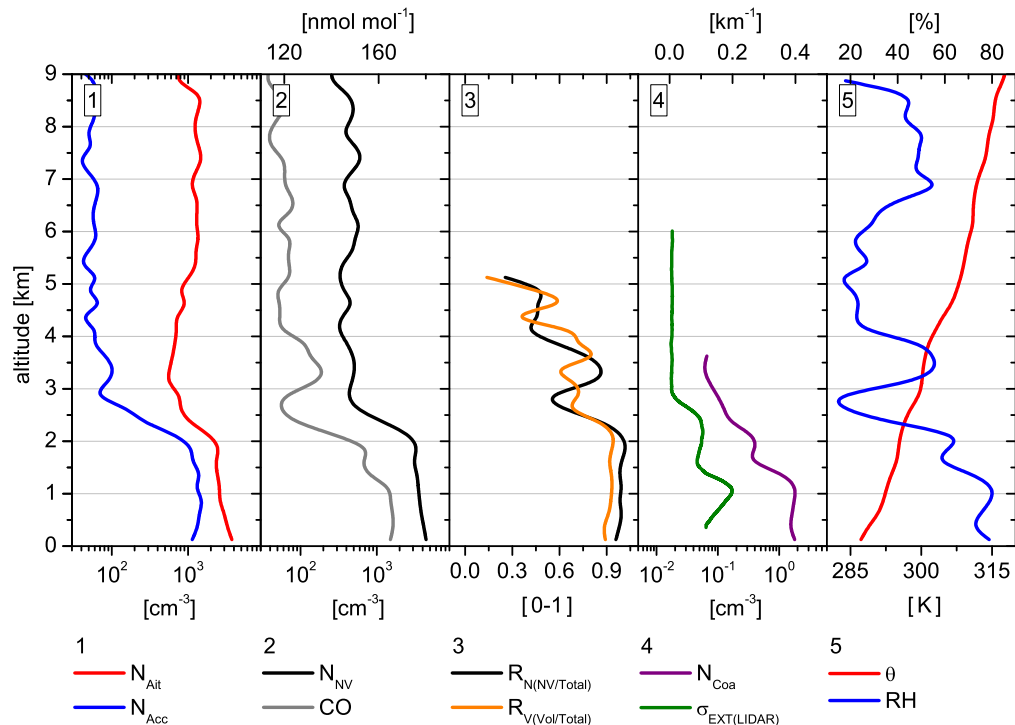


Figure 4.6: Vertical profiles showing: 1. number concentration of particles in diameter $>0.01 \mu\text{m}$ (N_{Ait} , red line) and in diameter $0.15\text{--}1.0 \mu\text{m}$ (N_{Acc} , blue line), 2. number concentration of non volatile ($250 \text{ }^\circ\text{C}$) particles in diameter $>0.014 \mu\text{m}$ (N_{NV} , black line) and CO mixing ratio (grey line), 3. ratio of non volatile to total number concentration ($R_{\text{N(NV/Total)}}$, black line) and ratio of volatile to total volume of particles in diameter $<2.5 \mu\text{m}$ ($R_{\text{V(Vol/Total)}}$, orange line), 4. number concentration of particles in diameter $>1.0 \mu\text{m}$ (N_{Coa} , purple line) and extinction coefficient at $\lambda=532 \text{ nm}$ retrieved from LIDAR measurements (olive line), 5. potential temperature (red line) and relative humidity (blue line).

ties in the European pollution layers. Figure 4.6 shows vertical profiles of aerosol, trace gas and meteorological measurements as well as the profile of the extinction coefficient $\sigma_{\text{EXT(LIDAR)}}$ at 532 nm retrieved from HSRL measurements. In-situ measurements were grouped into vertical bins of 250 metre depth each and median values were calculated for each vertical bin. The aerosol number concentrations are given at standard temperature and pressure.

Panel 1 shows the number concentrations of particles in diameter $>0.01 \mu\text{m}$ and in diameter $0.15\text{--}1.0 \mu\text{m}$ as representatives of Aitken mode and accumulation mode particles, respectively. Above 3 km altitude Aitken mode particle number concentrations were between $500\text{--}1500 \text{cm}^{-3}$ and accumulation mode particle number concentrations were between $40\text{--}100 \text{cm}^{-3}$. Between 2–3 km a transition from lower to higher number concentration occurred with decreasing altitude for both aerosol modes. Below 2 km particle number concentrations were highest reaching $2200\text{--}3800$ and $1100\text{--}1600 \text{particles/cm}^3$ for Aitken and accumulation mode particles, respectively. A similar structure can be found for non volatile particles (250°C) in panel 2 with number concentrations of $300\text{--}600 \text{particles/cm}^3$ above 3 km and $3000\text{--}4400 \text{particles/cm}^3$ below 2 km.

A layer of minimum CO mixing ratio (153nmol mol^{-1}) at approximately 1.6 km separates the layers above (156nmol mol^{-1}) and below (166nmol mol^{-1}) (panel 2). CO mixing ratios above 2 km were between $110\text{--}125 \text{nmol mol}^{-1}$ except one layer at approximately 3.5 km where mixing ratios reached 137nmol mol^{-1} . In contrast to the vertical CO profile the particle number concentrations mentioned above showed hardly any distinct layering below 2 km. A distinct layering showing three maxima of number concentrations could be found in the vertical profile of coarse mode particles (diameter $>1.0 \mu\text{m}$, panel 4): at $\sim 2 \text{km}$ ($0.4 \text{particles/cm}^3$), $\sim 1 \text{km}$ ($1.9 \text{particles/cm}^3$), and $\sim 0.1 \text{km}$ ($1.8 \text{particles/cm}^3$). The layering of the coarse mode particles, which have a wide influence on the optical properties of the aerosol, was also observed in the HSRL profile of the extinction coefficient (panel 4). By comparing the HSRL profile with the in-situ profiles one has to consider that the HSRL profile reflects an average of the measurements during high altitude flight legs 1–2 h before the in-situ vertical profile was performed. The extinction coefficient reached maximum values of 0.11km^{-1} at $\sim 2 \text{km}$ and 0.20km^{-1} at 1 km altitude. No values of the extinction coefficient from the HSRL were available below 0.3 km. Another profile showing the same structure like the coarse mode particles at and below 2 km was the vertical profile of the relative humidity in panel 5. The maxima of coarse mode number concentrations coincide with the maxima of relative humidity. This suggests an additional growth of particles due to increased humidity and on that account a considerable fraction of hygroscopic particles within the total aerosol concentration. Particles in marine air masses, here

air masses within the marine boundary layer below approximately 0.1 km, exhibit high hygroscopicity due to a large fraction of inorganic compounds (Swietlicki et al., 2000; Gysel et al., 2007). Particles within air masses originating from anthropogenic polluted regions increase in hygroscopicity during transport with increasing particle size (Cubison et al., 2006) or the change in morphology and mixing state (Zhang et al., 2008) due to condensation and coagulation.

The aerosol mixing state was analysed using the methods described in Section 3.1.3. More than 95 % of particles contained a non volatile core throughout the region below 2 km. This indicates an internal mixing state at low altitudes. On the other hand the volume ratio of volatile matter on the total particle volume for particles in diameter smaller than 2.5 μm reaches values of 90 % and more at low levels. Both, the high fraction of particles containing a non volatile core and the high volume fraction of volatile material suggest strong coating around the non volatile core. This coating of volatile matter and the internal mixing state are typical indications for aged aerosol originating from anthropogenic pollutions. Emitted particles coagulate and aerosol precursor gases condense on the existing particles during air mass transport leading to an internal mixed aerosol and coated particles. The coincidence below 2 km of increased CO mixing ratios, increased concentrations of non volatile particles and particles in all aerosol modes, except the nucleation mode, and increased extinction coefficients suggests that these layers contained aerosol originating from anthropogenic emissions and led to increased extinction in combination with the present meteorological conditions, i.e. the high relative humidity.

One further interesting layer worth to mention but decoupled from the region of increased aerosol concentrations below 2 km was located at approximately 3.5 km. As already mentioned above, this layer exhibits increased CO mixing ratios. In addition increased concentrations of accumulation mode particles (110 cm^{-3}) and of particles containing a non volatile core (520 cm^{-3}) could be observed. In contrast, the Aitken mode number concentration (530 cm^{-3}), the coarse mode number concentration (0.06 cm^{-3}), and the volume ratio of volatile matter (53 %) show local minima. The aerosol extinction coefficient shows no significant variation. The vertical profile of the potential temperature (panel 5) shows the enhanced vertical stability of this layer. The different microphysical properties within this layer compared to the layers below 2 km leads to the assumption of different source regions. The different transport pathways are discussed in Section 4.2.4.

4.2.3 Aerosol size distributions and deduced optical properties within the observed pollution layers

Below 2 km four horizontal flight legs were performed giving the possibility of detailed measurements at constant altitudes. The flight legs were performed at the following levels and classified into the following tropospheric layer (see Section 4.5.1): (1) at 1.8 km (decoupled layer; DL) for ~ 5 min, (2) at 1.2 km (DL) for ~ 5 min, (3) at 1.0 km (DL) for ~ 4 min, and (4) at 0.2 km (boundary layer; BL) for ~ 4 min. Aerosol size distributions could be measured precisely along these flight legs due to the constant pressure conditions and constant pitch angle of the aircraft reducing the uncertainties due to inlet effects.

Figure 4.7 shows the average number concentrations of the different aerosol modes. The labels along the x-axes describe the different modes as follows: Nuc: nucleation mode (0.004–0.01 μm), Ait: Aitken mode (0.01–0.15 μm), Acc: accumulation mode (0.15–1.0 μm), Coa: coarse mode (>1.0 μm). Two additional number concentrations measured in the free troposphere are shown in the plot (grey lines) to compare the pollution layers to clean air conditions. In addition averaged data for the four sequences are listed in Table 4.2.

The polluted and the clean air masses showed maximum number concentration of 2500–3800 and 730–1600 particles/ cm^3 in the Aitken mode, respectively. The nucleation mode was not present in polluted air masses whereas number concentrations in the free troposphere reached 130 particles/ cm^3 . Nevertheless the number concentrations of the nucleation mode in the free troposphere were still too small to indicate distinct nucleation events (Kulmala et al., 2004; Holmes, 2007). But the absence of nucleation mode particles in the polluted layers at low altitudes point out the occurrence of aged aerosol. The high aerosol load within the polluted layers could also be

Table 4.2: Altitude, average number concentrations of Aitken, accumulation and coarse mode particles [cm^{-3}], number ratio of non volatile particles and volume ratio of volatile matter (PM_{2.5}) [%], CO mixing ratio [nmol mol^{-1}] and relative humidity [%] measured during the horizontal flight sequences.

FL	Alt	Ait	Acc	Coa	$R_{N(NV/Total)}$	$R_{V(Vol/Total)}$	CO	RH
(1)	1.8	2600 \pm 90	1100 \pm 50	0.5 \pm 0.1	100 \pm 1	94 \pm 2	160 \pm 1	62 \pm 1
(2)	1.2	2700 \pm 50	1200 \pm 20	2.0 \pm 0.8	99 \pm 1	93 \pm 2	170 \pm 3	80 \pm 5
(3)	1.0	2500 \pm 40	1200 \pm 30	1.7 \pm 0.4	100 \pm 0	94 \pm 1	160 \pm 1	80 \pm 1
(4)	0.2	3800 \pm 50	1100 \pm 40	1.7 \pm 0.2	96 \pm 1	88 \pm 2	170 \pm 1	77 \pm 2

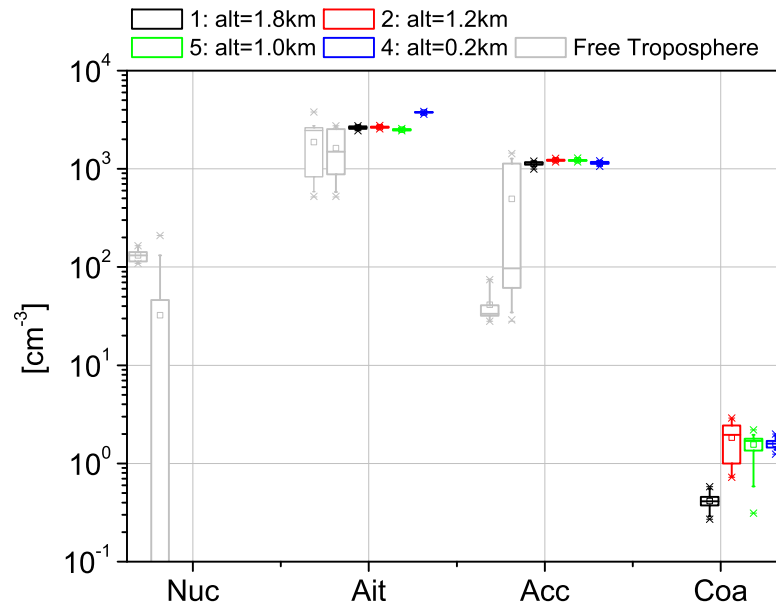


Figure 4.7: Number concentrations of aerosol modes at standard pressure and temperature. Labeling see description in the text.

observed in the accumulation mode size range with ~ 1200 particles/ cm^3 compared to ~ 40 particles/ cm^3 in the free troposphere. However, the small variances of the accumulation mode number concentrations within the similar air masses illustrate the stability of the accumulation mode aerosol. The coarse mode particles could not be satisfactorily observed in the free troposphere due to concentrations close to the detection limit at cloud free conditions and strong noise of the FSSP-300 at high altitudes. However, the size distributions showed in Section 4.5.3 and discussed in the following suggest negligible number concentrations of coarse mode particles in the free troposphere. In contrast, the coarse mode number concentrations in the polluted layers reach 0.5–2.0 particles/ cm^3 and have to be considered for optical aerosol properties in particular.

More detailed aerosol number size distributions are shown in Figure 4.8. The methods used to retrieve the size distributions and limitations that have to be considered while interpreting these size distributions are discussed in Sections 3.1.2 and 4.5.3. Figure 4.8 shows the manually fitted aerosol modes using the initial size distributions

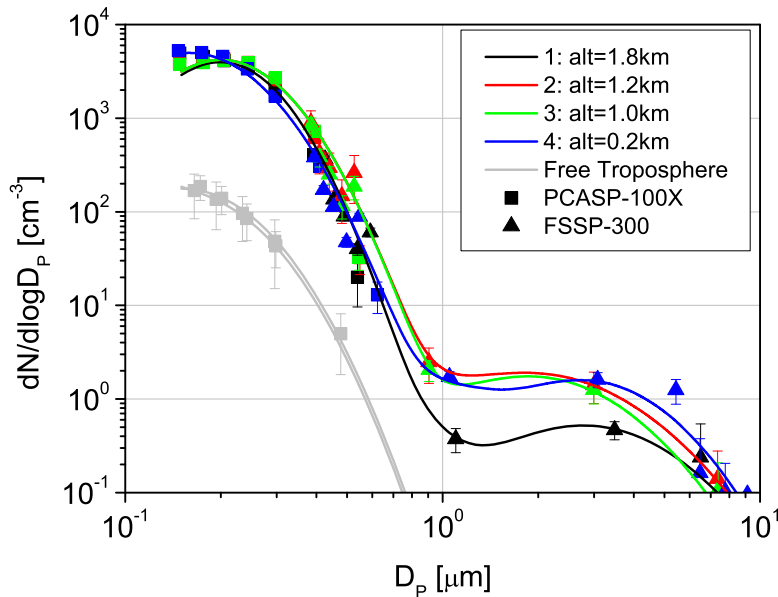


Figure 4.8: Fitted size distributions measured during four consecutive flight legs. The concentrations are given at standard pressure and temperature.

of PCASP-100X and FSSP-300. The size distributions were calculated for dry particle sizes using the refractive index for dry conditions in Table 4.3 and number concentrations at standard pressure and temperature. Corresponding to Figure 4.7 two size distributions measured in the free troposphere (grey lines) are added to the coloured size distributions of the selected pollution layer. The modal fitting parameters number concentration (N), count median diameter (CMD), and geometric standard deviation (GSD) are listed in Table 4.4 for accumulation and coarse mode particles. Smaller particle modes were not fitted due to the lack of size resolved information. N increased with decreasing altitude whereas the smallest CMD was observed at the lowest flight leg (4) at 0.2 km. This indicates a more aged aerosol with grown CMD on the cost of N in the accumulation mode at upper levels. The coarse mode showed a CMD of $1.9 \mu\text{m}$ at levels (2) and (3) and an increased CMD of $2.8 \mu\text{m}$, though a decreased N , at level (4). The increased CMD suggests different sources of coarse mode particles at the lowest level within the maritime boundary layer.

The fitted size distributions were used to calculate the extinction coefficient (σ_{EXT}) for the selected layers. Diameters and refractive indices were corrected for wet conditions

Table 4.3: Aerosol refractive indices (RF) of selected flight legs (FL 1–4; definition see text). The RF are calculated for dry and wet conditions at observed relative humidities (Table 4.2).

FL	RF _{dry}		RF _{wet}	
	D _P <1 μm	D _P >1 μm	D _P <1 μm	D _P >1 μm
(1)	1.542±0.026i	1.530±0.000i	1.459±0.016i	1.451±0.000i
(2)	1.546±0.034i	1.530±0.000i	1.405±0.012i	1.400±0.000i
(3)	1.544±0.031i	1.530±0.000i	1.405±0.011i	1.400±0.000i
(4)	1.561±0.068i	1.530±0.000i	1.418±0.026i	1.406±0.000i

Table 4.4: Modal fitting parameter for size distributions shown in Figure 4.8. Number concentrations N are given in [cm⁻³] and count median diameter CMD in [μm].

FL	Acc			Coa		
	N	CMD	GSD	N	CMD	GSD
(1)	1450	0.20	1.40	0.3	2.8	1.7
(2)	1700	0.20	1.45	1.2	1.9	1.8
(3)	1700	0.20	1.45	1.0	1.9	1.7
(4)	2200	0.16	1.50	0.8	2.8	1.6

(Table 4.3). Due to the dominant accumulation mode, which plays an important role in governing the aerosol optical properties (Robles González et al., 2003), and the significant coarse mode within the pollution layers it was assumed that the Aitken mode can be neglected to a certain extent. Calculations using the measured Aitken mode number concentrations and typical values for CMD and GSD for European continental aerosol (Neusüß et al., 2002) showed that the extinction coefficient can be underestimated by 0–20% by neglecting the Aitken mode. Estimated Aitken mode CMD and GSD using CPC measurements aboard the DLR Falcon 20 for the respective layers showed an underestimation of less than 2.5%. An error of ±25% was set for the extinction coefficients retrieved from in-situ measurements regarding number concentrations, composition, refractive indices and size distributions. Extinction coefficients estimated from in-situ measurements of accumulation and coarse mode particles and observed with HSRL measurements are shown in Figure 4.9. Despite the rough estimation of the extinction coefficient from in-situ measurements the agreement between in-situ measurements and HSRL measurements seems to be good within the limits of the observations. The extinction coefficients for the selected layers and in-situ and HSRL measurements were: (1) 0.086 and 0.095 km⁻¹, (2) 0.21 and 0.17 km⁻¹, (3) 0.20 and 0.20 km⁻¹, respectively, and (4) 0.16 km⁻¹ for in-situ measurements in the lowest

Table 4.5: Absorption coefficients σ_{abs} in $[\text{Mm}^{-1}]$ measured for fine mode aerosol with the 3 λ -PSAP at different wavelength.

FL	σ_{abs}		
	467 nm	530 nm	660 nm
(1)	2.7 \pm 0.1	2.2 \pm 0.1	1.8 \pm 0.1
(2)	3.5 \pm 0.2	2.8 \pm 0.2	2.2 \pm 0.2
(3)	3.9 \pm 0.2	3.1 \pm 0.2	2.4 \pm 0.1
(4)	5.2 \pm 0.1	4.2 \pm 0.1	3.3 \pm 0.1

layer. Hence maximum values for the extinction coefficient were measured at flight legs (2) and (3) above the maritime boundary layer. Nevertheless, the layers at ~ 2 km and within the maritime boundary layer exhibit local maxima. The vertical profile of the extinction coefficient which shows low values throughout the free troposphere above 2 km also reveals that the high AOD (Section 4.2.1) over the Atlantic south west of Ireland resulted from the increased aerosol load and thus from the increased light extinction within the air masses blow 2 km and at ~ 2 km, ~ 1 km, and ~ 0.1 km in particular. AOD values retrieved from satellite and airborne LIDAR measurements (Section 4.2.1) and aerosol in-situ measurements are listed in Table 4.6. The AOD retrieved from aerosol in-situ measurements ($\tau_{\text{in-situ}}$) was calculated using the average extinction coefficient $\bar{\sigma}_{\text{ext}(\text{in-situ})}$ for each distinct layer:

$$\bar{\sigma}_{\text{ext}(\text{in-situ})} = \frac{\sum_{i=0}^k \sigma_{\text{ext}(\text{in-situ}),i} \frac{\bar{N}_{\text{Coa}}}{N_{\text{Coa},i}}}{k}, \quad (4.3)$$

where k is the number of in-situ measurements within each layer, $\sigma_{\text{ext}(\text{in-situ}),i}$ and $N_{\text{Coa},i}$ the extinction coefficient and the coarse mode number concentration at a distinct in-situ measurement, and \bar{N}_{Coa} the average coarse mode number concentration of each layer. Hence the extinction coefficients measured during a flight leg were weighted with their relative magnitude to the average extinction coefficients within the selected layer by means of the relative magnitude of the coarse mode number concentration measured at the respective flight leg to the average coarse mode number concentration.

The AOD measured by different means (satellite, airborne LIDAR, aerosol in-situ) show good agreement with each other and are between 0.31–0.36. The LIDAR profile and the in-situ measurements give the possibility to analyse the contribution of the different layers on the overall AOD. As mentioned above the vertical profile of the extinction coefficient shows that the vast majority is contributed by the layers below 2 km. The AOD of the distinct layers obtained from in-situ measurements (Table 4.6) show that the maritime boundary layer caused only $\sim 10\%$ of the overall AOD and

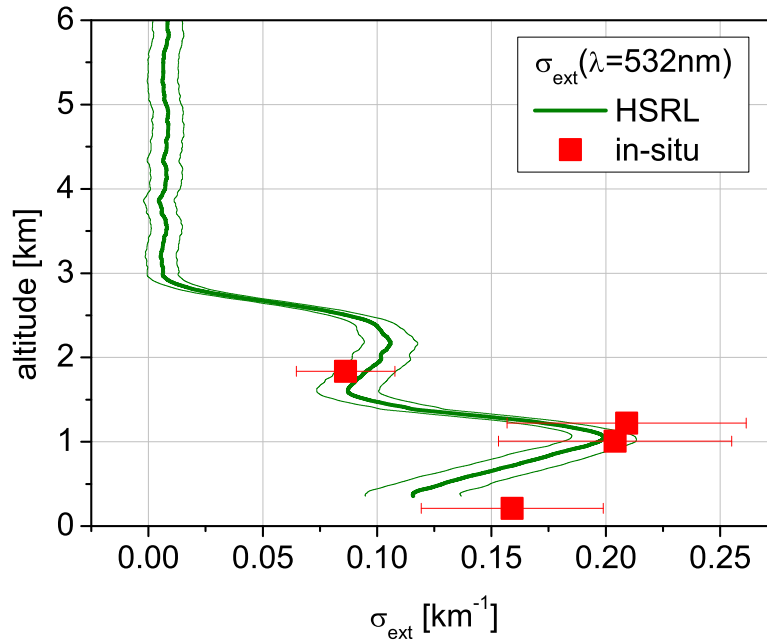


Figure 4.9: Aerosol extinction coefficient σ_{ext} at $\lambda=532$ nm retrieved from HSRL measurements (olive line) and calculated from in-situ measured size distributions (red horizontal lines).

Table 4.6: Average aerosol optical depth for the region south west of Ireland retrieved from satellite and airborne LIDAR measurements (Section 4.2.1) and aerosol in-situ measurements.

τ_{PARASOL}	τ_{HSRL}	$\sum \tau_{\text{in-situ}}$	Alt	$\tau_{\text{in-situ}}$
			1.5–2.5 km	0.06 ± 0.02
0.31 ± 0.03	0.36 ± 0.05	0.36 ± 0.10	0.2–1.5 km	0.26 ± 0.07
			0.0–0.2 km	0.04 ± 0.01

that $\sim 90\%$ of the AOD above the ocean were caused by the pollution layers below 2 km. Similar AOD values of 0.04 for the maritime boundary layer were also observed during previous studies (Pfaffenberger, 2009).

The differences in between the different pollution layers can be studied with the help of transport analysis to distinguish differences in source regions and transport pathways, which will be discussed in the following.

4.2.4 Transport analysis of polluted air masses

Air mass back trajectories were calculated from flight legs (1–4). In addition back trajectories were started from the region indicating a layer of increased aerosol concentrations and CO mixing ratio at approximately 3.5 km (0; see Section 4.2.2). Median transport pathways of trajectory bunches containing 400–500 back trajectories each (-120 hour) are shown in Figure 4.10. The colour scale of the left panel indicates the altitude, the mid panel the continental pollution index (CPI; see Section 3.2), and the right panel the cloud cover along the transport pathway. The median back trajectory starting from the layer at ~ 3.5 km (0) is only plotted in the left panel. It followed a different pathway (arriving from the south) than the back trajectories starting from flight legs (1–4). It did not show any contact with ground based sources and hardly any cloud processing within the last 120 h. Trajectories (1–3) were transported via the Baltic Sea, Central Europe and England towards the Atlantic south west of Ireland. They followed the anticyclonic flow pattern which governed the air mass transport pathways over Europe during this period. In contrast to trajectory (3), trajectories (1) and (2) showed contact with ground based sources over Germany, the Benelux States or the French coastline close to the English Channel. Back trajectory (4) starting from the lowermost flight leg at 0.2 km followed a pathway via the North Sea and England towards Ireland. It passed through the boundary layer across England. Consequently, these air masses had the possibility to mix with anthropogenic emissions. Trajectory (4) is the only trajectory showing contact with the maritime boundary layer over the North Sea and along the south coast of Ireland (not shown here). Negligible cloud cover occurred along all transport pathways for the last three days.

The trajectory analysis shows that the aerosol measured at flight leg (4) originates from rather fresh sources (15 h) compared to the aerosol observed at flight legs (2) and (3) (44 and 48 h). This is in agreement with the observed Aitken mode number concentrations which showed lower number concentrations for flight legs (2) and (3) (2700 and 2500 cm^{-3}) than for flight leg (1) (3800 cm^{-3}). In contrast the analysis of the mixing state showed almost complete internally mixed aerosol for all flight legs (Table 4.2). This observation indicates that primary particles already coagulated with secondary particles leading to an internal mixture during the first 15 h but the number concentration of Aitken mode particles still did not decrease to the same magnitude due to coagulation as observed in more aged aerosol after ~ 48 h. All four flight legs showed a distinct coarse mode. Based on the transport analysis a contribution of maritime aerosol (i.e. sea salt) on the coarse mode can be assumed at low altitudes (4).

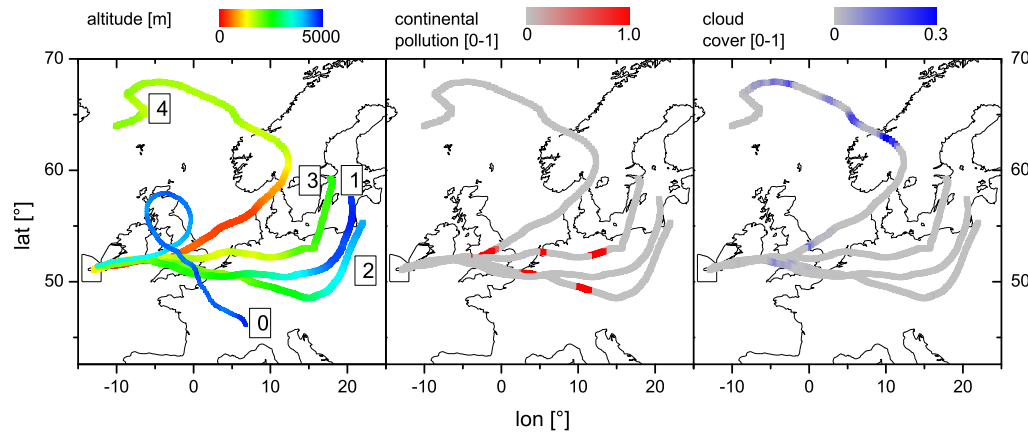


Figure 4.10: 120 h flytutl back-trajectories starting from the flight legs 1–4 (see text). The colourscale in the left panel denotes the altitude [m], in the centre panel the continental pollution index CPI [0-1] and in the right panel the cloud cover CC [0-1].

In contrast, no evidence of maritime aerosol contribution on the coarse mode could be found for flight legs (2) and (3) using the trajectory analysis. This suggests that the coarse mode grew out of the accumulation mode due to coagulation of particles and condensation of precursor gases on particles during transport and additionally increased in size due to hygroscopic growth within in the layers of high relative humidity.

4.2.5 Comparison of airborne measurements with previous studies at Mace Head, Ireland

The ground station at Mace Head underlies similar regional specifications like the region over the Atlantic south west of Ireland where the airborne measurements took place. This makes a comparison of the aircraft measurements during the specific polluted conditions on 14 May 2008 comparable to the long-term measurements of different air mass types at the ground station, which were made in the last decades. The Mace Head station is located in a region favourable for measurements of clean marine air masses which arrive in $\sim 50\%$ of all cases at the site (Jennings et al., 2003). But still 20% of the air masses are transported from Europe towards Mace Head and are accompanied by anthropogenic pollution as discussed in Section 4.3.2. These events occur most frequently in May (Huang et al., 2001).

Optical aerosol properties are continuously measured at Mace Head. Aerosol absorption and scattering coefficients are measured with Magee Scientific Aethalometer and integrating nephelometer from TSI, respectively. AOD is retrieved from Precision Filter Radiometer measurements (O'Connor et al., 2008). The absorption coefficient σ_{abs} lies in between $0.2\text{--}1.0\text{ Mm}^{-1}$ for clean marine air masses and increases up to 8.3 Mm^{-1} for polluted cases (Junker et al., 2006). Dall'Osto et al. (2010) reported average absorption coefficients of $\sim 0.5\text{ Mm}^{-1}$ and $\sim 5.0\text{ Mm}^{-1}$ for clean and polluted cases, respectively, in May 2008. The values for the polluted cases are in good agreement with the airborne 3λ -PSAP on 14 May, which reached 5.2 Mm^{-1} in the marine boundary layer at $\sim 200\text{ m}$ altitude for red light. Most of the absorption is caused by BC particles. Increased BC-mass concentrations of $0.30\text{ }\mu\text{g m}^{-3}$ were observed at Mace Head in May 2008 during polluted cases in contrast to $0.05\text{ }\mu\text{g m}^{-3}$ in clean air masses. Airborne measurements on 14 May with a Single Particle Soot Photometer (SP2) (Stephens et al., 2003) operating on the FAAM BAe-146 showed increased, though not highest concentrations of $0.10\text{--}0.15\text{ }\mu\text{g m}^{-3}$ inside the pollution layers (McMeeking et al., 2010). However, the airborne measured concentrations exceed typical values for clean marine air masses of $0.075\text{ }\mu\text{g m}^{-3}$ (Cooke et al., 1997).

The scattering coefficient σ_{sca} measured with the nephelometer varies for marine air masses between $5\text{--}20\text{ Mm}^{-1}$ (Kleefeld et al., 2002; Yoon et al., 2007). The main reason for increased scattering coefficients in marine cases are increased wind speeds and subsequently increased sea spray and sea salt concentrations. The scattering coefficient reached 30 Mm^{-1} during the occurrence of continental polluted air masses in May 2008. It is remarkable that the scattering coefficients measured aboard the DLR Falcon 20 and retrieved from the size distributions from PCASP-100X and FSSP-300 exceed the ground based measurements by the order of approximately one magnitude (maximum values $\sim 200\text{ Mm}^{-1}$). The study of Kleefeld et al. (2002) yields a similar result. Nephelometer measurements were compared to scattering coefficients retrieved from size distributions measured by DMPS (Wang and Flagan, 1990) and FSSP. The discrepancy of a factor of ~ 10 is similar to the factor between the ground based and airborne measurements in May 2008. Kleefeld et al. (2002) and O'Connor et al. (2008) explain the difference with the upper cut-off diameter of the nephelometer measurements at $5\text{--}10\text{ }\mu\text{m}$ and the dominating role of super-micron particles in light scattering.

The airborne AOD measurements (0.36) agree well with maximum AOD values of 0.38 measured at Mace Head (Jennings et al., 2003). However, the airborne AOD values of the specific pollution event are higher than average AOD values of 0.25 for polluted air masses in May 2008. AOD values average for clean air masses at 0.1.

The average single scattering albedo $\omega=0.941-0.997$ at Mace Head indicates that scattering of light is the main contribution to AOD. Dall'Osto et al. (2010) found that the chemical composition and subsequent the hygroscopic growth may result in 50 % impact on the AOD. The hygroscopic growth as well as its impact on AOD increase for aged polluted air masses like the ones observed during the case study on 14 May. The chemical composition of continental air masses at Mace Head was found to consist mainly of organic and sulphuric matter.

The comparison of the airborne measurements with the ground based measurements at Mace Head showed that cases of continental pollution transported towards the Atlantic give good examples on the impact of aerosol particles on the optical properties of the troposphere. The case study on 14 May could be used to demonstrate this impact using airborne and ground based in-situ measurements, remote sensing aboard the DLR Falcon 20 and satellites as well as air mass transport analysis.

This case study also depicts the usability of the combination of airborne and ground based measurements. The ground based measurements support the analysis of airborne measurements with a continuous recording of data. The combination of airborne and ground based measurements helps to assess the representativeness of airborne measurements within the temporal evolution of aerosol properties and the representativeness of ground based measurements within the spatial aerosol distribution. Six EUSAAR super-sites were selected for the present analysis to provide continuous measurements of atmospheric properties over Europe in May 2008. The evolution of the meteorological and pollution situation at these ground sites is discussed in the following section.

4.3 Temporal evolution of the pollution situation over Europe in May 2008: Analysis of ground based measurements

The present section gives an overview of the pollution situation over Europe in May 2008. We analyse the temporal evolution of pollution over Europe at selected EUSAAR ground sites in combination with the synoptic situations described in Section 4.1 (Hamburger et al., 2011). Six sites were selected to cover both, rural regions representing background conditions and sites situated in highly polluted regions in Central Europe (Figure 4.11). Airborne aerosol measurements within the boundary layer complete the analysis and will be compared to the ground based measurements.

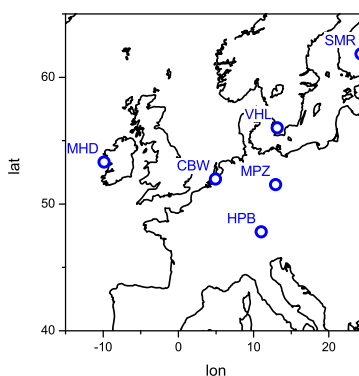


Figure 4.11: EUSAAR ground stations. CBW: Cabauw, MHD: Mace Head, MPZ: Melpitz, SMR: Hyytiälä, VHL: Vavihill, HPB: Hohenpeißenberg.

4.3.1 Ground based measurements: Time series data

Time series plots for ground stations are shown in Figures 4.12–4.17. Each graph consists of four panels. The uppermost time series displays the number concentration of the accumulation mode particles. In addition, airborne measurements of FAAM BAe-146 and DLR Falcon 20 are plotted in the graph, in cases where the aircraft were close to the EUSAAR sites. Only horizontal flight legs inside the boundary layer with a maximum distance of 150 km to the respective ground station were selected. Time series of BC measurements are shown in the second panel from the top. The original time resolution data are overlaid by a running average (3 h) to distinguish tendencies within highly variable time series like that observed during period (a) at Cabauw

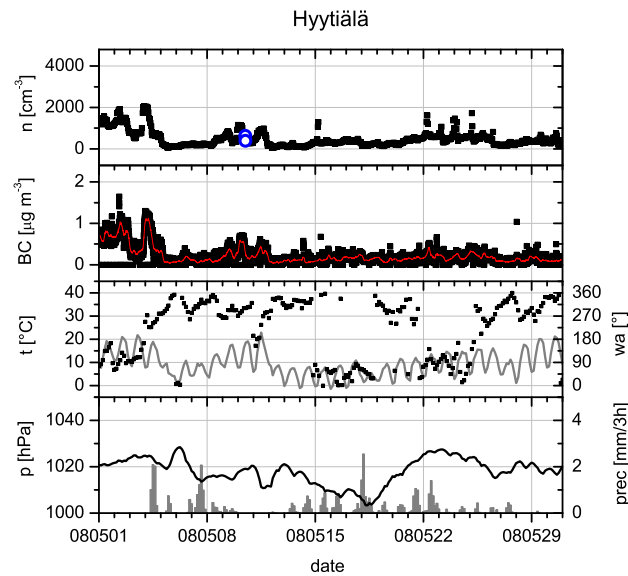


Figure 4.12: Time series of accumulation mode number concentrations (AM) in the size range $0.1\text{-}0.8\ \mu\text{m}$ [$\text{particles}/\text{cm}^3$] (1st panel, black squares), black carbon (BC) mass concentrations [$\mu\text{g m}^{-3}$] (2nd subplot, black squares), temperature [$^{\circ}\text{C}$] (3rd subplot, grey line), wind direction [$^{\circ}$] (3rd subplot, black squares), mean sea level pressure [hPa] (4th subplot, black line), and precipitation [mm/3h] (4th subplot, grey columns) for Hyttiälä. The AM number concentrations are overlaid by airborne measurements in the vicinity of the respective station inside the boundary layer. Blue circles denote measurements performed by the FAAM BAe-146, red circles measurements performed by the DLR Falcon 20. The BC mass concentrations are overlaid by an running average (red line).

(Figure 4.17). The third and fourth panels display the meteorological parameters temperature and wind direction and sea level pressure and precipitation, respectively.

Average values (median, 10th and 90th percentiles) of accumulation mode number concentrations and BC mass concentrations are presented in Table 4.7. The averaging time was split into two periods, between 1 May and 15 May (period a) and between 16 May and 31 May (period b). The two periods depict the time during and after the anticyclonic blocking event.

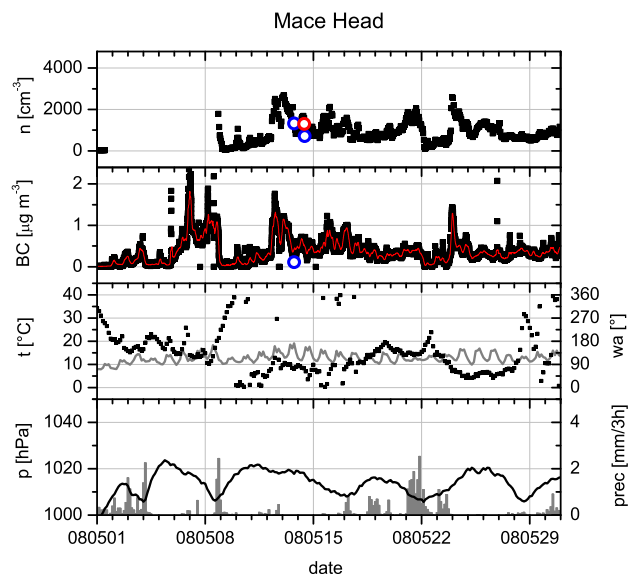


Figure 4.13: Same as Figure 4.12 for Mace Head.

Ground stations outside the high pressure core region

Hyytiälä and Mace Head

Regarding the time series data in Fig. 4.12 and the statistical values given in Table 4.7 the ground stations at Hyytiälä and Mace Head show no obvious coherence with the two distinctive synoptic situations during periods (a) and (b). The prevailing synoptic conditions at each station governed individual pollution events rather than the long-term pollution trends during the blocking event.

The northernmost ground station at Hyytiälä shows highest accumulation mode particle number concentrations for all wind directions except north. Peak values of individual events reached approximately 2000 accumulation mode particles cm^{-3} and BC mass concentrations of $1.30 \mu\text{g m}^{-3}$ in the first days of May before the initiation of the anticyclone blocking. Clean air conditions with respect to the accumulation mode load (~ 200 particles cm^{-3}) occur for air masses arriving from the north with increasing concentrations if the wind direction turns towards northeast or northwest.

At the Mace Head station, accumulation mode particle concentrations were 100 particles cm^{-3} five days before measurement flights were conducted south west of Ireland

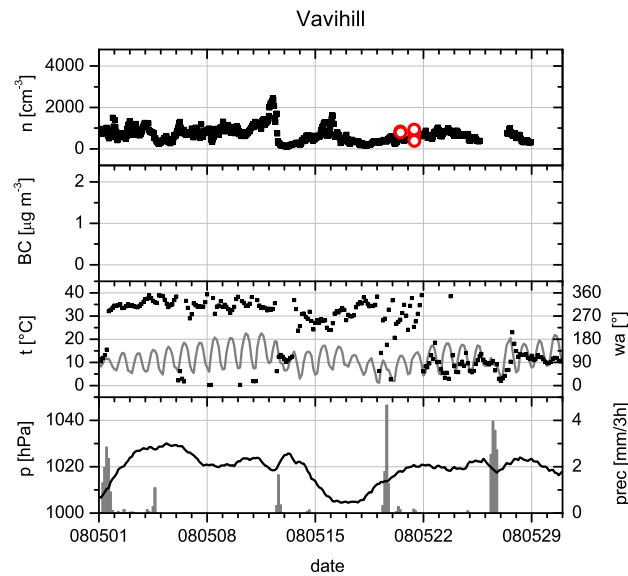


Figure 4.14: Same as Figure 4.12 for Vavihill.

to measure polluted air masses from Central Europe and Great Britain. BC-mass minimum concentrations at this time were $0.05 \mu\text{g m}^{-3}$. These observed minima were associated with wind directions from north and northeast. On 12 May the concentrations increased up to $2500 \text{ particles cm}^{-3}$ and BC-mass of $1.5 \mu\text{g m}^{-3}$ while the wind direction changed to east and continental European air masses were advected over Mace Head. The transport of European emissions towards Ireland was caused by the displacement of the anticyclone from the North Sea into the North East Atlantic and the pathway of cyclones over Southern Europe.

Ground stations within the high pressure core region measuring the atmospheric background

Vavihill and Hohenpeißenberg

The median accumulation mode number concentrations at the second Scandinavian station at Vavihill were $760 \text{ particles cm}^{-3}$ and $530 \text{ particles cm}^{-3}$ during period (a) and period (b), respectively. The prevailing wind direction averaged over period (a) was northwest. Minimum number concentrations occurred when the wind direction turned to north. A cold front occurred on 12 May and was accompanied by a shift of wind direction to east and followed by a decrease of accumulation mode number concentra-

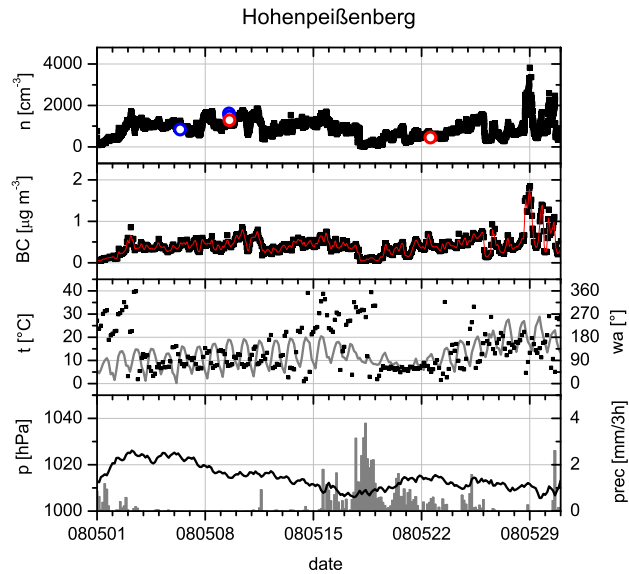


Figure 4.15: Same as Figure 4.12 for Hohenpeißenberg.

tions to $120 \text{ particles cm}^{-3}$ after a short prefrontal increase to $2500 \text{ particles cm}^{-3}$. The cold front was induced by a cyclone with its centre situated at Northern Scandinavia. It mainly increased the cloud cover but induced hardly any precipitation over Vavihill. A following maximum in accumulation mode particle number concentrations ($\sim 1500 \text{ particles cm}^{-3}$) occurred during air mass transport from west and southwest, covering the source regions of Copenhagen (Denmark), Helsingborg, and Malmo (both Sweden).

On the top of the Hohenpeißenberg (977 m a.s.l.) accumulation mode number concentrations during period (a) exceeded the concentrations during period (b) by a factor of approximately 1.5. A similar factor could be observed at Vavihill (see Table 4.7). Median accumulation mode number concentrations reached during anticyclonic conditions $1000 \text{ particles cm}^{-3}$, median BC-mass concentrations $0.39 \mu\text{g m}^{-3}$, and winds were easterly at Hohenpeißenberg. Frontal passages occurring between 15 and 19 May and inducing precipitation and change in wind direction towards west led to a decrease of the median accumulation mode number concentration ($680 \text{ particles cm}^{-3}$). Median BC-mass concentrations remained almost at the same level.

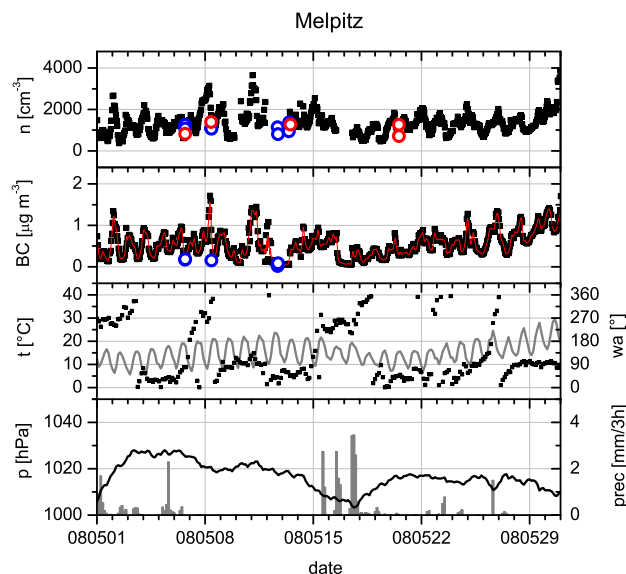


Figure 4.16: Same as Figure 4.12 for Melpitz.

Ground stations within the high pressure core region

Melpitz and Cabauw

The accumulation mode number concentrations at Melpitz varies between 690 and 2300 particles cm^{-3} . Median values were 1400 particles cm^{-3} for period (a) and 1300 particles cm^{-3} for period (b). Prevailing wind direction during the anticyclonic conditions was northeast and air masses were transported towards Melpitz via the Baltic Sea and the Baltic States. As described in Sect. 4.1 the westerly flow over Melpitz starting on 15 May lasted only 4 days and turned back to a northeasterly flow similar to period (a). Within this 4 day period frontal systems associated with two cyclones passed consecutively over Melpitz and a short decrease of the pollutants could be observed. The time series of BC-mass concentration varies between 0.12 and 0.89 $\mu\text{g m}^{-3}$. Both accumulation mode number concentration and BC-mass concentration time series follow a clear diurnal cycle with maximum concentrations in the morning and minimum concentrations in the afternoon. Maximum peaks could be observed at 3500 particles cm^{-3} and 1.50 $\mu\text{g m}^{-3}$. These maximum peaks are connected with wind directions west or east and can be associated with local sources like e.g. the open-cast mining area Lausitz east of Melpitz or with long-range transport events from Central and Eastern Europe (Spindler et al., 2010).

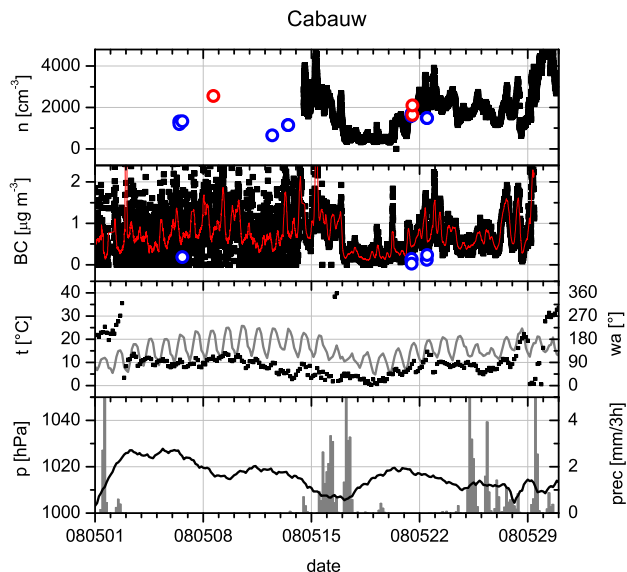


Figure 4.17: Same as Figure 4.12 for Cabauw.

The diurnal variation described for the Melpitz station was also observed at the Cabauw station. During period (a), daily averages of BC-mass concentrations increased from 0.50 to $1.40 \mu\text{g m}^{-3}$. Maximum peaks of the running average occur again in the morning and minima at early afternoon times. Absolute minimum and maximum BC-mass concentration of the highly variable time series were between approximately 0.00 – $2.50 \mu\text{g m}^{-3}$. The anticyclone induced an easterly wind direction over Cabauw. Decreasing concentrations of accumulation mode particles from 3500 to $500 \text{ particles cm}^{-3}$ and BC-mass from 1.30 to $0.20 \mu\text{g m}^{-3}$ were associated with the passage of two frontal systems occurring between 15 and 17 May and the change of the wind direction from east to northeast and north. Air mass trajectories (cf. Section 3.2) showed that the change of the wind direction resulted in a change from polluted air masses arriving from North Germany to clean air masses advected over the North Sea towards Cabauw. The concentrations increased again for wind directions turning back to E between 21 May and 23 May.

Table 4.7: Median, 10th and 90th percentile values of the accumulation mode number concentration, BC mass concentration and median sea level pressure at the selected ground stations. The averaging time was split up into two periods. Period (a) lasts from 01 May 2008 until 15 May 2008, period (b) from 16 May 2008 until 31 May 2008.

Ground site	$N_{0.1-0.8\mu\text{m}}$ [cm^{-3}]			BC [$\mu\text{g m}^{-3}$]			SLP [hPa]	Period
	Median	P10	P90	Median	P10	P90	Median	
Hyytiälä	330	120	1300	0.17	0.03	0.74	1019	a
	360	190	610	0.15	0.06	0.26	1019	b
Mace Head	550	82	1900	0.23	0.03	0.96	1017	a
	830	520	1500	0.33	0.18	0.55	1013	b
Vavihill	760	280	1200				1022	a
	530	300	820				1019	b
Hohenpeißenberg	1000	380	1400	0.39	0.20	0.59	1017	a
	680	270	1300	0.40	0.14	0.72	1011	b
Melpitz	1400	690	2300	0.44	0.12	0.89	1021	a
	1300	760	1900	0.56	0.19	1.00	1014	b
Cabauw				0.70	0.06	1.50	1019	a
	1700	490	3100	0.54	0.18	1.20	1012	b

4.3.2 Ground based measurements: Discussion

The transport of continental air masses caused by the anticyclonic conditions led to pollution events in regions usually dominated by clean atmospheric conditions, i.e. at the ground sites at Hyytiälä and Mace Head. Hyytiälä usually observes clean air conditions with respect to aged anthropogenic pollution especially for wind directions from north and northwest leading to conditions favourable for new particle formation (Tunved et al., 2003; Sogacheva et al., 2005). However two distinct pollution events could be observed during period (a). The first event during the onset of the anticyclone showed the maximum concentrations of accumulation mode number and BC-mass in May 2008 at the station. The wind direction occurring during this event (east-southeast) and FLEXPART analysis show that the air masses originated from Eastern Europe. The measured BC-mass concentrations for this case exceeded values observed for long-range transport cases from Eastern Europe during preceding studies (Niemi et al., 2009). The second pollution event lasted from 8 May until 12 May. It can be associated with the transport of Central European pollution within the anticyclone. However, the concentrations of the pollutants within the Central European air masses are smaller by a factor of 2–3 than the concentrations within the Eastern European air masses. This might be an effect of the frequently occurring precipitation at the Norwegian mountain range or of mixing with clean Arctic air masses during transport.

A detailed analysis of aerosol microphysical and chemical properties during the EU-CAARI intensive observing period at Mace Head was accomplished by Dall'Osto et al. (2010). In general the site provides favourable conditions for the study of natural air pollution like sea-salt or biogenic organic aerosol resulting from phytoplankton blooms (O'Connor et al., 2008). Roughly 20% of the air masses arriving at Mace Head per year, originate from continental Europe. They are most frequently observed in May (Huang et al., 2001; Junker et al., 2006). Due to the eastward transport of continental air masses induced by the blocking anticyclone in May 2008 continental European emissions could be measured at the Mace Head station. As discussed in Section 4.3.1 two pollution events were observed in May 2008 before the beginning of the intense observing period at the ground stations on 15 May. These two events were followed by a continuous occurrence of continental pollution until the end of May (Dall'Osto et al., 2010). Minimum values of accumulation mode number and BC-mass concentrations at the beginning of May were comparable to typical clean marine conditions in spring and summer (Cooke et al., 1997; Yoon et al., 2007).

A more continuously increased level of accumulation mode number concentrations related to the blocking event was observed at the continental background stations at Vavihill and Hohenpeißenberg. Both stations did not show the diurnal cycle of accumulation mode number and BC-mass concentrations, which could be observed at Melpitz and Cabauw. The latter two stations showed minimum concentrations in the afternoon and maximum concentrations in the morning. Diurnal cycles of particulate matter in urban areas have been analysed in several previous studies (e.g., Kukkonen et al., 2005; Schäfer et al., 2006; Pernigotti et al., 2007; Pitz et al., 2008). Minimum concentrations of particulate matter frequently occur in the afternoon hours in polluted and urban background regions. Vertical mixing during unstable stratification of the boundary layer due to surface heating during daytime leads to mixing of surface pollution into upper regions inside the increasing boundary layer. In contrast nocturnal temperature inversion close to the surface increases the vertical stability and consequently inhibits extensive vertical mixing of pollutants. Increasing traffic intensity in the morning is an additional dominating factor for increasing concentrations of pollutants.

The ground station at Melpitz is located in a region affected by several anthropogenic pollution sources (Hamed et al., 2010). Wind directions at Melpitz were most frequently northeast for period (a) as well as for period (b). Thus air masses were transported towards Melpitz via the Baltic Sea and the Baltic states. For similar transport conditions Engler et al. (2007) observed similar accumulation mode number concentrations

of 1100–1400 particles/cm³. The accumulation mode number concentrations measured during period (a) (1400 cm⁻³) and period (b) (1300 cm⁻³) also coincide with values for aged continental aerosol of 1200 particles/cm³ given by Birmili et al. (2001). Highest aerosol mass loadings usually occur during temperature inversion periods in wintertime (Müller, 1999). Spindler et al. (2010) reported elevated aerosol mass loadings during spring and summer, although not as high as during wintertime, for hot and dry meteorological periods. The four year study at Melpitz showed that elevated aerosol mass concentrations occurred in May 2008, but were below elevated mass concentrations observed in summer 2006 and spring 2007.

Highest median concentrations of anthropogenic pollutants at all six ground stations were observed at Cabauw during period (a) (BC mass 0.70 µg m⁻³, see Table 4.7). This is in agreement with the previously discussed transport of pollution from Germany towards the West and the Benelux states during the anticyclonic blocking event.

4.3.3 Anthropogenic origin of increased accumulation mode number concentrations measured at the ground stations

The time series of pollutants show weak correlation between the different ground stations. However, at each single ground station the time series of accumulation mode number and BC-mass concentrations show similar trends. These similar patterns in

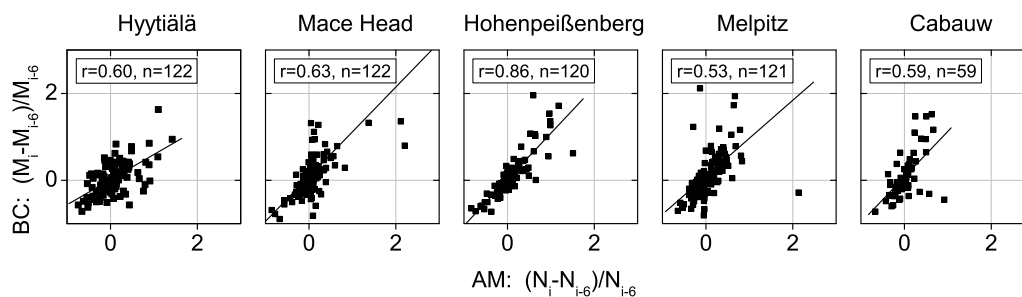


Figure 4.18: Relative increase (decrease) of 6 hourly averaged BC-mass concentrations versus relative increase (decrease) of 6 hourly averaged accumulation mode number concentrations. The legend indicates the regression coefficient r and the number of points n .

the temporal evolution indicate that air masses containing a high load of accumulation mode particles mainly originate from regions rich in sources of anthropogenic emissions from combustion processes (Hitzenberger and Tohno, 2001; Putaud et al., 2004). Figure 4.18 supports this observation. It shows the relative variation of BC-mass concentrations (M) in the last 6 hours $(M_i - M_{i-6})/M_{i-6}$ versus the relative variation of accumulation mode number concentrations (N) in the last 6 hours $(N_i - N_{i-6})/N_{i-6}$ where i is the time in hours. The correlation coefficient r obtained by linear regression varies between 0.53 (Melpitz) and 0.86 (Hohenpeißenberg). The correlation at all ground stations is statistically significant on a 99% confidence level. This means that in most cases the relative variation of one pollutant is accompanied by the relative variation of the other one. During several pollution events, the Central European ground stations showed a stronger relative increase of the BC-mass concentrations than the accumulation mode number concentrations. Different sources, source strengths and transport processes can contribute to different fractions of BC particles in different aerosol size ranges (e.g., Berner et al., 1996; Hitzenberger and Tohno, 2001; Rose et al., 2006). Thus, the relative variations of the accumulation mode particle concentrations and the BC-mass concentrations can differ in magnitude, although both were affected by similar anthropogenic sources.

4.3.4 Ground based measurements compared with airborne measurements

One objective of the EUCAARI-LONGREX campaign was to link the measurements at the ground stations within the EUCAARI intensive observing period to the airborne measurements in order to assess the spatial and, in particular, vertical representativeness of the ground measurements. We focus here on the comparison of accumulation mode number concentrations because of its small variability within the aerosol lifetime inside a given air mass (Williams et al., 2002). Thus, in the absence of sources, the spatial variation inside the given air mass should also remain small.

Figure 4.19 shows the accumulation mode number concentration of airborne measurements versus ground based measurements to illustrate the correlation between airborne and ground based measurements. The data used for the flight sequences were measured inside the boundary layer with a maximum distance of 150 km to the respective ground station. Each sequence covers one flight leg, i.e. a sequence during the flight when the aircraft was heading towards one direction on a constant level. The flight legs cover a large spatial area (~ 50 km per flight leg) but a short time span (~ 5 min per flight leg). The data of the ground based measurements were averaged using a time span of ± 3 h

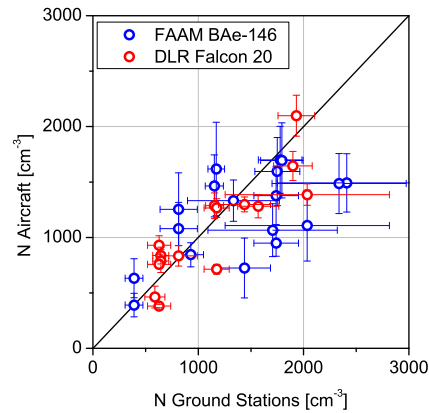


Figure 4.19: Comparison of accumulation mode particle number concentrations (particle diameter 0.1–0.8 μm) from ground based measurements with airborne measurements. Blue circles denote FAAM BAe-146, red circles DLR Falcon 20 data points. Airborne measurements are given at standard temperature and pressure (STP).

around the time, when the flight legs close to the stations were performed to account for the horizontal extension of the flight legs.

The correlation coefficient was 0.76 for FAAM BAe-146 measurements and 0.82 for DLR Falcon 20 measurements. The lower value of the correlation coefficient for FAAM BAe-146 measurements results from more frequent observations in more heterogeneous air masses as can be concluded from the higher standard deviations shown in Figure 4.19. The correlation of ground based and airborne measurements within the standard deviation of the selected sequences is statistically significant on a 99 % confidence level. Hence the assumption can be made that the selected flight sequences were performed within the same air mass as the one that was probed by the ground stations with respect to temporal relatively stable aerosol properties.

The size resolved comparison of number size distributions measured at the ground stations and aboard the DLR Falcon 20 (Figure 4.20) mostly show good correlations, too. Deviations occur most frequently if airborne number size distributions show a higher number and a larger median diameter of the accumulation mode than at the ground stations. In these cases, the airborne accumulation mode size distributions appear narrower and subsequently have a steeper slope towards super-micron particles. The median of the relative deviation of concentrations between airborne and ground based measurements was $\sim 40\%$. Maximum relative deviations occurred for particles

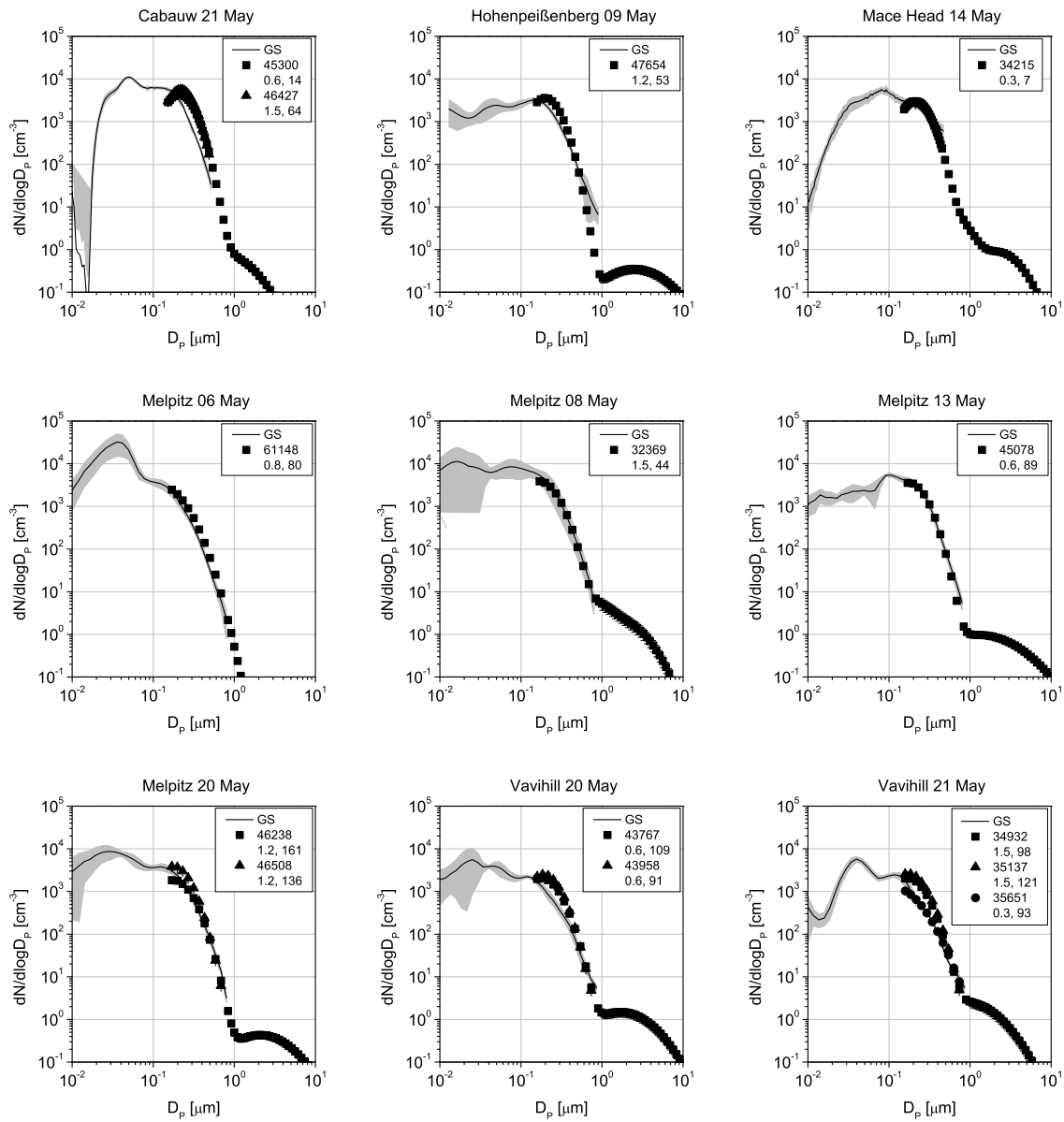


Figure 4.20: Comparison of number size distributions retrieved from measurements at ground stations (GS) and aboard the DLR Falcon 20 (cf. Section 4.3). The grey shade of the ground based measurements indicates the standard deviation. The label lists the start time (UT) of the respective flight leg in seconds after midnight, the flight altitude [km] and the distance to the ground station [km].

in diameter $<0.5 \mu\text{m}$. The higher deviation of smaller particles indicates a higher temporal and spatial variability of particles smaller than $0.5 \mu\text{m}$ than for larger particles.

4.4 The vertical aerosol distribution over Europe in May 2008

The major advantage of the aircraft field campaign was the possibility to derive in-situ measurements of meteorological and aerosol microphysical properties throughout the whole tropospheric column. The vertical extension of the in-situ measurements reached from the surface up to a maximum altitude of 12 km. Within the three weeks of the campaign the DLR Falcon 20 performed 42 vertical profiles (Figures B.1–B.5) and collected data covering 32 hours of measurements during the vertical profiles. The regional focus of the vertical profiles concentrated on the greater areas southwest of Ireland, the Benelux states, North-east Germany and the Baltic Sea and Southern Germany. Measurements were conducted as close as possible to the EUSAAR ground stations. An overview of the performed vertical profiles is given in Table A.4. Each vertical profile is labelled by the flight ID followed by the consecutive number of the profile during the respective flight (YYMMDDxVn, x: flight of the day, n: number of the vertical profile). Figures B.1–B.5 show the vertical distribution of CN number concentrations and virtual potential temperature of each vertical profile.

4.4.1 The temporal evolution of the vertical number concentration over South Germany

To summarize the vertical distribution and temporal evolution of the pollution situation, the vertical profiles over Southern Germany are examined. During take off from and landing to Oberpfaffenhofen a set of vertical profiles were obtained covering the whole time span of the EUCAARI-LONGREX campaign. Vertical CN profiles are compared to the CN concentrations measured at Hohenpeißenberg located about 35 km south west of Oberpfaffenhofen.

Figure 4.21 shows the CN number concentration measured during the vertical profiling with the DLR Falcon 20 and the time series of the CN number concentration measured at Hohenpeißenberg in May 2008. In addition the mixing layer height at each day at 12 UTC is shown. The mixing layer height was retrieved from radio soundings launched at Oberschleißheim / Munich (489 m a.s.l.) using the simple parcel method (Holzworth, 1964; Seibert et al., 2000). This gives the possibility to study a continuous evolution of the mixing layer height in the region of Munich (28 km northeast of Oberpfaffenhofen, 65 km northeast of Hohenpeißenberg).

In the first half of May during the stable anticyclonic conditions median CN num-

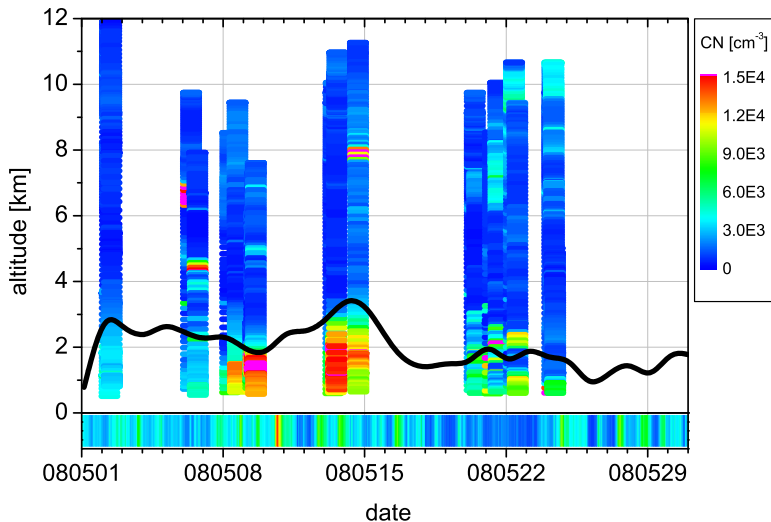


Figure 4.21: Vertical profiles of CN number concentrations in the vicinity of Hohenpeißenberg. The colour scale indicates the CN number concentration between 0 (blue) and 15000 (red) particles cm^{-3} . Concentrations exceeding 15000 particles cm^{-3} are marked in magenta. Airborne measurements are given at standard temperature and pressure (STP). The mixing layer height retrieved from soundings at Oberschleißheim/Munich at 12 UTC is shown as the black line with height shown on the left hand side vertical axis. The time series on the bottom of the graph depicts the CN number concentration measured at the ground station at Hohenpeißenberg.

ber concentrations in the free troposphere above 3 km a.s.l. were about 840–1200 particles/ cm^3 (see Table 4.8). Median values inside the boundary layer reached 8200 particles/ cm^3 . The boundary layer was well mixed vertically and increased in depth to 3.1 km above ground until 14 May. The time series at Hohenpeißenberg also showed maximum number concentrations within in the first half in May. The CN number concentrations measured at the ground station occasionally reached 10000 particles/ cm^3 , but median concentrations were at 3600 particles/ cm^3 . The vertical profile for period (a) shows that median number concentrations were highest in a layer between 1300–1600 m (12000 particles/ cm^3 ; Figure 4.21). With the change of the meteorological conditions, the change of wind directions and the occurrence of precipitation beginning on 15 May, number concentrations decreased and reached 2300 and 2700 particles/ cm^3 for airborne measurements blow 3 km a.s.l. and at Hohenpeißenberg, respectively. The vertical structure changed with changing synoptic conditions, too. The

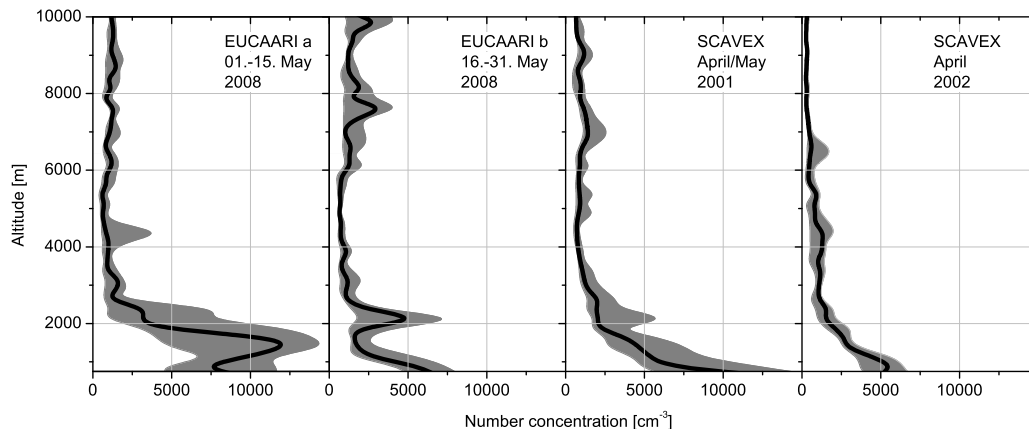


Figure 4.22: Comparison of the vertical distribution of total particle number concentrations during the EUCAARI-LONGREX campaign (May 2008) and the two SCAVEX campaigns (April/May 2001 and April 2002). Thick black lines indicate the median values of bins with a vertical depth of 250 m, gray shade values between 25th and 75th percentiles. Concentrations are given at standard temperature and pressure (STP).

well-mixed boundary layer shows a heterogeneous layering in the second half of May. The maximum mixing layer height during period (b) occurs on 21 May at 1.8 km above ground. Layers of enhanced CN number concentrations could be observed in the upper troposphere above 6 km a.s.l.. We suggest that this enhancement in the upper troposphere primarily occurs due to long-range transport of air masses which was inhibited during period (a) by the anticyclonic blocking.

The CN concentrations indicate only few similarities between ground based and airborne measurements. Maximum number concentrations in the boundary layer can be found during period (a) and decreasing number concentrations in the first half of period (b). However, absolute number concentrations cannot be correlated due to large deviations and a strong spatial and temporal variability of CN particles.

A comparison with previous airborne measurements performed from Oberpfaffenhofen (SCAVEX April/May 2001 and SCAVEX April 2002) reveals the highly polluted boundary layer observed during EUCAARI-LONGREX over Southern Germany (see Table 4.8 and Figure 4.22). The number concentrations between 0–3 km a.s.l. during period (b) of 2300 particles/cm³ lie in between the values of the two SCAVEX

Table 4.8: CN number concentration median, 10th and 90th percentile values calculated from altitude bins with a thickness of 3 km each. Concentrations are given at standard temperature and pressure (STP). The vertical profiles were measured during ascend and descend from and to Oberpfaffenhofen by the DLR Falcon 20 during several measurement campaigns. The measurements during the EUCAARI campaign in 2008 were split up into two periods, period a from 01 May 2008 until 15 May 2008 and period b from 16 May 2008 until 31 May 2008. The SCAVEX campaigns took place in April/May 2001 and April 2002. Number concentrations are given in particles cm^{-3} .

Altitude	Campaign	Median	P10	P90
9-12 km	EUCAARI	1200	730	3500
	EUCAARI a	1100	690	1700
	EUCAARI b	1600	760	4600
	SCAVEX 01	680	450	1300
	SCAVEX 02	310	170	470
6-9 km	EUCAARI	1200	620	2700
	EUCAARI a	1200	560	2000
	EUCAARI b	1400	720	3400
	SCAVEX 01	970	520	2100
	SCAVEX 02	350	160	840
3-6 km	EUCAARI	820	400	2000
	EUCAARI a	840	370	2200
	EUCAARI b	800	470	1800
	SCAVEX 01	880	490	2100
	SCAVEX 02	910	97	1600
0-3 km	EUCAARI	5500	970	13000
	EUCAARI a	8200	1000	14000
	EUCAARI b	2300	930	8300
	SCAVEX 01	3300	1200	13000
	SCAVEX 02	2100	650	5700
HPB	EUCAARI	3300	1600	6000
	EUCAARI a	3600	2500	6300
	EUCAARI b	2700	1400	5700

campaigns (3300 and 2100 particles/ cm^3 , respectively). In contrast, the number concentrations during the high pressure conditions of period (a) exceed these values with a median number concentration of 8200 particles/ cm^3 .

The median CN concentrations over South Germany of the ground based (3600 cm^{-3}) and airborne measurements below 3 km (8200 cm^{-3}) show quite large discrepancies re-

garding the absolute concentrations during period (a). The DLR Falcon 20 mainly flew above or west of Munich during take off from and landing to Oberpfaffenhofen, i.e. downwind of Munich during period (a). Thus rather fresh emissions from Munich were observed aboard the aircraft whilst the ground station at Hohenpeißenberg, 55 km southeast of the Munich, mainly measured the enhanced background aerosol concentrations during period (a). This local variation of CN number concentrations also emphasises the use of the less variable accumulation mode size range (Williams et al., 2002) for the comparison of absolute number concentrations between airborne and ground based measurements, which will be accomplished in Section 4.3.4.

The CN number concentrations serve to illustrate the vertical aerosol distribution (see Fig. 4.22). Whilst an almost continuous negative vertical gradient from the surface to the top of the boundary layer can be observed for period (b) and the two SCAVEX cases, the high number concentrations partly originating from the emissions of Munich occur throughout the whole vertical column of the boundary layer during period (a). Therefore a much more pronounced negative vertical gradient appears immediately above the polluted boundary layer at the intersection into the clean free troposphere. This is evident already from the averaged vertical profile in Fig. 4.22, which tends to smooth out the vertical gradients on a case by case basis because of varying boundary layer height. The gradient can be illustrated by the differences of the median values between 0–3 km and 3–6 km in Table 4.8. Whilst the number concentrations decreased with height by a factor 10 during period (a), the number concentrations during period (b) and the two SCAVEX cases decreased by a factor 2–4. This reflects the stable layering of the troposphere during period (a) and suggests a trapping of anthropogenic pollution particles during high pressure conditions inside the boundary layer.

4.4.2 Regional vertical profiles during anticyclonic conditions

An average of the vertical profiles has to be examined to get an overview of the vertical aerosol distribution over Europe during the LONGREX campaign. For this purpose statistics of vertical bins with a depth of 250 m each were calculated for several aerosol microphysical and meteorological properties. However, the extensive dataset measured during the vertical profiles covered a large horizontal area on a continental scale and a time span exceeding the lifetime of typical synoptic events. Thus a simple averaging of all data, although binned into several vertical levels, would lead to a loss of useful information.

The first important information is given by the locations of the performed vertical

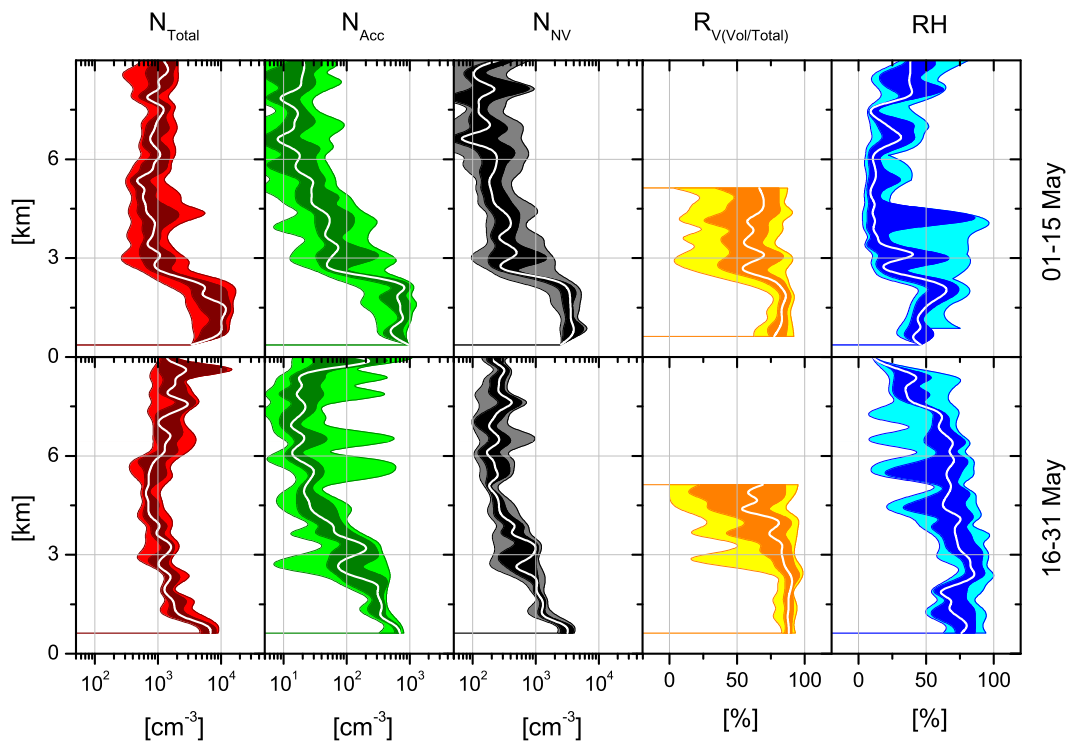


Figure 4.23: Vertical profiles of number concentration of particles in diameter larger $0.01\ \mu\text{m}$ (red), accumulation mode number concentration (green), number concentration of non volatile ($250\ ^\circ\text{C}$) particles (black), the volume fraction of volatile ($250\ ^\circ\text{C}$) $\text{PM}_{2.5}$ particles (orange/yellow), and relative humidity (blue). The upper (lower) panel shows values for the period between 1–15 (16–31) May. Each vertical profile contains P10, P25, median, P75, and P95 values. Observations were performed above South Germany.

profiles and their exposure towards different transport pathways. Local anthropogenic emissions over Europe add an essential contribution to the atmospheric aerosol load (van Dingenen et al., 2004; Putaud et al., 2004, 2010). Hence it can be expected that the different locations of the vertical profiles over urban, rural and remote sites show different characteristics. Consequently the vertical profiles were split up into four different regions: the Atlantic south west of Ireland, the Benelux states, North-east Germany and the Baltic Sea and South Germany (Figure 3.10).

Further the measured data was separated into the two synoptic periods during EUCAARI-

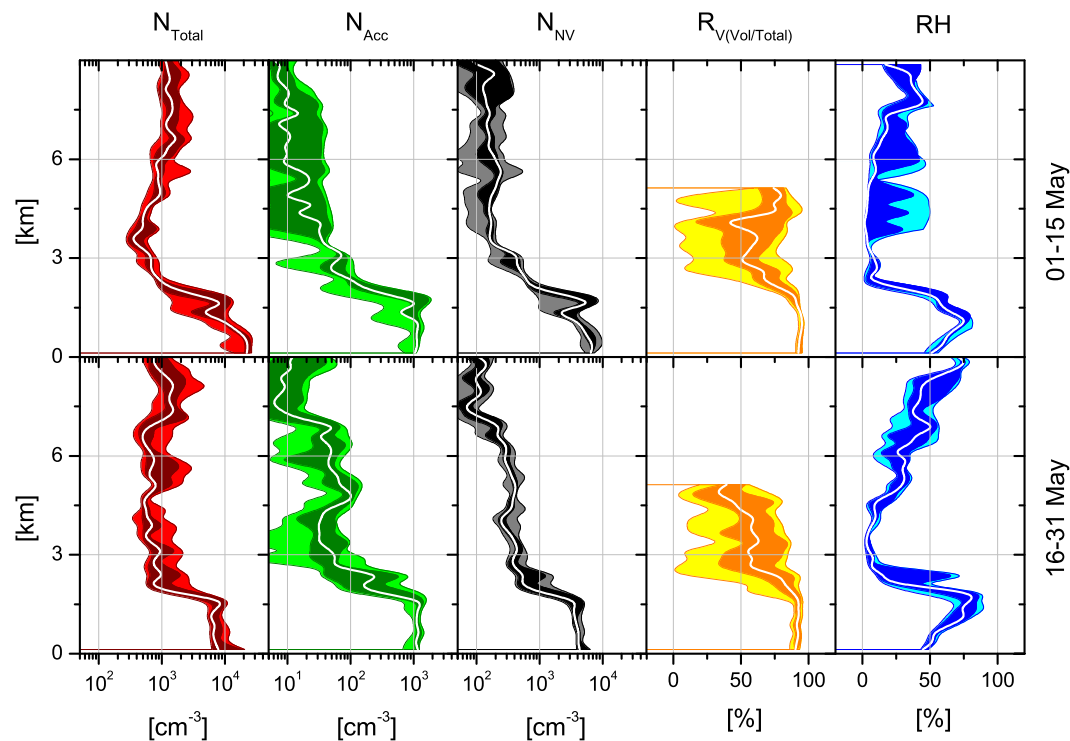


Figure 4.24: Like Figure 4.23. Observations were performed above the Benelux States.

LONGREX (periods (a) and (b), see Section 4.1). Figures 4.23, 4.24, and 4.25 show the vertical profiles measured above South Germany, the Benelux states and North-east Germany and the Baltic Sea. The vertical profiles south west of Ireland are discussed in detail separately in Section 4.2. The profiles discussed in this section show number concentrations of particles in diameter $D_P > 0.01 \mu\text{m}$ referred to as total particle number concentration N_{Total} in the following, accumulation mode particles N_{Acc} , and non volatile particles N_{NV} . In addition the volume ratio of volatile matter to the total aerosol volume for particles in diameter smaller $2.5 \mu\text{m}$ $R_{V(\text{Vol}/\text{Total})}$ and the relative humidity RH were plotted. Median, P10 and P90 values of N_{Total} , N_{Acc} , and N_{NV} calculated for 1.5 km vertical bins below 3 km altitude and 3 km vertical bins above 3 km are listed in Table 4.9.

The vertical profiles measured above South Germany (Figure 4.23) showed increased number concentrations for all discussed particle types within the boundary layer during period (a) compared to period (b). Median values within the lower 1.5 km were

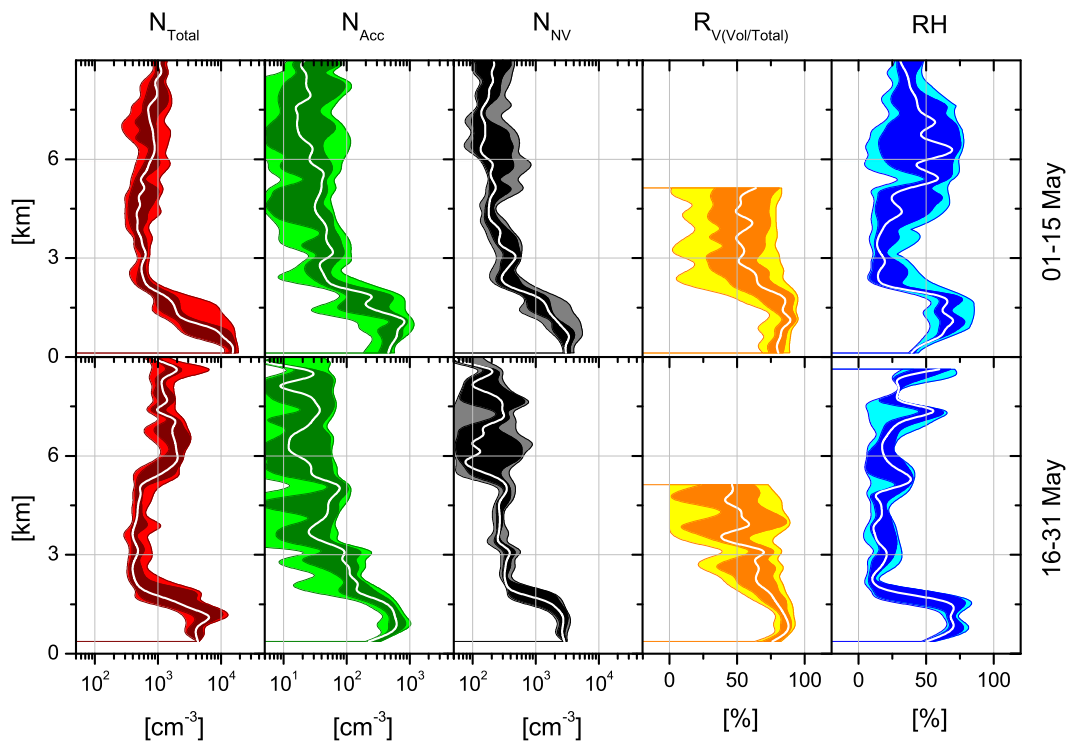


Figure 4.25: Like Figure 4.23. Observations were performed above the Baltic Sea and North East Germany.

increased by a factor of ~ 3 for N_{Total} and a factor of ~ 1.5 – 2 for N_{Acc} and N_{NV} whereas the median number concentrations between 3–6 km were similar for both periods. In contrast the median number concentrations at high altitudes between 6–9 km were increased during period (b) by a factor ~ 1.5 after the blocking anticyclone dissolved. This finding is similar to the temporal evolution of vertical profiles of total number concentrations measured during ascend and descend from and to Oberpfaffenhofen discussed in Section 4.4.1. The homogenous vertical mixing of particles inside the boundary layer during period (a) found for the total number concentration in Section 4.4.1 can also be seen in the accumulation mode size range and for non volatile particles below 2 km. Especially the strong negative gradient of N_{NV} , i.e. primary particles from ground sources, at the transition from the boundary to the free troposphere supports the indication of the trapping of aerosol particles inside the boundary layer during period (a). $R_{\text{V(Vol/Total)}}$ shows similar magnitudes for both periods. $R_{\text{V(Vol/Total)}}$ slightly increased at altitudes above the boundary layer during period (b). The lower $R_{\text{V(Vol/Total)}}$ values

during period (a) may result from an inhibition of aerosol precursor gases mixing from the boundary layer into the free troposphere or from the suppression of volatile material condensing on pre-existing particles due to subsiding air masses during the high pressure conditions which also led to low RH between 3–6 km. Relative humidity increased between periods (a) and (b) by a factor ~ 1.8 for low and high altitudes and by a factor ~ 5 between 3–6 km. The large difference of relative humidity between period (a) with RH=14 % and period (b) with RH=78 % at mid altitudes results from the dry conditions during the anticyclonic period. The change of relative humidity also reflects the change of the meteorological conditions from stable and cloud free conditions to less stable conditions accompanied by occurring cloud cover and precipitation.

The vertical profiles of the particle number concentrations above the Benelux states (Figure 4.24) show high particle load within the boundary layer during both periods. The particle concentrations inside the boundary layer underwent largest variations due to a diurnal variation of the mixing layer height in this region as analyzed in Section 4.3.1 for the ground station at Cabauw. The number concentrations at altitudes between minimum and maximum mixing layer heights strongly depend on the diurnal variation and thus on the time of day. This makes the analysis of the vertical profiles below 3 km more difficult and the median values in Table 4.9 have to be interpreted with care. Whereas the median concentrations for N_{Total} between 1.5 km and 3 km were 920 and 1300 cm^{-3} , median concentrations for N_{Total} below 1.5 km were 19000 and 6600 cm^{-3} for periods (a) and (b), respectively. This shows that the maximum particle load occurred during period (a) and was measured at low mixing layer depth. The non-volatile number concentration also showed highest concentrations and a well mixed layer below 1.5 km during period (a). Between 3–6 km enhanced non volatile particle concentrations were observed during period (b). This indicates that despite an average stable layering between boundary layer and free troposphere during period (b) primary particles were mixed into the free troposphere over Central Europe due to frontal passages in mid of May and transported towards the Benelux states. Although the relative humidity increased in the free troposphere during period (b) (15–45 %) it was observed to be dry in comparison with the relative humidity above South Germany (50–70 %). The relative humidity below 3 km remained the same during May above the Benelux States ($\sim 50\%$). As discussed in Section 4.1 the general flow pattern over Central Europe returned after a trough between 16–18 May to an anticyclonic North-Easterly pattern. Hence, the regions of the Benelux States and North Germany were influenced by a similar flow pattern during period (b) like during period (a). The similar flow pattern led to similar meteorological conditions during both periods.

This observation can be made even clearer by analysing the vertical profiles above

North-east Germany and the Baltic Sea (Figure 4.25). Within all vertical layers all number concentrations show similar magnitudes for periods (a) and (b). Only N_{Total} below 3 km showed enhanced values by a factor 1.5 during period (a) compared to period (b). In contrast maximum concentrations between 6–9 km increased during period (b) by a factor of ~ 2 and reached 1600 cm^{-3} . N_{Acc} and $R_{V(\text{Vol}/\text{Total})}$ at low altitudes were lowest over North-east Germany and the Baltic Sea compared to South Germany and the Benelux States during anticyclonic flow patterns. This illustrates less influence of secondary particle matter originating from anthropogenic sources due to the continuous north easterly flow above this region.

The vertical profiles separated into different regions and temporal periods show that the regions were affected differently by the occurring synoptic conditions. While the particle concentrations especially in the boundary layer showed clear variations between periods (a) and (b) above South Germany, the differences between periods (a) and (b) were less pronounced above the Benelux States. The particle load above North-east Germany and the Baltic Sea remained almost similar. The flow pattern over South Germany changed from an anticyclonic flow associated with the blocking event to a cyclonic flow induced by low pressure systems over the Mediterranean. The regions of the Benelux States and North-east Germany and the Baltic Sea were influenced by anticyclonic flow patterns during period (a) as well as during period (b). This anticyclonic flow was interrupted by a trough passing over Central Europe between 16–18 May. The different observations encourage the classification of the vertical profiles into different regions rather than averaging over the whole continental scale.

Table 4.9: Median values of particles in diameter $D_P > 0.01 \mu\text{m}$ (N_{Total}), accumulation mode (N_{Acc}) and non volatile particle (N_{NV} , 250°C) number concentrations [cm^{-3}] at standard pressure and temperature.

Altitude	N_{Total}			N_{Acc}			N_{NV}			Period
	P50	P10	P90	P50	P10	P90	P50	P10	P90	
South Germany										
6–9 km	1100	450	1900	16	3	44	130	23	560	a
	1600	820	24000	19	8	71	250	110	470	b
3–6 km	700	310	2000	40	9	200	240	140	1300	a
	860	550	1800	41	12	270	290	160	1100	b
1.5–3 km	3500	720	15000	640	41	1200	2400	230	4800	a
	1500	880	3900	270	42	450	1000	310	1500	b
0–1.5 km	9900	3500	14000	840	290	1100	3500	2500	4800	a
	3100	1200	8300	410	230	730	1400	930	4000	b
Benelux States										
6–9 km	1300	920	2700	12	3	35	160	64	330	a
	810	430	2000	20	3	85	150	56	290	b
3–6 km	640	300	1100	33	3	79	190	140	370	a
	650	470	1800	57	10	120	370	240	470	b
1.5–3 km	920	670	13000	110	40	1600	640	490	8900	a
	1300	540	12000	190	44	1600	590	350	5100	b
0–1.5 km	19000	5300	26000	1100	460	1300	5400	3600	8200	a
	6600	5500	11000	1200	970	1400	4100	3300	5200	b
North-east Germany and Baltic Sea										
6–9 km	920	500	1500	22	5	90	160	93	420	a
	1600	580	3000	29	4	57	190	43	470	b
3–6 km	500	340	970	43	6	86	220	150	570	a
	500	360	950	81	9	280	340	220	640	b
1.5–3 km	870	460	2200	120	27	720	660	250	1700	a
	530	350	3300	140	55	500	350	280	2300	b
0–1.5 km	6800	2100	17000	650	210	1100	2300	1700	5300	a
	4400	2500	13000	520	210	790	2800	1900	3400	b

4.5 The horizontal aerosol distribution over Europe in May 2008

The horizontal distribution of aerosol microphysical properties is analysed using the large amount of horizontal flight sequences. Horizontal flight sequences or flight legs describe sequences during the flight when the aircraft is heading towards one direction on a constant level. In addition start and end times of flight sequences are selected to describe measurement periods when the measured parameters do not vary significantly. These periods usually have a duration of a few minutes. This way, measurements covering well defined conditions can be used for analysing air mass properties. The conditions cover the air mass properties as well as well defined conditions regarding the measurement platform as already mentioned in Section 4.2. During one horizontal flight sequence aircraft speed, pressure, pitch and roll angles are constant and ensure optimum conditions for aerosol sampling using inlet systems. 91 horizontal flight legs were performed during the EUCAARI-LONGREX campaign over Europe covering the whole tropospheric column. Average core parameter of all sequences are listed in Table A. The horizontal flight sequences will be analysed in the following subsections.

4.5.1 Vertical classification of the troposphere

The horizontal sequences cover the whole tropospheric column. Hence the measured air masses will show high variations while comparing them with each other because of their vertical position within the troposphere. To take this variation into account a vertical classification is necessary which considers typical properties of distinct vertical layers. The vertical profiles of total number concentrations and relative humidity in Sections 4.4.1 and 4.4.2 already suggest a classification into three layers. The lowest layer covers the boundary layer and shows maximum aerosol number concentrations and high relative humidity during the anticyclonic conditions. A mid layer above the boundary layer shows minimum aerosol number concentrations and relatively dry conditions. The upper layer exhibits increasing total number concentrations and increasing relative humidity compared to the mid layer. Each horizontal sequence was manually analysed within the respective vertical profile of aerosol properties and meteorological conditions and classified into one of the following vertical layers (see Figures B.1–B.5): boundary layer (BL), lower free troposphere (LFT) and upper free troposphere (UFT). Several horizontal flight legs were performed inside stable layers right above the boundary layer showing high aerosol load and significantly different meteorological conditions than the LFT. These layers, clearly decoupled from the boundary layer, were classified as decoupled layers (DL). Table 4.10 shows the number of flight legs and altitude range

of each defined layer. Five horizontal sequences could not be clearly classified and remained undefined.

Table 4.10: Number of flight legs and altitude range of the layers used for the classification of horizontal sequences.

Layer	# FL	Alt a.s.l.
UFT	25	5.5–10.0
LFT	27	2.1–7.0
DL	12	1.0–3.9
BL	22	0.2–1.8

4.5.2 Horizontal distribution of aerosol microphysical properties during anticyclonic conditions

The wide horizontal distribution of the horizontal flight legs performed over Europe reached from 13° W–18° E and 48° N–55° N. This allows studying the horizontal aerosol distribution within the vertical layers defined above on a continental scale. To exclude variations due to changing synoptic flow patterns only horizontal sequences influenced by an anticyclonic flow pattern were selected for this analysis. Most horizontal flight legs were performed during anticyclonic flow patterns except the flight legs performed above South Germany during period (b) (see Section 4.4.2). Although the anticyclonic flow patterns were induced by different synoptic events they led to similar meteorological conditions and wind directions along a zonal transport path way covering the Baltic Sea, North Germany, the Benelux States and the British Isles.

Figure 4.26 shows the horizontal distribution of total and accumulation mode number concentrations within layers BL, DL and LFT. It can be clearly seen that maximum total number concentrations occurred inside the BL above Germany and the Benelux States ($N_{\text{Total}}=17000\text{ cm}^{-3}$). This region features the main sources of anthropogenic aerosol particles (e.g. van Dingenen et al., 2004). The total number concentrations decreased during the westward transport towards the British Isles ($\sim 4000\text{ cm}^{-3}$). In contrast, the accumulation mode concentration remained similar in number. The increase of the relative fraction of accumulation mode particles on the total number concentration from east to west suggests a growth of aerosol particles at the cost of total number concentrations. Highest accumulation mode number concentrations were observed above the Benelux States. The Benelux States were influenced by the first westward transport of pollutants from North-east Germany but still cover a region rich in anthropogenic aerosol sources leading to a high load of particle matter.

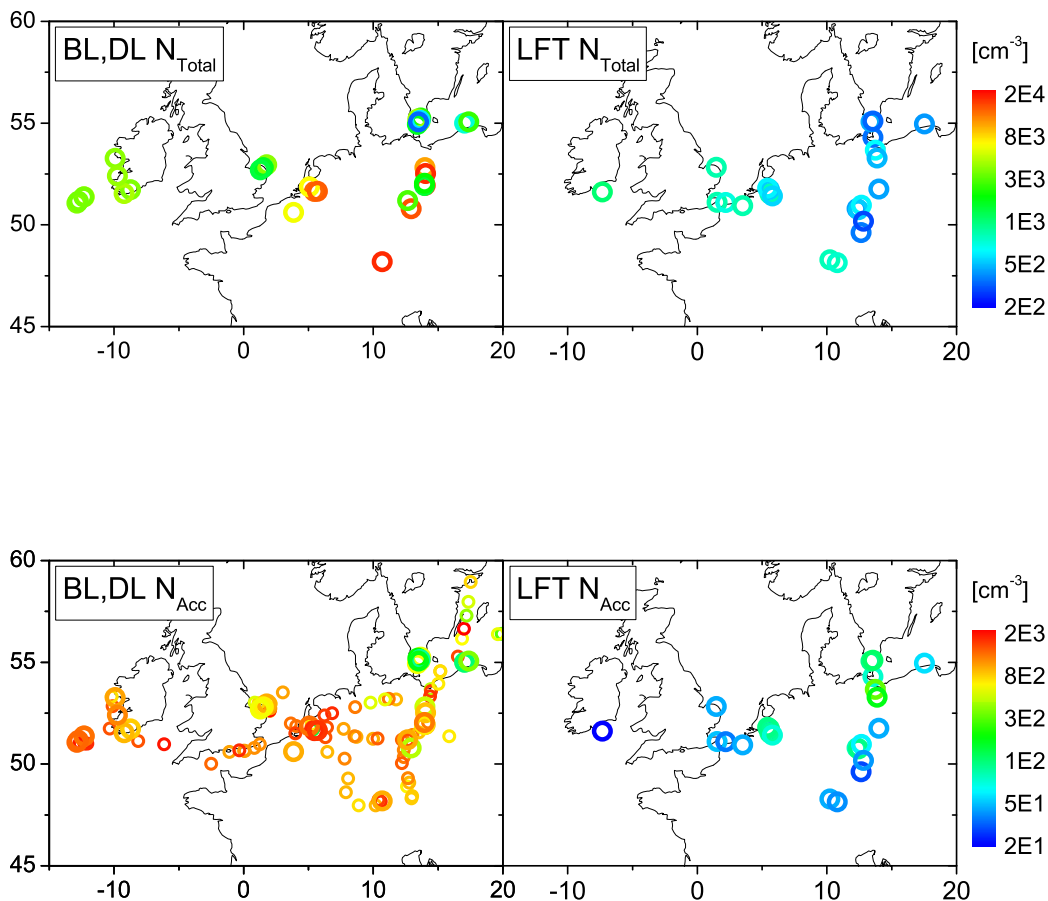


Figure 4.26: Horizontal distribution of total (N_{Total} , upper panel) and accumulation mode (N_{Acc} , lower panel) number concentration for BL and DL (left panels) and LFT (right panels). Small circles in the lower left panel denote measurements aboard the FAAM BAe-146.

In contrast to the BL and DL, total number concentrations are lowest and accumulation mode number concentrations highest in the LFT above East Germany and the Baltic Sea. This indicates that aged aerosol was observed inside the LFT above the BL, where recently emitted and formed aerosol particles could be observed. The aged aerosol in the LFT may originate from long range transport or recirculation of European air masses during the blocking event in period (a).

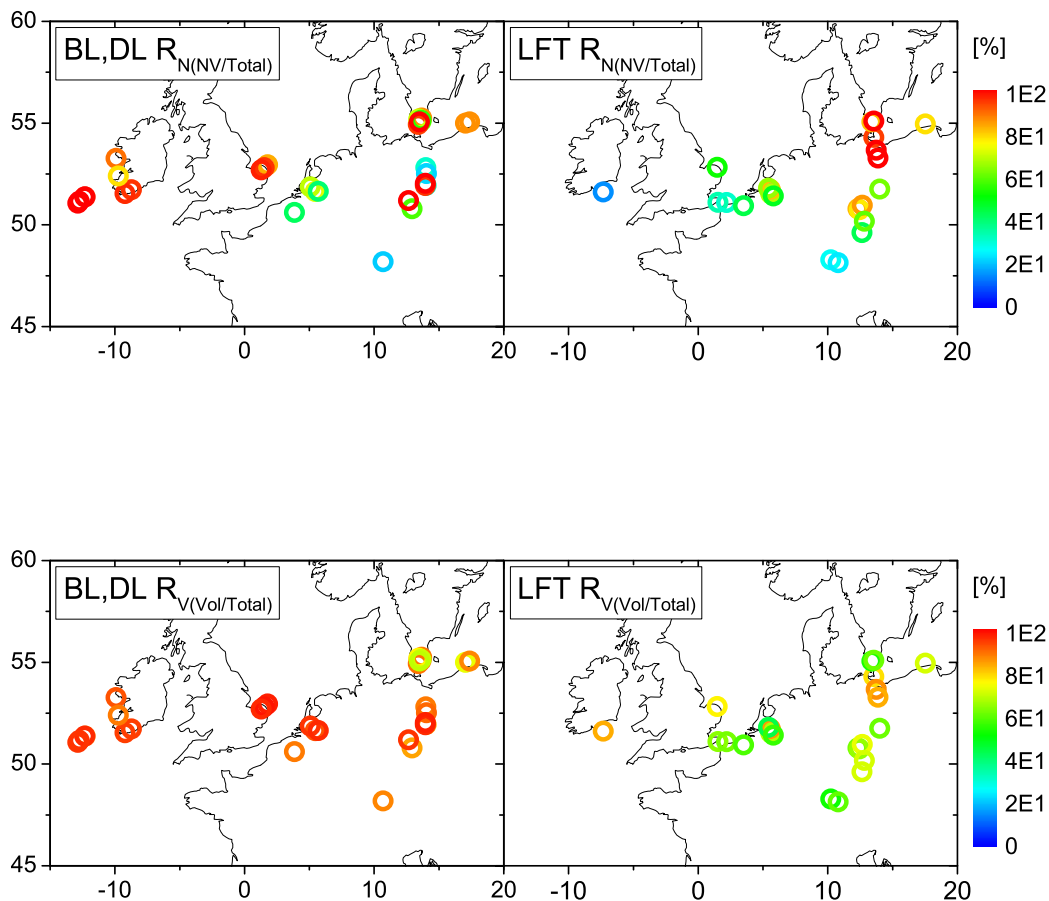


Figure 4.27: Horizontal distribution of non volatile number ratio ($R_{N(NV/Total)}$, upper panel) and volatile volume ratio ($R_{V(Vol/Total)}$, lower panel) for BL and DL (left panels) and LFT (right panels).

Aged aerosol can also be determined by analysing the aerosol mixing state. Figure 4.27 shows the number ratio of non volatile particles and the volume ratio of volatile matter for PM_{2.5}. The ratio of particles containing a non volatile core increases from east to west showing a transition from external to an internal mixing state, i.e. from fresh to aged aerosol. On the other hand an internal mixing state mainly occurs above North-east Germany in the LFT supporting the image of aged aerosol discussed above. The

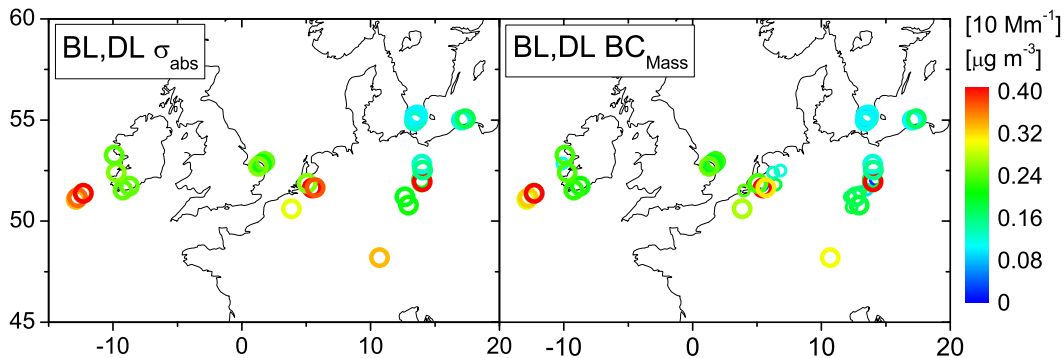


Figure 4.28: Horizontal distribution of absorption coefficient (σ_{abs}) retrieved from 3λ -PSAP measurements at 530 nm (left panel) and BC mass concentration (BC_{Mass} , right panel). Large circles in the right panel denote BC mass concentration calculated from 3λ -PSAP measurements, small circles denote SP-2 measurements aboard the FAAM BAe-146. All values are shown for standard temperature and pressure.

volume fraction of volatile matter was observed to be high throughout the BL and DL (~ 85 – 95 %). This emphasises that secondary aerosol particles and precursor gases play an important role in governing the aerosol mass inside the BL. In contrast the volatile volume fraction reached only ~ 60 – 70 % in the LFT. The low volatile volume fraction can be a result of low concentrations of aerosol precursor gases inside the LFT but also a result of subsiding air masses inside the LFT during the anticyclonic conditions suppressing the condensation of aerosol precursor gases and thus inhibiting the gas-to-particle conversion. This is in agreement with the analysis of the vertical profiles in Section 4.3.

The absorption coefficient and BC-mass concentrations in Figure 4.28 show a heterogeneous horizontal distribution inside the BL and DL. Individual maxima occurred above East Germany and the Netherlands. Air masses that were transported from Central Europe towards the Atlantic show strong absorption, too, reaching $\sigma_{\text{abs}} > 3 \text{ Mm}^{-1}$. This coincides with the previous observation of strong anthropogenic pollution over the Atlantic south west of Ireland (Section 4.2). Absorption minima could be observed most frequently over South Sweden indicating air masses clean of combustion aerosol particles that were transported within the anticyclonic flow pattern towards North-east

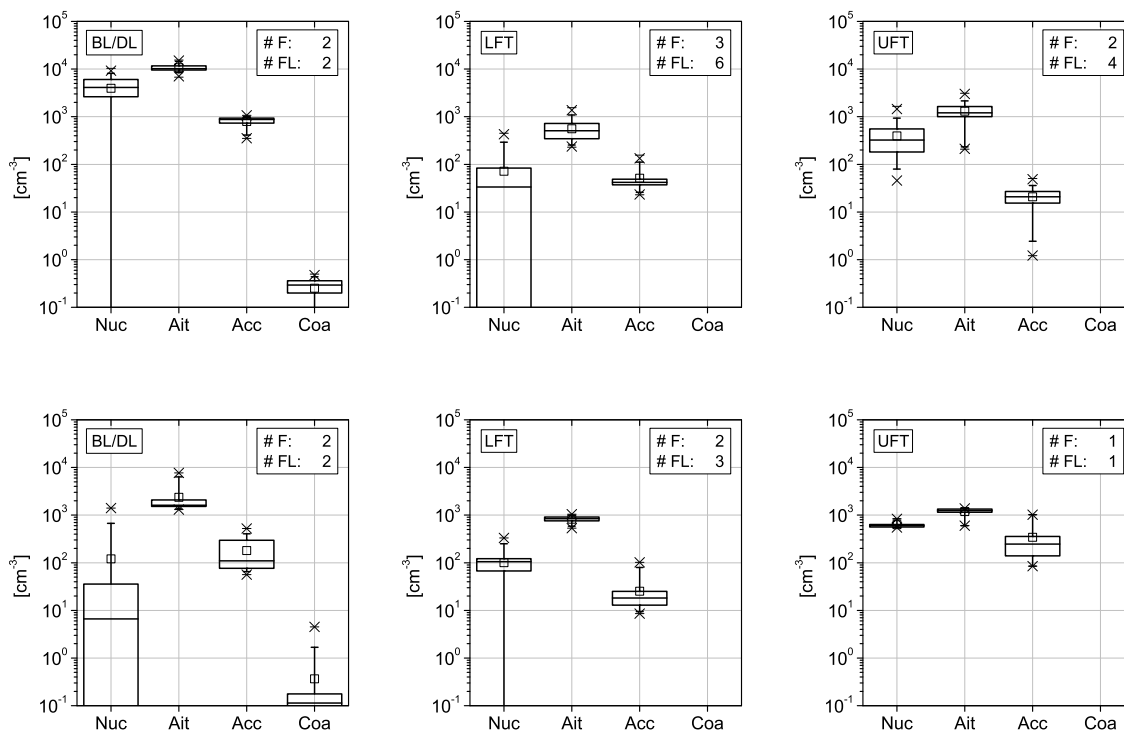


Figure 4.29: Average number concentrations at standard pressure and temperature over South Germany classified by aerosol modes. Nuc: nucleation mode, Ait: Aitken mode, Acc: accumulation mode, Coa: coarse mode. The panels show measurements performed during horizontal flight legs within the boundary layer and decoupled layers (BL/DL), the lower free troposphere (LFT) and upper free troposphere (UFT). Upper panels show period (a), lower panels period (b). Number of flights (# F) and number of flight legs (# FL) are listed.

Germany.

4.5.3 Size distributions measured over Europe

Horizontal flight sequences feature suitable conditions to measure aerosol size distributions in the troposphere. Especially the wing probes PCASP-100X and FSSP-300 and their inlet systems are sensitive to pitch and roll angles of the aircraft. Optimum measurement conditions can be found during horizontal flight sequences. In this section the aerosol size distributions are discussed based on the regional classification (Benelux States, North-east Germany and the Baltic Sea, and South Germany) introduced in Section 4.4 and the vertical classification discussed above. The analysis is divided into

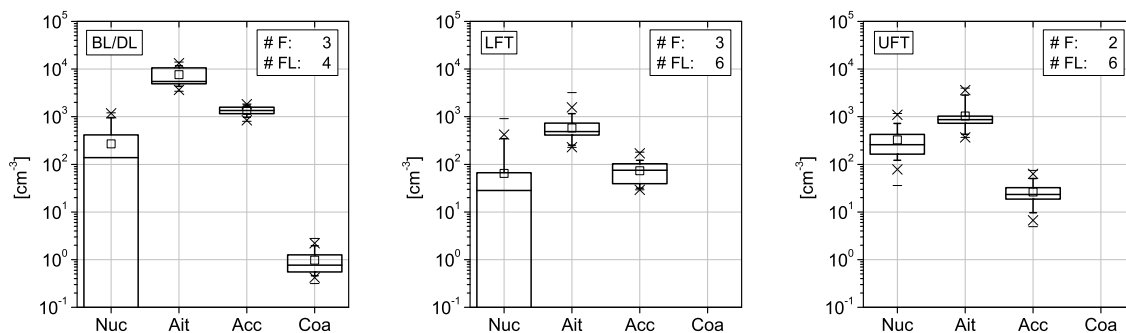


Figure 4.30: Same as Figure 4.29 for the Benelux States during May 2008.

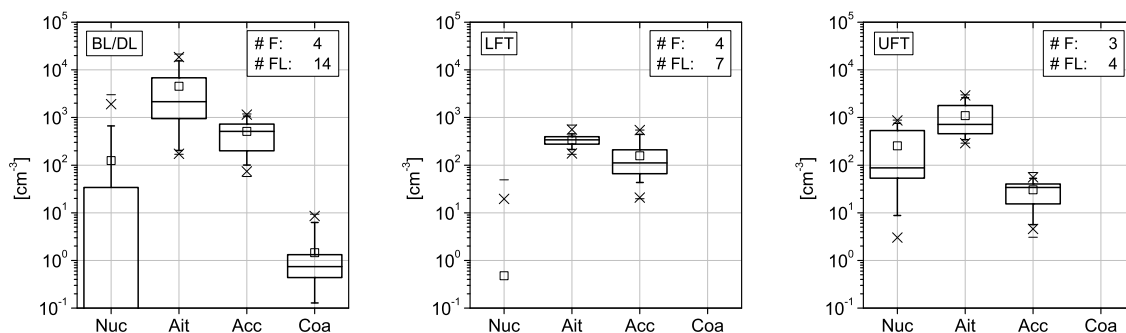


Figure 4.31: Same as Figure 4.29 for North-east Germany and the Baltic Sea during May 2008.

two parts. The first part covers the information of size resolved number concentrations of nucleation ($0.004\text{--}0.01\ \mu\text{m}$, Nuc), Aitken ($0.01\text{--}0.15\ \mu\text{m}$, Ait), accumulation ($0.15\text{--}1\ \mu\text{m}$, Acc), and coarse mode ($>1\ \mu\text{m}$, Coa) aerosol particles. By doing this, the Aitken mode, which covers the major number of particles, is taken into account. In addition, statistical deviations of each aerosol mode number concentration can be considered in a simple way. Size resolved information was not measured in the diameter range between $0.01\text{--}0.15\ \mu\text{m}$. Thus the size distributions discussed in the second part solely cover the size range of PCASP-100X and FSSP-300 ($0.15\text{--}30\ \mu\text{m}$).

Figures 4.29, 4.30 and 4.31 show the modal number concentrations for South Germany, the Benelux States, and North-east Germany and the Baltic Sea, respectively. A separation into the two meteorological periods (a) and (b) (Section 4.1) was only carried out for South Germany due to similar aerosol concentrations over the Benelux

Table 4.11: Modal fitting parameter for size distributions selected by regions and vertical levels. The corresponding size distributions are shown in Figures B.6–B.8. Average number concentrations \bar{N} are given in $[\text{cm}^{-3}]$ at standard temperature and pressure and average count median diameter $\overline{\text{CMD}}$ in $[\mu\text{m}]$.

Layer	Acc			Coa		
	\bar{N}	$\overline{\text{CMD}}$	$\overline{\text{GSD}}$	\bar{N}	$\overline{\text{CMD}}$	$\overline{\text{GSD}}$
South Germany, period (a)						
UFT	40	0.17	1.6	—	—	—
LFT	110	0.16	1.7	—	—	—
BL/DL	1500	0.16	1.5	0.3	2.5	2.2
South Germany, period (b)						
*UFT	400	0.15	1.3	—	—	—
LFT	84	0.14	1.6	—	—	—
*BL/DL	370	0.19	1.5	—	—	—
Benelux States						
UFT	44	0.17	1.6	—	—	—
LFT	180	0.15	1.7	—	—	—
BL/DL	2000	0.20	1.4	0.79	1.6	1.9
North-east Germany and Baltic Sea						
UFT	61	0.17	1.6	—	—	—
LFT	230	0.17	1.6	—	—	—
BL/DL	860	0.20	1.5	1.4	1.4	2.1

*only one sinlge event

States, and North-east Germany and the Baltic Sea during both periods as discussed in Section 4.4. All concentrations are given at standard temperature and pressure. Coarse mode number concentrations are only given for the boundary layer and decoupled layers due to low counting statistics and high noise in the free troposphere.

Highest number concentrations of all modes above South Germany can be found within the boundary layer during high pressure conditions. Aitken mode number concentrations averaged at 11000 cm^{-3} , accumulation mode number concentrations at 800 cm^{-3}

during period (a) compared to 2400 and 180 cm^{-3} during period (b) for the respective aerosol modes. Most variable concentrations can be found in the nucleation mode due to the short lifetime between the nucleation events and the growth into the Aitken mode. The nucleation mode number concentrations varied between 0–10000 cm^{-3} . The number concentrations of Aitken and accumulation mode show anticorrelated evolutions between periods (a) and (b) in the lower free troposphere. The Aitken mode concentrations increased (550 to 950 cm^{-3}) whereas the accumulation mode concentrations decreased (50 to 25 cm^{-3}). An increase of accumulation mode particles can be associated with a loss of Aitken mode particles if no additional sources were present like in the free troposphere during period (a). Differences in the upper free troposphere occurred in an increase of accumulation mode particles from period (a) to period (b) as it was already analysed in Section 4.4. In contrast to the lower free troposphere and boundary layer a less variable nucleation mode could be observed in the upper free troposphere.

The modal separated number concentrations measured above the Benelux States and the region of North-east Germany and the Baltic Sea show generally higher aerosol concentrations in the boundary layer of the Benelux States. This corresponds to the general flow pattern advecting polluted air masses from North Germany towards the Benelux States. It could be observed for both regions that number concentrations in the nucleation and Aitken mode in the lower free troposphere were lower than the respective concentrations in the upper free troposphere. In contrast, the accumulation mode number concentrations in the lower free troposphere exceed the concentrations at high altitudes. This finding supports the analysis in Section 4.4.

The size distributions obtained by PCASP-100X and FSSP-300 measurements were fitted to lognormal number size distributions in the accumulation and coarse mode size range. The resulting size distributions classified into regions and vertical levels are shown in Figures B.6–B.8. The respective average modal fitting parameters are listed in Table 4.11. The average accumulation mode number concentrations follow similar variations as already described above and will therefore not be discussed in detail here. The average count median diameter $\overline{\text{CMD}}$ in the free troposphere varies between 0.14–0.17 μm . Largest $\overline{\text{CMD}}$ values for the accumulation mode can be found in the boundary layer over the Benelux States, North-east Germany and the Baltic Sea and averaged at 0.2 μm . This indicates a grown accumulation mode in the respective regions. In addition a coarse mode with significant average number concentrations (0.79 and 1.4 cm^{-3}) occurred in the boundary layer above the same regions with $\overline{\text{CMD}}$ values of 1.6 and 1.4 μm . Both size distribution modes indicate the occurrence of grown and/or aged aerosol in the region of dominating anticyclonic flow from the Baltic Sea

via North Germany towards the Benelux States.

4.5.4 Chemical composition of aerosol particles measured aboard the BAe-146

The information retrieved from measurements during horizontal flight legs helps to assess the microphysical properties over Europe. The retrieved size distributions and volatile volume ratios indicate that the major sources of aerosol mass in the submicron size range originate from sources over Central Europe emitting secondary particles and their precursors. The increased residence time in the atmosphere due to the stable synoptic conditions leads to the transformation of the microphysical properties, e.g. through coagulation. As the microphysical measurements showed, the secondary aerosol mass fraction dominates the atmospheric submicron aerosol over Europe. The chemical composition of this secondary aerosol mass fraction plays an important role on particle properties and is governed by the aerosol sources and the conditions for the chemical reactions. Measurements of the chemical composition of aerosol particles within the boundary layer performed aboard the FAAM BAe-146 provide valuable information for further analysis of the aerosol distribution over Europe.

Size-resolved chemical composition of aerosol particles was measured by an Aerodyne compact Time-of-Flight Aerosol Mass Spectrometer (cToF-AMS, Drewnick et al. (2005)). The cToF-AMS provides chemical composition of non-refractory, i.e. secondary, particulate matter like organic matter (OM), sulphate, nitrate, ammonium, and chloride. A detailed analysis of the cToF-AMS measurements during EUCAARI-LONGREX can be found in Morgan et al. (2010). A zonal gradient of total secondary aerosol mass could be observed over Europe with increasing mass concentrations from the Baltic Sea towards the West with maximum mass concentrations above the Benelux States exceeding $25 \mu\text{g m}^{-3}$. Increased secondary mass concentrations were also observed on the East coast of England and within the pollution layers probed south west of Ireland. With increasing total concentrations of secondary mass the ratio between nitrate and sulphate changed from East to West, too. While sulphate mass concentrations exceed the mass concentrations of nitrate within the region of the Baltic Sea and Germany, nitrate mass concentrations increase and exceed the sulphate concentrations over the Benelux States and south west of Ireland. The high sulphate mass concentrations can be related to industrial dominated regions. In contrast, nitrate compounds frequently occur above regions with intense agricultural land use and the use of fertilizer like it appears in Northeast Germany and the Benelux states.

However, the highest mass fraction of non-refractory aerosol was observed to be organic aerosol (OA) with a relative mass fraction of 20–50%. In contrast to the static nature of e.g. sulphate, OA undergoes a dynamic chemical evolution with time. Most OA evolves due to oxidation to oxygenated organic aerosol (OOA). Two OOA compounds can be separated due to their state of oxidation. The less oxygenated semi-volatile SV-OOA and the more oxygenated low-volatile LV-OOA (Jimenez et al., 2009). As the state of oxidation increases with increasing time, air masses containing more or less aged aerosol can be identified. Morgan et al. (2010) reported that 50–65% of OM consist of the aged LV-OOA close to aerosol source regions in May 2008 while the fraction increases to 60–80% in the far field outflow like it could be observed south west of Ireland. This chemical analysis is in agreement with the ageing processes analysed above using the measurements of microphysical aerosol properties aboard the DLR Falcon 20. It shows in addition that aged aerosol could be already observed within the boundary layer of the source regions in Central Europe next to freshly emitted particles. Nevertheless, the fraction of chemically and physically aged aerosol particles increased during the transport from source regions towards remote regions.

Chapter 5

Application of a new trajectory analysis method

The aerosol properties discussed in the present work indicated a dependency on the aerosol source regions and the locations of the measurement sites where the aerosol properties were probed. This dependency can already be identified from the analysis of aerosol properties within the meteorological context and the prevailing flow patterns which was accomplished in the previous sections. Nevertheless, trajectory analysis is required for an objective analysis of aerosol properties within the context of the air mass history containing its transport pathway and meteorological conditions during the transport. Thus, source regions of aerosol particles can be identified and the measured aerosol properties can be connected to the specific sources.

The trajectory analysis discussed in this section follows the methods explained in Section 3.2. Back trajectories were started from DLR Falcon 20 flight tracks (-240 h) and from the six ground stations introduced in Section 4.3 (-168 h). Meteorological parameters derived from the ECMWF operational analysis will be compared to in-situ measurements of FAAM BAe-146 and DLR Falcon 20 to assess the usability of the model data for the trajectory analysis. Further, source contributions, cloud cover, and precipitation along the trajectories will be analysed in combination with the measured aerosol properties to determine the effects of different transport pathways on the aerosol. Hereinafter, the air masses arriving at the measurement sites will be classified into several age classes to examine the effect of emissions of different age on the probed aerosol.

5.1 Comparison of model data with in-situ measurements

The proper analysis of meteorological parameters along the calculated trajectories requires the verification of key parameters retrieved from the ECMWF model. During the aircraft field campaign meteorological parameters like temperature and specific humidity were measured aboard the FAAM BAe-146 and DLR Falcon 20. Both aircraft measure temperature with a Rosemount temperature sensor and the specific humid-

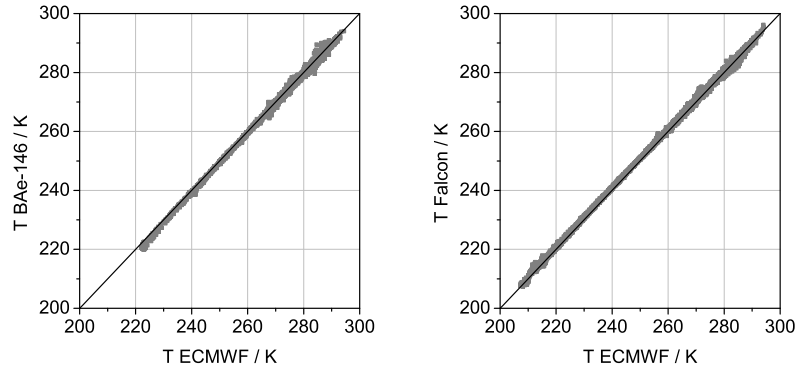


Figure 5.1: Comparison of temperature T [K] from in-situ measurements of FAAM BAe-146 (left panel) and DLR Falcon 20 (right panel) with ECMWF model analysis data. The black line denotes the 1:1 line.

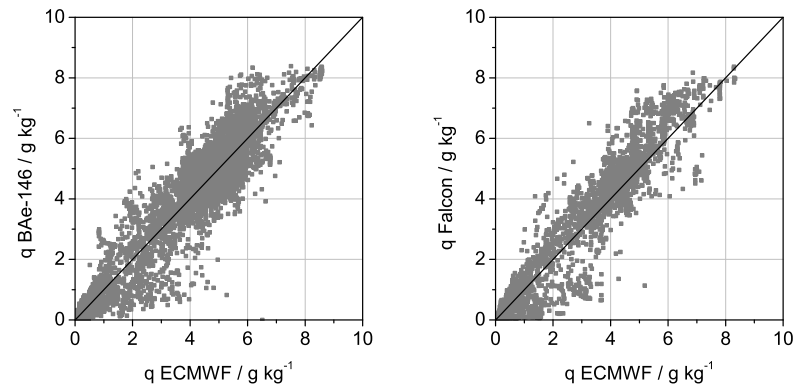


Figure 5.2: Comparison of specific humidity q [g kg^{-1}] from in-situ measurements of FAAM BAe-146 (left panel) and DLR Falcon 20 (right panel) with ECMWF model analysis data. The black line denotes the 1:1 line.

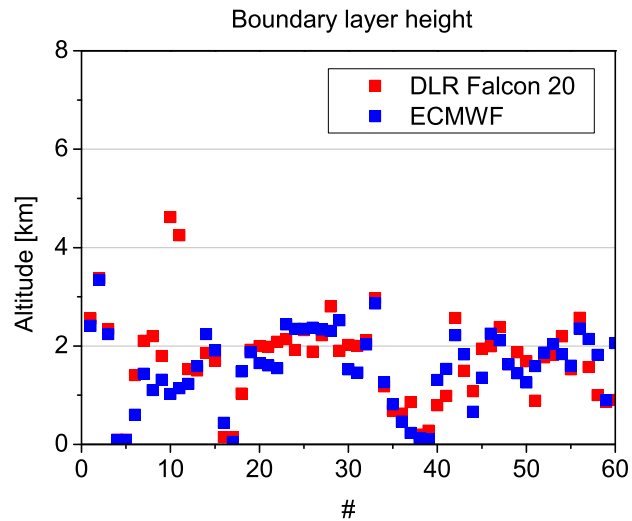


Figure 5.3: Comparison of boundary layer height blh [km a.s.l.] from in-situ measurements of DLR Falcon 20 (red) with ECMWF model analysis (blue) data.

ity with a Lyman-Alpha absorption hygrometer. These parameters can be used to compare in-situ measurements with model data. For comparison reasons the aircraft flight tracks were considered as air mass trajectories and the interpolation algorithm described in Section 3.2 was used to interpolate the regular gridded model data along each single flight track in space and time.

Figure 5.1 and Figure 5.2 show the comparison of temperature and specific humidity for FAAM BAe-146 and DLR Falcon 20, respectively. Linear regression of the compared data showed high correlation for all parameters. The correlation coefficient for the comparison of model data and FAAM BAe-146 data reaches 0.97 for temperature and 0.96 for specific humidity. Correlation coefficients of 1.0 and 0.97 result from the comparison of model data with DLR Falcon 20 data for temperature and specific humidity, respectively.

The major parameter to analyse the contribution of ground-based sources along a trajectory is the boundary layer height retrieved from the ECMWF. The boundary layer height is parameterised at the ECMWF using the parcel lifting method (or bulk Richardson method) proposed by Troen and Mahrt (1986). FLYTUL considers trajectories only as influenced by ground based sources if the air masses pass through the boundary layer, i.e. the trajectory altitude is lower than the boundary layer height.

All punctures of the DLR Falcon 20 through the boundary layer top were identified to compare the model boundary layer height with the observed one. The boundary layer top was identified using vertical temperature, humidity and aerosol concentration profiles as well as vertical profiles measured with the LIDAR aboard the DLR Falcon 20.

Figure 5.3 shows the boundary layer heights retrieved from in-situ measurements and the ECMWF. While comparing the boundary layer heights one has to consider several items leading to deviations. First, the ECMWF delivers the boundary layer height as the height of the mixing layer that is in contact to the surface. In contrast, it can appear that the top of the boundary layer identified from in-situ measurements can be the top of the uppermost layer amongst others showing similar properties and no significant separation. Second, the boundary layer height strongly depends on the nature of the surface and can show a high spatial variability above a heterogeneous surface like it occurs in Central Europe. The specifications of the surface govern the heat and humidity transfer from the surface into the boundary layer and thus its stability and capability of increasing depth. The average boundary layer height on a $0.5^\circ \times 0.5^\circ$ grid which results in a horizontal resolution of ~ 47 km does not cover all surface specifications which might lead to an deviation of the boundary layer height of a few tens to a hundreds of metres.

The correlation coefficient for the comparison of model boundary layer height and boundary layer height retrieved from DLR Falcon 20 measurements reaches 0.62. The correlation is still statistically significant on a 99 % confidence level.

The high correlations of the meteorological parameters give credibility to the use of the model data and the interpolation method used for the trajectory analysis. The boundary layer height retrieved from the ECMWF can be considered as suitable for the analysis of ground based source contributions to the air masses, which are advected along the calculated trajectories.

5.2 The effect of source strength and cloud cover along air mass transport path ways on the accumulation mode number concentration

The source strength along a trajectory pathway is examined using the continental pollution index *CPI*. The *CPI* covers all anthropogenic ground based sources, i.e. rural and industrial, given by the EDGAR archive (Section 3.2). The *CPI* varies between 0 (no anthropogenic sources) and 1 (strong anthropogenic sources). As described above sources will only be taken into account if the trajectory passes through the boundary layer. Figure 5.4 shows the average source strength along back trajectories binned into the accumulation mode number concentration measured at the ground stations. The single trajectories started in 6 hourly intervals from the respective ground station in May 2008. The *CPI* was averaged for bins covering a time interval of 24 h and a interval of the accumulation mode number concentration of $500 \text{ particles cm}^{-3}$. The right panel of each subfigure shows the number of trajectory bunches classified into the respective interval of number concentrations. Please note that the trajectories are back trajectories and the starting points of the trajectories, i.e. time = 0, are on the right side of each panel showing the average *CPI*.

A first overview of the source strength along the air mass trajectories points out three different regions. Regions hardly affected by anthropogenic emissions (Hyytiälä and Vavihill), regions affected by anthropogenic emissions but not directly located at the source regions (Mace Head and Hohenpeißenberg), and regions strongly affected by emissions and located closely to anthropogenic sources (Cabauw and Melpitz). By comparing this classification with the regional classification found in Section 4.3.1 a noticeable difference occurs. In Section 4.3.1 the stations could be classified into regions outside the anticyclone (Hyytiälä and Mace Head), regions at the borders of the anticyclone (Vavihill and Hohenpeißenberg), and regions located within the anticyclone core (Cabauw and Melpitz).

Figure 5.4 is of descriptive nature and shows the average contribution of pollution sources along the trajectory pathways. To quantify the results and to analyse the data shown in Figure 5.4 we have to define a parameter that describes the influence of fresh or aged pollution. We set the average source contributions of the last 24 h in relation to the source contributions between 48–72 h before the measurements, i.e. fresh pollution in relation to aged pollution:

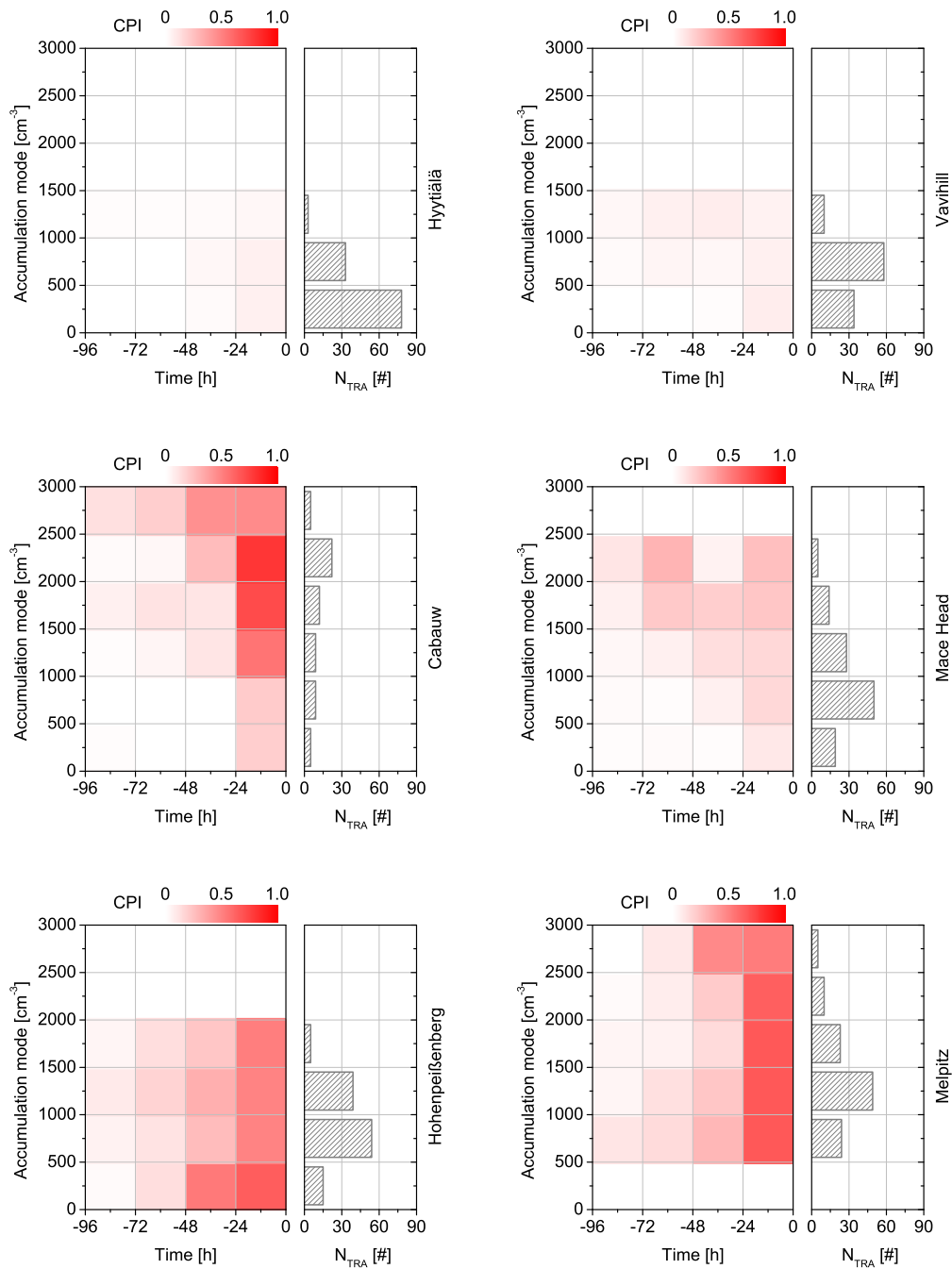


Figure 5.4: Continental pollution index (CPI) along air mass transport pathways. Back trajectories start from the ground stations indicated. The CPI is marked with the red shade. The back trajectories are sorted horizontally by the accumulation mode number concentration measured at the origin at time 0 h. The right panels show the number of trajectory bunches sorted into the respective bins of number concentrations.

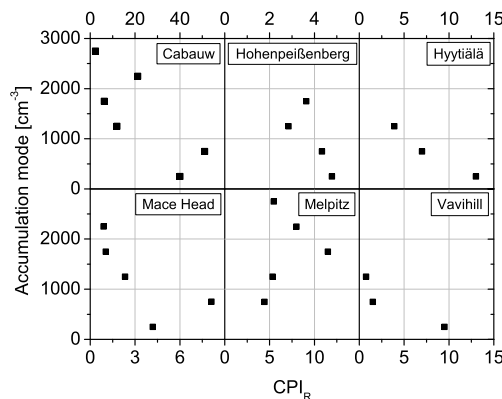


Figure 5.5: Average accumulation mode number concentration measured at the ground stations against CPI_R (see text for explanation).

$$CPI_R = \frac{\overline{CPI}_{(0-24)}}{\overline{CPI}_{(48-72)}}. \quad (5.1)$$

Figure 5.5 shows the accumulation mode number concentration related to CPI_R . The CPI_R varies for the different ground stations from fresh pollution at Cabauw ($CPI_R < 50$) to aged pollution most frequently observed at Hohenpeißenberg ($CPI_R < 5$). Although no statistically significant correlation can be found, the analysis indicates an increase of accumulation mode number concentrations for aged pollution at all stations except Melpitz. For example, the number concentration increase from 500–1000 cm^{-3} at $CPI_R = 50$ to 2500–3000 cm^{-3} at $CPI_R = 2$ at Cabauw and from 0–500 cm^{-3} at $CPI_R = 13$ to 1000–1500 cm^{-3} at $CPI_R = 4$ at Hyttiälä.

The absolute variations of the accumulation mode number concentrations cannot be compared between the ground stations due to the different locations in different source regions and their different exposure towards pollution sources. However, the relative variation, i.e. the increase of the accumulation mode number concentration with increasing age of the pollution, shows the effect of transported and aged aerosol at the distinct measurement sites. The aerosol concentration measured at each station depends on the surrounding aerosol sources and the air mass transport direction and the occurring wind field. Other meteorological parameter affecting the aerosol properties along the transport pathway are cloud cover and precipitation.

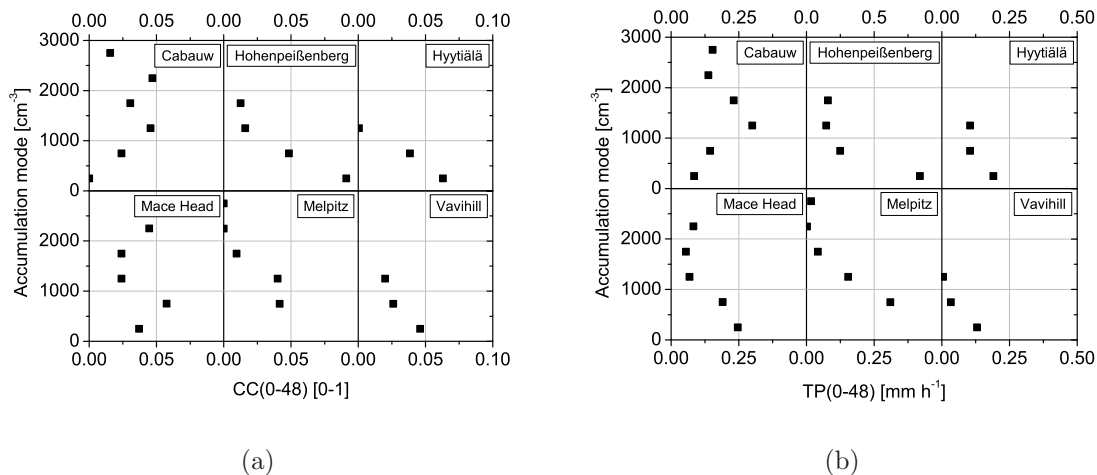


Figure 5.6: Average accumulation mode number concentration measured at the ground stations against average cloud cover ($\overline{CC}_{(0-48)}$, a) and average precipitation ($\overline{TP}_{(0-48)}$, b) (see text for explanation).

The analysis of air mass history regarding the meteorological parameter cloud cover (CC) underlies several limitations. The effects of clouds on the aerosol size distribution depends on one hand on the cloud types, i.e. if aerosol particles are activated by non-precipitating clouds (Hoppel et al., 1994) or undergo scavenging by precipitating clouds or deep convection (e.g., Flossmann, 1998; Raes et al., 2000; Reeves et al., 2010). On the other hand the chemical aerosol composition plays an important role in and which aerosol particles are activated as cloud condensation nuclei (Sellegri et al., 2003). In terms of the accumulation mode, clouds can have two effects. The removal of the aerosol in the accumulation mode size range is mainly through activation in clouds and subsequent precipitation (Raes et al., 2000). Hence, the number and / or mass concentration of accumulation mode particles will decrease due to in-cloud effects, serving as CCN and being removed by precipitation. In contrast, in-cloud scavenging and activation of aerosol within non-precipitating clouds can lead to a growth of particles into the accumulation mode size range (Hoppel et al., 1994). Non-precipitating clouds feature suitable conditions for a greater amount of gas-to-particle conversion through in-cloud aqueous phase oxidation processes than cloud free conditions. The grown accumulation mode particles also exhibit a larger fraction of volatile material (80–150 °C) (O’Dowd et al., 2000).

The findings in literature suggest that a simple analysis only using CC along the trans-

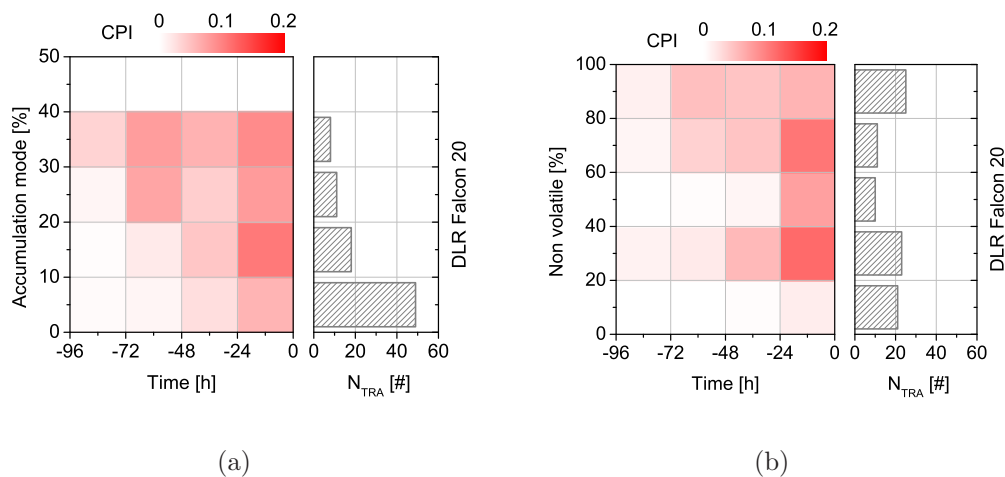


Figure 5.7: Continental pollution index (CPI) along air mass transport pathways. The CPI is marked with the red shade. The back trajectories are sorted horizontally by the relative number of accumulation mode (a) and non volatile particles (b) on the total number concentration measured at the origin at time 0 h. The origin corresponds to flight sequences performed with the DLR Falcon 20. The right panels show the number of trajectory bunches sorted into the respective bins of number ratios.

port pathway cannot give a complete satisfactory support for interpreting the measured accumulation mode number concentrations. For this reason CC and total precipitation (TP) are used for the analysis of the ground based measurements. However, the total precipitation retrieved from the ECMWF, which comprises large scale and convective precipitation, only supplies two-dimensional information at the surface level. Depending on the altitude of the precipitating cloud and the trajectory, aerosol may not undergo washout if precipitation is indicated at the surface. In contrast to the airborne measurements, the back trajectories used for the analysis of the ground based measurements started at low levels and usually did not vary significantly in altitude in the last days prior to the measurements. Thus, TP will be used for this analysis.

The analysis method is similar to the analysis used for the CPI above. Instead of the ratio CPI_R , average values of the last 48 h ($\overline{CC}_{(0-48)}$ and $\overline{TP}_{(0-48)}$) are applied to the respective bins of the accumulation mode number concentration. Although the cloud cover was small in all cases ($\overline{CC}_{(0-48)} < 0.1$) number concentrations decrease with increasing cloud cover at all stations except Cabauw and Mace Head (Figure 5.6). Similar patterns can be found for TP in Figure 5.6(b). Thus, it can be assumed that aerosol particles were removed by precipitating clouds resulting in a decrease of number concentrations by a factor $\sim 3-5$.

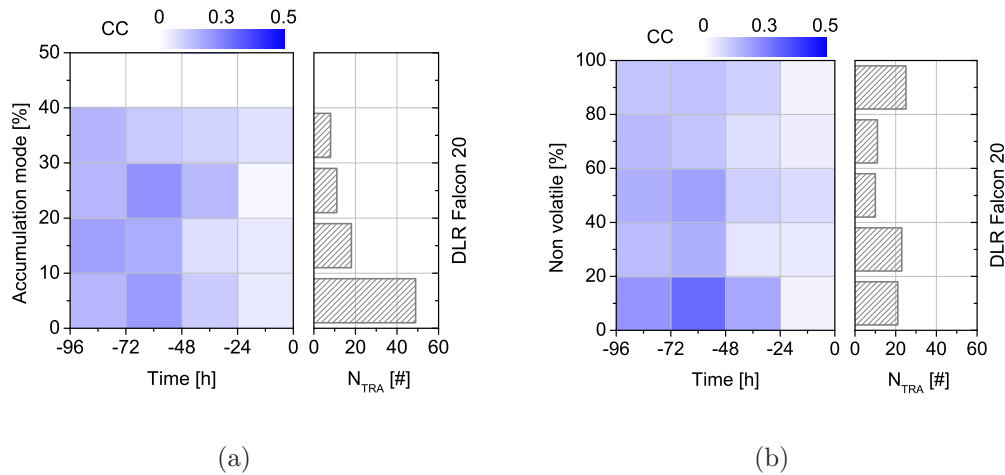


Figure 5.8: Cloud cover (CC) along air mass transport path ways. The CC is marked with the blue shade. The back trajectories are sorted horizontally by the relative number of accumulation mode (a) and non volatile particles (b) on the total number concentration measured at the origin at time 0 h. The origin corresponds to flight sequences performed with the DLR Falcon 20. The right panels show the number of trajectory bunches sorted into the respective bins of number ratios.

Source strength (Figure 5.7) and CC (Figure 5.8) were also analysed for back trajectories starting from horizontal flight sequences performed with the DLR Falcon 20. TP was not used for the analysis of the airborne measurements due to the uncertainties of the altitude of precipitating clouds. Both parameters, CPI and CC, were averaged for bins of 24 h time intervals and bins of the ratios of accumulation mode number concentrations to total number concentrations (10% intervals) and number concentrations of particles containing a non-volatile core to total number concentrations (20% intervals).

The fraction of accumulation mode particles increases from 0–20% for fresh pollution ($CPI_R \sim 7$) to 20–40% for aged pollution ($CPI_R \sim 1$) (Figure 5.9). A maximum fraction of non-volatile particles (60–100%) can be found for aged pollution, too. This reveals the frequently observed coagulation of particles during air mass transport. Most flights were performed during anticyclonic, i.e. dry conditions. This can be seen in Figure 5.8. Only few cloud cover occurred within the last 24 h ($\overline{CC}_{(0-24)} < 0.1$) before the measurements. The particle fractions show only little correlation with CC. However, the fraction of accumulation mode particles tends to increase towards larger CC. As described above, an increase of accumulation mode particles can occur due to processing and activation in non-precipitating clouds. This processing of particles in

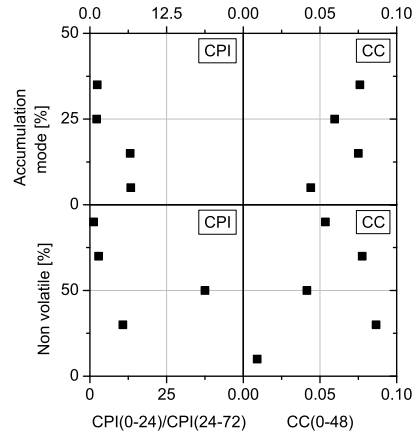


Figure 5.9: Average fraction of accumulation mode number concentrations (upper panels) and average fraction of non-volatile particles (lower panels) measured aboard the DLR Falcon 20 against CPI_R (left panels) and average cloud cover ($\overline{CC}_{(0-48)}$, right panels) (see text for explanation).

clouds is in contrast to the wet removal of particles observed at the ground stations.

The trajectory analysis of the ground stations and horizontal flight sequences supports the finding of previous sections that the aerosol containing a large relative amount of accumulation mode and non-volatile particles underwent ageing processes like condensation and coagulation. Thus, the aerosol grew with time, also on the cost of total number concentrations, and was transformed from an external into an internal mixture regarding the volatility state.

5.3 Air mass classification using temporal weighted averages

The trajectories used in the discussion above can also be used to classify the air masses arriving at the measurement sites. Thus the ground based stations can be considered with respect to their exposure towards different air masses in May 2008 and the flight sequences can be analysed with respect to the probed air masses. The temporal weighted averaging of the respective parameters will be used as described in Section 3.2 to classify the air masses.

5.3.1 Classification of air masses into defined age classes

The time weighting function will be used to classify the air masses into defined age classes. Thereby the effects of sources and ageing processes on aerosol particles along an air mass transport pathway can be considered. The respective air masses will be labelled depending on the age class with the dominating, though time weighted, source contributions. The continental pollution index CPI , the continental boundary layer index CBI , and the marine boundary layer index MBI are used for the classification. The latter ones are used to identify whether maritime or continental air masses were dominating. The time weighted averages \overline{CBI}_t and \overline{MBI}_t are calculated using Equation 3.21. Continental and maritime air masses were defined as follows:

$$\overline{CBI}_t > \overline{MBI}_t : \text{ Continental air mass} \quad (5.2)$$

$$\overline{CBI}_t < \overline{MBI}_t : \text{ Maritime air mass} \quad (5.3)$$

Of course, maritime air masses do not exclude contributions of continental sources and vice versa. If continental sources dominated, four age classes were defined for the analysis of the air masses:

- 00–12 h, fresh air masses close to the emission source,
- 12–24 h, young air masses, already some ageing processes happened,
- 24–48 h, aged air masses within the lifetime of aerosols inside the boundary layer,
- > 48 h, aged air masses.

To define the dominating age class of the measured air mass we calculate the integral of the time weighted CPI . The age class resulting in the maximum integral compared

to the other three age classes defines the air mass. The time weighted integrals of CPI can be written as follows for each age class using Equation 3.20:

$$CPI_{0-12} = \int_{t=0}^{12} w_{GAUSS}(t)CPI(t) dt \quad (5.4)$$

$$CPI_{12-24} = \int_{t=12}^{24} w_{GAUSS}(t)CPI(t) dt \quad (5.5)$$

$$CPI_{24-48} = \int_{t=24}^{48} w_{GAUSS}(t)CPI(t) dt \quad (5.6)$$

$$CPI_{>48} = \int_{t=48}^{t_{max}} w_{GAUSS}(t)CPI(t) dt. \quad (5.7)$$

All three sigma factors $sf = \{\frac{1}{3}; \frac{1}{2}; 1\}$ (cf. Equation 3.18) were used to calculate $w_{GAUSS}(t)$. As already mentioned for maritime and continental air masses, the domination of one age class does not exclude the existence of aerosol particles from sources classified into other age classes.

5.3.2 Air mass classification for ground based measurements

The classification of air masses is applied to the accumulation mode time series measured at the ground stations. A sigma factor $sf = 1$ was used for the time weighting function. Figure 5.10 shows the accumulation mode time series of each ground station (black squares). In addition, the air mass classification is highlighted by grey and white shade. White shade indicates air masses dominated by maritime sources. The grey shade depicts the dominating age class of continental sources. Very light grey indicates the age class 0–12 h, light grey 12–24 h, grey 24–48 h, and dark grey > 48 h.

The comparison of the time series of accumulation mode number concentrations and air mass classifications is in agreement with the findings in Section 4.3 and supports the statements made above. The remote ground stations at Hyytiälä and Mace Head were influenced by several single pollution events rather than long-term pollution caused by the anticyclone blocking. The pollution event on 13 May at Mace Head, which was probed by airborne measurements one day after over the Atlantic south west of Ireland can be highlighted. Aged European pollution (> 48 h) dominated these air masses as it was already indicated in Section 4.2. However, the time series at Mace Head shows that not all peaks in the accumulation mode can be related to continental pollution using the introduced analysis method. The analysis of the dominating air mass causes this effect, which does not explicitly show the contributions of further air masses.

The long-term contribution of aged polluted air masses at Vavihill illustrates the effect

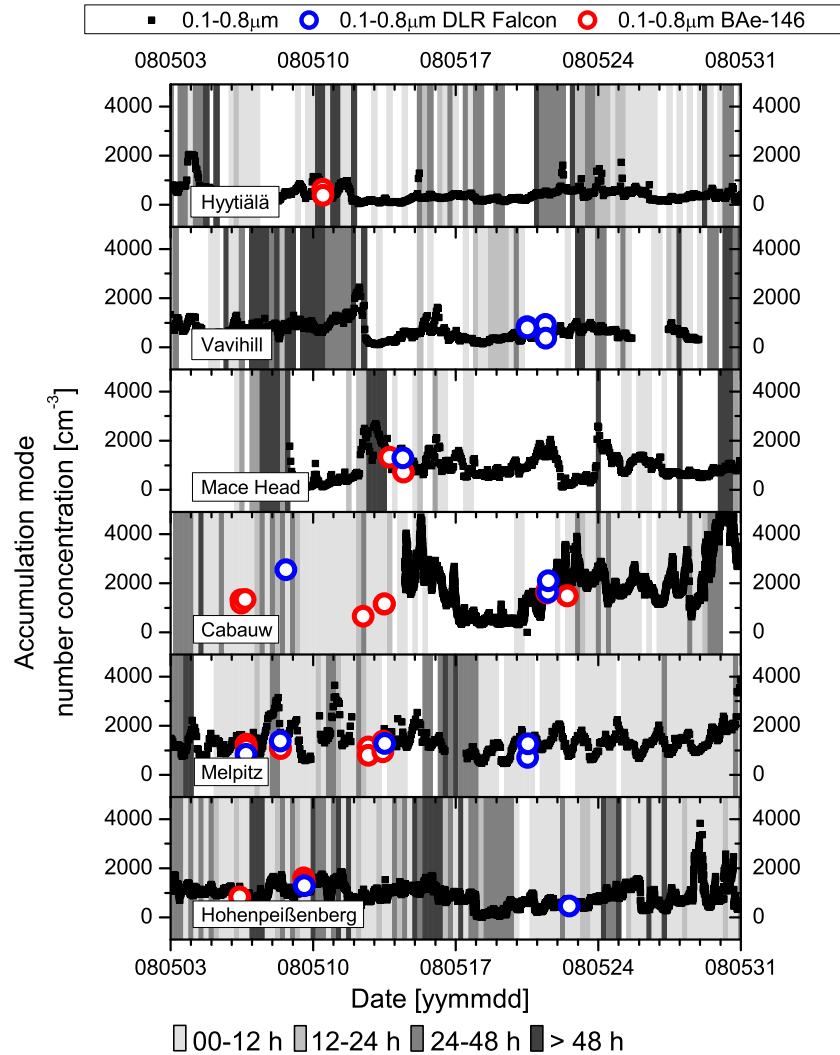


Figure 5.10: Time series of accumulation mode number concentrations at the ground stations. The gray shade indicates the age class of air masses dominated by continental pollution. A sigma factor $sf=1$ was used for time weighting.

of the anticyclone blocking until it left its stationary position over Denmark and the North Sea on 10 May. On the other hand, the analysis of the air masses shows that the stations at Cabauw and Melpitz were most frequently influenced by pollution emitted from nearby sources. Nevertheless, some aged pollution events occurred at Melpitz especially during the first half of May 2008 (period (a)). The coherence between maritime air masses arriving at Cabauw and the decrease of accumulation number concentra-

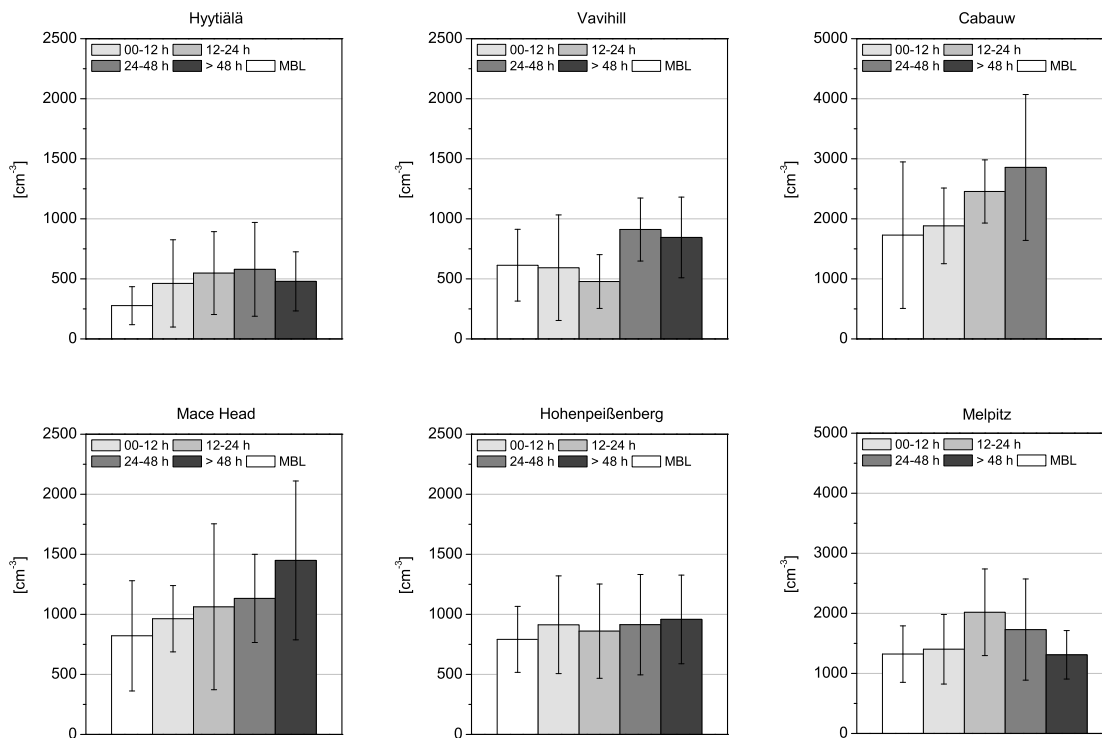


Figure 5.11: Average accumulation mode number concentrations for different age classes at the ground stations. A sigma factor $sf=1$ was used for time weighting.

tions between 16–22 May found in Section 4.3.1 was retrieved from manual analysis of backward trajectories. The automated analysis of the air mass classification used in this section reproduces this finding and supports its usability.

Average values of accumulation mode number concentrations were calculated for each age class to quantify the results of the trajectory analysis (Figure 5.11). Although most variations of accumulation mode number concentrations between the different air mass classifications lie within the range of the standard deviations they indicate an increase of concentrations towards aged air masses. The concentrations monotonically increase from maritime air masses to the age class 24–48 h from 280 to 580 cm^{-3} at Hyttiälä, from 820 to 1100 cm^{-3} at Mace Head, and from 1700 to 2900 at Cabauw. At Mace Head maximum concentrations of 1400 cm^{-3} can be found if the age class > 48 h is dominating. In contrast accumulation mode number concentrations start to decrease again for air masses dominated by this age class at Hyttiälä. A similar behaviour can be found at Vavihill and Melpitz. The decrease of the accumulation mode number

concentrations for pollution of age > 48 h at some ground stations indicates that the choice of ~ 48 h as maximum life time of aerosol particles inside the boundary layer is a good assumption.

The results of the air mass classification using the time weighted CPI_t and the accumulation mode number concentrations measured at the ground stations are limited by natural variations. These variations lower the significance of the results. However, they are part of field measurements and cannot be excluded. Despite the natural variations, the measurements are of great value for analysing ageing processes of aerosol particles.

5.3.3 Air mass classification using different sigma factors sf

As described in Section 3.2.5 and above the strength of the temporal weight can be changed by changing the factor sf , which is multiplied with the variance of the Gaussian distribution function, i.e. the lifetime of aerosol particles, whereas the ratio of the lifetimes within the boundary layer and the free troposphere remain the same. The change of the sigma factor sf can be used for the interpretation of the weighting function. A sigma factor $sf = \frac{1}{3}$ reduces the lifetime of particles and increases the weight for fresh sources whereas a sigma factor $sf = 1$ also takes aged source contributions into account for the analysis of the air mass history.

The frequency of the occurrence of the different air mass classifications at the respective ground stations is used to analyse the effect of the different sigma factors (Figure 5.12). It is evident that the remote ground stations close to the sea, i.e. Vavhill and Mace Head, are dominated by maritime air masses for all sf . The constant frequencies of all age classes at Vavhill indicate that hardly any aerosol sources are located near the station for the observed wind directions. In contrast, Mace Head was affected by some fresh emissions located on Ireland. A sigma factor $sf = \frac{1}{3}$ considers these fresh emissions. The maritime origin of the air masses is getting more evident for sigma factors of $\frac{1}{2}$ or 1.

A distinct decrease in frequency of fresh air masses (0–12 h) occurs for increasing sf at the continental stations. This indicates strong influence of nearby source regions on the air masses probed at the respective stations. Sigma factors of $\frac{1}{2}$ and 1 increase the lifetime of aerosols and the weight of aged source contributions and enable an analysis of the air mass history despite the dominance of fresh air masses. Nevertheless, the effect of fresh air masses is not neglected as can be seen at the Melpitz station.

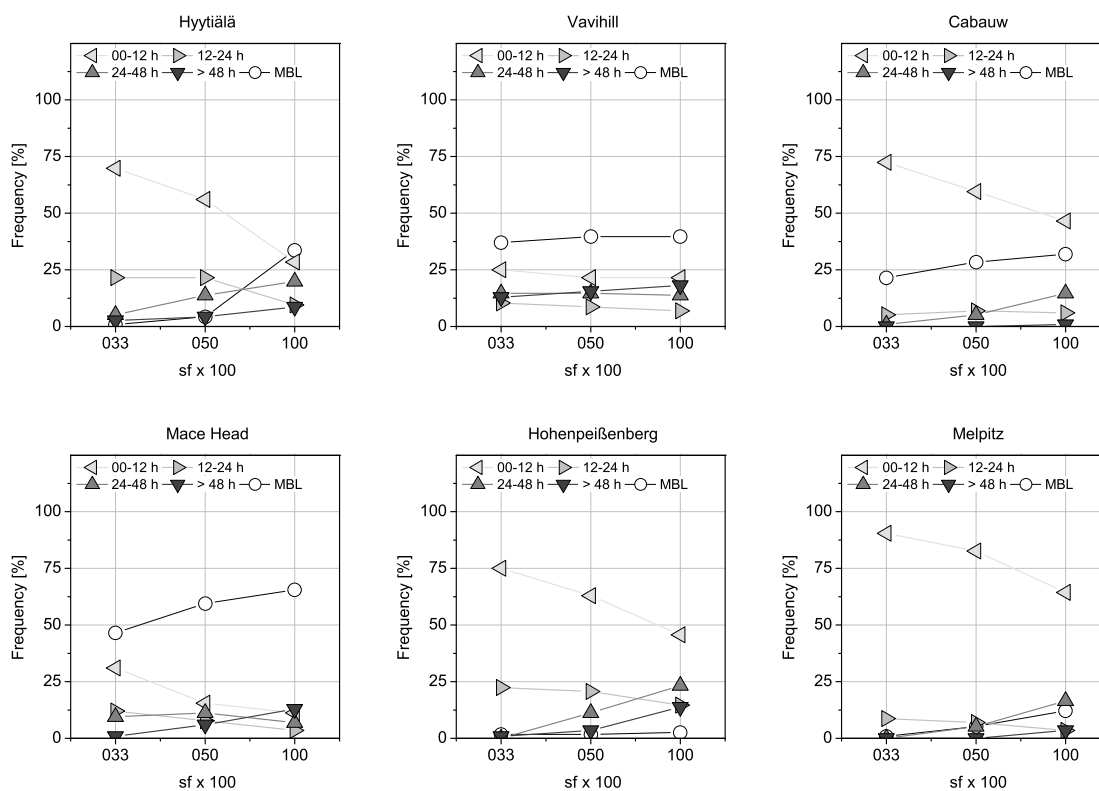


Figure 5.12: Frequency of the occurrence of different air mass classes at the ground stations for different sf .

Figure 5.13 shows the variation of the analysis of the air mass classification for ground based measurements for varying sf on the examples Hyytiälä and Cabauw. When the lifetime of aerosol particles is reduced, fewer measurements are classified as aged air masses and the weight increases for fresh air masses. As a result, aged source contributions are not taken into account for the analysis and less information about the air mass history is produced. Although the information of air masses older than 24 h is still available for remote sites like Hyytiälä, it gets lost for sites located close to pollution sources like Cabauw due to the increased weight for fresh air masses. However, the main conclusion, increasing accumulation mode number concentrations with increasing age of the dominating pollution, is not significantly changed. Nevertheless, a $sf = 1$ is recommended to account for the information of aged air masses.

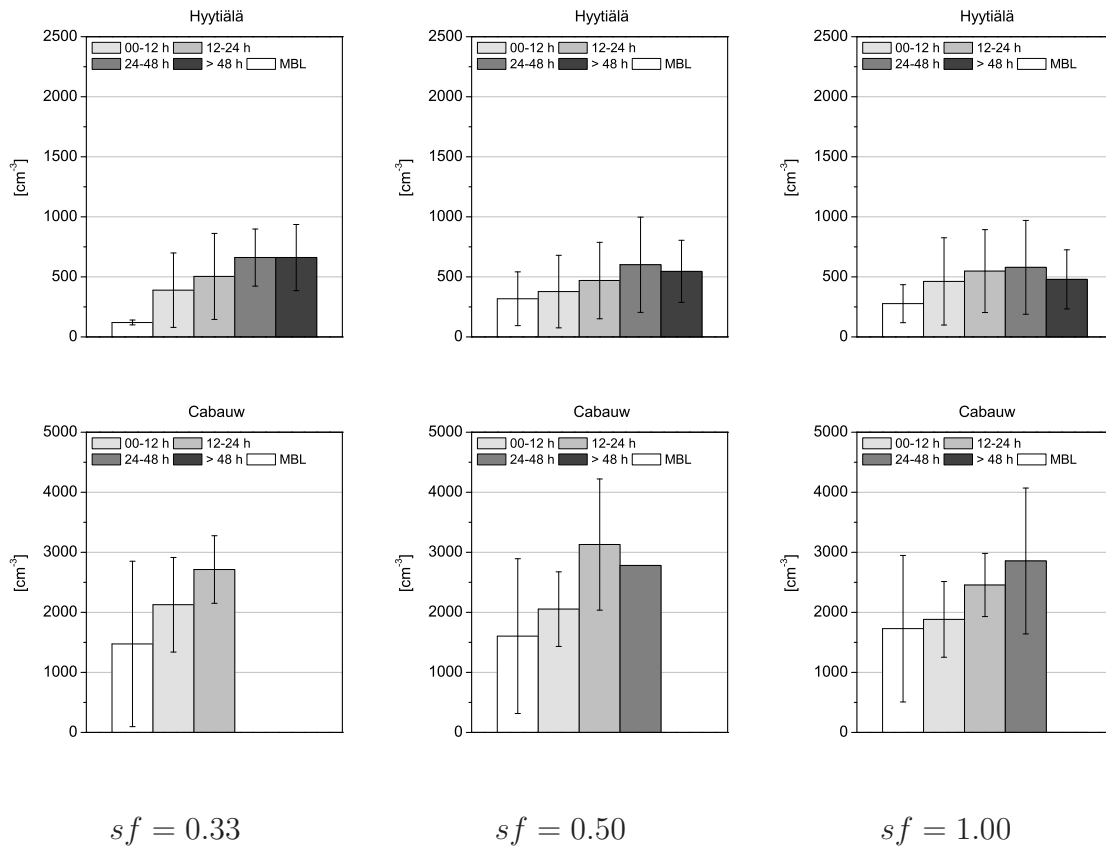


Figure 5.13: Average accumulation mode number concentrations for different age classes at the ground stations Hyytiälä and Cabauw calculated with $sf = \frac{1}{3}$, $sf = \frac{1}{2}$, and $sf = 1$.

5.3.4 Air mass classification for airborne measurements

The air mass classification was also used for airborne measurements performed aboard the DLR Falcon 20. Out of the 92 horizontal flight sequences, 26 flight sequences were performed within air masses that had contact to continental source regions within the last 10 days according to the trajectory analysis. A sigma factor $sf = 1$ was used for the time weighting function. The horizontal distribution of these flight sequences shows that air masses dominated by fresh pollution were found over Germany and the Benelux States whereas aged pollution was found on the East coast of England and over the Atlantic southwest of Ireland (Figure 5.14). This is consistent with the analysis of air masses at the ground stations.

Average aerosol number concentrations were analysed with respect to the different

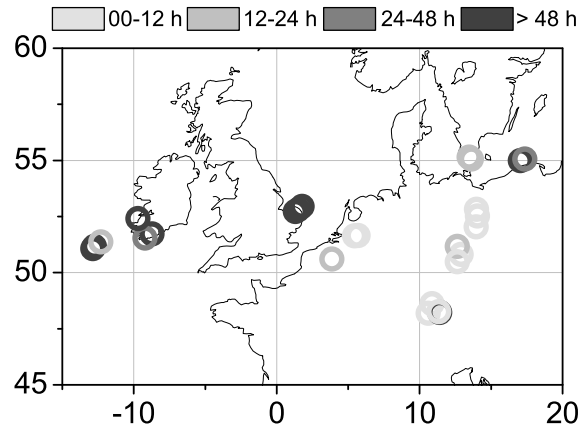


Figure 5.14: Horizontal distribution of age classes ($sf=1$).

age classes. Total number concentrations decrease strongly between the age class 0–12 h and 12–24 h from 11000 to 3600 particles cm^{-3} . The decrease of the total number concentration suggests a loss of particles in the Aitken mode size range. The increase of the relative fraction of accumulation mode particles from 12% to 20% indicates that the loss of Aitken mode particles happened due to coagulation processes rather than real loss of particulate matter. The coagulation process can also be seen in the increased fraction of particles containing a non-volatile core from 42% to 75%. The next age class is less represented as only two horizontal flight sequences were classified in the age class 24–48 h. However, the further increase of the relative fraction of accumulation mode particles and particles containing a non-volatile core towards the age class > 48 h shows further coagulation processes with increasing age.

The time weighted trajectory analysis indicates that the main coagulation process happens within the first 12–24 h. After one day the coagulation rate seems to decrease and, taking the results of the ground based measurements into account, reaches its minimum after two days.

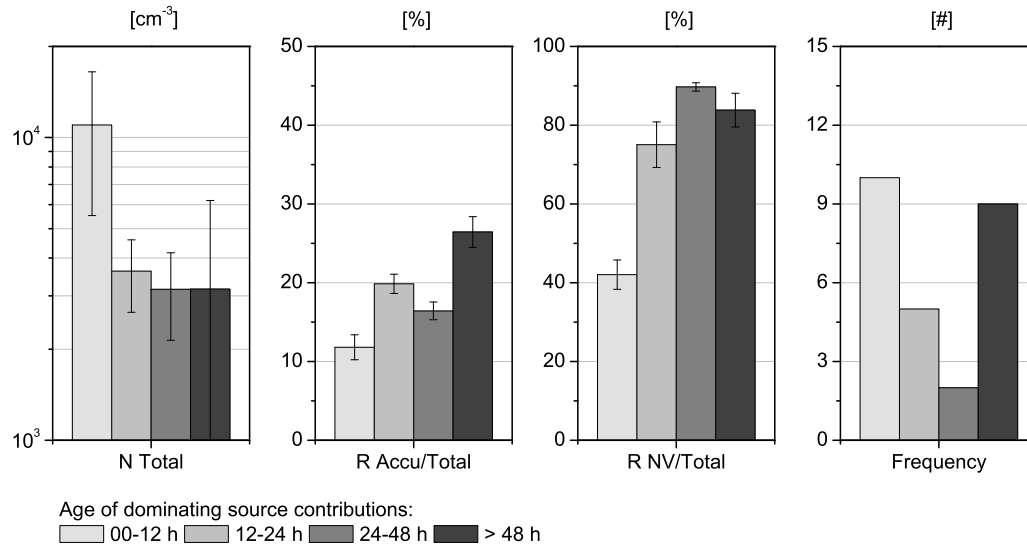


Figure 5.15: Averages of total number concentration, number ratio of non-volatile particles, volume ratio of volatile matter, and frequency of the age classes ($sf=1$).

5.4 The applicability of FLYTUL

The trajectory analysis method, which was newly developed in this work, showed good applicability to the aerosol measurements performed during the EUCAARI-LONGREX experiment with respect to the aerosol source contributions along the air mass transport pathway. The FLYTUL program proved easy handling to analyse airborne measurements and a wide field of application. The program can be used to calculate and graphically display meteorological parameters along a flight track from a three dimensional model field (Section 5.1), calculate back trajectories from a flight track or fixed region and analyse the trajectories with respect to the meteorological conditions and source contributions along the transport pathway. Each point along a trajectory can be directly analysed (Section 5.2) or a trajectory can be quantified using the temporal weighted averaging, which was set to the lifetime of aerosol particles in the boundary layer or the free troposphere if required (Section 5.3).

The analysis of the aerosol measurements with respect to the cloud cover and precipitation indicates that several effects have different impacts on the aerosol population. Wet deposition of particles was analysed as well as activation and processing of particles in

non-precipitating clouds. However, the significance of the analysis cannot completely demonstrate the effects of cloud cover and precipitation on the aerosol population. This is due to the complexity of cloud-aerosol interactions and the different effects of clouds on aerosol particles as discussed in Section 5.2. To demonstrate cloud-aerosol interactions a detailed model covering the physicochemical processes is required. However, the used analysis method gives valuable meteorological information for the interpretation of aerosol measurements.

The combination of trajectories with the EDGAR emission database and the subsequent analysis of the microphysical aerosol properties yielded to successful results. Pollution events at the measurement sites could be related to air masses originating from regions with high emissions. The analysis showed that the source contributions along the transport pathway are an important factor governing the aerosol microphysical properties in Europe. The multiplicity of different sources in the densely populated region did not allow a distinct source apportionment. However, a link between the aerosol properties and the age of the dominating source contributions could be established using the FLYTUL program. The temporal analysis of the polluted air masses was in agreement with the microphysical properties of aged aerosol, which were analysed in the Sections above. Ageing processes could be identified and quantified. The FLYTUL program can be used to analyse and classify air masses over densely populated or remote regions in particular for purposes of (airborne) aerosol measurements.

Chapter 6

Summary & conclusion

In the framework of the EUCAARI project we obtained a data set of airborne measurements unique in its spatial dimensions over Europe. The evolution of aerosol properties during stable synoptic conditions was observed for the first time on a continental scale and throughout the whole troposphere using airborne in-situ measurements. The spatial and temporal distribution and variability of aerosol particles, the influence of source contributions on the aerosol particles, and ageing processes over a densely populated region were measured and analysed.

A qualitative and quantitative analysis of microphysical aerosol properties measured within the troposphere above Europe can be provided. The analysis focussed on aerosol properties in the context of the prevailing meteorological conditions and the transport conditions affecting the probed air masses. The airborne measurements of microphysical aerosol properties were conducted aboard the DLR Falcon 20 research aircraft during the EUCAARI-LONGREX campaign in May 2008. The flights were performed from Oberpfaffenhofen and covered Central and Western Europe. Unlike many other aircraft campaigns the EUCAARI-LONGREX campaign did not only focus on one specific region or altitude level. The measurements covered the whole tropospheric column on a continental scale. Stable synoptic conditions enabled measurements at similar meteorological conditions during three weeks.

For the purpose of data analysis and interpretation, the trajectory analysis tool FLY-TUL was developed and optimised for airborne measurements. It comprises meteorological information from the ECMWF and source strength information from the EDGAR 3.2 Fast Track 2000 dataset. Trajectories can be classified using temporal distance weighting. The program code can be easily extended to add additional infor-

mation to the trajectory pathways if required.

The main results of the measurement and analysis of the microphysical properties are summarized in the following.

Dominating anticyclonic conditions. The meteorological situation in May 2008 could be separated into two different synoptic periods, during and after the blocking anticyclone. Northern Europe and the northern parts of Central and Western Europe were affected by an anticyclonic wind field throughout almost the whole measurement period. Differences between the stable and dry conditions during the first half of May and unstable and wet conditions during the second half of May could be observed above South Germany.

Increase of particulate matter inside the continental boundary layer. The stable meteorological conditions and anticyclonic wind field led to an increase of aerosol concentrations inside the boundary layer with a positive gradient following the westward transport of air masses from North-east Germany towards the Benelux States. Maximum number concentrations of total aerosol particles, particles containing a non-volatile core, and aerosol in the accumulation mode reached 22000 cm^{-3} , 8800 cm^{-3} , and 1600 cm^{-3} , respectively. A continuous high load of anthropogenic pollutions affected only regions inside the core of the anticyclone. However, one has to consider that the region which was directly affected by the anticyclone has a size of roughly 1000 km in diameter. Inside this large area, anthropogenic emissions of a multiplicity of sources could mix within the boundary layer.

Trapping of aerosol particles inside the boundary layer. The vertical profiles of aerosol concentrations showed a trapping of particles inside the boundary layer during the stable anticyclonic conditions. Regarding the particle load the boundary layer was vertically well mixed and showed high aerosol concentrations. In contrast, the lower free troposphere between 3–6 km above the boundary layer showed clean conditions in terms of aerosol particles with number concentrations reaching a maximum of 2000 cm^{-3} at standard temperature and pressure.

Increase of secondary aerosol mass. A strong accumulation of aerosol particles and condensation of aerosol precursor gases on pre-existing particles was verified. Due to the slower transport of locally produced pollutants an accumulation of anthropogenic pollution inside the boundary layer occurred. The volume ratio of volatile particle matter on submicron aerosol reached $\sim 85\text{--}95\%$. The volatile matter was dominated by organic aerosol. A zonal gradient from sulphate (east) to nitrate (west) was found.

Small spatial variability of accumulation mode particles on a regional scale.

The comparisons of ground-based and airborne aerosol measurements showed only small spatial variability of particles in the accumulation mode within a radius of ~ 150 km. The variability increased for particles in diameter less than $0.5 \mu\text{m}$ and reached a maximum for particles in the nucleation and Aitken mode.

Undisturbed transport of pollutants to remote regions and direct effect on radiative properties.

Long-range transport of the pollution from Central Europe led to pollution events outside the core region of the anticyclone. Continental European pollution particles were advected towards the Atlantic south west of Ireland and led to an increased aerosol optical depth above the affected region due to a high load of accumulation and coarse mode particles, which evolved during the undisturbed westward transport. The single case study demonstrates in a clear way the effect of anthropogenic emissions on the tropospheric aerosol optical depth.

Saturation of the coagulation process after two days. The meteorological analysis along air mass transport pathways using the new developed FLYTUL program showed no significant effect of cloud cover and precipitation on the measured aerosol properties during the stable anticyclonic conditions. Thus, ageing processes could be studied using the extensive dataset collected during the EUCAARI-LONGREX campaign. Although no real Lagrangian experiment could be accomplished during the aircraft campaign due to practical limitations, the stable meteorological conditions allowed studying transport processes at similar conditions. The time weighted trajectory analysis assess the age of the dominating source contributions and thus the age of the dominating aerosol fraction. It indicated that the main coagulation process happens within the first 12–24 h and reaches its minimum after two days. The maximum time of the measured ageing process agrees with the lifetime of aerosol particles inside the boundary layer of 48 h reported in previous studies (e.g. Riemer et al., 2004).

The multiplicity of different sources in Europe contributing to the aerosol measurements was one of the major difficulties in analysing the collected data. The aerosol measurements had to be classified in time and in space. However, the aerosol properties are not only affected by the current conditions. The history of the air mass containing the aerosol has a major impact on the properties of the particles, in particular in a region of varying source contributions like Europe. Thus, the analysis of the transport pathway using e.g. air mass trajectories is an essential procedure for the accurate interpretation of the measurements. The FLYTUL program is an easy to use tool to analyse the meteorological history and source contributions along an air mass

transport pathway. It proved its usability for the analysis of the EUCAARI-LONGREX campaign. However, it is not designed to reproduce detailed physicochemical processes.

The measurements performed during the EUCAARI-LONGREX campaign showed, that single and regional limited measurements are not sufficient to represent the aerosol distribution over Europe. The analysis of this work and reporting from accompanying work also shows that a detailed connection between airborne measurements and the respective sources is a yet unsolved task. The following comment made at the EUCAARI Annual meeting 2009 in Stockholm obtained common consent:

Europe is a big patchwork rug that emits a vast diversity of gases and particles. The boundary layer is its huge mixing chamber and that's where we make our measurements . . .

It shows that despite the international effort and success of the EUCAARI project only a minor fraction of the processes affecting atmospheric aerosol is well understood or can be reproduced or observed in the field. The results of this analysis can be used and are already used to support global aerosol and climate models. The collaboration of the measurement and model community ensures the improvement of today's knowledge to gain a more detailed insight into the physics of atmospheric aerosol.

Bibliography

- Ångström, A.: Atmospheric turbidity, global illumination and planetary albedo of the earth, *Tellus*, 14, 435–450, 1962.
- Ångström, A.: The parameters of atmospheric turbidity, *Tellus*, 16, 64–75, 1964.
- Addlesee, A.: Anisokinetic sampling of aerosols at a slot intake, *Journal of Aerosol Science*, 11, 483–493, 1980.
- Agarwal, J. K. and Sem, G. J.: Continuous flow, single-particle-counting condensation nucleus counter, *Journal of Aerosol Science*, 11, 343–357, 1980.
- Ansmann, A., Wandinger, U., Wiedensohler, A., and Leiterer, U.: Lindenberg Aerosol Characterization Experiment 1998 (LACE 98): Overview, *Journal of Geophysical Research*, 107, 8129, 2002.
- Banse, D. F., Esfeld, K., Hermann, M., Sierau, B., and Wiedensohler, A.: Particle counting efficiency of the TSI CPC 3762 for different operating parameters, *Journal of Aerosol Science*, 32, 157–161, 2001.
- Barriopedro, D., García-Herrera, R., Lupo, A. R., and Hernández, E.: A Climatology of Northern Hemisphere Blocking, *Journal of Climate*, 19, 1042–1063, 2006.
- Baumgardner, D. and Huebert, B.: The airborne aerosol inlet workshop: Meeting report, *Journal of Aerosol Science*, 24, 835–846, 1993.
- Belyaev, S. and Levin, L.: Techniques for collection of representative aerosol samples, *Journal of Aerosol Science*, 5, 325–338, 1974.
- Berner, A., Sidla, S., Galambos, Z., Kruisz, C., Hitzenberger, R., ten Brink, H. M., and Kos, G. P. A.: Modal character of atmospheric black carbon size distributions, *Journal of Geophysical Research*, 101, 19 559, 1996.

- Birmili, W., Wiedensohler, A., Heintzenberg, J., and Lehmann, K.: Atmospheric particle number size distribution in central Europe: Statistical relations to air masses and meteorology, *Journal of Geophysical Research*, 106, 32 005, 2001.
- Bohren, C. F. and Huffman, D. R.: *Absorption and scattering of light by small particles*, John Wiley & Sons, Inc., New York, 1983.
- Bond, T. C. and Bergstrom, R. W.: *Light Absorption by Carbonaceous Particles: An Investigative Review*, *Aerosol Science and Technology*, 40, 27–67, 2006.
- Bond, T. C., Anderson, T. L., and Campbell, D.: Calibration and Intercomparison of Filter-Based Measurements of Visible Light Absorption by Aerosols, *Aerosol Science and Technology*, 30, 582–600, 1999.
- Charlson, R. J. and Pilat, M. J.: Climate: The Influence of Aerosols, *Journal of Applied Meteorology*, 8, 1001–1002, 1969.
- Charlson, R. J., Horvath, H., and Pueschel, R. F.: The direct measurement of atmospheric light scattering coefficient for studies of visibility and pollution, *Atmospheric Environment* (1967), 1, 469–478, 1967.
- Chin, M., Kahn, R. A., and Schwartz, S. E.: *Atmospheric Aerosol Properties and Climate Impacts, Final Report, Synthesis and Assessment Product 2.3*, U.S. Climate Change Science Program, CCSP, 2009.
- Chýlek, P., Srivastava, V., Pinnick, R. G., and Wang, R. T.: Scattering of electromagnetic waves by composite spherical particles: experiment and effective medium approximations, *Applied Optics*, 27, 2396–2404, 1988.
- Ciddor, P. E.: Refractive index of air: new equations for the visible and near infrared, *Applied Optics*, 35, 1566–1573, 1996.
- Cooke, W. F., Jennings, S. G., and Spain, T. G.: Black carbon measurements at Mace Head, 1989, *Journal of Geophysical Research*, 102, 25 339, 1997.
- Crosby, P. and Koerber, B. W.: Scattering of Light in the Lower Atmosphere, *J. Opt. Soc. Am.*, 53, 358–359, 1963.
- Cubison, M. J., Alfarra, M. R., Allan, J., Bower, K. N., Coe, H., McFiggans, G. B., Whitehead, J. D., Williams, P. I., Zhang, Q., Jimenez, J. L., Hopkins, J., and Lee, J.: The characterisation of pollution aerosol in a changing photochemical environment, *Atmospheric Chemistry and Physics*, 6, 5573–5588, 2006.

- dal Maso, M., Sogacheva, L., Aalto, P. P., Riipinen, I., Komppula, M., Tunved, P., Korhonen, L., Suur-Uski, V., Hirsikko, A., Kurtén, T., Kerminen, V.-M., Lihavainen, H., Viisanen, Y., Hansson, H.-C., and Kulmala, M.: Aerosol size distribution measurements at four Nordic field stations: identification, analysis and trajectory analysis of new particle formation bursts, *Tellus B*, 59, 350–361, 2007.
- Dall’Osto, M., Ceburnis, D., Martucci, G., Bialek, J., Dupuy, R., Jennings, S. G., Berresheim, H., Wenger, J., Healy, R., Facchini, M. C., Rinaldi, M., Giulianelli, L., Finessi, E., Worsnop, D., Ehn, M., Mikkilä, J., Kulmala, M., and O’Dowd, C. D.: Aerosol properties associated with air masses arriving into the North East Atlantic during the 2008 Mace Head EUCAARI intensive observing period: an overview, *Atmospheric Chemistry and Physics*, 10, 8413–8435, 2010.
- DMT: Passive Cavity Aerosol Spectrometer Probe (PCASP-100X) Manual DOC-0228, Rev A, Droplet Measurement Technologies, Inc., Boulder, CO 80301 USA, 2009.
- Drewnick, F., Hings, S. S., DeCarlo, P., Jayne, J. T., Gonin, M., Fuhrer, K., Weimer, S., Jimenez, J. L., Demerjian, K. L., Borrmann, S., and Worsnop, D. R.: A New Time-of-Flight Aerosol Mass Spectrometer (TOF-AMS)-Instrument Description and First Field Deployment, *Aerosol Science and Technology*, 39, 637–658, 2005.
- Edlén, B.: The Refractive Index of Air, *Metrologia*, 2, 71, 1966.
- Eggleton, A.: The chemical composition of atmospheric aerosols on tees-side and its relation to visibility, *Atmospheric Environment* (1967), 3, 355–372, 1969.
- Engler, C., Rose, D., Wehner, B., Wiedensohler, A., Brüggemann, E., Gnauk, T., Spindler, G., Tuch, T., and Birmili, W.: Size distributions of non-volatile particle residuals ($D_p < 800$ nm) at a rural site in Germany and relation to air mass origin, *Atmospheric Chemistry and Physics*, 7, 5785–5802, 2007.
- Esselborn, M., Wirth, M., Fix, A., Tesche, M., and Ehret, G.: Airborne high spectral resolution lidar for measuring aerosol extinction and backscatter coefficients, *Applied Optics*, 47, 346–358, 2008.
- Feldpausch, P., Fiebig, M., Fritzsche, L., and Petzold, A.: Measurement of ultrafine aerosol size distributions by a combination of diffusion screen separators and condensation particle counters, *Journal of Aerosol Science*, 37, 577–597, 2006.
- Fenn, R., Shettle, E., Hering, W., and Johnson, R.: Atmospheric optical properties and meteorological conditions, *Atmospheric Environment* (1967), 15, 1911–1918, 1981.

- Fiebig, M.: Das troposphärische Aerosol in mittleren Breiten - Mikrophysik, Optik und Klimaantrieb am Beispiel der Feldstudie LACE 98, Dissertation, Fakultät für Physik der Ludwig-Maximilians-Universität München, Institut für Physik der Atmosphäre Oberpfaffenhofen, DLR, 2001.
- Flossmann, A. I.: Interaction of Aerosol Particles and Clouds, *Journal of the Atmospheric Sciences*, 55, 879–887, 1998.
- Forster, P., Ramaswamy, V., Artaxo, P., Berntsen, T., Betts, R., Fahey, D., Haywood, J., Lean, J., Lowe, D., Myhre, G., Nganga, J., Prinn, R., Raga, G., Schulz, M., and Van Dorland, R.: Changes in Atmospheric Constituents and in Radiative Forcing, In: *Climate Change 2007: The Physical Science Basis, Contribution of Working Group I to the Fourth Assessment Report of the Intergovernmental Panel on Climate Change* [Solomon, S., D. Qin, M. Manning, Z. Chen, M. Marquis, K.B. Averyt, M. Tignor and H.L. Miller (eds.)], 2007.
- Gentry, J. W.: The legacy of John Tyndall in aerosol science, *Journal of Aerosol Science*, 28, 1365–1372, 1997.
- Gerstengarbe, F.-W. and Werner, P. C.: Katalog der Grosswetterlagen Europas 1881–2004 nach P. Hess und H. Brezowsky. 6. Auflage, PIK Report, 100, 2005.
- Goovaerts, P.: Geostatistical approaches for incorporating elevation into the spatial interpolation of rainfall, *Journal of Hydrology*, 228, 113–129, 2000.
- Grimm: Aerosolspektrometer SERIE 1.129 SKY-OPC, Vorläufige Version 1.4, GRIMM Aerosol Technik GmbH, 83404 Ainring, Germany, 2007.
- Gucker, F. T. and Rose, D. G.: A photoelectronic instrument for counting and sizing aerosol particles, *British Journal of Applied Physics*, 5, S138, 1954.
- Gysel, M., Crosier, J., Topping, D. O., Whitehead, J. D., Bower, K. N., Cubison, M. J., Williams, P. I., Flynn, M. J., McFiggans, G. B., and Coe, H.: Closure study between chemical composition and hygroscopic growth of aerosol particles during TORCH2, *Atmospheric Chemistry and Physics*, 7, 6131–6144, 2007.
- Hamburger, T., McMeeking, G., Minikin, A., Birmili, W., Dall’Osto, M., O’Dowd, C., Flentje, H., Henzing, B., Junninen, H., Kristensson, A., de Leeuw, G., Stohl, A., Burkhardt, J. F., Coe, H., Krejci, R., and Petzold, A.: Overview of the synoptic and pollution situation over Europe during the EUCAARI-LONGREX field campaign, *Atmospheric Chemistry and Physics*, 11, 1065–1082, 2011.

- Hamed, A., Birmili, W., Joutsensaari, J., Mikkonen, S., Asmi, A., Wehner, B., Spindler, G., Jaatinen, A., Wiedensohler, A., Korhonen, H., Lehtinen, K. E. J., and Laaksonen, A.: Changes in the production rate of secondary aerosol particles in Central Europe in view of decreasing SO₂ emissions between 1996 and 2006, *Atmospheric Chemistry and Physics*, 10, 1071–1091, 2010.
- Hänel, G.: The Properties of Atmospheric Aerosol Particles as Functions of the Relative Humidity at Thermodynamic Equilibrium with the Surrounding Moist Air, 19, 73–188, 1976.
- Haywood, J. and Boucher, O.: Estimates of the direct and indirect radiative forcing due to tropospheric aerosols: A review, *Rev. Geophys.*, 38, 513, 2000.
- Heard, M. and Wiffen, R.: Electron microscopy of natural aerosols and the identification of particulate ammonium sulphate, *Atmospheric Environment (1967)*, 3, 337–340, 1969.
- Hess, P. and Brezowsky, H.: Katalog der Grosswetterlagen Europas, *Berichte des Deutschen Wetterdienstes in der US-Zone*, 33, 1952.
- Hinds, W. C.: *Aerosol Technology: Properties, Behavior, and Measurement of Airborne Particles*, John Wiley & Sons, Inc., New York, 1982.
- Hinds, W. C.: *Aerosol Technology: Properties, Behavior, and Measurement of Airborne Particles*, John Wiley & Sons, Inc., New York, 2 edn., 1999.
- Hitzenberger, R. and Tohno, S.: Comparison of black carbon (BC) aerosols in two urban areas - concentrations and size distributions, *Atmospheric Environment*, 35, 2153–2167, 2001.
- Hock, N., Schneider, J., Borrmann, S., Römpp, A., Moortgat, G., Franze, T., Schauer, C., Pöschl, U., Plass-Dülmer, C., and Berresheim, H.: Rural continental aerosol properties and processes observed during the Hohenpeissenberg Aerosol Characterization Experiment (HAZE2002), *Atmospheric Chemistry and Physics*, 8, 603–623, 2008.
- Holmes, N.: A review of particle formation events and growth in the atmosphere in the various environments and discussion of mechanistic implications, *Atmospheric Environment*, 41, 2183–2201, 2007.
- Holzworth, G. C.: Estimates of mean maximum mixing depths in the contiguous United States, *Monthly Weather Review*, 92, 235–242, 1964.

- Hoppel, W. A., Frick, G. M., Fitzgerald, J. W., and Wattle, B. J.: A Cloud Chamber Study of the Effect That Nonprecipitating Water Clouds Have on the Aerosol Size Distribution, *Aerosol Science and Technology*, 20, 1–30, 1994.
- Horvath, H.: Atmospheric visibility, *Atmospheric Environment* (1967), 15, 1785–1796, 1981.
- Hoyningen-Huene, W. V. and Wendisch, M.: Variability of aerosol optical parameters by advective processes, *Atmospheric Environment*, 28, 923–933, 1994.
- Huang, S., Arimoto, R., and Rahn, K. A.: Sources and source variations for aerosol at Mace Head, Ireland, *Atmospheric Environment*, 35, 1421–1437, 2001.
- Huntrieser, H., Feigl, C., Schlager, H., Schröder, F., Gerbig, C., van Velthoven, P., Flatøy, F., Théry, C., Petzold, A., Höller, H., and Schumann, U.: Airborne measurements of NO_x, tracer species, and small particles during the European Lightning Nitrogen Oxides Experiment, *Journal of Geophysical Research*, 107, 4113, 2002.
- James, P. M.: An objective classification method for Hess and Brezowsky Grosswetterlagen over Europe, *Theoretical and Applied Climatology*, 88, 17–42, 2007.
- Jennings, S.: The mean free path in air, *Journal of Aerosol Science*, 19, 159–166, 1988.
- Jennings, S. G., Kleefeld, C., O’Dowd, C. D., Junker, C., Spain, T. G., O’Brien, P. and Roddy, A. F., and O’Connor, T. C.: Mace Head Atmospheric Research Station - characterization of aerosol radiative parameters, *Boreal Environment Research*, 8, 303–314, 2003.
- Jimenez, J. L., Canagaratna, M. R., Donahue, N. M., Prevot, A. S. H., Zhang, Q., Kroll, J. H., DeCarlo, P. F., Allan, J. D., Coe, H., Ng, N. L., Aiken, A. C., Docherty, K. S., Ulbrich, I. M., Grieshop, A. P., Robinson, A. L., Duplissy, J., Smith, J. D., Wilson, K. R., Lanz, V. A., Hueglin, C., Sun, Y. L., Tian, J., Laaksonen, A., Raatikainen, T., Rautiainen, J., Vaattovaara, P., Ehn, M., Kulmala, M., Tomlinson, J. M., Collins, D. R., Cubison, M. J., E., Dunlea, J., Huffman, J. A., Onasch, T. B., Alfarra, M. R., Williams, P. I., Bower, K., Kondo, Y., Schneider, J., Drewnick, F., Borrmann, S., Weimer, S., Demerjian, K., Salcedo, D., Cottrell, L., Griffin, R., Takami, A., Miyoshi, T., Hatakeyama, S., Shimono, A., Sun, J. Y., Zhang, Y. M., Dzepina, K., Kimmel, J. R., Sueper, D., Jayne, J. T., Herndon, S. C., Trimborn, A. M., Williams, L. R., Wood, E. C., Middlebrook, A. M., Kolb, C. E., Baltensperger, U., and Worsnop, D. R.: Evolution of Organic Aerosols in the Atmosphere, *Science*, 326, 1525–1529, 2009.

- Junge, C. E.: The Chemical Composition of Atmospheric Aerosols, I: Measurements at Round Hill Field Station, June–July 1953, *Journal of Meteorology*, 11, 323–333, 1954.
- Junker, C., Jennings, S. G., and Cachier, H.: Aerosol light absorption in the North Atlantic: trends and seasonal characteristics during the period 1989 to 2003, *Atmospheric Chemistry and Physics*, 6, 1913–1925, 2006.
- Kahl, J. D.: A cautionary note on the use of air trajectories in interpreting atmospheric chemistry measurements, *Atmospheric Environment. Part A. General Topics*, 27, 3037–3038, 1993.
- Kennedy, I. M.: The health effects of combustion-generated aerosols, *Proceedings of the Combustion Institute*, 31, 2757–2770, 2007.
- Kleefeld, C., O’Dowd, C. D., O’Reilly, S., Jennings, S. G., Aalto, P., Becker, E., Kunz, G., and de Leeuw, G.: Relative contribution of submicron and supermicron particles to aerosol light scattering in the marine boundary layer, *Journal of Geophysical Research*, 107, 8103, 2002.
- Knobelspiesse, K. D., Pietras, C., Fargion, G. S., Wang, M., Frouin, R., Miller, M. A., Subramaniam, A., and Balch, W. M.: Maritime aerosol optical thickness measured by handheld sun photometers, *Remote Sensing of Environment*, 93, 87–106, 2004.
- Knutson, E. and Whitby, K.: Aerosol classification by electric mobility: apparatus, theory, and applications, *Journal of Aerosol Science*, 6, 443–451, 1975.
- Kukkonen, J., Pohjola, M., Sokhi, R. S., Luhana, L., Kitwiroon, N., Fragkou, L., Rantamäki, M., Berge, E., Ødegaard, V., Slørdal, L. H., Denby, B., and Finardi, S.: Analysis and evaluation of selected local-scale PM₁₀ air pollution episodes in four European cities: Helsinki, London, Milan and Oslo, *Atmospheric Environment*, 39, 2759–2773, 2005.
- Kulmala, M.: Atmospheric aerosols: global effects, *Journal of Aerosol Science*, 30, S1–S2, 1999.
- Kulmala, M., Vehkamäki, H., Petäjä, T., Maso, M. D., Lauri, A., Kerminen, V. M., Birmili, W., and McMurry, P. H.: Formation and growth rates of ultrafine atmospheric particles: a review of observations, *Journal of Aerosol Science*, 35, 143–176, 2004.
- Kulmala, M., Asmi, A., and Lappalainen, H.: EUCAARI: Description of Work, University of Helsinki, Helsinki, 2007.

- Kulmala, M., Asmi, A., Lappalainen, H. K., Carslaw, K. S., Pöschl, U., Baltensperger, U., Hov, O., Brenquier, J.-L., Pandis, S. N., Facchini, M. C., Hansson, H.-C., Wiedensohler, A., and O'Dowd, C. D.: Introduction: European Integrated Project on Aerosol Cloud Climate and Air Quality interactions (EUCAARI) – integrating aerosol research from nano to global scales, *Atmospheric Chemistry and Physics*, 9, 2825–2841, 2009.
- Laj, P., Klausen, J., Bilde, M., Plaß-Duelmer, C., Pappalardo, G., Clerbaux, C., Baltensperger, U., Hjorth, J., Simpson, D., Reimann, S., Coheur, P.-F., Richter, A., Mazière, M. D., Rudich, Y., McFiggans, G., Torseth, K., Wiedensohler, A., Morin, S., Schulz, M., Allan, J., Attié, J.-L., Barnes, I., Birmili, W., Cammas, J., Dommen, J., Dorn, H.-P., Fowler, D., Fuzzi, S., Glasius, M., Granier, C., Hermann, M., Isakson, I., Kinne, S., Koren, I., Madonna, F., Maione, M., Massling, A., Moehler, O., Mona, L., Monks, P., Müller, D., Müller, T., Orphal, J., Peuch, V.-H., Stratmann, F., Tanré, D., Tyndall, G., Riziq, A. A., Roozendael, M. V., Villani, P., Wehner, B., Wex, H., and Zardini, A.: Measuring atmospheric composition change, *Atmospheric Environment*, 43, 5351–5414, 2009.
- Liu, B., Zhang, Z., and Kuehn, T.: A numerical study of inertial errors in anisokinetic sampling, *Journal of Aerosol Science*, 20, 367–380, 1989.
- Liu, B. Y. and Pui, D. Y.: On the performance of the electrical aerosol analyzer, *Journal of Aerosol Science*, 6, 249–254, IN3–IN4, 255–264, 1975.
- Liu, J., Mauzerall, D. L., and Horowitz, L. W.: Evaluating inter-continental transport of fine aerosols:(2) Global health impact, *Atmospheric Environment*, 43, 4339–4347, 2009.
- Liu, P. S. K., Leitch, W. R., Strapp, J. W., and Wasey, M. A.: Response of Particle Measuring Systems Airborne ASASP and PCASP to NaCl and Latex Particles, *Aerosol Science and Technology*, 16, 83–95, 1992.
- Lloyd, C.: Assessing the effect of integrating elevation data into the estimation of monthly precipitation in Great Britain, *Journal of Hydrology*, 308, 128–150, 2005.
- Lohmann, U. and Feichter, J.: Global indirect aerosol effects: a review, *Atmospheric Chemistry and Physics*, 5, 715–737, 2005.
- Lu, G. Y. and Wong, D. W.: An adaptive inverse-distance weighting spatial interpolation technique, *Computers & Geosciences*, 34, 1044–1055, 2008.

- Lupo, A. R.: A Diagnosis of Two Blocking Events That Occurred Simultaneously in the Midlatitude Northern Hemisphere, *Monthly Weather Review*, 125, 1801–1823, 1997.
- Lupo, A. R. and Smith, P. J.: The Interactions between a Midlatitude Blocking Anticyclone and Synoptic-Scale Cyclones That Occurred during the Summer Season, *Monthly Weather Review*, 126, 502–515, 1998.
- Lyubovtseva, Y. S., Sogacheva, L., Dal Maso, M., Bonn, B., Keronen, P., and Kulmala, M.: Seasonal variations of trace gases, meteorological parameters, and formation of aerosols in boreal forests, *Boreal Environment Research*, 10, 493–510, 2005.
- Mayer, H.: Air pollution in cities, *Atmospheric Environment*, 33, 4029–4037, 1999.
- McMeeking, G. R., Hamburger, T., Liu, D., Flynn, M., Morgan, W. T., Northway, M., Highwood, E. J., Krejci, R., Allan, J. D., Minikin, A., and Coe, H.: Black carbon measurements in the boundary layer over western and northern Europe, *Atmospheric Chemistry and Physics*, 10, 9393–9414, 2010.
- Merrill, J. T., Bleck, R., and Avila, L.: Modeling Atmospheric Transport to the Marshall Islands, *Journal of Geophysical Research*, 90, 12 927, 1985.
- Methven, J., Arnold, S. R., Stohl, A., Evans, M. J., Avery, M., Law, K., Lewis, A. C., Monks, P. S., Parrish, D. D., Reeves, C. E., Schlager, H., Atlas, E., Blake, D. R., Coe, H., Crosier, J., Flocke, F. M., Holloway, J. S., Hopkins, J. R., McQuaid, J., Purvis, R., Rappenglück, B., Singh, H. B., Watson, N. M., Whalley, L. K., and Williams, P. I.: Establishing Lagrangian connections between observations within air masses crossing the Atlantic during the International Consortium for Atmospheric Research on Transport and Transformation experiment, *Journal of Geophysical Research*, 111, D23S62, 2006.
- Mie, G.: Beiträge zur Optik trüber Medien, speziell kolloidaler Metallösungen, *Annalen der Physik*, 330, 377–445, 1908.
- Minikin, A., Petzold, A., Ström, J., Krejci, R., Seifert, M., van Velthoven, P., Schlager, H., and Schumann, U.: Aircraft observations of the upper tropospheric fine particle aerosol in the Northern and Southern Hemispheres at midlatitudes, *Geophys. Res. Lett.*, 30, 1503, 2003.
- Morgan, W. T., Allan, J. D., Bower, K. N., Highwood, E. J., Liu, D., McMeeking, G. R., Northway, M. J., Williams, P. I., Krejci, R., and Coe, H.: Airborne measurements of the spatial distribution of aerosol chemical composition across Europe and evolution of the organic fraction, *Atmospheric Chemistry and Physics*, 10, 4065–4083, 2010.

- Müller, K.: A 3 year study of the aerosol in northwest Saxony (Germany), *Atmospheric Environment*, 33, 1679–1685, 1999.
- Neusüß, C., Wex, H., Birmili, W., Wiedensohler, A., Koziar, C., Busch, B., Brüggemann, E., Gnauk, T., Ebert, M., and Covert, D. S.: Characterization and parameterization of atmospheric particle number, *Journal of Geophysical Research*, 107, 8127, 2002.
- Niemi, J. V., Saarikoski, S., Aurela, M., Tervahattu, H., Hillamo, R., Westphal, D. L., Aarnio, P., Koskentalo, T., Makkonen, U., Vehkamäki, H., and Kulmala, M.: Long-range transport episodes of fine particles in southern Finland during 1999-2007, *Atmospheric Environment*, 43, 1255–1264, 2009.
- Oberdörster, G., Oberdörster, E., and Oberdörster, J.: Nanotoxicology: An Emerging Discipline Evolving from Studies of Ultrafine Particles, *Environ Health Perspect*, 113, 2005.
- O'Connor, T., Jennings, S., and O'Dowd, C.: Highlights of fifty years of atmospheric aerosol research at Mace Head, *Atmospheric Research*, 90, 338–355, 2008.
- O'Dowd, C. D., Lowe, J. A., and Smith, M. H.: The effect of clouds on aerosol growth in the rural atmosphere, *Atmospheric Research*, 54, 201–221, 2000.
- Olivier, J.: Part III: Greenhouse gas emissions: 1. Shares and trends in greenhouse gas emissions; 2. Sources and Methods; Greenhouse gas emissions for 1990 and 1995., CO₂ emissions from fuel combustion 1971-2000. International Energy Agency (IEA), Paris., pp. III.1–III.31., 2002.
- Patterson, R. K. and Wagman, J.: Mass and composition of an urban aerosol as a function of particle size for several visibility levels, *Journal of Aerosol Science*, 8, 269–279, 1977.
- Penner, J. E., Dong, X., and Chen, Y.: Observational evidence of a change in radiative forcing due to the indirect aerosol effect, *Nature*, 427, 231–234, 2004.
- Pernigotti, D., Rossa, A. M., Ferrario, M. E., Sansone, M., and Benassi, A.: Influence of ABL stability on the diurnal cycle of PM10 concentration: illustration of the potential of the new Veneto network of MW-radiometers and SODAR, *Meteorologische Zeitschrift*, 16, 505–511(7), 2007.
- Persson, A. and Grazzini, F.: User Guide to ECMWF forecast products v4.0, ECMWF Meteorological Bulletin, M3.2, 2007.

- Petzold, A., Fiebig, M., Flentje, H., Keil, A., Leiterer, U., Schröder, F., Stifter, A., Wendisch, M., and Wendling, P.: Vertical variability of aerosol properties observed at a continental site during the Lindenberg Aerosol Characterization Experiment (LACE 98), *Journal of Geophysical Research*, 107, 8128, 2002.
- Petzold, A., Weinzierl, B., Huntrieser, H., Stohl, A., Real, E., Cozic, J., Fiebig, M., Hendricks, J., Lauer, A., Law, K., Roiger, A., Schlager, H., and Weingartner, E.: Perturbation of the European free troposphere aerosol by North American forest fire plumes during the ICARTT-ITOP experiment in summer 2004, *Atmospheric Chemistry and Physics*, 7, 5105–5127, 2007.
- Petzold, A., Hasselbach, J., Lauer, P., Baumann, R., Franke, K., Gurk, C., Schlager, H., and Weingartner, E.: Experimental studies on particle emissions from cruising ship, their characteristic properties, transformation and atmospheric lifetime in the marine boundary layer, *Atmospheric Chemistry and Physics*, 8, 2387–2403, 2008.
- Pfaffenberger, L.: Partikelemissionen des Schiffsverkehrs und deren Einfluss auf das Aerosol der maritimen Grenzschicht - Ergebnisse der QUANTIFY SHIPS Studie 2007, Diplomarbeit, Meteorologisches Institut der Ludwig-Maximilians-Universität München, Institut für Physik der Atmosphäre Oberpfaffenhofen, DLR, 2009.
- Pinnick, R. and Auvermann, H.: Response characteristics of knollenberg light-scattering aerosol counters, *Journal of Aerosol Science*, 10, 55–74, 1979.
- Pinnick, R. and Rosen, J.: Response of Knollenberg light-scattering counters to non-spherical doublet polystyrene latex aerosols, *Journal of Aerosol Science*, 10, 533–535, 537–538, 1979.
- Pitz, M., Schmid, O., Heinrich, J., Birmili, W., Maguhn, J., Zimmermann, R., Wichmann, H.-E., Peters, A., and Cyrys, J.: Seasonal and Diurnal Variation of PM_{2.5} Apparent Particle Density in Urban Air in Augsburg, Germany, *Environmental Science & Technology*, 42, 5087–5093, 2008.
- Pluchino, A. B., Goldberg, S. S., Dowling, J. M., and Randall, C. M.: Refractive-index measurements of single micron-sized carbon particles, *Applied Optics*, 19, 3370–3372, 1980.
- Porter, J. N., Clarke, A. D., Ferry, G., and Pueschel, R. F.: Aircraft Studies of Size, *Journal of Geophysical Research*, 97, 3815, 1992.
- Pöschl, U.: Atmospheric Aerosols: Composition, Transformation, Climate and Health Effects, *Angewandte Chemie International Edition*, 44, 7520–7540, 2005.

- Poynting, J. H.: On the Transfer of Energy in the Electromagnetic Field, *Philosophical Transactions of the Royal Society of London*, 175, 343–361, 1884.
- Putaud, J.-P., Raes, F., Dingenen, R. V., Brüggemann, E., Facchini, M. C., Decesari, S., Fuzzi, S., Gehrig, R., Hüglin, C., Laj, P., Lorbeer, G., Maenhaut, W., Mihalopoulos, N., Müller, K., Querol, X., Rodriguez, S., Schneider, J., Spindler, G., ten Brink, H., Tørseth, K., and Wiedensohler, A.: A European aerosol phenomenology–2: chemical characteristics of particulate matter at kerbside, urban, rural and background sites in Europe, *Atmospheric Environment*, 38, 2579–2595, 2004.
- Putaud, J.-P., Dingenen, R. V., Alastuey, A., Bauer, H., Birmili, W., Cyrys, J., Flentje, H., Fuzzi, S., Gehrig, R., Hansson, H., Harrison, R., Herrmann, H., Hitzenberger, R., Hüglin, C., Jones, A., Kasper-Giebl, A., Kiss, G., Koussa, A., Kuhlbusch, T., Löschau, G., Maenhaut, W., Molnar, A., Moreno, T., Pekkanen, J., Perrino, C., Pitz, M., Puxbaum, H., Querol, X., Rodriguez, S., Salma, I., Schwarz, J., Smolik, J., Schneider, J., Spindler, G., ten Brink, H., Tursic, J., Viana, M., Wiedensohler, A., and Raes, F.: A European aerosol phenomenology - 3: Physical and chemical characteristics of particulate matter from 60 rural, urban, and kerbside sites across Europe, *Atmospheric Environment*, 44, 1308–1320, 2010.
- Raes, F., Dingenen, R. V., Vignati, E., Wilson, J., Putaud, J.-P., Seinfeld, J. H., and Adams, P.: Formation and cycling of aerosols in the global troposphere, *Atmospheric Environment*, 34, 4215–4240, 2000.
- Reeves, C. E., Formenti, P., Afif, C., Ancellet, G., Attie, J.-L., Bechara, J., Borbon, A., Cairo, F., Coe, H., Crumeyrolle, S., Fierli, F., Flamant, C., Gomes, L., Hamburger, T., Lambert, C., Law, K. S., Mari, C., Matsuki, A., Methven, J., Mills, G. P., Minikin, A., Murphy, J. G., Nielsen, J. K., Oram, D. E., Parker, D. J., Richter, A., Schlager, H., Schwarzenboeck, A., and Thouret, V.: Chemical and aerosol characterisation of the troposphere over West Africa during the monsoon period as part of AMMA, *Atmospheric Chemistry and Physics Discussions*, 10, 7115–7183, 2010.
- Riemer, N., Vogel, H., and Vogel, B.: Soot aging time scales in polluted regions during day and night, *Atmospheric Chemistry and Physics*, 4, 1885–1893, 2004.
- Robles González, C., Schaap, M., de Leeuw, G., Builtjes, P. J. H., and van Loon, M.: Spatial variation of aerosol properties over Europe derived from satellite observations and comparison with model calculations, *Atmospheric Chemistry and Physics*, 3, 521–533, 2003.

- Rose, D., Wehner, B., Ketzler, M., Engler, C., Voigtländer, J., Tuch, T., and Wiedensohler, A.: Atmospheric number size distributions of soot particles and estimation of emission factors, *Atmospheric Chemistry and Physics*, 6, 1021–1031, 2006.
- Sakerin, S. and Kabanov, D.: Some results of shipboard measurements of the aerosol optical thickness (AOT) at visible and near-IR wavelengths, *Journal of Aerosol Science*, 28, 107–108, 1997.
- Schäfer, K., Emeis, S., Hoffmann, H., and Jahn, C.: Influence of mixing layer height upon air pollution in urban and sub-urban areas, *Meteorologische Zeitschrift*, 15, 647–658, 2006.
- Seibert, P., Beyrich, F., Gryning, S.-E., Joffre, S., Rasmussen, A., and Tercier, P.: Review and intercomparison of operational methods for the determination of the mixing height, *Atmospheric Environment*, 34, 1001–1027, 2000.
- Seinfeld, J. H.: *Atmospheric chemistry and physics of air pollution*, John Wiley & Sons, Inc., New York, 1986.
- Seinfeld, J. H. and Pandis, S. N.: *Atmospheric chemistry and physics: From air pollution to climate change*, John Wiley & Sons, Inc., New York, 1998.
- Sellegri, K., Laj, P., Dupuy, R., Legrand, M., Preunkert, S., and Putaud, J.: Size, *Journal of Geophysical Research*, 108, 4334, 2003.
- Sheridan, P. J. and Norton, R. B.: Determination of the passing efficiency for aerosol chemical species through a typical aircraft, *Journal of Geophysical Research*, 103, 8215, 1998.
- Slanina, J., Lamoen-doornenbal, L. V., Lingerak, W. A., Meilof, W., Klockow, D., and Nießner, R.: Application of a Thermo-Denuder Analyser to the Determination of H₂SO₄, HNO₃ and NH₃ in Air, *International Journal of Environmental Analytical Chemistry*, 9, 59–70, 1981.
- Sogacheva, L., Dal Maso, M., Kerminen, V.-M., and Kulmala, M.: Probability of nucleation events and aerosol particle concentration in different air mass types arriving at Hyytiälä, *Boreal Environment Research*, 10, 479–491, 2005.
- Sogacheva, L., Saukkonen, L., Nilsson, E. D., Dal Maso, M., Schultz, D. M., De Leeuw, G., and Kulmala, M.: New aerosol particle formation in different synoptic situations at Hyytiälä, Southern Finland, *Tellus B*, 60, 485–494, 2008.

- Spindler, G., Brüggemann, E., Gnauk, T., Grüner, A., Müller, K., and Herrmann, H.: A four-year size-segregated characterization study of particles PM₁₀, PM_{2.5} and PM₁ depending on air mass origin at Melpitz, *Atmospheric Environment*, 44, 164–173, 2010.
- Srivastava, V., Chýlek, P., Pinnick, R. G., Dod, R. L., and Novakov, T.: Graphitic Carbon in Snow, *Aerosol Science and Technology*, 10, 151–160, 1989.
- Stein, C., Schröder, F., and Petzold, A.: The condensation particle size analyzer: A new instrument for the measurement of ultrafine aerosol size distributions, *Journal of Aerosol Science*, 32, 381–382, 2001.
- Stephens, M., Turner, N., and Sandberg, J.: Particle Identification by Laser-Induced Incandescence in a Solid-State Laser Cavity, *Applied Optics*, 42, 3726–3736, 2003.
- Stohl, A.: Computation, accuracy and applications of trajectories—A review and bibliography, *Atmospheric Environment*, 32, 947–966, 1998.
- Stohl, A., Wotawa, G., Seibert, P., and Kromp-Kolb, H.: Interpolation Errors in Wind Fields as a Function of Spatial and Temporal Resolution and Their Impact on Different Types of Kinematic Trajectories, *Journal of Applied Meteorology*, 34, 2149–2165, 1995.
- Stohl, A., Haimberger, L., Scheele, M. P., and Wernli, H.: An intercomparison of results from three trajectory models, *Meteorological Applications*, 8, 127–135, 2001.
- Stohl, A., Forster, C., Frank, A., Seibert, P., and Wotawa, G.: Technical note: The Lagrangian particle dispersion model FLEXPART version 6.2, *Atmospheric Chemistry and Physics*, 5, 2461–2474, 2005.
- Swietlicki, E., Zhou, J., Covert, D., Hameri, K., Busch, B., Vakeva, M., Dusek, U., Berg, O., Wiedensohler, A., Aalto, P., Makela, J., Martinsson, B., Papaspiropoulos, G., Mentes, B., Frank, G., and Stratmann, F.: Hygroscopic properties of aerosol particles in the north-eastern Atlantic during ACE-2, *Tellus B*, 52, 201–227, 2000.
- Toon, O. B., Pollack, J. B., and Khare, B. N.: The Optical Constants of Several Atmospheric Aerosol Species: Ammonium Sulfate, Aluminum Oxide, and Sodium Chloride, *Journal of Geophysical Research*, 81, 5733, 1976.
- Troen, I. B. and Mahrt, L.: A simple model of the atmospheric boundary layer; sensitivity to surface evaporation, *Boundary-Layer Meteorology*, 37, 129–148, 1986.

- Tunved, P., Hansson, H.-C., Kulmala, M., Aalto, P., Viisanen, Y., Karlsson, H., Kristensson, A., Swietlicki, E., Dal Maso, M., Ström, J., and Komppula, M.: One year boundary layer aerosol size distribution data from five nordic background stations, *Atmospheric Chemistry and Physics*, 3, 2183–2205, 2003.
- Tunved, P., Nilsson, E. D., Hansson, H., Ström, J., Kulmala, M., Aalto, P., and Viisanen, Y.: Aerosol characteristics of air masses in northern Europe: Influences of location, transport, sinks, and sources, *Journal of Geophysical Research*, 110, D07201, 2005.
- Tuomi, T. J.: Light scattering by aerosols with layered humidity-dependent structure, *Journal of Aerosol Science*, 11, 367–375, 1980.
- Twitty, J. T. and Weinman, J. A.: Radiative Properties of Carbonaceous Aerosols, *Journal of Applied Meteorology*, 10, 725–731, 1971.
- Twomey, S.: *Atmospheric aerosols*, Elsevier, Amsterdam, 1977a.
- Twomey, S.: On the Minimum Size of Particle for Nucleation in Clouds, *Journal of the Atmospheric Sciences*, 34, 1832–1835, 1977b.
- Twomey, S.: The Influence of Pollution on the Shortwave Albedo of Clouds, *Journal of the Atmospheric Sciences*, 34, 1149–1152, 1977c.
- Tyrllis, E. and Hoskins, B. J.: Aspects of a Northern Hemisphere Atmospheric Blocking Climatology, *Journal of the Atmospheric Sciences*, 65, 1638–1652, 2008.
- van Aardenne, J. A., Dentener, F. J., Olivier, J. G. J., Peters, J. A. H. W., and Ganzeveld, L. N.: The EDGAR 3.2 Fast Track 2000 dataset (32FT2000), 2005.
- van Dingenen, R., Raes, F., Putaud, J.-P., Baltensperger, U., Charron, A., Facchini, M. C., Decesari, S., Fuzzi, S., Gehrig, R., Hansson, H.-C., Harrison, R. M., Hüglin, C., Jones, A. M., Laj, P., Lorbeer, G., Maenhaut, W., Palmgren, F., Querol, X., Rodriguez, S., Schneider, J., ten Brink, H., Tunved, P., Tørseth, K., Wehner, B., Weingartner, E., Wiedensohler, A., and Wählin, P.: A European aerosol phenomenology–1: physical characteristics of particulate matter at kerbside, urban, rural and background sites in Europe, *Atmospheric Environment*, 38, 2561–2577, 2004.
- Venzac, H., Sellegri, K., Villani, P., Picard, D., and Laj, P.: Seasonal variation of aerosol size distributions in the free troposphere and residual layer at the puy de Dôme station, France, *Atmospheric Chemistry and Physics*, 9, 1465–1478, 2009.
- Virkkula, A.: Correction of the Calibration of the 3-wavelength Particle Soot Absorption Photometer (3? PSAP), *Aerosol Science and Technology*, 44, 706–712, 2010.

- Virkkula, A., Ahlquist, N. C., Covert, D. S., Arnott, W. P., Sheridan, P. J., Quinn, P. K., and Coffman, D. J.: Modification, Calibration and a Field Test of an Instrument for Measuring Light Absorption by Particles, *Aerosol Science and Technology*, 39, 68–83, 2005.
- Voigt, C., Schumann, U., Jurkat, T., Schäuble, D., Schlager, H., Petzold, A., Gayet, J.-F., Krämer, M., Schneider, J., Borrmann, S., Schmale, J., Jessberger, P., Hamburger, T., Lichtenstern, M., Scheibe, M., Gourbeyre, C., Meyer, J., Kübbeler, M., Frey, W., Kalesse, H., Butler, T., Lawrence, M. G., Holzäpfel, F., Arnold, F., Wendisch, M., Döpelheuer, A., Gottschaldt, K., Baumann, R., Zöger, M., Sölch, I., Rautenhaus, M., and Dörnbrack, A.: In-situ observations of young contrails – overview and selected results from the CONCERT campaign, *Atmospheric Chemistry and Physics*, 10, 9039–9056, 2010.
- Volz, F. E.: Infrared Absorption by Atmospheric Aerosol Substances, *Journal of Geophysical Research*, 77, 1017, 1972.
- Waggoner, A. P., Weiss, R. E., Ahlquist, N. C., Covert, D. S., Will, S., and Charlson, R. J.: Optical characteristics of atmospheric aerosols, *Atmospheric Environment* (1967), 15, 1891–1909, 1981.
- Wang, S. C. and Flagan, R. C.: Scanning Electrical Mobility Spectrometer, *Aerosol Science and Technology*, 13, 230–240, 1990.
- Went, F. W.: Blue Hazes in the Atmosphere, *Nature*, 187, 641–643, 1960.
- Wernli, H.: A lagrangian-based analysis of extratropical cyclones. II: A detailed case-study, *Quarterly Journal of the Royal Meteorological Society*, 123, 1677–1706, 1997.
- Wernli, H. and Davies, H. C.: A lagrangian-based analysis of extratropical cyclones. I: The method and some applications, *Quarterly Journal of the Royal Meteorological Society*, 123, 467–489, 1997.
- Whitby, K. T.: The physical characteristics of sulfur aerosols, *Atmospheric Environment*, 12, 135–159, 1978.
- White, W. H. and Roberts, P. T.: On the nature and origins of visibility-reducing aerosols in the los angeles air basin, *Atmospheric Environment* (1967), 11, 803–812, 1977.
- Wiedensohler, A., Orsini, D., Covert, D. S., Coffmann, D., Cantrell, W., Havlicek, M., Brechtel, F. J., Russell, L. M., Weber, R. J., Gras, J., Hudson, J. G., and Litchy, M.: Intercomparison Study of the Size-Dependent Counting Efficiency of 26 Condensation Particle Counters, *Aerosol Science and Technology*, 27, 224–242, 1997.

- Williams, J., de Reus, M., Krejci, R., Fischer, H., and Ström, J.: Application of the variability-size relationship to atmospheric aerosol studies: estimating aerosol lifetimes and ages, *Atmospheric Chemistry and Physics*, 2, 133–145, 2002.
- Yoon, Y. J., Ceburnis, D., Cavalli, F., Jourdan, O., Putaud, J. P., Facchini, M. C., Decesari, S., Fuzzi, S., Sellegri, K., Jennings, S. G., and O’Dowd, C. D.: Seasonal characteristics of the physicochemical properties of North Atlantic marine atmospheric aerosols, *Journal of Geophysical Research*, 112, D04 206, 2007.
- Zhang, R., Khalizov, A. F., Pagels, J., Zhang, D., Xue, H., and McMurry, P. H.: Variability in morphology, hygroscopicity, and optical properties of soot aerosols during atmospheric processing, *Proceedings of the National Academy of Sciences*, 105, 10 291–10 296, 2008.
- Zielinski, T. and Zielinski, A.: Aerosol extinction and aerosol optical thickness in the atmosphere over the Baltic Sea determined with lidar, *Journal of Aerosol Science*, 33, 907–921, 2002.

Appendix A

Tables

Table A.1: Flight sequences within the boundary layer and decoupled pollution layers and parameters to detect the stokes number of the isokinetic inlet.

Mission ID	Start [s]	End [s]	Alt [m]	p [hPa]	T [K]	v_{tas} [m s ⁻¹]	$D_{p,50}$ [μ m]	μ [kg/ms]	λ [μ m]	C_c	St
080506a	41654	41825	1210	876	281	119	1.44	1.76e-05	7.13e-02	1.12	0.434
080506a	41839	42032	1210	876	281	112	1.43	1.76e-05	7.14e-02	1.13	0.403
080506a	42090	42280	804	920	284	109	1.28	1.77e-05	6.90e-02	1.14	0.315
080506b	61148	61542	814	919	285	111	1.83	1.78e-05	6.93e-02	1.10	0.627
080508a	32369	33169	1460	850	279	102	1.73	1.75e-05	7.29e-02	1.11	0.529
080508a	39221	39398	1820	813	275	114	1.39	1.73e-05	7.47e-02	1.14	0.397
080508a	39572	39722	707	931	282	110	1.38	1.76e-05	6.75e-02	1.12	0.366
080508b	56729	56960	1520	844	282	115	1.49	1.76e-05	7.45e-02	1.13	0.445
080509a	47654	49030	1190	878	287	104	1.43	1.79e-05	7.32e-02	1.13	0.369
080513a	44071	44275	1820	813	277	115	1.31	1.74e-05	7.56e-02	1.15	0.354
080513a	44562	44776	1170	881	281	113	1.62	1.76e-05	7.11e-02	1.11	0.515
080513a	45078	45357	562	948	287	108	1.80	1.79e-05	6.77e-02	1.09	0.586
080513b	61628	61844	1820	813	279	118	1.82	1.75e-05	7.62e-02	1.11	0.676
080513b	61993	62230	1180	879	285	120	1.80	1.78e-05	7.24e-02	1.10	0.662
080513b	63065	63354	1180	879	284	133	1.39	1.77e-05	7.20e-02	1.13	0.447
080514a	34215	34369	266	982	284	107	1.40	1.77e-05	6.46e-02	1.12	0.365
080514a	43446	43770	1190	879	282	114	1.78	1.76e-05	7.16e-02	1.10	0.619
080514a	44080	44303	974	902	284	113	1.41	1.77e-05	7.02e-02	1.13	0.392
080514a	44455	44679	178	992	287	107	1.63	1.79e-05	6.47e-02	1.10	0.479
080520a	42725	43053	2430	753	270	116	1.83	1.70e-05	7.87e-02	1.11	0.696
080520a	43334	43554	1670	828	273	111	1.46	1.72e-05	7.28e-02	1.13	0.427
080520a	43767	43958	602	943	278	108	1.73	1.74e-05	6.55e-02	1.09	0.559
080520a	43958	44136	603	943	279	107	1.77	1.75e-05	6.56e-02	1.09	0.579
080520a	46238	46460	1190	878	277	114	1.35	1.74e-05	6.98e-02	1.13	0.368
080520a	46508	46754	1190	878	277	113	1.43	1.74e-05	7.00e-02	1.12	0.407
080521a	34932	35137	1520	844	271	113	1.47	1.71e-05	7.09e-02	1.12	0.440
080521a	35137	35339	1520	844	272	113	1.36	1.71e-05	7.10e-02	1.13	0.380
080521a	35651	35834	276	981	283	102	1.80	1.76e-05	6.42e-02	1.09	0.559
080521b	45300	45889	566	947	284	109	1.80	1.77e-05	6.69e-02	1.09	0.596
080521b	46427	46822	1520	844	276	102	1.81	1.73e-05	7.23e-02	1.10	0.582
080522a	42264	42371	1520	844	277	93	1.47	1.74e-05	7.29e-02	1.12	0.357
080522b	49018	49260	1200	877	280	116	0.71	1.75e-05	7.09e-02	1.25	0.115
080524a	33050	33319	3950	621	266	138	1.39	1.69e-05	9.41e-02	1.17	0.508

Table A.2: Upper bin limits for PCASP-100X and FSSP-300. The bin limits are given for polystyrene latex spheres (PSL, refractive index $1.59 \pm 0i$), Di-Ethyl-Hexyl-Sebacat (DEHS, refractive index $1.42 \pm 0i$), and ammonium sulphate particles (refractive index $1.53 \pm 0i$).

CH	Upper D_p PCASP-100X				Upper D_p FSSP-300			
	^m $1.59 \pm 0i$	[*] $1.59 \pm 0i$	[*] $1.42 \pm 0i$	^t $1.53 \pm 0i$	^m $1.59 \pm 0i$	^t $1.59 \pm 0i$	^c $1.42 \pm 0i$	^t $1.53 \pm 0i$
0	0.100	0.116	0.129	0.120	0.300	0.299	0.337	0.310
1	0.120	0.132	0.147	0.136	0.350	0.349	0.397	0.364
2	0.140	0.158	0.177	0.164	0.400	0.395	0.444	0.409
3	0.170	0.184	0.208	0.191	0.450	0.473	0.526	0.489
4	0.200	0.213	0.243	0.222	0.500	0.498	0.557	0.516
5	0.250	0.259	0.301	0.271	0.550	0.535	0.593	0.551
6	0.300	0.308	0.367	0.325	0.600	0.595	0.642	0.606
7	0.400	0.418	0.548	0.455	0.650	0.662	0.714	0.676
8	0.500	0.522	0.682	0.570	0.700	1.024	0.765	1.067
9	0.700	0.739	0.956	0.792	0.800	1.120	1.335	1.177
10	0.900	1.003	1.163	1.038	0.900	1.459	1.408	1.282
11	1.200	1.557	1.470	1.464	1.000	1.497	1.464	1.617
12	1.500	1.773	1.645	1.828	1.200	1.941	1.510	1.645
13	2.000	2.043	2.388	2.208	1.400	2.020	1.627	2.204
14	2.500	2.616	3.133	2.764	1.700	2.080	2.706	2.267
15	3.000	3.197	3.758	3.436	2.000	3.356	2.834	3.667
16					2.500	4.416	3.933	3.846
17					3.000	4.654	4.156	5.038
18					3.500	7.380	6.701	7.119
19					4.000	8.419	7.477	8.212
20					4.500	10.119	8.616	9.815
21					5.000	12.199	10.164	11.461
22					6.000	13.498	11.416	12.757
23					7.000	14.387	12.557	13.668
24					8.000	15.863	13.342	15.027
25					9.000	16.748	14.078	15.914
26					10.000	17.999	15.008	16.896
27					12.000	19.306	16.319	18.535
28					14.000	21.782	18.108	20.663
29					16.000	24.432	20.713	23.081
30					18.000	28.060	23.482	26.826
31					20.000	31.545	26.431	29.811

Bin limits retrieved from :

^m : Manufacturer, ^{*} : Calibration by Fiebig (2001), ^c : Calibration, ^t : Mie theory

Table A.3: Upper bin limits for Grimm Sky-OPCs. The bin limits are given for polystyrene latex spheres (PSL, refractive index $1.59 \pm 0i$), Di-Ethyl-Hexyl-Sebacat (DEHS, refractive index $1.42 \pm 0i$), and ammonium sulphate particles (refractive index $1.53 \pm 0i$).

CH	Upper D_p Grimm Sky-OPC #1				Upper D_p Grimm Sky-OPC #2			
	^m $1.59 \pm 0i$	^c $1.59 \pm 0i$	^c $1.42 \pm 0i$	^c $1.53 \pm 0i$	^m $1.59 \pm 0i$	^c $1.59 \pm 0i$	^c $1.42 \pm 0i$	^c $1.53 \pm 0i$
0	0.250	0.270	0.264	0.258	0.250	0.283	0.268	0.259
1	0.280	0.289	0.300	0.293	0.280	0.301	0.308	0.294
2	0.300	0.306	0.340	0.334	0.300	0.310	0.344	0.335
3	0.350	0.348	0.394	0.382	0.350	0.351	0.390	0.383
4	0.400	0.390	0.472	0.440	0.400	0.392	0.466	0.432
5	0.450	0.448	0.548	0.513	0.450	0.456	0.550	0.513
6	0.500	0.513	0.616	0.578	0.500	0.526	0.619	0.583
7	0.580	0.576	0.716	0.666	0.580	0.592	0.733	0.675
8	0.650	0.677	0.892	0.769	0.650	0.703	0.888	0.782
9	0.700	0.788	1.024	0.888	0.700	0.793	1.045	0.908
10	0.800	0.895	1.215	1.028	0.800	0.883	1.247	1.056
11	1.000	1.099	1.445	1.190	1.000	1.059	1.494	1.229
12	1.300	1.314	1.722	1.380	1.300	1.255	1.793	1.433
13	1.600	1.657	2.055	1.600	1.600	1.579	2.158	1.672
14	2.000	2.000	2.455	1.858	2.000	1.942	2.601	1.953
15	2.500	2.445	2.938	2.158	2.500	2.337	3.139	2.283
16	3.000				3.000			
17	3.500				3.500			
18	4.000				4.000			
19	5.000				5.000			
20	6.500				6.500			
21	7.500				7.500			
22	8.500				8.500			
23	10.000				10.000			
24	12.500				12.500			
25	15.000				15.000			
26	17.500				17.500			
27	20.000				20.000			
28	25.000				25.000			
29	30.000				30.000			
30	32.000				32.000			
31	34.000				34.000			

Bin limits retrieved from :

^m : Manufacturer, ^c : Calibration, ^t : Mie theory

Table A.4: Vertical profiles performed with the DLR Falcon 20 during EUCAARI-LONGREX.

Mission ID	Profile ID	Start [s]	End [s]	Lon [°E]	Lat [°N]	min Alt [km]	max Alt [km]
080502a	080502aV1	32472	35790	10.99	46.78	0.6	12.0
080502a	080502aV2	39920	42960	11.66	46.77	0.9	12.3
080506a	080506aV1	34604	35775	10.37	48.04	0.8	9.8
080506a	080506aV2	39605	42715	1.51	52.82	0.6	9.9
080506a	080506aV3	43622	44675	3.81	51.96	0.1	3.2
080506b	080506bV1	55629	56773	5.55	52.08	0.1	9.6
080506b	080506bV2	58282	62118	12.51	50.88	0.9	9.5
080506b	080506bV3	62420	64814	12.02	48.57	0.6	8.0
080508a	080508aV1	29330	30262	12.00	48.05	0.6	8.6
080508a	080508aV2	30262	34695	12.65	50.71	0.2	9.2
080508a	080508aV3	37065	40721	17.15	55.07	0.8	10.0
080508a	080508aV4	40961	42449	13.32	54.45	0.1	8.6
080508b	080508bV1	49565	50849	11.05	53.48	0.2	10.4
080508b	080508bV2	53554	58211	5.64	51.57	1.6	10.7
080508b	080508bV3	60783	63041	10.63	47.71	0.7	9.5
080509a	080509aV1	42004	54228	10.43	48.26	0.6	7.7
080513a	080513aV1	38472	40442	12.31	49.27	0.6	10.1
080513a	080513aV2	42797	45842	13.99	52.23	0.6	10.1
080513a	080513aV3	49362	50113	11.65	48.34	0.6	2.5
080513b	080513bV1	53819	55685	10.78	49.12	0.6	11.0
080513b	080513bV2	59526	63798	-7.91	51.84	0.1	11.0
080514a	080514aV1	33397	35792	-9.80	53.25	0.1	9.2
080514a	080514aV2	41630	45379	-12.58	51.28	0.1	9.2
080514a	080514aV3	45379	46708	-9.86	52.31	0.1	6.1
080514b	080514bV1	51682	53278	-7.29	52.44	0.1	10.7
080514b	080514bV2	57177	59869	9.73	49.18	0.6	11.3
080520a	080520aV1	37510	38972	12.06	48.90	0.6	9.8
080520a	080520aV2	41331	44912	13.50	55.08	0.6	9.7
080520a	080520aV3	45398	47484	13.93	52.74	1.2	7.4
080520a	080520aV4	48718	50539	12.28	48.62	0.6	7.4
080521a	080521aV1	28795	29776	11.75	48.35	0.6	8.6
080521a	080521aV2	31660	37031	13.37	54.66	0.3	9.2
080521a	080521aV3	38357	40277	5.80	52.62	0.2	9.2
080521b	080521bV1	45111	50925	5.64	51.60	0.1	10.1
080521b	080521bV2	51861	54641	9.94	48.05	0.6	10.1
080522a	080522aV1	32108	33608	11.32	48.88	0.6	10.7
080522a	080522aV2	38849	42926	1.62	50.93	0.2	9.8
080522b	080522bV1	45876	46835	5.17	50.57	0.2	9.5
080522b	080522bV2	47397	49440	10.20	49.02	0.6	9.5
080524a	080524aV1	23191	24831	12.69	47.61	0.6	10.7
080524a	080524aV2	30112	34141	13.44	46.87	1.5	10.8
080524a	080524aV3	35998	37326	11.60	47.82	0.6	4.9

Table A.5: Average core parameters measured during horizontal flight sequences aboard the DLR Falcon 20: altitude (Alt), pressure (p), absolute temperature (T), number concentration of nucleation mode (Nuc), Aitken mode (Ait), accumulation mode (Acc), coarse mode (Coa), non volatile particles (NV), and volume mixing ratio of CO.

Mission ID	Profile ID	Layer	Start [s]	End [s]	Alt [km]	p [hPa]	T [K]	Nuc [cm ⁻³]	Ait [cm ⁻³]	Acc [cm ⁻³]	Coa [cm ⁻³]	NV [cm ⁻³]	CO [nmol mol ⁻¹]
080506a	080506aV2	UFT	39614	39816	9.7	275	220	223 ± 24	1298 ± 26	8 ± 3	—	135 ± 10	142 ± 1
080506a	080506aV2	UFT	40295	40464	6.1	466	250	202 ± 55	651 ± 21	13 ± 3	—	146 ± 17	143 ± 1
080506a	080506aV2	LFT	40982	41331	3.3	671	271	23 ± 32	1001 ± 238	45 ± 5	—	493 ± 46	184 ± 1
080506a	080506aV2	BL	41654	41825	1.2	876	281	0 ± 0	2927 ± 166	873 ± 30	—	2985 ± 151	217 ± 3
080506a	080506aV2	BL	41839	42032	1.2	878	281	0 ± 0	1282 ± 125	659 ± 52	—	1647 ± 73	199 ± 5
080506a	080506aV2	BL	42090	42280	0.8	921	284	35 ± 140	1347 ± 864	597 ± 68	—	1537 ± 361	194 ± 3
080506b	080506bV2	UFT	57968	58335	9.4	288	222	141 ± 69	784 ± 41	19 ± 4	—	242 ± 24	127 ± 2
080506b	080506bV2	UFT	58764	58881	8.5	330	229	135 ± 28	340 ± 10	2 ± 1	—	17 ± 1	123 ± 1
080506b	080506bV2	UFT	58900	59009	8.5	330	229	209 ± 68	225 ± 11	2 ± 1	—	11 ± 1	123 ± 1
080506b	080506bV2	UFT	59408	59617	6.1	466	250	510 ± 60	1152 ± 239	3 ± 1	—	22 ± 2	125 ± 1
080506b	080506bV2	UFT	59617	59680	6.1	466	250	434 ± 22	1328 ± 10	6 ± 2	—	32 ± 2	127 ± 1
080506b	080506bV2	LFT	60091	60269	4.3	596	263	0 ± 1	360 ± 29	90 ± 5	—	352 ± 10	133 ± 2
080506b	080506bV2	LFT	60394	60575	3.3	671	269	0 ± 0	424 ± 37	113 ± 16	—	401 ± 28	143 ± 5
080506b	080506bV2	LFT	60644	60817	3.3	671	269	1 ± 3	573 ± 76	61 ± 8	—	508 ± 82	158 ± 11
080506b	080506bV2	BL	61148	61542	0.8	919	285	36 ± 94	12708 ± 1471	442 ± 47	—	7359 ± 802	167 ± 2
080508a	080508aV2	LFT	30924	31186	5.5	507	254	44 ± 67	297 ± 28	30 ± 5	23.9 ± 2.5	144 ± 5	131 ± 3
080508a	080508aV2	LFT	31421	31628	3.6	645	267	0 ± 1	253 ± 11	41 ± 5	19.8 ± 5.1	166 ± 19	131 ± 3
080508a	080508aV2	BL	32369	33169	1.5	850	279	44 ± 326	2294 ± 97	891 ± 65	3.6 ± 1.1	2973 ± 125	162 ± 2
080508a	080508aV3	UFT	37043	37302	10.0	262	218	69 ± 10	733 ± 41	40 ± 9	36.5 ± 0.8	354 ± 40	147 ± 1
080508a	080508aV3	UFT	38150	38365	5.5	507	253	12 ± 6	436 ± 30	37 ± 5	7.9 ± 2.5	192 ± 8	137 ± 1
080508a	080508aV3	LFT	38631	38813	3.9	620	262	0 ± 0	367 ± 24	57 ± 7	16.0 ± 1.8	316 ± 39	141 ± 1
080508a	080508aV3	BL	39221	39398	1.8	813	275	0 ± 0	753 ± 44	128 ± 9	3.4 ± 1.5	680 ± 18	149 ± 1
080508a	080508aV3	BL	39572	39722	0.7	931	282	0 ± 0	2435 ± 192	339 ± 30	6.1 ± 0.7	2173 ± 77	161 ± 1
080508b	080508bV2	UFT	53152	53492	10.4	250	217	221 ± 104	884 ± 110	43 ± 12	18.0 ± 3.1	319 ± 30	116 ± 3
080508b	080508bV2	UFT	54069	54302	7.3	393	239	449 ± 124	1300 ± 231	22 ± 4	6.8 ± 0.6	170 ± 18	154 ± 1
080508b	080508bV2	UFT	54302	54417	7.3	393	239	850 ± 198	3036 ± 574	23 ± 4	4.4 ± 0.5	310 ± 57	154 ± 1
080508b	080508bV2	UFT	54676	55016	5.5	506	255	238 ± 122	824 ± 119	25 ± 4	9.9 ± 3.5	217 ± 19	147 ± 2
080508b	080508bV2	LFT	55342	55816	3.5	658	270	145 ± 164	394 ± 139	36 ± 3	6.3 ± 3.5	178 ± 18	145 ± 2
080508b	080508bV2	LFT	56027	56384	2.4	753	278	40 ± 59	791 ± 129	102 ± 6	2.2 ± 0.9	608 ± 26	158 ± 1
080508b	080508bV2	BL	56729	56960	1.5	844	282	31 ± 115	10810 ± 424	1612 ± 104	1.8 ± 0.3	8757 ± 226	258 ± 27
080509a	080509aV1	LFT	42527	43087	2.7	725	276	161 ± 103	715 ± 245	44 ± 5	0.1 ± 0.1	237 ± 21	113 ± 3
080509a	080509aV1	UFT	45840	46494	6.1	466	251	368 ± 281	1295 ± 476	26 ± 8	0.1 ± 0.1	329 ± 238	118 ± 3

Continued on next page

Table A.5 – continued from previous page

Mission ID	Profile ID	Layer	Start [s]	End [s]	Alt [km]	P [hPa]	T [K]	Nuc [cm ⁻³]	Ait [cm ⁻³]	Acc [cm ⁻³]	Coa [cm ⁻³]	NV [cm ⁻³]	CO [nmol mol ⁻¹]
080509a	080509aV1	BL	47654	49030	1.2	878	287	5052 ± 1803	10155 ± 1434	896 ± 80	0.3 ± 0.1	3277 ± 315	150 ± 4
080509a	080509aV1	LFT	49701	50248	3.6	645	268	69 ± 81	755 ± 156	39 ± 6	0.1 ± 0.1	195 ± 20	107 ± 1
080509a	080509aV1	UFT	51353	51822	7.3	393	240	318 ± 206	1234 ± 206	23 ± 4	8.5 ± 3.6	137 ± 36	118 ± 1
080509a	080509aV1	UFT	52366	52694	7.6	377	238	624 ± 294	1789 ± 465	14 ± 3	7.1 ± 0.9	134 ± 19	117 ± 1
080513a	080513aV2	DL	44071	44275	1.8	813	277	0 ± 0	1150 ± 166	688 ± 62	4.6 ± 3.4	1549 ± 140	143 ± 3
080513a	080513aV2	DL	44562	44776	1.2	881	281	0 ± 0	1157 ± 98	1097 ± 50	1.7 ± 1.3	2115 ± 56	150 ± 1
080513a	080513aV2	BL	45078	45357	0.6	947	287	133 ± 158	13667 ± 1640	825 ± 67	0.8 ± 0.1	4643 ± 737	179 ± 26
080513a	080513aV2	LFT	45732	45902	2.1	783	276	4 ± 12	443 ± 71	46 ± 5	0.1 ± 0.0	272 ± 20	111 ± 3
080513a	—	LFT	47100	47290	2.1	784	277	3599 ± 1298	18661 ± 1863	1167 ± 60	0.7 ± 0.2	4861 ± 499	141 ± 2
080513b	080513bV2	—	60041	60162	9.7	275	222	—	—	—	—	—	108 ± 4
080513b	080513bV2	LFT	60871	61016	4.9	550	259	226 ± 11	997 ± 38	20 ± 3	0.1 ± 0.0	174 ± 16	126 ± 1
080513b	080513bV2	DL	61628	61844	1.8	813	279	0 ± 0	3039 ± 377	816 ± 86	0.4 ± 0.1	3328 ± 413	158 ± 5
080513b	080513bV2	DL	61993	62230	1.2	879	285	0 ± 0	3867 ± 245	851 ± 52	0.3 ± 0.1	4142 ± 321	165 ± 3
080513b	080513bV2	DL	63065	63354	1.2	879	284	0 ± 0	2967 ± 90	1060 ± 49	0.6 ± 0.1	2958 ± 31	152 ± 1
080514a	080514aV1	BL	34215	34369	0.3	982	284	0 ± 0	3083 ± 141	929 ± 45	2.4 ± 0.3	3336 ± 107	157 ± 1
080514a	080514aV2	UFT	41960	42091	9.1	301	226	131 ± 17	726 ± 37	41 ± 14	1.6 ± 0.2	230 ± 13	115 ± 1
080514a	080514aV2	UFT	42333	42466	7.3	393	240	17 ± 15	1572 ± 94	37 ± 8	1.0 ± 0.7	640 ± 32	120 ± 1
080514a	080514aV2	DL	43039	43352	1.8	815	278	0 ± 0	2636 ± 87	1135 ± 47	0.4 ± 0.1	3510 ± 86	157 ± 1
080514a	080514aV2	DL	43446	43770	1.2	879	282	0 ± 0	2660 ± 53	1225 ± 22	1.8 ± 0.7	3541 ± 47	167 ± 3
080514a	080514aV2	DL	44080	44303	1.0	902	284	0 ± 0	2503 ± 40	1226 ± 25	1.6 ± 0.4	3494 ± 38	164 ± 1
080514a	080514aV2	BL	44455	44679	0.2	992	287	0 ± 0	3752 ± 53	1150 ± 37	1.6 ± 0.2	4432 ± 58	165 ± 1
080514b	080514bV2	—	57834	57909	9.7	275	222	411 ± 278	1695 ± 275	46 ± 18	0.7 ± 0.2	281 ± 28	113 ± 1
080514b	080514bV2	—	58918	59102	1.8	813	283	969 ± 405	17329 ± 2011	661 ± 56	1.9 ± 1.4	5550 ± 559	138 ± 3
080514b	080514bV2	—	59566	59731	1.2	875	289	1780 ± 2247	10929 ± 1440	609 ± 35	0.2 ± 0.1	4589 ± 507	144 ± 3
080520a	080520aV2	UFT	41216	41548	9.7	275	221	97 ± 48	522 ± 192	41 ± 8	0.2 ± 0.1	220 ± 41	91 ± 18
080520a	080520aV2	DL	42725	43053	2.4	753	270	34 ± 46	505 ± 205	97 ± 17	0.2 ± 0.1	328 ± 35	156 ± 2
080520a	080520aV2	DL	43334	43554	1.7	828	273	0 ± 0	196 ± 26	189 ± 10	0.4 ± 0.1	352 ± 16	158 ± 2
080520a	080520aV2	BL	43767	43958	0.6	943	278	77 ± 119	4435 ± 1284	549 ± 53	1.3 ± 0.3	2764 ± 205	167 ± 1
080520a	080520aV2	BL	43958	44136	0.6	943	279	0 ± 0	1968 ± 213	571 ± 83	0.6 ± 0.1	1977 ± 79	163 ± 1
080520a	080520aV2	LFT	44900	45390	3.0	698	268	0 ± 0	294 ± 40	78 ± 25	0.1 ± 0.1	311 ± 37	145 ± 5
080520a	080520aV3	LFT	45390	45879	3.0	698	269	0 ± 0	380 ± 75	333 ± 107	0.1 ± 0.0	672 ± 124	161 ± 8
080520a	080520aV3	LFT	45879	45993	3.0	698	268	0 ± 0	345 ± 37	184 ± 25	0.0 ± 0.0	487 ± 42	165 ± 4
080520a	080520aV3	BL	46238	46460	1.2	879	277	303 ± 304	9372 ± 1744	480 ± 25	0.5 ± 0.1	3046 ± 425	155 ± 1
080520a	080520aV3	BL	46508	46754	1.2	878	277	1019 ± 823	15358 ± 2822	824 ± 59	0.4 ± 0.1	3442 ± 229	156 ± 1
080521a	080521aV2	UFT	32917	33322	7.0	411	244	622 ± 143	2126 ± 463	12 ± 6	0.1 ± 0.0	51 ± 22	131 ± 2
080521a	080521aV2	LFT	33602	33778	5.2	528	257	1 ± 4	363 ± 25	106 ± 15	0.7 ± 0.1	355 ± 33	142 ± 4
080521a	080521aV2	LFT	34385	34636	2.4	753	273	0 ± 0	233 ± 39	132 ± 17	0.2 ± 0.1	320 ± 41	157 ± 5

Continued on next page

Table A.5 – continued from previous page

Mission ID	Profile ID	Layer	Start [s]	End [s]	Alt [km]	p [hPa]	T [K]	Nuc [cm ⁻³]	Ait [cm ⁻³]	Acc [cm ⁻³]	Coa [cm ⁻³]	NV [cm ⁻³]	CO [nmol mol ⁻¹]
080521a	080521aV2	BL	34932	35137	1.5	844	271	0 ± 0	3007 ± 383	486 ± 23	1.6 ± 0.4	2535 ± 215	168 ± 1
080521a	080521aV2	BL	35137	35339	1.5	845	272	0 ± 0	1350 ± 272	605 ± 60	0.8 ± 0.1	1649 ± 111	170 ± 2
080521a	080521aV2	BL	35651	35834	0.3	981	283	0 ± 0	4129 ± 72	205 ± 6	0.5 ± 0.1	2809 ± 41	165 ± 1
080521b	080521bV1	BL	45300	45889	0.6	947	284	136 ± 158	4954 ± 282	1197 ± 101	0.6 ± 0.1	4250 ± 163	167 ± 4
080521b	080521bV1	BL	46427	46822	1.5	844	276	528 ± 300	10553 ± 1288	1592 ± 127	1.2 ± 0.2	4939 ± 585	202 ± 21
080521b	080521bV1	LFT	47111	47346	2.1	783	275	0 ± 0	451 ± 27	108 ± 33	0.1 ± 0.0	422 ± 34	142 ± 2
080521b	080521bV1	LFT	48022	48215	4.9	550	260	27 ± 20	484 ± 69	107 ± 13	0.7 ± 0.1	400 ± 12	124 ± 1
080521b	080521bV1	LFT	48709	48902	7.0	411	244	30 ± 37	429 ± 104	80 ± 8	0.6 ± 0.1	252 ± 12	118 ± 1
080521b	080521bV1	UFT	49344	49628	9.1	302	226	168 ± 48	500 ± 93	22 ± 11	0.3 ± 0.2	67 ± 26	107 ± 2
080521b	080521bV1	UFT	49628	49828	9.1	301	225	431 ± 65	908 ± 98	12 ± 4	0.1 ± 0.1	51 ± 3	111 ± 1
080522a	080522aV2	UFT	39500	39635	9.1	301	226	210 ± 176	2652 ± 719	26 ± 5	1.0 ± 0.2	677 ± 97	108 ± 1
080522a	080522aV2	UFT	39890	40123	7.6	377	238	170 ± 200	2131 ± 520	26 ± 6	0.3 ± 0.1	385 ± 87	104 ± 2
080522a	080522aV2	LFT	40628	40944	4.9	550	260	79 ± 28	787 ± 144	50 ± 4	0.3 ± 0.1	295 ± 22	103 ± 3
080522a	080522aV2	LFT	41075	41230	4.3	596	264	48 ± 27	667 ± 139	35 ± 3	0.3 ± 0.1	233 ± 18	107 ± 3
080522a	080522aV2	LFT	41817	42026	2.7	725	272	50 ± 80	1012 ± 597	46 ± 3	0.2 ± 0.0	381 ± 53	114 ± 1
080522a	080522aV2	DL	42264	42371	1.5	844	277	558 ± 413	4612 ± 875	944 ± 112	0.6 ± 0.1	2425 ± 81	159 ± 5
080522b	080522bV2	UFT	47735	47812	8.8	315	228	632 ± 83	1190 ± 235	341 ± 273	0.6 ± 0.1	169 ± 33	110 ± 1
080522b	080522bV2	LFT	48548	48699	2.7	726	273	0 ± 0	835 ± 34	70 ± 17	0.2 ± 0.1	377 ± 40	124 ± 1
080522b	080522bV2	BL	49018	49260	1.2	877	280	337 ± 403	3973 ± 2045	355 ± 71	0.9 ± 1.3	1144 ± 192	165 ± 7
080524a	080524aV2	LFT	30803	31270	7.0	411	246	135 ± 60	909 ± 55	14 ± 4	2.9 ± 1.1	186 ± 34	121 ± 2
080524a	080524aV2	LFT	32404	32761	5.0	539	261	97 ± 37	708 ± 112	22 ± 5	0.1 ± 0.0	154 ± 7	113 ± 2
080524a	080524aV2	DL	33050	33319	3.9	621	266	8 ± 11	1533 ± 117	90 ± 22	0.1 ± 0.0	674 ± 98	120 ± 4
080524a	080524aV3	—	35913	36173	4.9	551	262	21 ± 10	566 ± 38	16 ± 4	0.0 ± 0.0	227 ± 24	112 ± 1

Appendix B

Figures

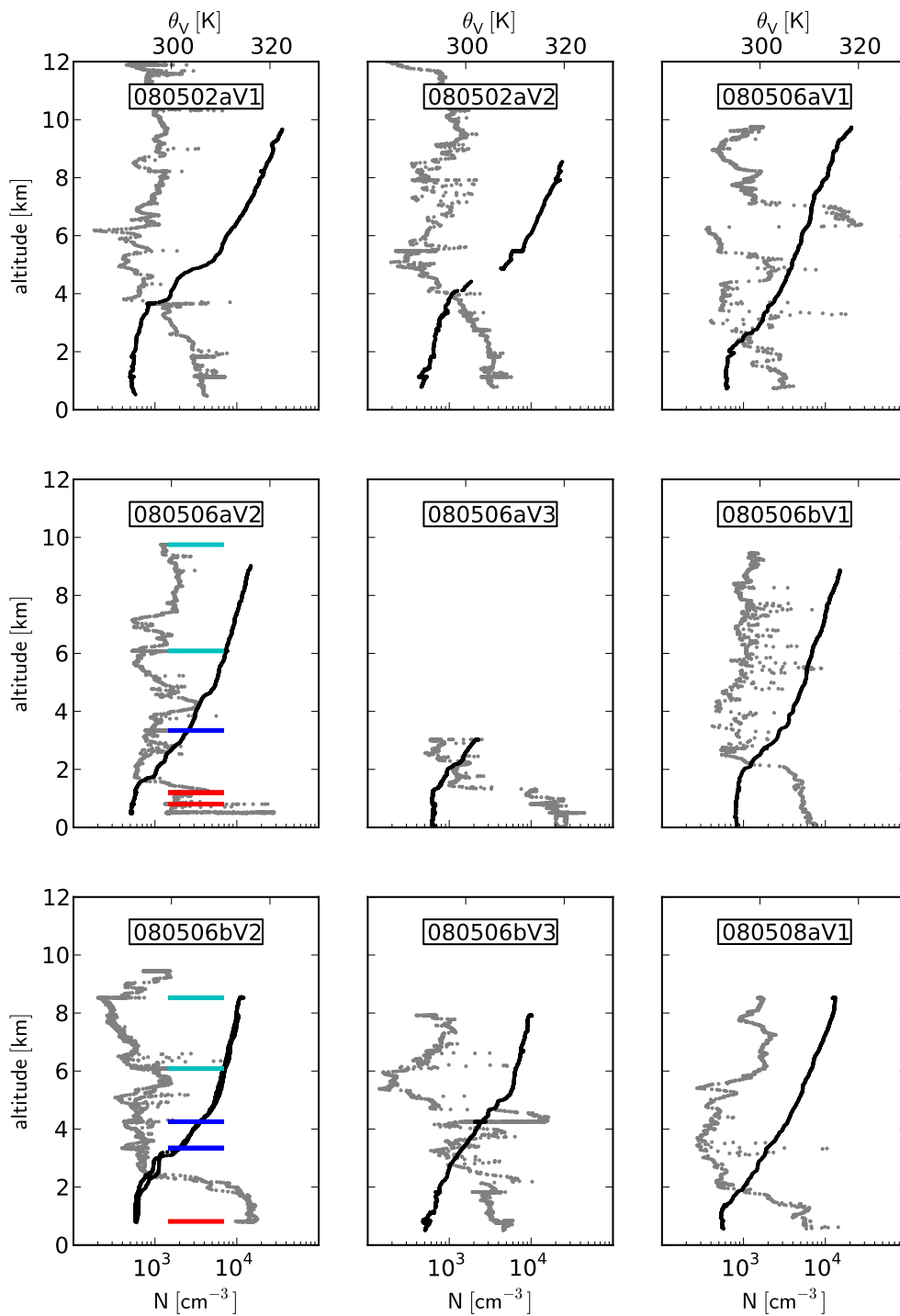


Figure B.1: Vertical profiles of Aitken mode particle number concentration [cm^{-3}] (grey) and virtual potential temperature [K] (black). Coloured horizontal lines indicate the level of horizontal flight legs within the vertical profile (red: inside boundary layer; magenta: pollution layer decoupled from boundary layer; blue: lower free troposphere; cyan: upper free troposphere).

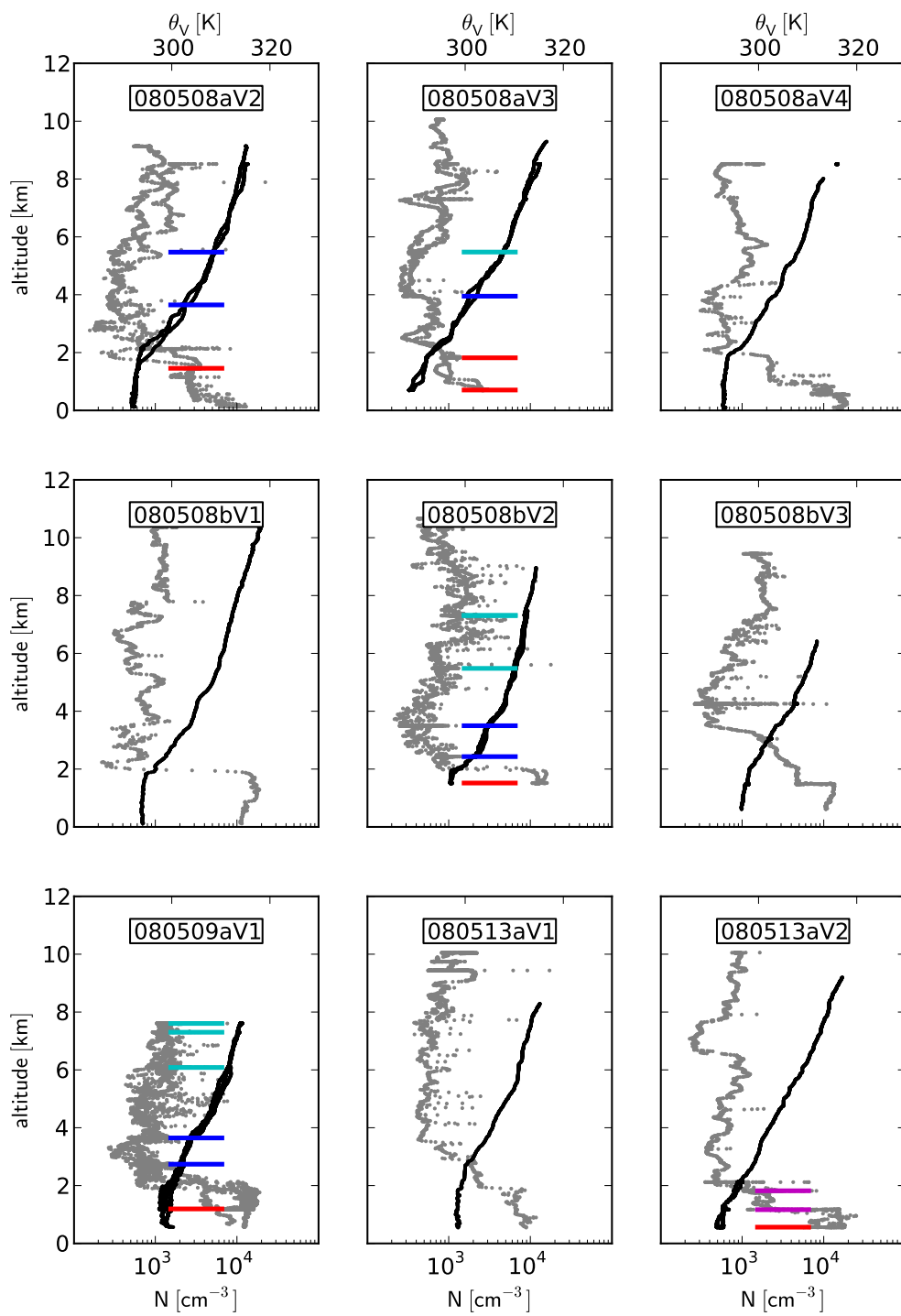


Figure B.2: See figure B.1.

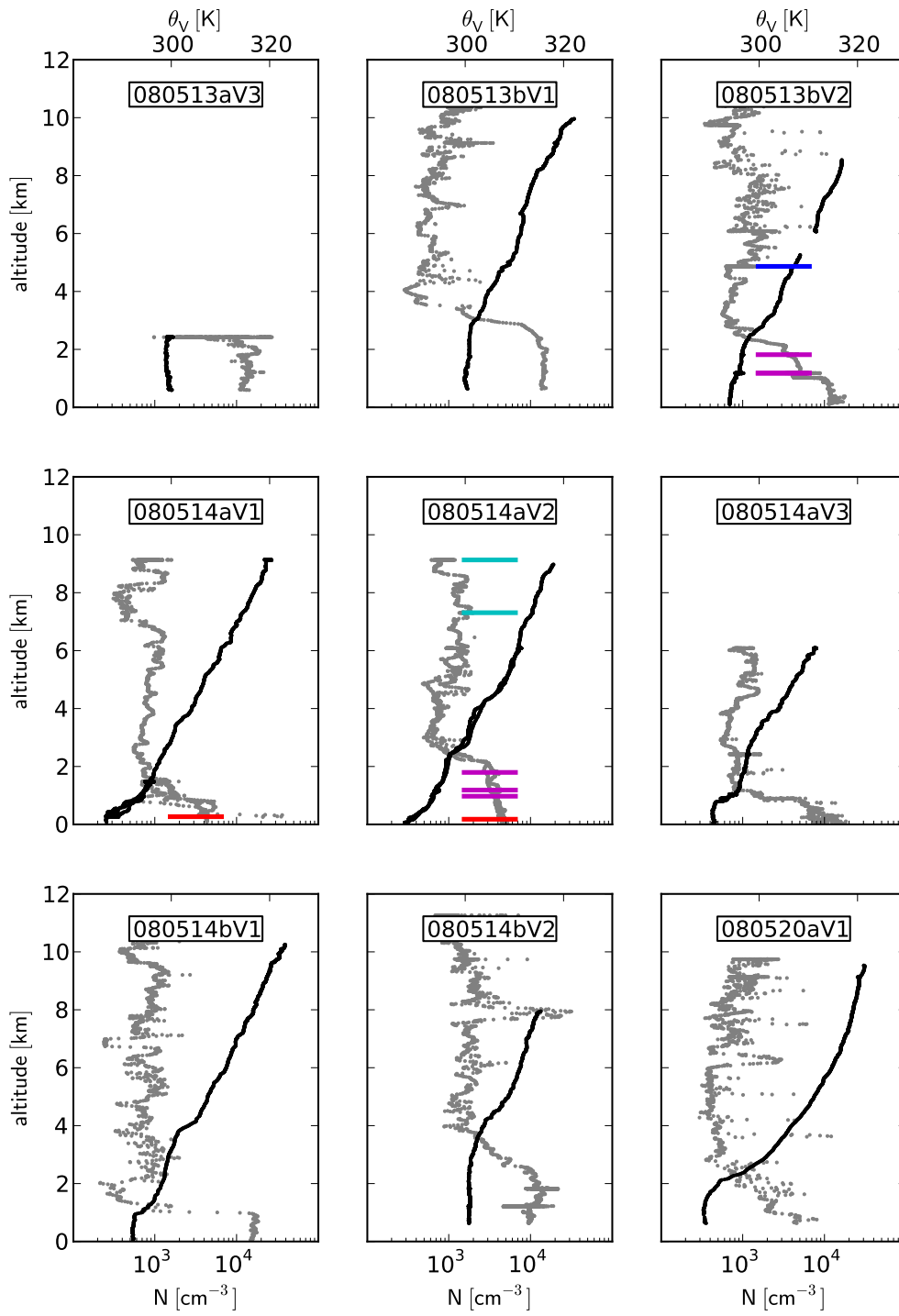


Figure B.3: See figure B.1.

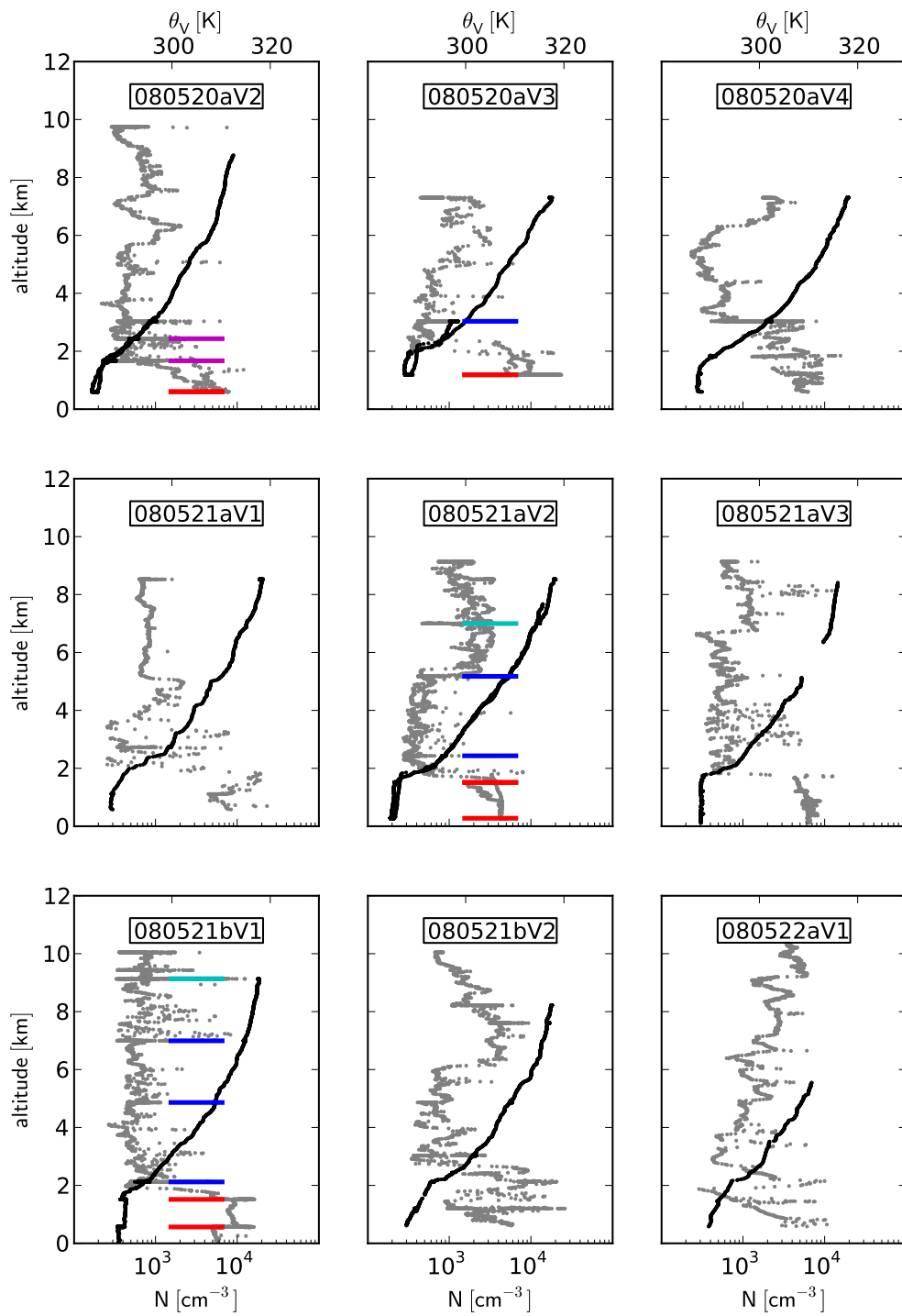


Figure B.4: See figure B.1.

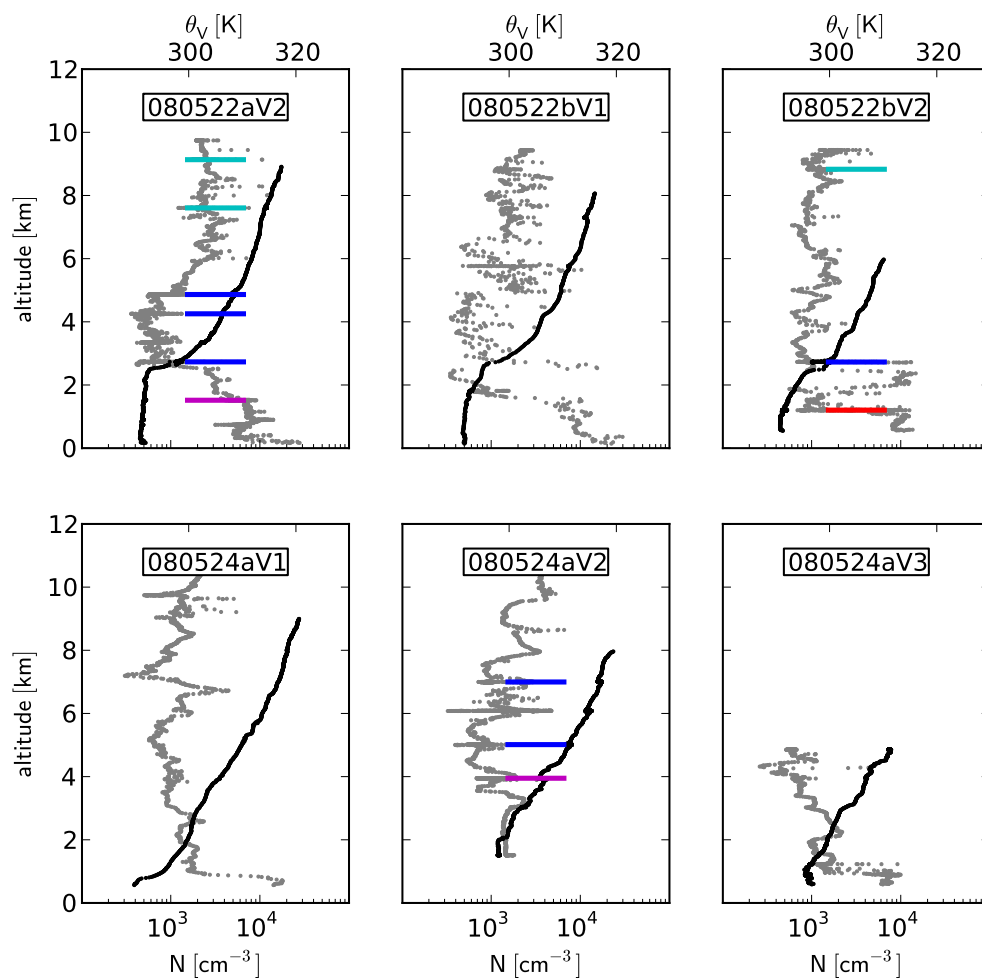


Figure B.5: See figure B.1.

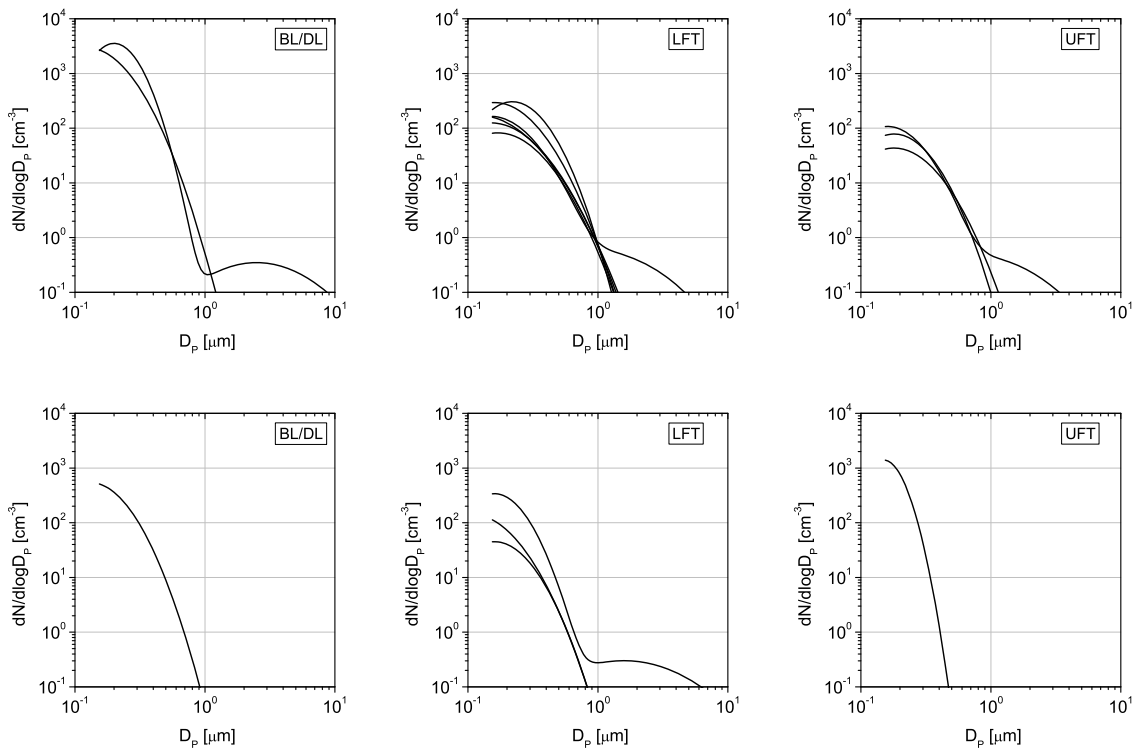


Figure B.6: Number size distributions over South Germany. Concentrations are given at standard pressure and temperature. The panels show measurements performed during horizontal flight legs within the boundary layer and decoupled layers (BL/DL), the lower free troposphere (LFT) and upper free troposphere (UFT). Upper panels show period (a), lower panels period (b).

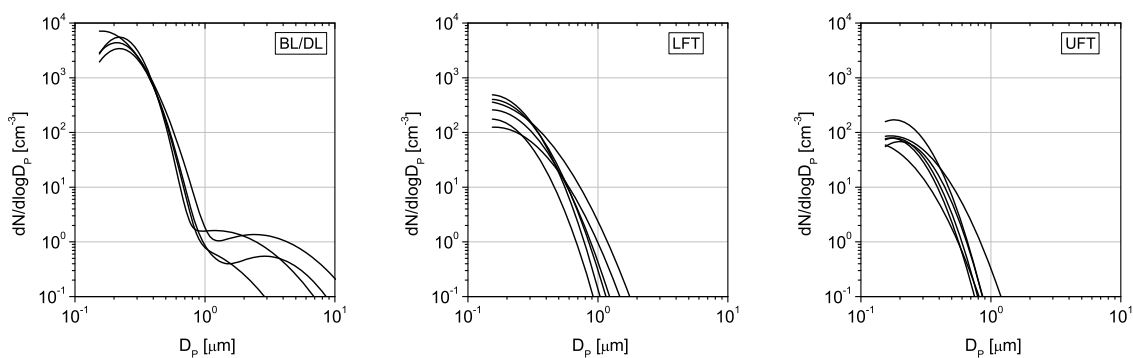


Figure B.7: Same as Figure B.6 for the Benelux States during May 2008.

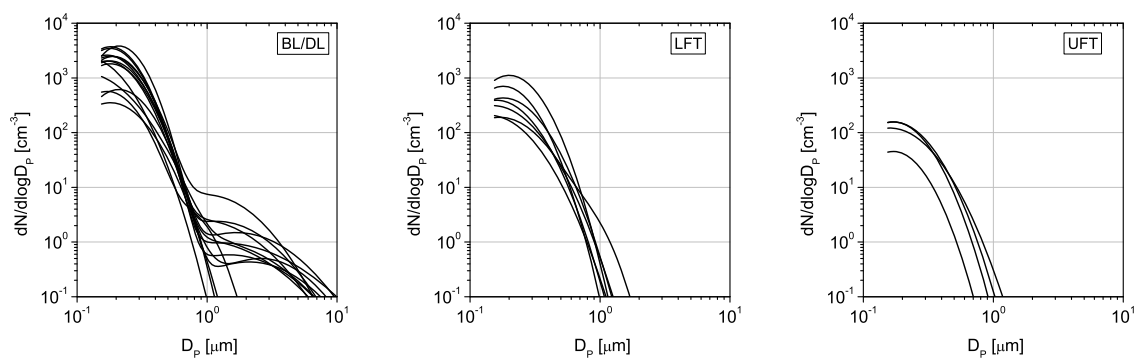


Figure B.8: Same as Figure B.6 for North-east Germany and the Baltic Sea during May 2008.



Figure B.9: High aerosol concentration within the boundary layer during high pressure conditions over Europe.

List of symbols

Symbol	Description
α	Ångström exponent
λ	Wavelength
μ	Mean of the gaussian distribution function
μ_a	Viscosity in air
μ_m	Linear mass increase coefficient
ω_0	Single scattering albedo
ϕ	Azimuthal scattering angle
ρ	Density
σ	Free surface energy
σ^2	Variance
σ_0	Uncorrected PSAP response
σ_{abs}	Absorption coefficient
σ_{ext}	Extinction coefficient
σ_{PSAP}	PSAP signal
σ_{sca}	Scattering coefficient
τ	Aerosol optical depth
θ	Scattering angle
A	Area
BI	Boundary layer index
C_{abs}	Absorption cross section
C_C	Cunningham factor
C_{ext}	Extinction cross section
C_{sca}	Scattering cross section
CBI	Continental boundary layer index
CH	Channel number
CI	Continental index
CMD	Count median diameter

Continued on next page

continued from previous page

Symbol	Description
CPI	Continental pollution index
d_i	Inner diameter of sampling tube
D_p	Particle diameter
E	Sampling efficiency
\mathbf{E}	Electric field
E_{GLOBAL}	Set of E_{SUM} not zero
E_{NORM}	Normalized anthropogenic emissions at one grid point
E_{P95}	95th percentile of E_{GLOBAL}
E_{SUM}	Sum of anthropogenic emissions at one grid point
f	Relative humidity
G	Cross sectional area
ΔG	Change of Gibbs free energy
GSD	Geometric standard deviation
\mathbf{H}	Magnetic field
I	Irradiance
I_0	Incoming irradiance
I_s	Scattered irradiance
k	Imaginary part of complex refractive index
m	Complex refractive index
M	Molecular mass
MBI	Maritime boundary layer index
MI	Maritime index
n	Real part of complex refractive index
N	Number concentration
N_m	Refractive index of medium
N_p	Refractive index of particle
Q	Flow
Q_{abs}	Absorption efficiency
Q_{ext}	Extinction efficiency
Q_{sca}	Scattering efficiency
r	Particle radius
r^*	Critical particle radius
R	Gas constant
S	Total surface of particles
\mathbf{S}	Poynting-Vector
$\tilde{\mathbf{S}}$	Amplitude scattering matrix
S_R	Saturation ratio
sf	Sigma factor

Continued on next page

continued from previous page

Symbol	Description
St	Stokes number
t	Time
T	Temperature
Tr	Transmission
V	Total volume of particles
w	Weighting factor
W_{abs}	Change of energy due to absorption
W_{ext}	Change of energy due to extinction
w_{GAUSS}	Gaussian weighting factor
W_{sca}	Change of energy due to scattering
x	Aersol size parameter

List of abbreviations

Abbreviation	Description
Acc	Accumulation mode
AERONET	Aerosol robotic network
Ait	Aitken mode
AOD	Aerosol optical depth
ATC	Air traffic control
BC	Black carbon
BHMIE	Mie-scattering algorithm by Bohren and Huffman
BL	Boundary layer
CC	Cloud cover
CCN	Cloud condensation nucleus
CN	Condensation nucleus
CNC	Condensation nucleus counter
Coa	Coarse mode
CPC	Condensation particle counter
DL	Decoupled layer
DLR	Deutsches Zentrum für Luft- und Raumfahrt
DMA	Differential mobility analyzer
DWD	Deutscher Wetterdienst
ECMWF	European centre for medium-range weather forecasts
EDGAR	Emissions database for global atmospheric research
EUCAARI	European aerosol cloud climate and air quality interactions
EUFAR	European facility for airborne research
EUSAAR	European supersites for atmospheric aerosol research
FAAM	Facility for airborne atmospheric measurements
FLYTUL	Flight analysis tool using LAGRANTO
FSSP	Forward scattering spectrometer probe
GWL	Grosswetterlage (large-scale circulation pattern)

Continued on next page

continued from previous page

Abbreviation	Description
HSRL	High spectral resolution lidar
IDW	Inverse distance weighting
IfT	Leibniz-Institut für Troposphärenforschung
IMPACT	Intensive observation period at Cabauw tower
IOP	Intensive observing period
LAGRANTO	Lagrangian analysis tool
LFT	Lower free troposphere
LIDAR	Light detection and ranging
LONGREX	Long-range experiment
LV-OOA	Low-volatile OOA
MSLP	Mean sea level pressure
NAIS	Neutral cluster - air ion spectrometer
Nuc	Nucleation mode
NV	Non-volatile
OA	Organic aerosol
OM	Organic matter
OOA	Oxygenated organic aerosol
OPC	Optical particle counter
PCASP	Passive cavity aerosol spectrometer probe
PSAP	Particle soot absorption photometer
SAFIRE	Avions français instrumentés pour la recherche en environnement
SV-OOA	Semi-volatile OOA
TRA	Temporary reserved area
UFT	Upper free troposphere

Acknowledgements

I would like to thank Dr. Andreas Petzold and Dr. Andreas Minikin for discussions, the advices and positive criticism that helped me to improve the thesis and my way of working and for supervising my work in the last years.

I also would like to thank Prof. Dr. Bernhard Mayer for co-examining this work and detailed comments and contributions leading to major improvements of the thesis.

I'm grateful to Prof. Dr. Ulrich Schumann and Dr. Hans Schlager for the possibility to learn and work at the department of Atmospheric Trace Species at the Institut für Physik der Atmosphäre, DLR, Oberpfaffenhofen.

Dr. Andreas Dörnbrack supported me in weather forecasting and analysis. He helped me with problems on meteorology, trajectory calculation, and data retrieval from the ECMWF.

A major part of this work would not have been possible without the great help and support of Hans Rüba with the aerosol instrumentation.

I also would like to thank Amir Ibrahim and all my other colleagues at the department for the creative working environment, the enjoyable breaks and the very good co-operation.

I'm grateful to the scientists providing the data of the ground based measurement sites, the whole team of the EUCAARI-LONREX campaign, the flight department, and the team operating aboard the BAe-146 for the outstanding teamwork during the campaign and all workshops after the campaign. Special thanks go to Prof. Hugh Coe, PI of the BAe-146 measurements, and Dr. Radovan Krejci, PI of the EUCAARI-LONREX aircraft campaign.

This work has been partly funded by EUCAARI (European Integrated project on Aerosol Cloud Climate and Air Quality interactions) No 036833-2.

Mein privater Dank geht an alle meine Freunde, die mich weiterhin in allem unterstützen obwohl ich sie im letzten Jahr sträflich vernachlässigt habe.

Danke auch meiner Familie, Linda, Markus, Eddie und Tom für eure Geduld. Auch euch habe ich viel zu wenig Zeit gewidmet.

Am meisten Dank geht allerdings an meine Eltern. Ihr habt mich immer bedingungslos unterstützt und mir immer euer vollstes Vertrauen geschenkt. Ihr habt den größten Teil dieser Arbeit geleistet.

Curriculum Vitae

Personal Data

Name: Thomas Hamburger
Place of Birth: München
Date of Birth: 22 January 1981
Nationality: German

Work Experience and Professional Training

2006–2011 Deutsches Zentrum für Luft und Raumfahrt DLR,
Oberpfaffenhofen
(Diploma thesis and PhD thesis on airborne
aerosol measurements and air mass transport)
2000–2001 Civilian Service - Sheltered workshop in Munich

Education

2008–2011 PhD thesis at Deutsches Zentrum für Luft und Raumfahrt DLR,
Oberpfaffenhofen
PhD thesis: Aerosol microphysical properties during
anticyclonic flow conditions over Europe
2001–2007 Studies of Meteorology at University of Munich
Diploma thesis: The impact of mesoscale convective systems on
tropospheric aerosol in the West African Monsoon System
Minor field of study: Computer Sciences
2000 Abitur (school leaving certificate) at
Wilhelm-Hausenstein-Gymnasium, Munich